Academic Press is an imprint of Elsevier
Linacre House, Jordan Hill, Oxford OX2 8DP, UK
32 Jamestown Road, London NW1 7BY, UK
Radarweg 29, PO Box 211, 1000 AE Amsterdam, The Netherlands
30 Corporate Drive, Suite 400, Burlington, MA 01803, USA
525 B Street, Suite 1900, San Diego, CA 92101-4495, USA

First edition 2011

British Library Cataloguing in Publication Data
A catalogue record for this book is available from the British Library

Library of Congress Cataloging-in-Publication Data
A catalog record for this book is available from the Library of Congress

ISBN: 978-0-08-097074-5
ISSN: 0066-4103

Printed and bound in Great Britain

11 12 13 10 9 8 7 6 5 4 3 2 1

CONTRIBUTORS

Bradley J. Butler
School of Chemistry, University of New South Wales, Sydney, New South Wales, Australia

Stefano Caldarelli
Aix Marseille Université, ISm2 UMR 6263, Campus de Saint Jérôme, Marseille, France

Jerry C. C. Chan
Department of Chemistry, National Taiwan University, Taipei, Taiwan

Songi Han
Department of Chemistry and Biochemistry, University of California, Santa Barbara, California, USA

Jason B. Harper
School of Chemistry, University of New South Wales, Sydney, New South Wales, Australia

James M. Hook
Mark Wainwright Analytical Centre, University of New South Wales, Sydney, New South Wales, Australia

Mark D. Lingwood
Department of Chemistry and Biochemistry, University of California, Santa Barbara, California, USA

János Rohonczy
Department of Inorganic Chemistry, Institute of Chemistry, Eötvös Loránd University, Budapest, Hungary

Zsófia Szalay
Department of Inorganic Chemistry, Institute of Chemistry, Eötvös Loránd University, Budapest, Hungary

Lynmarie K. Thompson
Department of Chemistry, University of Massachusetts Amherst, Massachusetts, USA

Tim W. T. Tsai
Department of Chemistry, National Taiwan University, Taipei, Taiwan

PREFACE

It is my pleasure to introduce Volume 73 of Annual Reports on NMR. In common with previous volumes, it contains reports from a few of the many areas of NMR active research. The first contribution is by T. W. T. Tsai and J. C. C. Chan on 'Recent Progress in the Solid-State NMR Studies of Biomineralization'; the topic 'Recent Advances in the NMR Spectroscopy of Chlorine, Bromine and Iodine' is covered by B. J. Butler, J. M. Hook and J. B. Harper; M. D. Lingwood and S. Han report on 'Solution-State Dynamic Nuclear Polarization'; the topic of 'Solid-State NMR of Membrane Proteins: Moving Towards Greater Complexity' is covered by L. K. Thompson; 'Chromatographic NMR' is the topic chosen by S. Caldarelli; the final contribution on 'Kinetic Monte Carlo Simulation of DNMR Spectra' is by Z. Szalay and J. Rohonczy. My grateful thanks are due to all of these reporters for their interesting and timely contributions.

G. A. Webb
Royal Society of Chemistry
Burlington House
Piccadilly, London, UK

CHAPTER 1

Recent Progress in the Solid-State NMR Studies of Biomineralization

Tim W. T. Tsai and **Jerry C. C. Chan**[1]

Contents

Department of Chemistry, National Taiwan University, Taipei, Taiwan
[1] Corresponding author.

Annual Reports on NMR Spectroscopy, Volume 73
ISSN 0066-4103, DOI: 10.1016/B978-0-08-097074-5.00001-3

Abstract Biomineralization is a challenging research area because it is extremely difficult to study the interaction between two dissimilar organic and inorganic nanophases. In this review, we have briefly discussed some advanced solid-state NMR techniques developed for the study of biominerals or related *in vitro* model systems. The P-31 NMR parameters of a list of model compounds have been compiled. These data should be useful for analyzing the NMR spectra of biominerals. We intend to provide an account of how one can employ the state-of-the-art solid-state NMR techniques to extract valuable structural information of biominerals that would be difficult to obtain otherwise.

Key Words: Biomineralization, Solid-state NMR, Biominerals, Calcium phosphate, Hydroxyapatite, Bone, Dentin, Ca-43 NMR, P-31 NMR, HAp.

1. INTRODUCTION

Biomineralization is a process describing the formation of composite materials in organisms.[1] It is a particularly challenging research area because it is extremely difficult to study the interaction between two dissimilar organic and inorganic nanophases by diffraction techniques. Thus, it has long been a mystery how living organisms control the mineral deposition with hierarchical structures. Because calcium phosphate is commonly found in the biominerals of vertebrates, ^{31}P solid-state NMR spectroscopy is a very important technique for the studies of bones and teeth. As discussed in a comprehensive review by Kolodziejski, most of the ^{31}P solid-state NMR studies on biomineralization during the 1980s and 1990s are focusing on bone and related model compounds.[2] Recently, the application of ^{29}Si solid-state NMR to the study of silica biomineralization has been reviewed extensively and some interesting applications of ^{31}P NMR to the study of biominerals have also been discussed.[3,4] The pioneering works by the Drobny group on the statherin–apatite interface have been reviewed regularly.[5–8] In an overview of the latest development in solid-state NMR and its application in the characterization of inorganic materials, an informative account of the current studies of

apatite systems and biomaterials has been given.[9] These reviews altogether provide an excellent introduction to the different facets of biomineralization. The advantage of solid-state NMR spectroscopy in the study of biomineralization needs no further elaboration. Nonetheless, solid-state NMR study of biomineralization is such a vibrant research field that many new concepts and exciting findings have been reported in the past few years. In fact, development of new solid-state NMR methods is often required to tackle challenging scientific issues, whereas those novel experimental strategies would further extend the realm of applications in solid-state NMR. Such beautiful synergy between problems and solutions is well illustrated in the study of biomineralization by solid-state NMR.

Although there are a lot of novel techniques developed in the past few years in solid-state NMR,[10–13] we will only discuss those methods which have been applied in the study of biomineralization. After an exposition of some advanced NMR techniques, we will discuss the NMR data obtained for certain important model compounds. We have compiled a list of inorganic phosphate compounds and summarized the relevant ^{31}P NMR parameters in a table. Then, we will review the studies of biomineralization carried out on some carefully designed *in vitro* model systems. Finally, selected examples of how solid-state NMR can provide important structural information of biominerals will be discussed. In this review, we simply cannot include every important aspect of the field. Regrettably, a thorough discussion of biomaterials as well as soft tissues such as gelatin and collagen is beyond the scope of the present review. Another omission is that the theoretical calculations of the chemical shielding and electric field gradient tensors of the model compounds of biominerals are not discussed. Literature reviews of these important areas in biomineralization are definitely in order.

2. METHODOLOGY

In this section, some NMR techniques which have been applied to the study of biomineralization are introduced. The NMR techniques discussed below are all under the condition of magic-angle spinning (MAS). The discussion is largely descriptive and qualitative. Readers who are interested in a more rigorous exposition of the NMR theories are referred to the original literature. The implications of the NMR results in biomineralization are discussed in other sections.

2.1. Cross polarization MAS

Cross polarization under MAS condition (CPMAS) is nowadays a ubiquitous technique in the studies of crystalline and amorphous systems. $^{31}P\{^{1}H\}$ CPMAS is well suited for the study of biomineralization because

the protonation states of phosphate ions are of primary concern in the study of biominerals containing calcium phosphate. A comparison of the CP and direct excitation (Bloch decay) spectra could provide valuable information concerning the speciation of the ^{31}P environment. On the basis of chemical shift data, it is usually quite straightforward to assign the ^{31}P signals arising from HPO_4^{2-} and PO_4^{3-} ions in model compounds. However, counter-ion effects can also make the ^{31}P chemical shift of the HPO_4^{2-} ions become significantly deshielded (6.6 ppm), just as in the case of Na_2HPO_4.[14] Also, a direct detection of the ^{31}P or ^{1}H signals of HPO_4^{2-} in biominerals has shown to be very difficult,[15–17] presumably because of the resolution problem arising from the very disordered structural environment. Because the chemical shift anisotropy (CSA) of HPO_4^{2-} is significantly larger than that of PO_4^{3-}, it has been suggested to quantify HPO_4^{2-} ions by monitoring the signal intensities of the spinning sidebands of the ^{31}P Bloch decay spectrum acquired under slow spinning frequency.[18] However, it should be cautious to apply this strategy to analyze CPMAS spectra because the CP dynamics of the spinning sidebands are very complicated.[15] Alternatively, one may assign the ^{31}P signals by monitoring the $^{31}P\{^{1}H\}$ CP dynamics of each resolved signal because the signal buildup of HPO_4^{2-} is substantially faster than PO_4^{3-}. This distinctive feature of HPO_4^{2-} has been used as a spectral marker for its detection in dentin samples.[16] Unfortunately, the motional dynamics of HPO_4^{2-} ions and their hydrogen bonds to neighbouring water molecules would affect the ^{31}P CSA and $^{1}H \rightarrow {}^{31}P$ polarization transfer efficiency substantially. These considerations together make an accurate quantification of HPO_4^{2-} ions in biominerals very difficult. On the other hand, $^{1}H\{^{31}P\}$ CPMAS has also been applied for the studies of enamel, dentin, and cementum of teeth, with a recycle delay of 600 s. The resolution of the ^{1}H dimension is good enough to provide a quantitative estimation of the hydroxyl groups in the apatite structure, viz. $73 \pm 3\%$, $18 \pm 3\%$, $18 \pm 1\%$, respectively, for the enamel, dentin, and cementum.[19]

For most of the $^{31}P\{^{1}H\}$ CPMAS measurements of phosphate compounds, the CP dynamics can be described by the following equation:

$$M(t) = M_0\{1 - \exp(-t/\tau_{CP})\}\exp\left(-t/T_{1\rho}\right) \quad (1)$$

where the parameter τ_{CP} is related to the proximity of the ^{1}H and ^{31}P species; $T_{1\rho}$ describes the ^{1}H relaxation in the spin lock field. Note that the values of τ_{CP} and $T_{1\rho}$ are quite sensitive to the experimental parameters such as spinning frequency and rf fields. In principle, more sophisticated CP model can be applied if the spin diffusion rate is not fast enough to establish a common spin temperature for a particular spin species.[20] In any case, it is advisable to measure all the samples in a back-to-back manner under the same set of experimental conditions. Even so, one can at best discuss the data trend of τ_{CP} and $T_{1\rho}$ in a qualitative manner.

Very recently, $^{43}Ca\{^{1}H\}$ CPMAS has received considerable attention because of its great potential in the study of biominerals.[21] It should be noted that spin locking of the central transition of half-integer quadrupole nuclei such as ^{43}Ca (spin 7/2) under MAS is not trivial. As discussed by Vega, efficient spin locking of the central transition can be achieved in either the adiabatic or the sudden regimes.[22] The former corresponds to the conditions of strong spin locking rf field and slow spinning, whereas the latter refers to the conditions of weak rf field and fast spinning. The degree of adiabaticity is quantified by the following empirical parameter:

$$\alpha = \frac{\nu_{rf}^2}{\nu_r \nu_Q} \tag{2}$$

where ν_r, ν_{rf}, and ν_Q denote the spin rate, rf field, and the quadrupole frequency, respectively. The quadrupole frequency is defined as

$$\nu_Q \equiv \frac{3e^2qQ}{2I(2I-1)h} \tag{3}$$

where I is the spin quantum number and e^2qQ/h is the nuclear quadrupole coupling constant. The adiabaticity parameter α should be larger than unity for adiabatic spin locking. For spin locking in the sudden regime, α should be close to zero.[22] Generally speaking, it is preferable to carry out the experiments of $^{43}Ca\{^{1}H\}$ CPMAS and the like at the sudden regime because of the less stringent requirement of the spin locking fields. The very first $^{43}Ca\{^{1}H\}$ CPMAS spectrum was reported for the ^{43}Ca-enriched acetate compound.[23] The optimal contact time was determined to be ca. 30 ms under the condition of relatively strong rf spin lock field. Such stringent CP condition is not desirable for most NMR instruments. A recent attempt of the $^{43}Ca\{^{1}H\}$CPMAS measurement on hydroxyapatite (HAp) is more successful in terms of sensitivity and practicability.[21]

2.2. HETCOR

Heteronuclear correlation (HETCOR) spectroscopy is a standard two-dimensional NMR technique. The resolution of $^{31}P\{^{1}H\}$ CPMAS spectra is generally not sufficient to unequivocally detect the HPO_4^{2-} ions and the apatitic OH^- ions in bone or dentin samples.[15] In this regard, the breakthrough came from the first application of $^{31}P\{^{1}H\}$ HETCOR to HAp and bone samples,[24] where the correlation peak at 0.2 and 3 ppm of the ^{1}H and ^{31}P dimensions, respectively, has been established as the spectral marker of apatitic OH^- ions. To enhance the spectral resolution in the ^{1}H dimension, ^{1}H homonuclear decoupling was employed during the t_1

evolution.[24] This sophisticated multiple-pulse based approach, which can suppress ^{1}H–^{1}H spin diffusion during the contact time period, has not been widely applied in the study of calcified tissues because of the rather involved setup procedure. Alternatively, the Lee-Goldburg CP (LG-CP) method, which was originally developed for the study of ^{1}H–^{13}C multiple-spin systems to suppress homonuclear dipole–dipole interaction,[25,26] can be easily applied for the study of biominerals. For the sake of spectral sensitivity, a contact time of 2 ms or longer may be desirable for LG-CP type HETCOR measurements because LG irradiation and the like will attenuate the rate of polarization transfer considerably.[25,26] Figure 1 shows a typical $^{31}P\{^{1}H\}$ LG-CP HETCOR spectrum measured for a dentin sample, where the signals corresponding to the phases of HAp and the amorphous calcium phosphate (ACP) are indicated. In a study of bone and dental materials, it has also been shown that CP with very short contact time will selectively enhance the signals of the phosphorus species near the apatite surface.[27] By measuring a series of $^{31}P\{^{1}H\}$ HETCOR spectra with a systematic variation of the CP contact time, the hydroxyl groups in the apatitic phase of bone samples have been estimated to be about 20% of the amount expected in stoichiometric HAp.[28] Some other alternative methods for the detection of apatitic hydroxyl groups will be discussed below. Nevertheless, $^{31}P\{^{1}H\}$ HETCOR remains the method of choice if the systems of interest have good resolution in the ^{31}P dimension.

As discussed above, CP involving half-integer quadrupole nucleus is not trivial and $^{43}Ca\{^{1}H\}$ CP experiments are in general of rather low

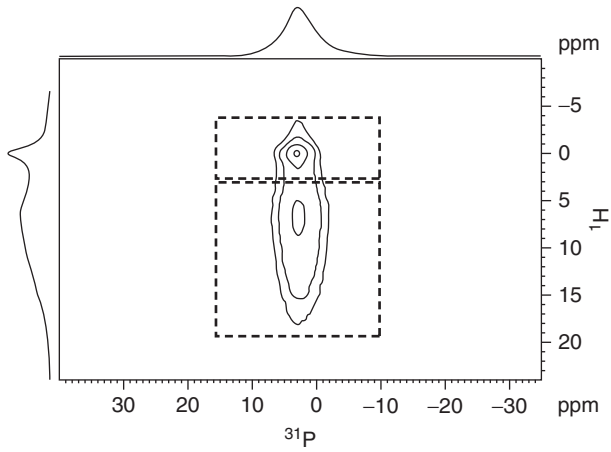

Figure 1 $^{31}P\{^{1}H\}$ LG-CP HETCOR spectrum of a dentin sample with contact time equal to 2 ms. The signal contributions from the apatite and amorphous components were obtained by integrating the two rectangular regions centred at the ^{1}H chemical shifts of 0.2 and 11 ppm, respectively. (Reprinted with permission from Ref. 16. © 2007 American Chemical Society.)

efficiency. Very recently, it has been found that $^{1}H\{^{43}Ca\}$ heteronuclear multiple-quantum coherence (HMQC) experiments can be carried out with good efficiency, based on the technique of rotary resonance recoupling (R^3).[29]

2.3. Spectral editing

Any NMR technique which can modify or ''edit'' a high-resolution MAS spectrum may provide useful information for the spectral assignment. For the systems of calcium phosphates, the difference in CP dynamics has been exploited to distinguish the signals arising from HPO_4^{2-} and PO_4^{3-}.[30] In the differential CP (DCP) method developed by Wu and co-workers, the contact time between the proton and phosphorus has two periods.[30] Initially, both the HPO_4^{2-} and PO_4^{3-} polarization would build up at different rates under the regular Hartmann–Hahn matching condition. In the second period, the spin temperature of the proton reservoir is inverted by changing the rf phase of the proton spin locking pulse by 180°. Such a change in spin temperature will cause a decay of the ^{31}P polarization. Because the polarization of HPO_4^{2-} and PO_4^{3-} will again decay at different rates, selective signal suppression can be realized by a judicious choice of the first and second contact periods. The technical concern of this approach, however, is that the contact times determined for brushite or HAp may not be applicable to real biominerals, for which the ^{1}H–^{31}P dipole–dipole interaction may be somewhat different from the model compounds.

A rather simple method to provide a quick identification of HPO_4^{2-} and PO_4^{3-} ions is the $^{31}P\{^{1}H\}$ dipolar dephasing technique.[31] The idea is to attenuate the ^{31}P signal of HPO_4^{2-} through the anisotropic ^{31}P–^{1}H dipole–dipole interaction. In the original implementation, the HPO_4^{2-} signal is suppressed by a free precession period without proton decoupling. In its latest version, one can actively recouple the ^{31}P–^{1}H dipolar interaction by the rotational echo double resonance (REDOR)[32] technique.[33] Consequently, the ^{31}P signal in close proximity to protons would be attenuated. Figure 2 shows the ^{31}P spectra of HAp and octacalcium phosphate (OCP) after the dipolar dephasing for 2 ms. As expected, most of the ^{31}P signals are significantly attenuated except for those from the PO_4^{3-} ions which are only remotely coupled to proton species. These results show that dipolar dephasing can provide a good opportunity for spectral editing in ^{31}P NMR of biominerals. The ^{31}P signals of the HAp phase, the hydroxyl deficient apatitic phase (HDAp), and the ACP phase are poorly resolved in biominerals. Using the dipolar dephasing technique, it would then be possible to select the signal of HDAp,[16,33] which is deficient in proton species, for further manipulation such as spin diffusion or double-quantum (DQ) excitation.

Recently, it has been shown that a Gaussian-shaped pulse can be used for selective excitation under the condition of MAS.[34] This strategy has

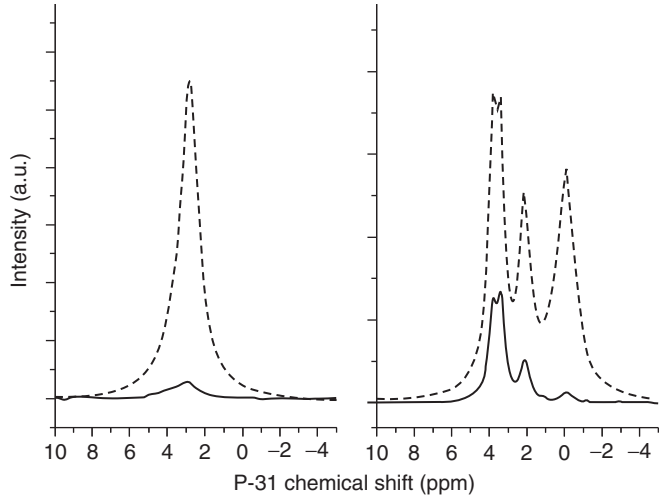

Figure 2 REDOR-based dipolar dephasing spectra obtained for HAp (left) and OCP (right). The solid and dashed lines represent the MAS spectra obtained with and without dipolar dephasing. In other words, any ^{31}P signals retained after the dipolar dephasing must arise from species remote from protons.

been successfully applied to realize ^{1}H selective excitation in HAp and monetite at a spin rate of 10 kHz.[35] Referring to the ^{1}H spectrum of HAp, the two ^{1}H signal at 0.2 and 5 ppm originate from OH^{-} groups and water molecules, respectively.[36] Because the ^{1}H signal of the OH^{-} group is well resolved and inhomogeneously broadened[37], it is easy to invert or nullify this signal selectively. Selective polarization transfer has also been realized by the delays alternating with nutation for tailored excitation (DANTE) sequence in $^{31}P\{^{1}H\}$ HETCOR measurements of carbonated apatite.[38] We anticipate that this spectral editing feature will find useful applications in spin diffusion or REDOR-like measurements of biominerals.

Quantification of apatitic hydroxyl groups using the $^{31}P\{^{1}H\}$ HETCOR approach or the $^{1}H\{^{31}P\}$ CPMAS method are time-consuming. As an alternative, Jäger et al. shows that one may record the difference signal of the ^{1}H spin locking spectra with and without ^{31}P irradiation under the Hartmann–Hahn matching condition.[39] In principle, the difference spectrum is equivalent to the ^{1}H projection of the corresponding $^{31}P\{^{1}H\}$ HETCOR spectrum, which can readily provide a reliable quantification of the apatitic hydroxyl groups. To apply this technique, however, one need to adjust the phase of both spectra carefully before their subtraction. Another method to acquire a resolution enhanced ^{1}H spectrum is the $^{1}H \rightarrow {}^{31}P \rightarrow {}^{1}H$ strategy suggested by Duer and co-workers.[40] After the first CP transfer, the ^{31}P magnetization is flipped to the z-axis, followed by a saturation comb (a series of

$\pi/2$ pulses) in the ^{1}H channel. The ^{1}H spectrum is then obtained by the LG-CP, in order to suppress spin diffusion among the ^{1}H spins. This strategy should be generally applicable to the study of bone or teeth samples. However, the signal intensities would critically depend on the CP conditions, rendering the quantitative analysis quite difficult. Also, the overall efficiency of the two CP processes is somewhat limited. To date, detection of the HPO_4^{2-} ions in biominerals remains a difficult task because the chemical moieties including $H_2O\cdots PO_4^{3-}$, $OH^{-}\cdots HPO_4^{2-}$, $H_2O\cdots HPO_4^{2-}$, and HPO_4^{2-} would constitute a very broad chemical shift distribution, particularly in the ^{1}H dimension.

2.4. HARDSHIP

Characterization of the dimension of the nanocrystallites is an interesting issue in the study of biological apatites. As a reasonable simplification, biological apatites can be considered as apatite crystallites embedded in organic matrix. For such a structural scenario, ^{31}P{^{1}H} REDOR NMR is of limited value because the ^{31}P spins of PO_4^{3-} will interact with the ^{1}H spins of both the inorganic and the organic phases. To selectively suppress the ^{31}P–^{1}H dipolar interaction arising from within the inorganic phase, a truly innovative technique known as heteronuclear recoupling with dephasing by strong homonuclear interactions of protons (HARDSHIP) has been developed by Schmidt-Rohr and co-workers.[41] The beauty of the method lies in the design of a basic cycle, which comprises a short REDOR period and a T_2 filter, to differentiate the spin dynamics associated with dilute ^{1}H spins and with a strongly coupled ^{1}H spin network. As a result, the ^{31}P–^{1}H dipolar interaction within the inorganic phase is refocused, whereas the dephasing effect due to the weaker ^{31}P–^{1}H dipolar interaction between the two phases would be retained. The key issue for the successful application of HARDSHIP is that the transverse relaxation time of the ^{1}H signals in the inorganic phase must be significantly longer than that in the organic phase, which is usually the case in apatitic systems. The HARDSHIP data curve can be easily analyzed by the following empirical biexponential curve:[41]

$$S(t;z) = f_{\text{fast}}(z)\exp[-t/\tau_{\text{fast}}(z)] + [1 - f_{\text{fast}}(z)]\exp[-t/\tau_{\text{slow}}(z)] \qquad (4)$$

where the factor f_{fast} is a weighting factor and τ_{slow} and τ_{fast} are the decay constants. These parameters are all dependent on the thickness of the inorganic phase. ^{31}P{^{1}H} HARDSHIP has been applied to study the size of the apatite nanocrystallites in mouse bone. The data were analyzed under the assumption that the crystallites are platelets of equal thickness embedded in collagen matrix, for which the proton density was set to $1/(0.29\ \text{nm})^3$. The hence obtained thickness is approximately 2.5 nm.

Although the assumption that all apatite platelets are of equal thickness may not be well justified, it provides a useful approximation to the real situation. In fact, such assumption is inevitable for an ensemble technique like NMR. It is anticipated that HARDSHIP may be well suited to determine the relative thickness of apatite crystallites in different bone or dentin samples. We note in passing that C-REDOR, which is a heteronuclear recoupling technique with active suppression of homonuclear dipolar interaction,[42,43] can be used to probe for the size of nanoparticles embedded in polymer matrix,[44] provided that the nanoparticles do not contain any ^{1}H species.

2.5. Double-quantum NMR

When two or more nuclear spins are close in proximity, they become coupled through the homonuclear dipole–dipole interaction. The magnitude of such interaction is inversely proportional to the third power of the internuclear distance. The so-called DQ coherence is a concerted evolution of coupled spins, which can be excited and detected under the irradiation of carefully designed rf pulse sequence. DQ NMR spectroscopy under MAS has been the major research area in the solid-state NMR community for many years. Since the pioneering work of Tycko,[45] numerous pulse sequences designed for DQ NMR have been reported in the literature.[46–48] In particular, the symmetry theory developed by Levitt, and co-workers has led to the development of a splendid collection of windowless pulse sequences suitable for DQ NMR spectroscopy under fast MAS.[49–54] On the other hand, the very robust technique of finite pulse radio frequency driven recoupling (fpRFDR)[55] has the advantage that all the pulses are well separated, which allows the implementation of active rotor synchronization to provide a stable timing for the pulse sequence. Because the average Hamiltonian of fpRFDR has the same operator form as the static homonuclear dipolar interaction, it is rather straightforward to incorporate fpRFDR into various *static* pulse sequences developed for multiple-quantum excitation to realize DQ excitation under MAS.[56]

Figure 3 shows a typical pulse sequence developed for DQ excitation. A systematic variation in the DQ excitation and reconversion periods can be used to probe the van Vleck's second moment of the coupled spins,[57] whose magnitude depends on both the number of interacting spins and the internuclear distances:

$$M_2 = \frac{3}{5}\gamma^4\hbar^2 I(I+1)\sum_j \frac{1}{r_j^6} \tag{5}$$

The DQ signals as a function of the excitation time can be analyzed on the basis of the following equation:

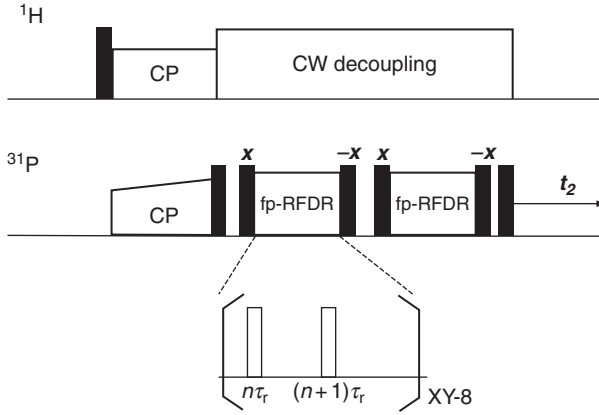

Figure 3 Pulse sequences used for the ^{31}P DQ experiment. The filled and open rectangles denote $\pi/2$ and π pulses, respectively.

$$I(\tau_{\mathrm{exe}}) = A\tau_{\mathrm{exe}}^2 \exp\{-\tau_{\mathrm{exe}}^2/B\} \tag{6}$$

In the above equation, the buildup of the DQ signal is described by a parabolic function[58,59] and the decay of the DQ signal is approximated by a Gaussian function.[60] In principle, the parameter A can be used to determine the van Vleck's second moment of the coupled spins. However, such quantification of the second moment is difficult because the DQ excitation efficiency also depends on the CSA and the efficacy of proton decoupling. Nevertheless, the variation of the parameter A in a series of similar spin systems should reflect the same variation in the second moment. On the other hand, because the values of the parameter B are affected by both the ^{31}P spin–spin relaxation times and the spatial arrangement of the interacting phosphorus species, it is difficult to interpret the data trend of B unequivocally. Alternatively, it has been shown that a constant-time dephasing of DQ coherence could be employed to deduce the homonuclear second moment of the resonating nuclei.[61]

The aforementioned DQ technique is well suited to characterize the spatial distributions such as phosphorus nuclei in biomaterials or apatitic systems (vide infra). However, it should be noted that the variation in the parameter A, if any, could be due to a number of factors such as the change in the protonation states and motional dynamics, not necessarily reflecting any change in the second moment. Therefore, ^{31}P DQ NMR is a very useful method in the study of biomineralization but the results should be largely interpreted in a qualitative manner. In principle, the second moment can also be obtained by measuring the attenuation of

spin-echo intensities as a function of inter-pulse delay under static condition.[27] However, the issue of spectral resolution favours the techniques developed for MAS.

2.6. Spin diffusion

Spin diffusion is a useful technique to probe spatial proximity of homonuclear spin clusters. When two spin clusters, viz. A and B, are spectroscopically well resolved, one can selectively excite the NMR signal of cluster A and then flip the signal onto the z-axis. If clusters A and B are in close proximity, the flip-flop term of the homonuclear dipolar interaction will equilibrate the polarizations of A and B. The time constant for the polarization transfer can provide a semi-quantitative measure of the spatial proximity of A and B. This idea has been applied to the study of biominerals. It has been found that rat dentin contains three distinct inorganic phases, viz. HAp, HDAp, and ACP.[16,33] As discussed before, one can use $^{31}P\{^{1}H\}$ HETCOR to resolve the NMR signals of HAp and ACP, whereas the HDAp can be selected by the dipolar dephasing technique. Using the pulse sequence shown in Figure 4A, one can exploit the effect of ^{31}P–^{31}P spin diffusion to probe the proximity of HAp to HDAp, and that of ACP to HDAp.[33] Accordingly, after the ^{1}H–^{31}P LG-CP period, the ^{31}P magnetizations of HAp and ACP are flipped onto the z-axis. The ^{31}P–^{31}P spin diffusion would occur during the mixing time. Because the ^{31}P chemical shifts of HAp, HDAp, and ACP are very similar (ca. 3.2 ppm)

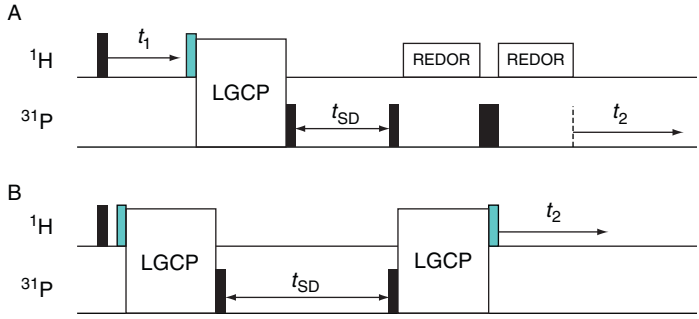

Figure 4 Pulse sequences employed to probe the proximity of different phosphorus phases in rat dentin. During the LG-CP period, the ^{1}H rf field and its offset are adjusted to fulfill the LG condition, whereas the rf field of ^{31}P is ramped through the Hartmann–Hahn matching condition. LG irradiation can suppress the ^{1}H–^{1}H spin diffusion during the CP period. The rectangles in black denote $\pi/2$ or π pulses. The greyish rectangles before the LG-CP blocks denote the theta pulses that align the magnetization onto the effective spin locking field. The one after the LG-CP block flips the magnetization onto the x-axis. The period t_{SD} denotes the mixing time for ^{31}P–^{31}P spin diffusion. (Reprinted with permission from Ref. 33. © 2009 American Chemical Society.)

and their signal linewidths are quite similar ($\leq$600 Hz), it is not necessary to apply ^{1}H decoupling or recoupling during the mixing time. The REDOR dephasing period is then used to select the ^{31}P signals which are relatively remote from ^{1}H species, that is, the HDAp signals. Experimentally, a REDOR dephasing period of 2 ms can effectively suppress the PO_4^{3-} signal of HAp or the HPO_4^{2-} signal of OCP (see Figure 2). From a series of ^{31}P{^{1}H} HETCOR spectra measured at different spin diffusion times, one can analyze the intensities of the HAp $\rightarrow$ HDAp signal as a function of spin diffusion time by the following set of equations:

$$\frac{dM_{HAp}}{dt} = -\frac{M_{HAp} - M_{HAp}^{eqm}}{\tau_{SD}} + \frac{M_{HDAp} - M_{HDAp}^{eqm}}{\tau_{SD}} \quad (7)$$

$$\frac{dM_{HDAp}}{dt} = -\frac{M_{HDAp} - M_{HDAp}^{eqm}}{\tau_{SD}} + \frac{M_{HAp} - M_{HAp}^{eqm}}{\tau_{SD}} \quad (8)$$

$$M_{HAp}(t=0) = M_{HAp}^{eqm} + M_{HDAp}^{eqm} = 1 \quad (9)$$

The time constant τ_{SD} can then be used to characterize the transfer rate. For simplicity, the transfer between HAp and ACP is not considered, which turns out to be considerably slower in comparison.[33] Another set of coupled equations can be similarly derived for the polarization transfer of ACP $\rightarrow$ HDAp. Figure 4B shows the pulse sequence to probe the proximity of HAp to ACP,[33] which is followed from the ^{1}H $\rightarrow$ ^{31}P $\rightarrow$ ^{1}H strategy discussed above.[40] The first LG-CP module prepares the ^{31}P signals of HAp and ACP. After the mixing period for ^{31}P–^{31}P spin diffusion, the ^{31}P signals are transferred back to ^{1}H for detection by the second LG-CP module. By a judicious choice of the first LG-CP contact time, the relative ^{1}H signal intensities of HAp and ACP could be made different from their equilibrium values.[33] As the spin diffusion time increases, the relative signals of HAp and ACP will approach their equilibrium values. Again, the time constant for the transfer rate can be quantified by the simple spin diffusion model discussed above.

Another interesting application of spin diffusion is the centerband-only detection of exchange (CODEX) experiment.[62–64] Assume that we have two neighbouring spins I and S coupled by dipole–dipole interaction and that the two spins have different chemical shift tensors (either in orientation or magnitude). In its simplest version, CODEX contains three basic modules. The first one is a recoupling period of CSA. For the second module, the magnetizations are flipped on the *z*-axis for spin diffusion. If the spin diffusion time is sufficiently long, half the polarization of I will transfer to S and vice versa. Finally, the polarizations are flipped into the *xy*-plane for another CSA recoupling. The two CSA recoupling modules are carefully prepared so that the average Hamiltonians of them differ in sign only.

That is, the signals of the pathways I → I and S → S will be refocused but those of I → S and S → I will be dephased because the chemical shift tensors of I and S are different. Consequently, if the CSA recoupling period is sufficiently long, only half the total signal of I and S would be left. Note that I and S are considered to be magnetically equivalent if their chemical shift tensors are identical, both in their magnitude and orientation. Such magnetic equivalence is rarely found in biominerals. The signal attenuation discussed above will only occur for magnetically inequivalent spins with non-vanishing CSAs. For a unit cell containing M magnetically inequivalent sites, the resultant signal would be equal to $1/M$ of its reference signal.[62] Hence, CODEX could be used to estimate the number of magnetically inequivalent sites per unit cell. Results obtained for the model compounds including HAp, brushite, and α-tricalcium phosphate (α-TCP) are in favourable agreement with the values expected from the known crystal structures.[65] The CODEX experiment has many other applications such as the characterization of slow segmental dynamics in polymers. Readers interested in the details are referred to the literature.[62–64]

2.7. Multiple-quantum MAS

The method of multiple-quantum MAS (MQMAS) is the most important high-resolution technique for half-integer quadrupole nuclei,[66,67] from which one can determine the chemical shifts of the resonating nuclei and the information of the electric field gradient at the nuclear sites. With the tremendous gain in sensitivity brought by ^{43}Ca isotope enrichment, ^{43}Ca MQMAS becomes feasible to characterize multiple Ca^{2+} environments in both crystalline[21,29] and non-crystalline materials.[68,69] In particular, ^{43}Ca 5QMAS is necessary to distinguish the multiple Ca^{2+} sites in some amorphous systems.[68,69] The resolution provided by MQMAS technique can be exploited in other heteronuclear dipolar recoupling techniques to provide site specific structural information. As an illustration, ^{43}Ca 3QMAS has been combined with ^{43}Ca{^{1}H} REDOR to distinguish the two calcium sites in a ^{43}Ca labeled HAp sample.[29] In comparison with the aforementioned ^{1}H{^{43}Ca} HMQC technique, however, the ^{43}Ca{^{1}H} 3Q-REDOR method is less robust and it is more time-consuming.[29] Furthermore, the very low natural abundance of ^{43}Ca (0.145%) renders the MQMAS technique not very promising for the study of bones and teeth.

3. NMR OF MODEL COMPOUNDS

Model compounds with well-defined chemical compositions and structures are indispensable for any study of biominerals or biomineralization processes. The solid-state NMR parameters of selected model compounds

are discussed in the following, whereas their general physicochemical properties can be found in other comprehensive reviews.[70,71]

3.1. ^{1}H, ^{31}P, and ^{13}C NMR

Although ^{1}H MAS spectra of biominerals are poorly resolved in general, techniques such as $^{31}P\{^{1}H\}$ HETCOR can still provide sufficient resolution to characterize the ^{1}H chemical shifts of the apatitic hydroxyl groups. The ^{1}H isotropic chemical shifts of various model compounds of calcium phosphates are shown both experimentally and theoretically to be strongly correlated with the strength of hydrogen bonding, as exemplified in the distance between the oxygen atoms in OH···O.[36,72,73] Usually, an increase in the strength of hydrogen bonding would cause a deshielding shift of the ^{1}H resonance. A similar trend of the ^{1}H chemical shift is found in the OH···F distance of fluorapatite (FAp).[36] The reference standards for the chemical shift scales of ^{1}H, ^{13}C are tetramethylsilane (TMS), whereas the standard for ^{31}P is 85% phosphoric acid.

3.1.1. Calcium carbonate

Calcite is the most stable form of calcium carbonate. Samples of ^{13}C-enriched calcite have been studied by Phillips and co-workers.[74] The variation of the ^{13}C CPMAS signal as a function of the contact time resembles closely to what expected for an isolated ^{13}C–^{1}H spin pair and therefore the extracted internuclear distance (1.9 ± 0.1 Å) provides a strong evidence for the presence of bicarbonate defects. Interestingly, both the $^{13}C\{^{1}H\}$ CPMAS spectrum (contact time of 0.3 ms) and the ^{13}C Bloch decay spectrum show a single resonance at 168.7 ppm but their associated spinning sideband patterns at a spin rate of 1 kHz are quite different. Apparently, the isotropic ^{13}C chemical shift is not a good spectral maker to distinguish the carbonate groups and the bicarbonate defects in calcite. From the $^{13}C\{^{1}H\}$ HETCOR measurement, the ^{1}H signal at 7.4 ppm, which can also be observed in the ^{1}H MAS spectrum, is assigned to the bicarbonate defects of calcite.[74] This relatively sharp peak at 7.4 ppm is also observed in the ^{1}H MAS spectra of natural calcite samples.[74] We note in passing that the ^{13}C chemical shifts and CSA of K_2CO_3 and $KHCO_3$ are very different from those of calcite, presumably due to their difference in the hydrogen bond strength.[74–76]

3.1.2. Monetite and brushite

Monetite is the common name of dicalcium phosphate anhydrous (DCPA, $CaHPO_4$), which is found neither in normal nor pathological calcified tissues.[77] According to a neutron diffraction study,[78] there are several crystallographically inequivalent HPO_4^{2-} groups with significant intermolecular hydrogen bondings among them. The shortest

intermolecular O···H distance is 1.27 Å. The ^{1}H spectrum of monetite has two resolved peaks with an intensity ratio of 1:3.[36] The more deshielded ^{1}H peak at 16.2 ppm is assigned to the acidic proton which participates more extensively in hydrogen bonding. The peak at 13.6 ppm corresponds to other acidic proton sites.[36] The corresponding ^{31}P MAS spectrum has two resolved peaks (−1.5 and −0.2 ppm).[79] The more shielded resonance is assigned to the HPO_4^{2-} sites with less intermolecular hydrogen bonding.[80] The more protonated sites have larger ^{31}P CSA because of the larger distortion of the electronic environment.[18]

Dicalcium phosphate dihydrate (DCPD), also known as brushite, is another useful model compound of HPO_4^{2-} ions. It has a chemical formula of $CaHPO_4 \cdot 2H_2O$. Brushite is biologically important because it is often found in pathological calcifications such as dental calculi and urinary stone.[80] Brushite has been proposed as an intermediate in biomineralization processes such as bone formation and the dissolution of enamel in acids (dental caries).[77] The two inequivalent proton signals of brushite resonates at 4.1 and 6.4 ppm.[15] Both of them are due to the structural water and the one at the more deshielded position is assigned to the water molecule with stronger hydrogen bonding. The acidic proton, which participates less extensively in hydrogen bonding than that of monetite, resonates at 10.4 ppm.[15,36] The ^{31}P spectrum of brushite exhibits a single resonance at 1.3 ppm.[79] In brushite, the hydrogen phosphate group is quite isolated and is not involved in any significant hydrogen bonding network. The shortest intermolecular O···H distance is 2.54 Å.[81]

Consider the ^{31}P{^{1}H} CP dynamics of monetite and brushite, both of their τ_{CP} values (see Equation (1)) are more or less the same,[16] showing that the ^{1}H–^{31}P dipolar interaction within the HPO_4^{2-} species dominates the polarization transfer.[82] On the other hand, the $T_{1\rho}$ value of monetite is considerably longer than that of brushite.

3.1.3. Hydroxyapatite

The major inorganic species in the calcified tissues of vertebrae is known as the biological apatite, whose crystal lattice is very similar to that of HAp.[83] HAp, with a chemical formula of $Ca_{10}(PO_4)_6(OH)_2$, has two crystalline forms, viz. the monoclinic and hexagonal forms. These two forms differ only in the long-range orientation of the hydroxyl groups along the *c*-axis and the monoclinic form, which is difficult to prepare, is less biologically relevant.[2] The apatitic hydroxyl group of HAp resonates at 0.2 ppm, suggesting a relatively weak hydrogen bonding between two neighbouring OH^- groups.[36] The quantification of the structural OH^- groups in well crystalline HAp can be achieved by ^{1}H Bloch decay experiments. Using adamantane and NH_4Cl as the spin-counting standards, the hydroxyl groups in HAp after calcination at 800 K is

determined to be ca. 94% of the stoichiometric value, revealing a slight dehydroxylation of the apatite structure.[19] In addition, the ^{1}H chemical shift of the water peak of the calcined sample is more shielded by 0.5 ppm than that of the hydrated sample. Based on this observation it has been suggested that after the calcination the residual water molecules form smaller clusters with less extensive hydrogen bonding.[15] However, this kind of interpretation should be considered as tentative because the ^{1}H chemical shifts of surface water in HAp may also be affected by chemical exchange with the surface hydroxyl or acid phosphate groups.[36] Concerning the peak at 5.6 ppm, the exchange of HAp with D_2O provides a solid evidence for its assignment to surface-adsorbed water.[36] This relatively narrow signal has negligible spinning sidebands even under slow-spinning condition. Presumably, the adsorbed water molecules still have considerable mobility. There are three crystallographically distinct phosphorus sites in the monoclinic form, whereas the hexagonal form (more biologically relevant) has one phosphorus site only. Nevertheless, the ^{31}P NMR spectra of both forms are identical, featuring a single resonance at around 2.8 ppm.

The correlation peak at 0.2 and 2.8 ppm in the ^{1}H and ^{31}P dimension, respectively, of a $^{31}P\{^{1}H\}$ HETCOR spectrum can be considered as a spectral marker of HAp.[28,36] The τ_{CP} of HAp is larger than that obtained for brushite or monetite because the ^{1}H–^{31}P dipolar coupling of HAp (855 Hz) is significantly weaker than that of brushite or monetite (4.6 kHz). The $T_{1\rho}$ of HAp is usually too long to be characterized in a regular variable-contact time experiment. In a study of nanosized HAp samples, Jäger et al. use $^{31}P\{^{1}H\}$HETCOR and proton spin diffusion techniques to show that a substantial amount of hydrogen phosphate ions are present in HAp, presumably on the crystallite surface.[84] In other words, the structural model is proposed to be an interior crystalline HAp core covered by a disordered surface layer containing mainly the hydrogen phosphate units. This core-shell model provides important insights into the study of bone or dentin samples because the apatite crystallites in biominerals are also nanosized.

HAp is a good model compound for the study of DQ coherence excitation profile.[85] The closest P···P distance in HAp is 4.143 Å. The numerical simulations and the experimental data were shown in Figure 5. The maximum DQ coherence excitation efficiency decreases as the spin cluster size increases. The reason is simply due to the fact that all the spins in the cluster will contribute (different combinations of two spins) to the DQ coherence. The passive spins in close proximity would provide a strong dipolar dephasing of the excited DQ coherence. As expected, the simulation results converge towards the experimental data as the cluster size increases.

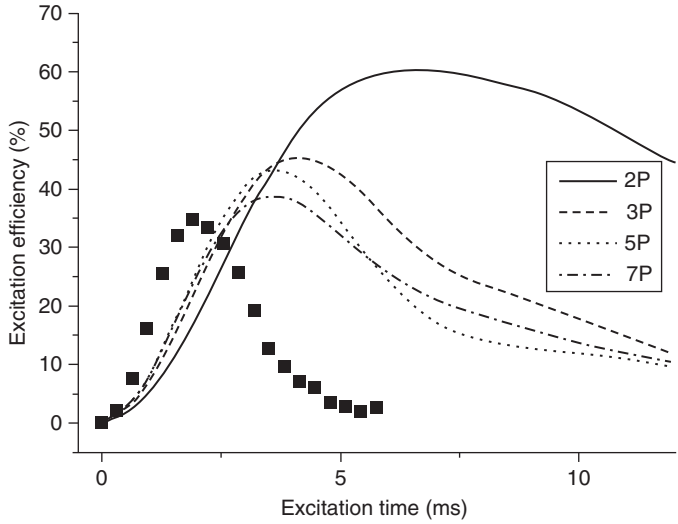

Figure 5 Numerical simulations and experimental measurements of the excitation profile of the ^{31}P DQ coherence of HAp based on fpRFDR at a spin rate of 25 kHz. The squares, representing the experimental data, are larger than the error bars. The simulations correspond to different spin clusters containing 2–7 phosphorus spins. The geometrical parameters were taken from the X-ray structure of HAp.

3.1.4. Carbonate HAp

Type A carbonate HAp (CHAp-A) is obtained when the OH^- ions of HAp are substituted by CO_3^{2-} ions, whereas the type B (CHAp-B) corresponds to the substitution of PO_4^{3-} by CO_3^{2-} ions. CHAp-AB refers to the substitution of both PO_4^{3-} and OH^- ions by CO_3^{2-} ions. To date, it is a consensus that CHAp-B is a good model compound for bone samples.[15,17] All the three types of CHAp compounds, where the carbonate contents are usually less than 10%, have different charge balance requirements, resulting in different structural features.[2,86,87] Indeed, there are quite many possibilities of charge compensation for the substitution of CO_3^{2-} ions in HAp so that the resultant apatite structure of CHAp may well depend on the method of sample preparation. In the following, selected examples from the literature will be discussed to illustrate this point.

For the samples of CHAp-A prepared by high temperature treatment (900 °C) of HAp in CO_2 atmosphere, the ^{13}C MAS spectrum would have a sharp resonance at 166.5 ppm with a full width at half maximum (FWHM) of about 1 ppm.[88] Interestingly, a total of four peak components was found in the ^{31}P MAS spectrum, ranging from 2.5 to 5.5 ppm.[31] For the samples of CHAp-B prepared by wet chemistry at 80 °C and those of CHAp-AB prepared by thermal crystallization of carbonated ACP at 500–600 °C, both of their ^{13}C MAS spectra contain peak components

with FWHM of about 2.5 ppm. The maximum peak intensity of CHAp-B occurs at 170.2 ppm. In addition to the peak components of CHAp-A and CHAp-B, the spectrum of CHAp-AB has an additional peak at 168.2 ppm, which is assigned to disordered CO_3^{2-} ions close to surface water.[88] At a moderate spinning frequency (11 kHz), the ^1H signals of CHAp-B and CHAp-AB have two resolved signals at −0.6 and 4.8 ppm, which can be readily assigned to hydroxyl group and H_2O, respectively.[36,88] The ^{31}P NMR spectrum of CHAp-B has a single broad peak positioned at 3 ppm with FWHM of about 5 ppm. Such spectral feature is observed for all the ^{31}P spectra of CHAp-B with carbonate content ranging from 3.2% to 14.5%.[31] The ^{31}P CSA of CHAp-B is larger than that of HAp. Note that a discernable difference in the ^{31}P MAS and the $^{31}P\{^1H\}$ CPMAS regarding to the spinning sideband pattern is observed, revealing that there are two types of phosphate groups in CHAp-B.[31] Another CHAp-B sample was prepared by reaction of $CaHPO_4$ with ammonium carbonate solution at 70 °C for 3 days.[89] The ^{13}C MAS spectrum shows a slightly asymmetric peak at 168.4 ppm. The broad ^1H signal at 5.86 ppm was assigned to structural water in the OH channels instead of surface-adsorbed water.[89]

Samples of nanocrystalline CHAp-AB can also be prepared in aqueous solution at room temperature (pH = 10) and then heat treated at 400 °C to remove any carbonate species near the surface.[90] The corresponding $^{31}P\{^1H\}$ CPMAS spectrum contains a single peak positioned at 3.3 ppm with FWHM of 1.7 ppm. As expected, the ^1H spectrum contains two peak components, viz. the H_2O signal at 5.1 ppm and the OH signal at 0.0 ppm. Measurements of $T_{1\rho}$ show that these two proton species belong to two different spin baths. The $T_{1\rho}$ of the OH signal is larger than 50 ms, whereas that of H_2O is equal to 1.7 ms. Therefore, these two species are not in close proximity. The $^{13}C\{^1H\}$ spectrum contains four well-resolved components at 166.2 (CHAp-A), 168.0, 169.8, and 170.6 ppm. The peaks from 168.0 to 170.6 ppm were tentatively assigned to CHAp-B,[90] although the peak at 168.0 ppm was previously assigned to the disordered phase.[88] The $^{13}C\{^1H\}$ HETCOR measurements show that there is no correlation observed between the water signal and the carbon species. Apparently, the water molecules are located on the crystallite surface. In addition, the study of $^{13}C\{^1H\}$ CP dynamics completely rules out the presence of HCO_3^- species. The $^{13}C-^{31}P$ correlation spectrum indicates that all the carbon peaks are correlated to the ^{31}P signal of PO_4^{3-}. Interestingly, there is an addition ^{31}P peak at 5 ppm correlated to the ^{13}C peak at ca. 170 ppm, but the assignment of this correlation peak is not obvious.[90]

Another CHAp-AB samples prepared under aqueous condition (90 °C, pH = 8.5–9.5) have strikingly different NMR spectroscopic features. The ^{13}C MAS spectrum contains only two components, viz. 169.8 and 170.8 ppm, which are not very well resolved.[76] By monitoring the τ_{CP}

values extracted from the variable contact-time $^{13}C\{^{1}H\}$ HETCOR measurements, the two ^{13}C signals observed at 169.8 and 170.8 ppm are assigned to bicarbonate ions with moderate hydrogen bonds to neighbouring moieties. These two bicarbonate species also have similar $^{13}C\{^{31}P\}$ REDOR behaviour, indicating that they are well embedded in the HAp lattice. Also, their NMR properties are quite similar to those of the bicarbonate defects of calcite.[74,76] Some convincing spectroscopic evidence have been given to show that the proton signal of bicarbonate ions residing at the hydroxyl site of CHAp-AB occurs at 5.5 ppm.[76] At the present stage, it is not well understood why the CHAp-AB samples prepared by Mason et al. and those by Babonneau et al. are so different with regard to the speciation of the carbonate ions.

Yet another method based on vapor diffusion has been developed to prepare CHAp-AB.[91] The $^{13}C\{^{1}H\}$ CPMAS spectrum has three components at 166.1, 168.4, and 170.1 ppm, where the spectral resolution is quite poor. Nevertheless, the morphology, crystallite size, and Ca/P molar ratio of the samples are very close to those of mature bovine bone. The relatively strong resonance at 168 ppm is assigned to carbonated ACP. Because the high-resolution transmission electron microscopic (HRTEM) images of the samples do not show any evidence for the presence of amorphous layer, which has been easily identified in other systems,[92] therefore, the authors suggest that the carbonated ACP species exist as some discontinuous small patches (presumably near the surface). The ^{31}P MAS spectrum features a broad peak positioned at about 3 ppm. Furthermore, a strong correlation peak between the OH and H_2O signals has been observed in the two-dimensional ^{1}H exchange spectroscopy (EXSY) NMR spectrum (mixing time = 100 ms), suggesting that these two species are not in separated phases. This observation is at odd with what concluded in the study by Babonneau and co-workers.[90] It is quite possible that the CHAp-AB samples prepared in different laboratories indeed have different structures.

3.1.5. Fluorapatite

FAp has the same crystal structure as HAp except that the hydroxyl groups of HAp are replaced by fluoride ions in FAp. In the study of a series of solid solutions of fluorohydroxyapatites, it has been shown that the ^{1}H chemical shift of the OH group is a sensitive measure of its hydrogen-bonding configuration with the fluoride ions.[36] As expected, the ^{31}P spins of FAp have the same NMR parameters as those in HAp.[18] The ^{19}F chemical shift of FAp was reported to be -100.4 ± 0.5 ppm with reference to $CFCl_3$,[93] whereas a more recent report gives the value of -102.8 ppm.[94] FAp has also been taken as the model compound for $^{19}F-^{31}P$ double resonance experiments.[42,43,95]

For carbonate FAp, its ^{13}C MAS spectrum has a single peak at 170 ppm. Because this chemical shift is quite similar to what observed

for carbonate HAp, it has been inferred that there is no CO_3F^{3-} species present.[96] For a study of staffelite, a synthetic carbonate FAp has been taken as the model compound, for which the $^{13}C\{^{19}F\}$ CPMAS spectrum has a single resonance at 170.7 ppm.[97] From the $^{13}C\{^{19}F\}$ CP dynamics, the signal has been assigned to type B carbonate. Also, the absence of CO_3F^{3-} ions has been confirmed by more advanced $^{13}C-^{19}F$ double resonance experiments.[97]

3.1.6. Octacalcium phosphate

OCP is an important model system in the study of biomineralization and it has a chemical formula of $Ca_8(HPO_4)_2(PO_4)_4{\cdot}5H_2O$. Because of its structural similarity to HAp, OCP has been hypothesized as the precursor phase of biological apatite.[98] The six non-equivalent phosphorus sites of OCP can be categorized into two groups, viz. PO_4^{3-} (P1–P4) and HPO_4^{2-} (P5, P6). OCP can be described as an alternating layer structure of an apatite layer and a hydrated layer,[99] where the apatite layer is structurally very similar to HAp.[100,101] The apatite layer contains the species P1–P4, whereas the hydrogen phosphate groups of P5 and P6 are found in the hydration layer. P1 is the most distant PO_4^{3-} species from the water molecules. P4 has a distance of about 3.6 Å from the nearest water molecule, whereas P2 is slightly further away from water. P3 and P6 are close to the interface of the apatite and the hydration layers, where the phosphate oxygen of P3 is hydrogen bonded to the acidic proton of P6. The phosphorus species located in the central region of the hydrated layer is P5. The high-resolution ^{31}P NMR studies of OCP can be dated back to the 1980s,[18,31] and the complete spectral assignment has been made only very recently.[102,103] Solid-state ^{31}P NMR has proved to be an effective spectroscopic technique for the study of OCP.[4,80,102,104] The ^{31}P spectrum of OCP as shown in Figure 6 has four resolved peaks at 3.7 ppm (P1), 3.3 ppm (P2/P4), 2.0 ppm (P3), and −0.2 ppm (P5, P6). On the basis of the chemical formula of OCP, we expect that the ^{31}P signals of the PO_4^{3-} and HPO_4^{2-} groups should have an intensity ratio of 1:0.5. However, experimentally the intensity ratio was found to be 1:0.92, for which it has been postulated that some of the orthophosphate groups at the P2 and P4 sites in OCP would react with water to form hydrogen phosphates: $PO_4^{3-} + H_2O \rightarrow HPO_4^{2-} + OH^-$.[102,105] In the literature, a recent ^{31}P MAS spectrum measured under similar conditions is very similar to Figure 6 except that the peak intensity of the P2/P4 site is significantly higher.[106] Apparently, the extent of PO_4^{3-} hydrolysis at P2 and P4 is largely dependent on the conditions of sample preparation.

The two-dimensional ^{31}P DQ spectrum of OCP is shown in Figure 7, in which there are eight sets of auto- and cross-correlation peaks. Although the ^{31}P CSA of HPO_4^{2-} is quite sizable,[107] the relatively high intensity of the P5–P5/P5–P6 correlation peak demonstrates that the DQ excitation

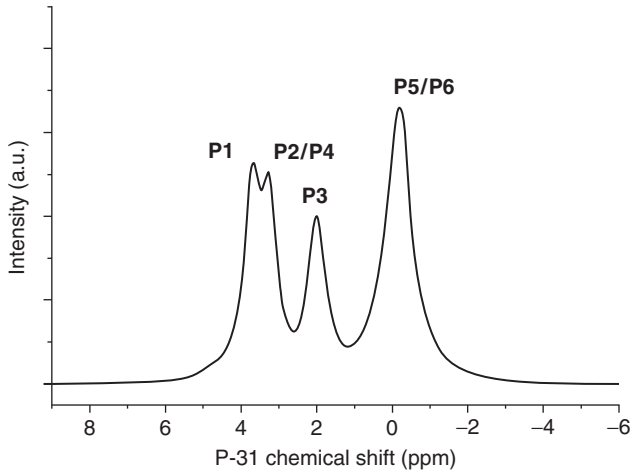

Figure 6 ^{31}P MAS spectrum of OCP measured at 10 kHz. ^{1}H decoupling at 80 kHz was applied during acquisition. Recycle delay was set to 610 s.

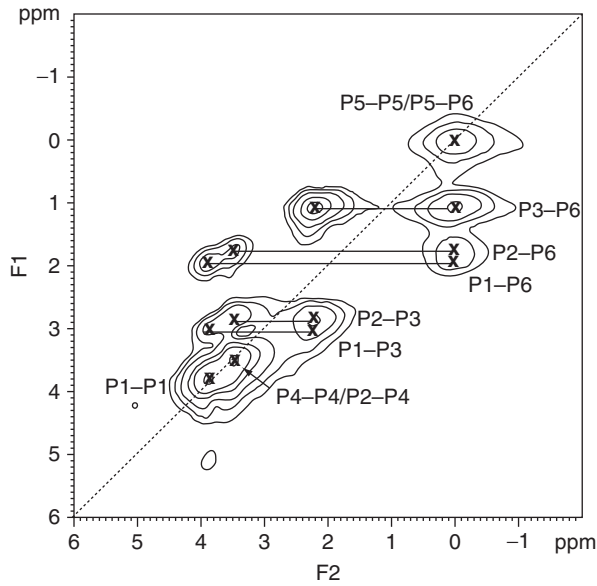

Figure 7 Two-dimensional ^{31}P DQ−SQ correlation spectrum of OCP measured at 10 kHz. (Reprinted with permission from Ref. 85. © 2005 Elsevier.)

efficiency is not significantly attenuated by large CSA effect. Figure 8 shows the ^{31}P{^{1}H} HETCOR measured for OCP. The correlation peaks at 0.18 and 3.3 ppm of the ^{1}H and ^{31}P dimensions, respectively, is assigned to

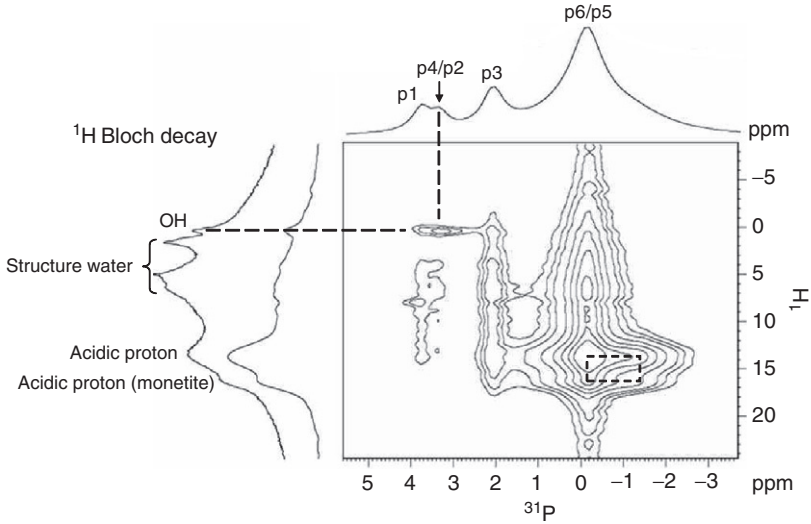

Figure 8 ^{31}P{^{1}H} HETCOR spectrum of OCP. For comparison, the ^{1}H MAS spectrum is appended next to the ^{1}H projection spectrum. The vertices of the rectangular box correspond to the cross-peaks of monetite (impurity phase). Note that the OCP signal also contributes to the cross-peak at −0.2 ppm (^{31}P) and 13.6 ppm (^{1}H). (Reprinted with permission from Ref. 102. © 2004 Elsevier.)

both P2 and P4, which are in close proximity to the water molecule residing at the OH site of the apatite layer. As expected, the ^{31}P peak at −0.2 ppm (P5 and P6) is correlated to the ^{1}H signals at 5.5 and 13.3 ppm, which have been assigned to the structural water and the acidic proton of HPO_4^{2-}.[36]

3.1.7. Amorphous calcium phosphate

In biomineralization, ACP always refers to the disordered phase of calcium orthophosphate. Because ACP has been considered as a possible precursor of bone minerals in vertebrates, it serves as an important model compound for the study of biominerals.[108] The ^{31}P MAS spectrum of ACP contains a single broad peak at about 3 ppm.[31] The ^{31}P CSA of ACP is intermediate between those of HAp and protonated phosphates. On the basis of low temperature measurements, it has been suggested that ACP does not contain HPO_4^{2-} groups undergoing rapid reorientation.[109] The ^{31}P CSA of the dried ACP sample (vacuum dried at 400 °C) is very similar to that of ACP, but the ^{31}P{^{1}H} CP efficiency is dramatically reduced for the dried sample. It indicates that most of the orthophosphate groups in ACP are not protonated.[109]

3.1.8. Monocalcium phosphate monohydrate

Monocalcium phosphate monohydrate (MCPM) has a chemical formula of $Ca(H_2PO_4)_2 \cdot H_2O$. Because of its relatively high acidity and solubility, MCPM is never found in biological hard tissues.[77] Nevertheless, the orthophosphate groups of MCPM have a remarkably high protonation state and it may serve as a useful model compound. The ^{31}P spectrum of MCPM shows two peaks at −4.2 and 0.3 ppm with approximately equal intensities, which correspond to two crystallographically distinctive $H_2PO_4^-$ sites.[18,73] The substantial difference in isotropic chemical shift between the two phosphates is most likely a reflection of their different extents in hydrogen bonding.[18] In another ^{31}P MAS spectrum of MCPM, a shoulder peak at −3 ppm is also observed.[79] It is not clear whether this unassigned component is due to an impurity phase or not.

3.1.9. Tricalcium phosphate

TCP, $Ca_3(PO_4)_2$, exists in two crystal forms, viz. α-TCP and β-TCP. Both forms can only be prepared by calcination at high temperature (>800 °C).[70] α-TCP is meta stable at room temperature and is more soluble than β-TCP in water. The crystal structure of α-TCP shows that there are 16 inequivalent phosphorus sites.[110] Its ^{31}P MAS spectrum contains only 14 peaks, where the chemical shifts range from −3 to 5 ppm.[111] Although there are only three crystallographically inequivalent phosphorus sites for β-TCP,[112,113] there are as many as 16 resolved peaks in the ^{31}P MAS spectrum because of the presence of some calcium vacancies.[114] The ^{31}P chemical shifts of β-TCP are in the same range as reported for α-TCP, but the overall patterns of their ^{31}P MAS spectra are quite different. In addition, it has also been found that even a minor substitution of Ca^{2+} by Na^+, Mg^{2+} or Zn^{2+} ions will perturb the ^{31}P MAS spectrum, revealing the substantial effect of the counter ions near the phosphorus sites.[114,115]

3.2. ^{31}P NMR parameters of calcium phosphates

Up to this point, we have summarized the NMR parameters of some selected crystalline compounds. Model crystalline compounds of calcium phosphates are important structural reference for the study of biominerals because the highly complex hierarchical structures of bones and teeth contain different phosphorus species such as unprotonated orthophosphate (PO_4^{3-}) and protonated orthophosphate (HPO_4^{2-}).[70,77] It is beyond doubt that ^{31}P chemical shifts are the most important spectroscopic parameters for the characterization of calcium phosphates. While the ^{31}P chemical shift can reflect the protonation state of a phosphate species, ^{31}P CSA is a sensitive measure of the symmetry of the electronic

environment of the resonating nucleus. In the literature, there are several conventions employed to quantify the anisotropy of a chemical shift tensor. Here, we adopt the convention proposed by a group of NMR spectroscopists in a meeting at the University of Maryland in 1992.[116] Accordingly, all the measured chemical shift tensors are to be reported in terms of the isotropic (δ_{iso}) , span (Ω) and skew (κ) values defined by the tensor principal components (δ_{ii}):

$$\delta_{11} \geq \delta_{22} \geq \delta_{33} \tag{10}$$

$$\delta_{iso} = \frac{(\delta_{11} + \delta_{22} + \delta_{33})}{3} \tag{11}$$

$$\Omega = \delta_{11} - \delta_{33} \geq 0 \tag{12}$$

$$\kappa = 3\frac{\delta_{22} - \delta_{iso}}{\Omega} \tag{13}$$

Referring to the data summarized in Table 1, in general the phosphorus species with chemical shifts $\geq$2 ppm are usually assigned to PO_4^{3-}. From the data of OCP, one can infer that the more isolated the phosphate groups from water molecules, the more deshielded the chemical shifts would become. Indeed, the P3 of OCP, which is involved in hydrogen bonding, has a chemical shift of 2.0 ppm, whereas the relatively isolated P1 is at 3.7 ppm. On the other hand, hydrogen phosphates usually have chemical shifts less than 2 ppm, as illustrated in the data of OCP. To certain extent, protonated and unprotonated orthophosphates can be distinguished from their chemical shift span. As shown in Table 1, the ^{31}P Ω of brushite is considerably larger than that of monetite, which can be correlated to the fact that there are significant intermolecular hydrogen bonding among the HPO_4^{2-} groups of monetite. The chemical shift span of PO_4^{3-} is significantly smaller than those of HPO_4^{2-} and $H_2PO_4^{-}$, because unprotonated orthophosphates have more symmetric electronic environment than hydrogen phosphates at the phosphorus sites. The ^{31}P Ω of HPO_4^{2-} species in OCP is considerably smaller than that in brushite.[18] One possible explanation is that the HPO_4^{2-} groups and/or the water molecules in OCP are undergoing molecular motions which would partially average the ^{31}P CSA. On the other hand, there is no obvious trend for the ^{31}P chemical shift skew with respect to hydrogen bond strengths or protonation states. In the studies of biominerals, it is very useful to extract the ^{31}P CSA parameters in order to identify the mineral phases present in the samples. It should be cautious, however, to infer the protonation states of the phosphate species from the chemical shift data alone. As mentioned before, the ^{31}P chemical shift of Na_2HPO_4 is very deshielded,[14] which may be due to the substantial counter-ion effect. We reiterate again that the best method to distinguish unprotonated orthophosphate from hydrogen phosphate is to monitor the transfer kinetics of the $^{31}P\{^1H\}$ CPMAS experiment.

TABLE 1 Summary of ^{31}P NMR parameters of selected model crystalline compounds for the study of biomineralization

Sample	Assignment	Method	δ_{iso} (ppm)	δ_{11} (ppm)	δ_{22} (ppm)	δ_{33} (ppm)	Span (ppm)	Skew	Reference
HAp		BD[a]	2.8	10.4	8.8	−10.7	21.1	0.85	80
PO_4^{3-}, one site		CP	2.8	16.0	0.8	−8.3	24.4	−0.25	80
			2.8	19 ± 3	4 ± 6	−15 ± 1	34.0	0.12	18
		CP	3.1	24.5	0.2	−15.4	40.0	−0.22	107
		CP	2.8	22.8	2.8	−17.2	40.0	0.00	30
		BD	2.9						223
		BD	2.8						31
CHAp-A		BD	5.5						31
PO_4^{3-}, one site		BD	4.6						31
		BD	3.8						31
		BD	2.5						31
CHAp-B (3.2% carbonate) PO_4^{3-}		BD	2.8						31
CHAp-B (14.5% carbonate) PO_4^{3-}		BD	3.0						31
Calcium deficient HAp PO_4^{3-}		BD	3.0						223
FAp PO_4^{3-}, one site			2.8 ± 0.2						18
ACP		BD	3.0						31
PO_4^{3-} mainly		CP	2.8						30
DCPD (brushite)		BD	1.4	66.5	−5.1	−57.2	123.7	−0.16	80
HPO_4^{2-}, one site		CP	1.4	67.0	−5.9	−57.0	124.0	−0.17	80
		CP	1.7	65.7	−4.4	−56.3	122.0	−0.15	107
			1.6	64.7	−5.6	−54.2	118.9	−0.18	73
			1.7 ± 0.3	70 ± 6	−12 ± 6	−53 ± 3	123.0	−0.33	18

		CP	1.4	63.5	−1.7	−57.6	121.0	−0.08	30
		BD	1.4						31
		BD	1.3						223
DCPA (monetite)		BD	−1.7	51.5	−11.2	−45.2	96.6	−0.30	80
HPO_4^{2-}, two sites		BD	−0.1	30.3	−1.3	−29.3	59.6	−0.06	80
		CP	−1.7	50.8	−10.9	−45.0	95.8	−0.29	80
		CP	−0.1	29.2	−0.4	−29.1	58.3	−0.02	80
		BD	−0.3						31
		BD	−1.7						31
			0 ± 0.4						18
			−1.5 ± 0.4						18
		BD	−1.5						223
		BD	−0.2						223
		BD	−0.6						14
OCP	P1	BD	3.6	15.8	6.5	−11.4	27.2	0.31	80
PO_4^{3-} (P1–P4)	P2/P4	BD	3.1	15.4	5.7	−11.8	27.2	0.29	80
HPO_4^{2-} (P5, P6)	P3	BD	1.9	24.3	6.3	−24.9	49.2	0.27	80
	P5/P6	BD	−0.4	33.1	−7.7	−26.4	59.5	−0.37	80
	P1	CP	3.6	20.4	3.4	−13.0	33.4	−0.02	80
	P2/P4	CP	3.1	22.9	−2.5	−11.0	34.0	−0.50	80
	P3	CP	1.9	27.6	6.8	−28.7	56.3	0.26	80
	P5/P6	CP	−0.4	36.8	−7.8	−30.1	67.0	−0.33	80
	P1	CP	3.7[b]	15.9	3.6	−8.5	24.4	–0.01	143
	P2/P4	CP	3.3[b]						143
	P3	CP	2.0	28.3	5.0	−27.2	55.5	0.16	143
	P5/P6	CP	−0.2				≤59	n.d.	143
	P1	CP	3.7						102
	P2/P4	CP	3.3						102
	P3	CP	2.0						102

(*continued*)

TABLE 1 (*continued*)

Sample	Assignment	Method	δ_{iso} (ppm)	δ_{11} (ppm)	δ_{22} (ppm)	δ_{33} (ppm)	Span (ppm)	Skew	Reference
	P5/P6	CP	−0.2						102
	PO_4^{3-}	BD	2.8						31
	HPO_4^{2-}	BD	−0.5						31
	PO_4^{3-}	CP	2.8	23.5	−0.5	−14.5	38.0	−0.26	30
	HPO_4^{2-}	CP	−0.5	34.5	−5.6	−30.5	65.0	−0.23	30
MCPM	P1		−4.2	65.0	−4.2	−73.4	138.4	0.00	73
$H_2PO_4^-$ (P1, P2)	P2		0.3	54.4	−2.3	−51.2	105.6	−0.07	73
	P1		−4.6 ± 0.3	59 ± 6	−7 ± 6	−66 ± 3	125.0	−0.06	18
	P2		−0.1 ± 0.3	49 ± 4	−1 ± 4	−48 ± 2	97.0	−0.03	18
	$H_2PO_4^-$	CP	0.2						30
MCPA			0.5 ± 0.4						18
$H_2PO_4^-$, two sites			−0.5 ± 0.4						18
$NH_4H_2PO_4$		BD	0.9	23.6	−5.6	−15.4	39.0	−0.50	14
$H_2PO_4^-$, one site									
$(NH_4)_2HPO_4$		BD	1.5	48.0	−9.9	−33.6	81.6	−0.42	14
HPO_4^{2-}, one site									
$(NH_4)_3PO_4{\cdot}3H_2O$		BD	1.4	36.5	16.1	−48.4	84.9	0.52	80
PO_4^{3-}, one site									
		CP	1.4	51.4	−13.6	−33.6	85.0	−0.53	80
$MgNH_4PO_4{\cdot}6H_2O$		BD	6.4	17.4	17.4	−15.8	33.2	1.00	80
PO_4^{3-}, one site		CP	6.4	16.5	16.5	−13.9	30.3	1.00	80
			6.0						224
			6.1						225
$MgHPO_4{\cdot}3H_2O$			−8.0						226
HPO_4^{2-}, one site			−7.2						227
Amorphous $MgHPO_4$			−2.4						227

$Mg_3(PO_4)_2$		−0.5					228
PO_4^{3-}, one site							
$Mg_3(PO_4)_2{\cdot}22H_2O$		1.1					228
PO_4^{3-}, one site							
$Mg_3(PO_4)_2{\cdot}8H_2O$		4.3 ± 0.3					228
PO_4^{3-}, one site		4.6					227
	BD	4.6					14
Amorphous $Mg_3(PO_4)_2$		0.5					228
K_3PO_4	BD	−11.7 ± 0.5	−11.7	−11.7	−11.7	0.0	1.00	229
PO_4^{3-}, one site							
$Na_3PO_4{\cdot}12H_2O$	BD	7.8					14
PO_4^{3-}, one site							
$NaH_2PO_4{\cdot}H_2O$	BD	2.3	61.1	23.1	−77.3	138.4	0.45	14
$H_2PO_4^-$, one site							
Na_2HPO_4	BD	6.6	74.5	−5.7	−48.9	123.4	−0.30	14
HPO_4^{2-}, one site							
$NaNH_4HPO_4{\cdot}4H_2O$	BD	5.1	56.5	−4.2	−36.9	93.4	−0.30	14
HPO_4^{2-}, one site							
KH_2PO_4	BD	4.3	24.8	3.9	−15.6	40.4	−0.03	14
$H_2PO_4^-$, one site							
$K_2HPO_4{\cdot}3H_2O$	BD	2.1	57.8	−6.5	−45.0	102.8	−0.25	14
HPO_4^{2-}, one site							
β-TCP	BD	−1.6	58.2	−16.2	−46.7	104.9	−0.42	80
PO_4^{3-} (P1, P2, P3)	BD	0.2	42.6	−5.1	−36.9	79.5	−0.20	80
	BD	2.9	16.2	2.8	−10.4	26.5	−0.01	80
	CP	−1.6	55.5	−13.3	−47.0	102.5	−0.34	80
	CP	0.2	37.7	−4.2	−33.0	70.7	−0.18	80

(*continued*)

TABLE 1 (*continued*)

Sample	Assignment	Method	δ_{iso} (ppm)	δ_{11} (ppm)	δ_{22} (ppm)	δ_{33} (ppm)	Span (ppm)	Skew	Reference
		CP	2.8	16.1	2.4	−10.1	26.2	−0.05	80
		BD	3.0						14
	P1	BD	−0.5						114
	P1	BD	2.3						114
	P2	BD	5.0						114
	P2	BD	1.5						114
	P3	BD	0.1						114
		CP	1.5						30
		CP	4.3						30
		BD	0.1						223
		BD	1.2						223
		BD	4.2						223
α-TCP			−0.3 to 4.7						111
PO_4^{3-}, 12 sites									
$Na_4P_2O_7$		BD	−1.2[c]	37.0	37.0	−80.0	117.0	1.0	230
$P_2O_7^{4-}$, two sites		BD	−2.4[c]						230
α-$Mg_2P_2O_7$		BD	−14.0						231
$P_2O_7^{4-}$, two sites		BD	−20.3						231
β-$Mg_2P_2O_7$		BD	−19.2						231
$P_2O_7^{4-}$									

[a] Bloch decay.
[b,c] Because of resolution problem, the CSA data correspond to the average of these two sites.

3.3. ^{43}Ca NMR

Calcium is such a ubiquitous element in biominerals that ^{43}Ca NMR is clearly an important spectroscopic technique in the study of biomineralization. However, ^{43}Ca is a spin 7/2 nucleus and it is a difficult NMR nucleus because of its low gyromagnetic ratio, low isotopic natural abundance (0.145%), and the presence of nuclear quadrupole moment. Thanks to the advancement in NMR instrumentation, ^{43}Ca NMR becomes more accessible in recent years. In general, the nuclear quadrupole coupling constant and the CSA of ^{43}Ca are not significant in calcium orthophosphates. Therefore, a moderate spinning frequency (2–3 kHz) can usually provide sufficient resolution for the ^{43}Ca MAS spectra. In many cases, only the ^{43}Ca isotropic chemical shifts and the signal line widths can be obtained in the ^{43}Ca spectra.[117–122] For the calcium ions whose first coordination spheres contain oxygen atoms only, the ^{43}Ca chemical shifts would have a linear correlation with the mean Ca···O distance.[117–121] Accordingly, the ^{43}Ca isotropic chemical shift increases as the mean Ca···O bond distance decreases. However, different classes of compounds such as silicates and carbonates have different correlation lines.[121] Furthermore, the correlation between the calcium coordination numbers and ^{43}Ca chemical shifts is not evident.[118]

The choice of the primary reference standard for the ^{43}Ca chemical shift scale has been carefully examined. The IUPAC recommendation of the standard is 0.1 M of $CaCl_2$ aqueous solution. However, the low natural abundance of ^{43}Ca has rendered the acquisition of a reference spectrum very time-consuming. Dupree et al. suggested to use a saturated aqueous solution of $CaCl_2$ as an alternative.[117] However, it has been found that the resonance frequency of the ^{43}Ca signal of the saturated $CaCl_2$ solution could have significant variation, depending on the conditions of sample preparation.[121] Consequently, it has been recommended to use 1.0 M of $CaCl_2$ solution as the primary standard or to use solid calcium oxide as the secondary reference standard (136.0 ppm).[121,123]

3.3.1. Hydroxyapatite

There are two crystallographically inequivalent calcium sites, viz. Ca(I) and Ca(II), in the crystal lattice of HAp. Ca(I) ions are coordinated by the oxygen atoms of PO_4^{3-} only, whereas Ca(II) ions are coordinated by both the oxygen atoms of PO_4^{3-} and OH^- ions.[99] ^{43}Ca 3QMAS has been used to resolve the two calcium sites at 14.1 T.[21] The resonances of Ca(I) and Ca(II) are also well resolved in the ^{43}Ca MAS spectrum measured at the B_0 field of 18.8 T.[124] Because the site occupancies of Ca(I) and Ca(II) are in a ratio of 2:3, the signals at −1.8 and 11.2 ppm are assigned to Ca(I) and Ca(II), respectively, by comparing their signal intensities. This assignment was subsequently verified in the ^{43}Ca{^{1}H} double resonance measurements of

^{43}Ca labeled HAp samples, where it had been exploited the fact that Ca (II) is in close proximity to the hydroxyl group.[21,29]

3.3.2. Calcium carbonate

Of many polymorphs of calcium carbonate, calcite and aragonite are widely found in biominerals. Another polymorph known as vaterite is also found in pathogenic biominerals such as gallstones. Given the importance of these polymorphs of calcium carbonate, the ^{43}Ca NMR studies of calcite, aragonite, and vaterite are of considerable interest in the study of biomineralization.[117,123] In particular, the chemical shift and electric field gradient tensors of the calcium sites of the three polymorphs have been characterized by first-principle calculations.[123] The fidelity of the calculations has been verified by the favourable agreement between the experimental and calculated ^{43}Ca NMR parameters of model compounds such as calcite and aragonite. Then, the ^{43}Ca MAS spectrum of vaterite was analyzed by first-principle calculations based on different structural scenarios proposed in the literature. However, the poor signal-to-noise ratio of the spectrum renders an accurate analysis of the ^{43}Ca NMR parameters very difficult. Nevertheless, both the ^{43}Ca and ^{13}C NMR data suggest that the structure of vaterite is better represented by the hexagonal $P6_3/mmc$ space group.[123] Overall, these three polymorphs of calcium carbonate have rather distinctive chemical shift properties and quadrupolar coupling constants. The extracted ^{43}Ca chemical shift data and the mean Ca···O distances of the three polymorphs have linear correlation as documented in the literature.[117,118] ^{43}Ca NMR spectroscopy should be an effective method for their detection in biominerals or *in vitro* model systems.

3.4. Double resonance NMR

To determine orientation of an adsorbed molecule relative to the mineral surface, one would need to employ dipolar recoupling techniques to extract the distance constraints between the selected spin species of the molecule and of the surface. For polypeptide–HAp systems, ^{13}C{^{31}P} REDOR has been carried out for uniformly ^{13}C labeled molecules, where numerical simulations show that the effect of ^{13}C dipole–dipole interaction is relatively minor.[125] For a study of bone sample, *o*-phospho-L-serine was taken as the model compound for the setup of the ^{13}C{^{31}P} REDOR experiments, where the data can be well analyzed by a ^{13}C–^{31}P spin-pair model with the internuclear distance equal to 2.7 Å.[126] Concerning the effect of ^{31}P homonuclear dipolar interaction on the spin dynamics, Drobny and co-workers have carried out a detailed REDOR NMR study of polycrystalline diammonium hydrogen phosphate ($(NH_4)_2HPO_4$).[127,128] The results show that the ^{15}N{^{31}P} REDOR data can

be adequately analyzed based on either a spin system containing an ^{15}N spin with 4 or 5 nearest ^{31}P spins, or an ^{15}N–^{31}P–^{31}P system where the ^{31}P–^{31}P dipolar coupling constant is set to the effective coupling constant obtained from ^{31}P homonuclear dipolar recoupling experiments. The three-spin model is particularly advantageous in the study of peptide–HAp systems because the explicit inclusion of the ^{31}P dipolar coupled network of HAp for any NMR data analysis is computationally very demanding. The three-spin model has been applied for the study of statherin–HAp interaction,[125,128,129] where an effective dipolar coupling of 600 Hz was set for the two ^{31}P spins.

Calcium benzoate trihydrate, with a chemical formula of $Ca(C_6H_5COO)_2 \cdot 3H_2O$, has been employed for the measurement of ^{43}Ca–^{13}C double resonance experiments.[130] This compound can serve as a good model system for the study of calcium in biological systems because its Ca^{2+} ions are coordinated to carboxylate groups and water molecules. In particular, the $^{13}C\{^{43}Ca\}$ transfer of populations in double resonance (TRAPDOR)[131] experiments have been carried out for the 60% ^{43}Ca-labeled compound.[130] It is remarkable that a Ca···C distance of 5.64 Å can be detected. It can be surmised that $^{13}C\{^{43}Ca\}$ experiments can provide useful structural constraints for the characterization of protein–HAp interaction.

4. MODEL SYSTEMS OF BIOMINERALIZATION

Biomineralization is a slow and complicated *in vivo* process. Many simple *in vitro* systems have been developed to model a particular aspect of the biomineralization process. Although in most cases the biological relevance of the *in vitro* systems may require further justification, the results can provide important insights into the processes being mimicked. In the near future, this divide-and-conquer approach will remain the most effective strategy for the study of biomineralization.

4.1. Transformation of OCP to HAp

Biomineralization is a biological process describing the formation of minerals in living organisms.[132] Whether biological apatite is formed by direct precipitation or through an intermediate phase remains an unsettled issue in the field of biomineralization.[77,133] According to the OCP precursor model proposed by Brown,[98] the first calcium phosphate crystals formed in a supersaturated solution under physiological conditions are OCP-like. The subsequent hydrolysis step leads to the formation of HAp during the structural transition. An *in vitro* system has been developed to model this process,[104,134] where the transformation of OCP to HAp is achieved by raising the pH condition from acidic to alkaline.

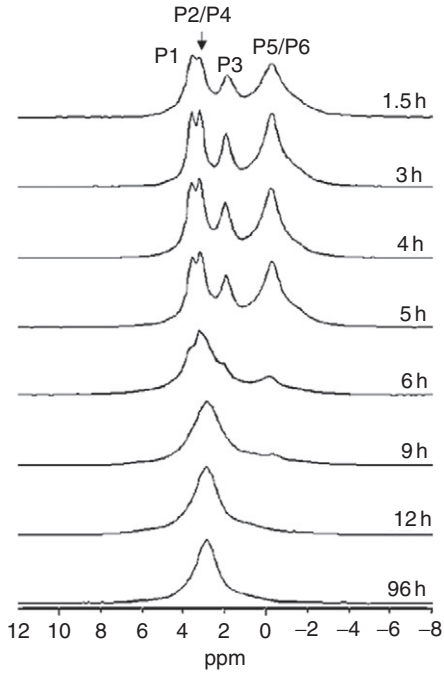

Figure 9 ^{31}P MAS spectra measured for a series of samples obtained at different reaction times. The transformation of OCP to HAp is well represented by the ^{31}P spectra. (Reprinted with permission from Ref. 104. © 2006 American Chemical Society.)

While all the phosphorus atoms in a unit cell of HAp are equivalent, there are six crystallographically non-equivalent phosphorus sites in OCP. As such, solid-state ^{31}P NMR is well suited to characterize the OCP to HAp transformation at the molecular level.

Figure 9 shows the ^{31}P MAS spectra measured for a sample series obtained for an OCP to HAp transformation reaction.[104] This series of MAS spectra demonstrates that the transformation of OCP to HAp is a gradual process and the resolution of the ^{31}P spectra of the first few samples is sufficient to allow a detailed analysis of the ^{31}P{^{1}H} CP dynamics of each resolved signal. The parameters τ_{CP} and $T_{1\rho}$ (see Equation (1)) obtained are consistent with the facts that (i) P5 and P6 are HPO_4^{2-} species; (ii) P3 is hydrogen bonded to one of the HPO_4^{2-} groups; (iii) P2 and P4 are in close vicinity to neighbouring water molecules; and (iv) P1 is rather isolated from all the water molecules (distance > 4.6 Å).[101] From the variation of the τ_{CP} and $T_{1\rho}$ data of P1, P2/P4, the following events have been inferred. The OCP crystals obtained initially contain a lot of structural waters, rendering the crystallinity rather poor. When the pH of the reaction mixture increases slowly, those water molecules in excess

will be eventually driven out of the lattice, resulting in an improvement of the crystallinity. As the pH increases to around 5, water molecules will re-enter the OCP lattice, presumably through the hydration layer of the OCP structure. This reversal in water flow direction is accompanied by a significant lengthening of the crystallographic *a* and *b* axes, causing an expansion of the OCP lattice as verified in the X-ray diffraction (XRD) measurements. The ''crowded'' water molecules in the hydration layer then provide a collisional mechanism for the relocation of the HPO_4^{2-} groups (P5 and P6).[104]

As discussed in Section 2, by monitoring the buildup rate of the homonuclear DQ signals, one may extract the empirical parameter *A* which is related to the van Vleck's second moment of the coupled spins. The variation of the parameter *A* should reflect the same variation in the second moment for a particular DQ signal, provided that the efficacy of the proton decoupling remains approximately the same. Therefore, one could calculate the percentage change of the *A* values corresponding to the same DQ coherence and compare the results with what one would expect from a proposed model for the OCP transformation. Assuming that the phosphorus groups of OCP will take the shortest pathways to migrate to the nearest phosphorus sites of HAp, an OCP to HAp transformation model has been built by superimposing the HAp lattice onto the OCP lattice. That is, the mappings between the OCP phosphorus sites and those HAp sites have been identified by computer-assisted lattice matching. Consequently, the DQ experimental data are more consistent with the scenario in which the crystallographic *c* axes of OCP and HAp are in opposite direction at the OCP–HAp interface. In addition, it has been shown that during the structural transformation the *b* axis of OCP is parallel to the $[2\bar{1}\bar{1}0]_{HAp}$ axis of HAp. In other words, the interface between OCP and HAp occurs parallel to the *bc* plane of OCP.[135]

Overall, the above NMR data provide hitherto the most detailed description of the OCP to HAp transformation mechanism at the molecular level.[104] As illustrated in Figure 10, initially the phosphate ions of the apatite and hydration layers of the OCP lattice will drift to form HAp sublattices (the dashed parallelograms). These sublattices are contiguous along the OCP *b* axis, but for clarity, only one HAp sublattice per row across the OCP *a* axis is shown. The apatite layers of OCP are structurally very similar to those of the HAp lattice, and therefore, they are readily available as seeding sites for HAp crystal growth. One can visualize in Figure 10 that the HAp sublattices of neighbouring apatite layers, viz. a-I and a-II, are not equivalent in the sense that they cannot be matched along the OCP *b* axis. As an illustration, one could take the a-I and a-II types of HAp sublattices as the top and bottom seeding sites, respectively, for the epitaxial growth of the HAp crystal. The parallelograms in solid red lines depict the translational shifts of the dashed parallelograms as a result of

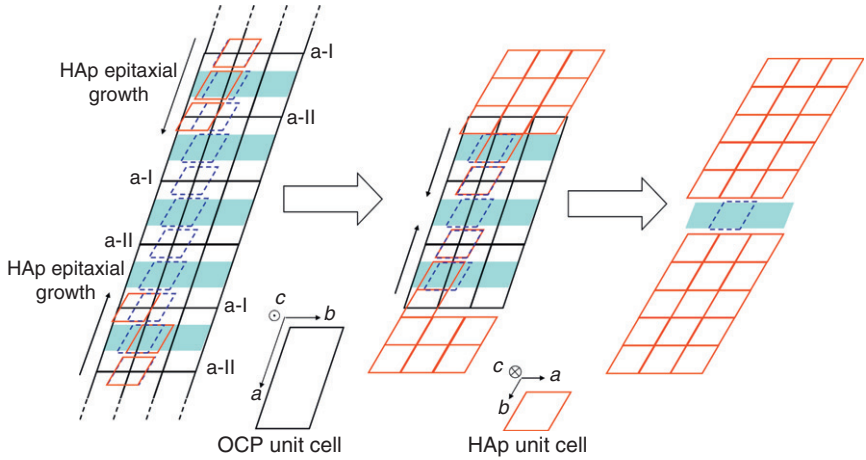

Figure 10 Formation of the central dark lines in biological apatites is most likely due to the lattice mismatch when OCP is hydrolyzed to form HAp. (Reprinted with permission from Ref. 104. © 2006 American Chemical Society.)

crystal growth. Eventually, the top and bottom HAp lattices will find a significant mismatch at a junction corresponding to the water layer of OCP. The ''trapped'' OCP water layer has a close resemblance to the ''central dark line'' (CDL) in biological apatites. Indeed, the HRTEM images of dentin crystals measured by Cuisinier and co-workers indicate that the molecular structure of a CDL corresponds closely to the water layer of OCP and that the hydrolysis of OCP in the formation of biological crystals develops along (100) crystal planes.[136] One may surmise that if two neighbouring seeding sites are of the same type of HAp sublattice, either a-I or a-II, there will be no mismatch junction in between. Consequently, if there are N seeding sites, the probability of CDL formation would become $1 - (0.5)^{N-1}$. This simple calculation explains the likelihood of multiple CDL formations in synthetic apatites.[137]

4.2. OCP incorporated with succinate

Earlier biochemical studies had reported that the Krebs cycle in mitochondria are closely associated with the intramitochondrial precipitation of electron-dense mineral granules,[138] which have been suggested as ACP containing OCP-carboxylate components.[139] Previous studies have shown that succinate ions ($OOCC_2H_4COO^{2-}$) can be incorporated into the lattice of OCP,[139–142] leading to the formation of the OCP-succinate (OCPS) compound.[139] Consequently, OCPS prepared *in vitro* could serve as a model system to mimic the biomineralization process in mitochondria. The XRD

patterns of OCPS and OCP are very similar except that the characteristic peak of OCP at 2θ equal to 4.751 is shifted to 4.181 in OCPS, which is interpreted as the elongation of the *d*-spacing of the (100) plane from 1.86 to 2.13 nm. As described previously for OCP,[102,105] the PO_4^{3-} groups at sites P2 and P4 may have a strong tendency to react with the neighbouring water molecule to form HPO_4^{2-}. That is, the number of the hydrogen phosphate groups is more than what implied in the chemical formula of OCP because of the change in the spectroscopic parameters of the phosphorus species at P4 and/or P2. Not surprisingly, the same phenomenon is observed for OCPS, which implies that the loss of crystal water during the formation of OCPS may have caused a change in the hydrogen bonding environment of other phosphorus sites.[143] In particular, the similarity of their τ_{CP} values suggests that the ''excessive'' P1 may come from P2 and/or P4. In any case, it is doubtless that the site occupation at P5 is significantly reduced upon the incorporation of succinate. From the literature,[99] it is known that each unit cell of OCP contains two formula units of $Ca_8(HPO_4)_2(PO_4)_4{\cdot}5H_2O$. Consequently, the structure of OCPS can be qualitatively described as a compound comprising one succinate molecule per unit cell of OCPS, in which one of the two P5s will be replaced by succinate ions.[143] Such replacement is accompanied by a significant loss of structural water. The hydrogen bonding of the remaining P5 with water molecules would be weakened considerably as indicated by the significant increase of its chemical shift span. Such incorporation of the succinate ions must be driven by the enthalpy gain of certain well-defined interactions, leading to a uniform change in the periodicity of the cell dimension.

The ^{31}P MAS spectrum of OCPS has been assigned by ^{31}P homonuclear DQ spectroscopy. On the basis of the deconvolution data of the ^{31}P MAS spectrum and the thermogravimetric analysis results, the molecular formula of OCPS was determined to be $Ca_{7.81}(HPO_4)_{1.82}(PO_4)_{3.61}(\text{succinate})_{0.56}{\cdot}zH_2O$, where $z \leq 0.5$.[143] When succinate ions are incorporated to form the OCPS lattice, mainly the phosphorus species at the P5 site will be displaced. The stability of OCPS is significantly higher than OCP with respect to the hydrolysis reaction at high pH condition. Apparently, the succinate ions will considerably dampen the dynamics of the water molecules within the hydration layer, rendering the relocation of the phosphate ions within the hydration layer very difficult. Previously, it has been shown that the transformation of OCP to HAp upon an increase in pH is accomplished by structural rearrangement in the hydration layer, followed by the concatenation of the hence formed HAp sublattices.[104] Together with the results of OCPS, it is clearly shown that the structure of the hydration layer of OCP is rather versatile and is playing the key role in the structural transformation of OCP. We note in passing that some organic molecules such as citrate ions can also be incorporated into synthetic calcite by coprecipitation.[144]

4.3. Morphology control of apatite

A detailed understanding of the precipitation process of calcium phosphate in the presence of biomolecules is the key to unravelling the molecular mechanism of biomineralization.[132] Many studies and *in vitro* studies have been carried out to shed light on different facets of this important topic.[77,145] The apatite crystals found in calcified tissues are nanosized and may have specific spatial arrangement as shown in the tooth enamel of rat incisor.[145] It has been suggested that such intriguing arrangement of the crystallites is brought by the so-called boundary-organized mineralization, which involves the interactions between the inorganic surface and a large variety of biomolecules such as phospholipids, polypeptides, and polysaccharides.[132] Studies of this kind of organic–inorganic interaction have provided continuous inspiration for the discipline of biomaterials.[146–150] Numerous efforts have been made to tailor the crystal morphology of HAp by a large variety of organic species including amino acids,[151–153] monosaccharides,[154] dendrimers,[155] surfactants,[156–158] and reverse micelles.[159]

Referring to the systematic study by Mann and co-workers on amino acid-functionalized HAp nanorods, the crystallites of HAp precipitated in the presence of aspartic acid are elongated nanorods.[151] On the other hand, XRD measurements were used to show that glutaric acid (GA; $HOOC(CH_2)_3COOH$) has a prominent effect on the crystal morphological of HAp, but not the aspartic acid.[160] Such ''discrepancy'' highlights the dramatic effects of temperature, pH, and concentrations on the morphology control of crystallites. The GA-HAp sample was prepared by the following reaction:

$$10Ca^{2+} + 6H_2PO_4^- + 2H_2O \rightarrow Ca_{10}(PO_4)_6(OH)_2 + 14H^+$$

In the presence of GA, the HAp crystallites are formed via the OCP to HAp transformation pathway.[160] The phosphorus species at the organic–inorganic interface were characterized by $^{31}P\{^1H\}$ HETCOR, where the frequency-switched LG irradiation was applied during the t_1 evolution.[161] Although there is no specific spectral marker observed for the interfacial interaction, the results suggest that some mobile water molecules are trapped in the GA–mineral interface during the transformation of OCP to HAp. In a recent $^{31}P\{^1H\}$ CPMAS study of the chemical interaction of phosphoric acid ester with HAp, the signal of pyrophosphate at ca. −15 ppm was observed, showing that P–O–P linkages are formed between the ester molecules and the phosphate groups on the HAp surface.[162] However, there is no spectroscopic evidence for any P–O–P linkages in the GA-HAp system. In other words, the interaction of GA and HAp surface is non-covalent and water molecules are important structural entity between the GA molecules and the HAp surface.

4.4. Molecule−Surface Interaction

The primary function of the proteins involved in biomineralization process, such as statherin, is to mediate the cellular function at the mineral surface. Substantial efforts have been made to control nucleation and growth of crystals from organic templates by *in vitro* experiments[146,163–165] and in natural biomineralizing systems.[145,166] These studies suggest that nucleation of the mineral phase occurs on the peptide surfaces so that repetitive patterns of anionic groups are exposed to concentrate the inorganic cations, leading to the nucleation of crystal. On the other hand, it has been argued in a very recent review that protein–surface interaction may largely involve electrostatic interaction instead of arrays of complementary charges.[167] It is currently accepted that polyacidic regions commonly found in proteins which interact with HAp are responsible for adhering the proteins to HAp.[168] However, the molecular mechanism of the interaction between biopolymers and mineral surfaces remains largely unknown because of the lack of structural data with atomistic resolution. It is unclear whether the charged residues near the N-terminus of statherin will recognize the spatial arrangement of the ions on the HAp surface, or the statherin–HAp binding is simply the result of electrostatic interaction.

Since the last decade, solid-state NMR has proved to be an effective analytical tool to probe the molecule–surface interaction.[5,128,169–172] These works represent the first successful step in unravelling the mechanism of biomineralization at the molecular level, and a lot of valuable structural information concerning the orientations of the statherin or its N-terminal fragment with respect to the HAp surface has been obtained.[7] However, experimental high-resolution structural models of the polypeptides adsorbed on the mineral surface are still not available. The major difficulty in the solid-state NMR studies is the poor signal sensitivity. With reference to the protocol of sample preparation documented in these studies, the peptide sample was chemisorbed to HAp by mixing the peptide and the crystalline HAp samples in a buffer solution. The surface area of a commercial HAp sample is in general less than 80 m^2/g. Given that the polypeptide–HAp sample packed in a 4-mm rotor (a typical sample holder in solid-state NMR experiments) is about 40 mg and that the statherin coverage on HAp is about 5.2×10^{-7} mol/m^2,[173] the amount of peptide amenable to measurement is estimated to be 0.8 μmol. This limited peptide content renders it difficult to acquire the one-dimensional ^{13}C solid-state NMR spectra with good signal-to-noise ratio, let alone the two-dimensional ^{13}C–^{13}C correlation spectra. Without the resolution enhancement offered by two-dimensional NMR techniques, the information content per sample becomes very limited. Fortunately, this sensitivity problem has been alleviated very recently by an

in situ preparation of HAp in the presence of the target polypeptides.[174] In particular, the 15-residue peptide, which is derived from the N-terminal of the salivary protein statherin (SN15), was chosen for the *in situ* HAp preparation. As a result, the amount of SN15 adsorbed on the HAp surface can be increased to 4.3 μmol per 40 mg of peptide–HAp sample. It is noteworthy that this protocol of sample preparation is readily applicable to the study of other protein–HAp interactions. Because of this significant enhancement in NMR sensitivity, it becomes possible to measure a two-dimensional ^{13}C–^{13}C correlation spectrum for a ^{13}C uniformly labeled peptide sample adsorbed on mineral surface. Figure 11 shows the ^{13}C–^{13}C correlation spectra measured for the ^{13}C uniformly labeled SN15 adsorbed on HAp surface and for the labeled SN15 in free form. For simplicity, only K6 and G12 of the SN15 are ^{13}C uniformly labeled. The data for K6 are consistent with the finding that SN15 in free form adopts a helical conformation.[175] With reference to the spectrum of the SN15 in bound state, the chemical shifts of G12 do not have any appreciable changes, and yet there are two sets of cross-peaks observed for K6. The C_α chemical shift of the major component (66%) bears a close resemblance to that observed for SN-15 in free form, while the minor component (34%) has the chemical shift very close to the random-coil value.[176] In fact, the line width data of the minor components are in the range from

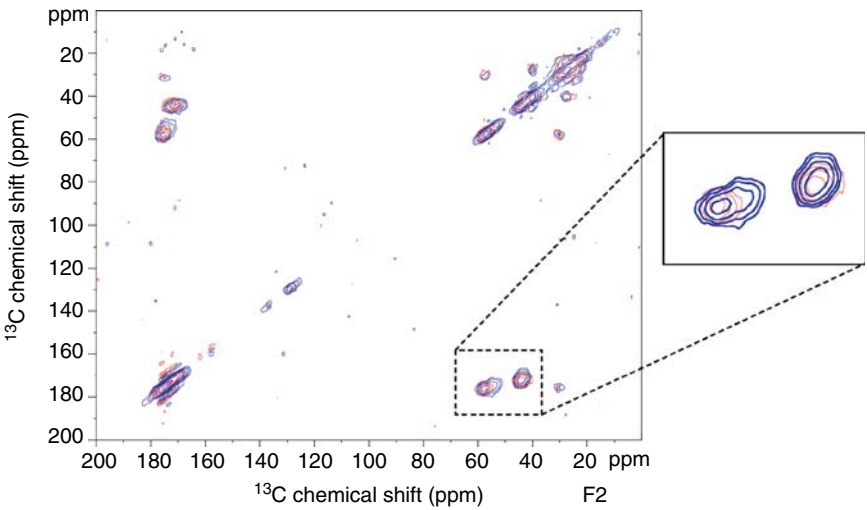

Figure 11 Overlay ^{13}C–^{13}C correlation spectrum of SN15 in free form (red) and SN15 adsorbed to HAp (blue). The inset highlights the C^{α}–C′ cross-peaks of K6 and G12, which were uniformly labeled. (Reprinted with permission from Ref. 174. © 2008 American Chemical Society.)

3.8 to 4.3 ppm, which is typically found for the random aggregates of polypeptides.[177] The two-dimensional NMR measurement was repeated after sample rehydration. The resultant spectrum confirms that the observed structural heterogeneity is not due to lyophilization. A possible rationalization is that there are two types of SN15–HAp interacting mechanisms. The presence of two binding mechanisms is also supported by the thermodynamic studies of statherin adsorption onto HAp, in which it is concluded that there are two different binding sites for the statherin–HAp interaction.[173,178] The mechanism corresponding to the minor component requires the peptide to undergo a conformational change at K6 from a helical to random-coil structure, whereas the conformation near the region of G12 does not have any major changes. This mechanism is consistent with the data reported by Drobny et al.,[8] where it has been demonstrated that the residue G12 has very little interaction with the HAp surface[179] and that the residue K6 is in close proximity to the HAp surface.[170] On the other hand, the mechanism corresponding to the major peak component may be either due to a simple electrostatic interaction between the peptide and the mineral surface, or due to the fact that conformation of the statherin in its free form can recognize the binding sites on HAp surface. In both cases, no significant alternation of the backbone conformation would be induced on the polypeptide.

A significant progress in computational studies of statherin–HAp interaction has been observed in recent years.[180–182] These theoretical studies have identified a lot of structural scenarios awaiting for further verification by solid-state NMR studies. In particular, Gray and co-workers have identified in their calculations a novel structural motif, viz. Interstice of the Phosphate-Oxygen Triad (IPOT) on the HAp (001) surface, which may account for the statherin–HAp interaction.[181,182] The binding sites of IPOT can be readily recognized by the basic residues of statherin so that it would not undergo significant rearrangement upon adsorption to HAp surface.[182] As shown in Figure 12, it has been predicted that the residues K6, R9, R10, and R13 of statherin fit well into a IPOT pocket and therefore they should be close to the (001) surface of HAp. However, $^{13}C\{^{31}P\}$ REDOR results indicate that R13 is at a distance larger than 7 Å from the crystal surface.[125] Figure 13 shows the model deduced from the distance constraints obtained by solid-state NMR measurements.[125] It is not yet clear whether the discrepancy of the two models is due to the scenario that the preferred binding surface of statherin includes crystal facets other than (001), or that the computational approach has not captured the native conformation of statherin in the bound state. In any case, it is doubtless that molecular modelling and solid-state NMR are two complementary techniques for the study of protein–surface interaction.

Recently, there is a new hypothesis that the organic–mineral interface in bone and teeth is mediated by polysaccharides in addition to

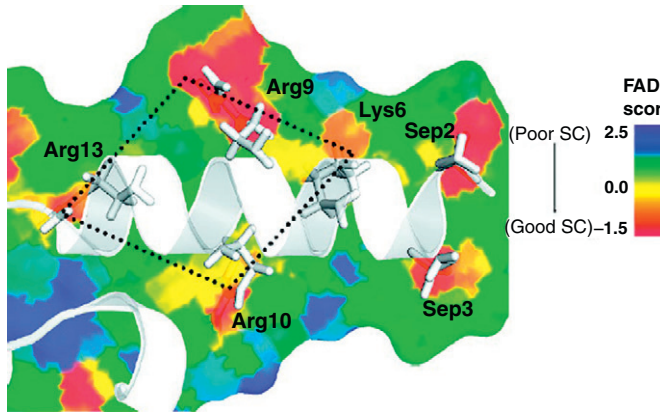

Figure 12 Conformation of statherin on HAp surface determined by molecular modelling. The four basic residues (K6, R9, R10, and R13) fit nicely to the IPOT motif (outlined in dots). FADE scores are quantitative measure of shape complementarity. (Reprinted with permission from Ref. 181. © 2007 American Chemical Society.)

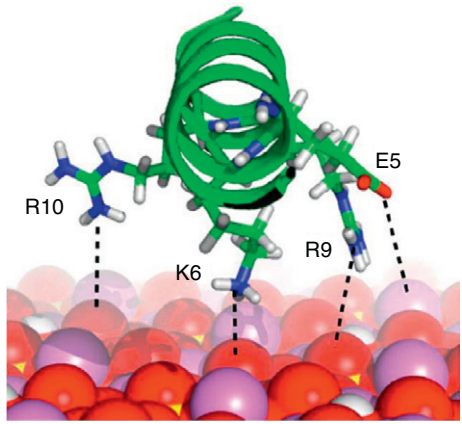

Figure 13 Model of statherin on the HAp surface based on solid-state NMR measurements. (Reprinted with permission from Ref. 125. © 2010 Elsevier.)

proteins.[126,183,184] The authors have designed some model compounds to test the hypothesis that glycosaminoglycans (GAGs), which have many negatively charged functional groups such as sulphates and carboxylates, will interact with HAp surface.[185] Accordingly, the so-called pre-formed HA model was prepared by mixing chondroitin sulphate (ChS), which is one family of GAGs, with slurry of HAp crystallites for 2 h, whereas the *in situ* HA model was prepared by precipitation of HAp in the presence

of ChS. For the *in situ* HA sample, the $^{13}C\{^{31}P\}$ REDOR data indeed suggest that all ^{13}C sites of ChS are in close contact with the mineral surface. Interestingly, the ^{13}C chemical shifts of the adsorbed ChS are very similar to those of free ChS (deviation < 1 ppm), which means that the change in the magnetic susceptibility when the ChS molecules deposit on the HAp surface is not very large. Because the $^{13}C\{^{31}P\}$ REDOR dephasing effect is less prominent in the pre-formed HA model, it has been inferred that the ChS physically adsorbed on the HAp surface is mediated by a water layer. Overall, the binding mode of ChS to the HAp surface is quite different in the two models.[185] This finding immediately suggests that a difference in binding mode may also occur in the two sample preparation protocols developed by Drobny[8] and Chan[174] for the study of SN15–HAp interface (vide supra).

Another important contribution to our understanding of organic–inorganic interface is a recent study of ^{43}Ca-enriched CHAp-B containing osteocalcin protein.[186] Figure 14 shows the ^{43}Ca 3QMAS spectrum, which clearly shows that there would be a significant change in the environment of calcium ions upon the interaction between the bone protein and the mineral surface. The dramatic changes in the ^{43}Ca chemical shift and the quadrupolar coupling constant of the two calcium sites can serve as valuable bench marks for theoretical studies to unravel the nature of the interaction.[187]

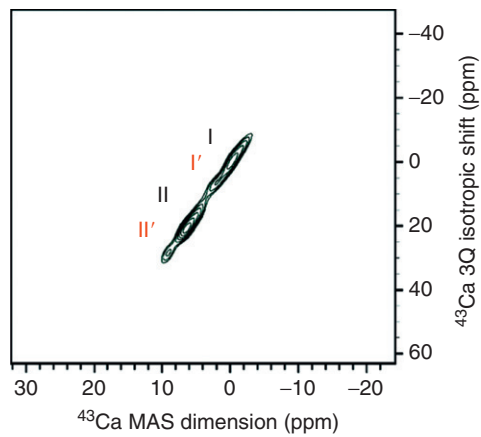

Figure 14 ^{43}Ca 3QMAS spectrum of ^{43}Ca-enriched carbonated apatite powder sample, to which bovine osteocalcin was physically adsorbed. (Reprinted with permission from Ref. 186. © 2010 American Chemical Society.)

5. BIOMINERALS

Hierarchical structures are often found in biominerals such as sea shell, teeth, and bone. These structures display a large variety of mechanical, chemical, and biological functions in living organisms.[132] Therefore, understanding their structural features is very helpful for the development of functional materials with sophisticated structure.

5.1. Nacre

Calcite is thermodynamically the most stable polymorph of calcium carbonate under ambient conditions, whereas aragonite is stable under high-pressure conditions. Interestingly, natural occurring aragonite crystals can be found in the nacre produced by pearl oysters under ambient conditions.[188] According to the diffraction study, nacre contains layered crystalline aragonite platelets with the [001] direction pointing toward the β-chitin layers.[1] Such crystal alignment within the organic matrix may be a consequence of the relatively high polarity of the (001) face.[189] ^{13}C solid-state NMR has proved to be a valuable technique for the study of nacreous systems. The $^{13}C\{^{1}H\}$ CPMAS spectrum of *Pinctada fucata* (*P. fucata*) shows a resonance at 171 ppm (FWHM 4 ppm), indicating either a very poor crystallinity of the aragonite crystallites or, more likely, an insufficient proton decoupling during the acquisition period.[190] The carbonate signal exhibits a higher CP efficiency than pure aragonite and synthetic $CaCO_3$ composites. The ^{13}C T_1 relaxation time of the carbonates in nacre (90 s) is significantly shorter than that of pure calcite (180 s).[190] That is, the carbonates in the aragonite platelets of nacre should have a proton reservoir in close vicinity. Overall, the spectroscopic data suggest that the nacreous layer of *P. fucata* is formed by a perfectly ordered assembly of nano aragonite crystallites, which can thus account for the electron diffraction results.[190]

In contrast to *P. fucata*, the aragonite platelets in the nacre of *Haliotis laevigata* (*H. laevigata*) have shown to be covered by a continuous layer of amorphous calcium carbonate (ACC).[191] Accordingly, the measured ^{13}C T_1 relaxation time for the aragonites in *H. laevigata* is about 2000 s.[191] The ^{13}C Bloch decay spectrum, dominated by the signal attributable to the bulk crystalline aragonite, exhibits a single sharp resonance at 171 ppm (FWHM, 0.6 ppm),[191] which is consistent with the HRTEM data.[92] The $^{13}C\{^{1}H\}$ CPMAS spectrum, which shows a broader signal (FWHM, 1.5 ppm), is dominated by the signals of the ACC layer. With reference to the $^{13}C\{^{1}H\}$ HETCOR spectra, the ^{13}C signals assigned to the ACC phase is correlated to the ^{1}H signals at 5.5 and 14.4 ppm.[191] The ^{1}H signal at 5.5 ppm is assigned to water molecules undergoing fast but hindered

reorientations, whereas the one at 14.4 ppm is to the hydrogen carbonate. Hence, it can be concluded that the ACC phase contains water molecules and hydrogen carbonates. No observable correlations between the aliphatic carbons of the organic matrix and the proton species of the ACC layer are found.[191] Furthermore, the ^{1}H T_1 relaxation times of the organic matrix (ca. 300 ms), the mobile water molecules (2 s), and the hydrogen carbonate units (12 s) are very different, suggesting that these proton species are not in close proximity. Overall, the NMR data lead to a conclusion that the proteins are not in direct contact with the aragonite crystal, which contradicts the traditional view that the surface of biominerals should have an epitaxial match with the organic matrix.[191]

5.2. Coccoliths

Coccoliths are oval-shaped plates of calcium carbonate produced by the unicellular marine alga *Emiliania huxleyi* (*E. huxleyi*).[132] In general, it is very difficult to study the biomolecules incorporated into biominerals because ^{13}C and ^{15}N solid-state NMR studies are difficult for natural abundance samples. As such, it is truly remarkable that ^{15}N and ^{13}C enriched *E. huxleyi* samples have been prepared from isotopically enriched growth media.[192] Both the ^{13}C Bloch decay and $^{13}C\{^{1}H\}$ CPMAS spectra contain a carbonate signal at 168.6 ppm. The sharp peak (FWHM, 0.2 ppm) observed in the Bloch decay spectrum is assigned to the highly crystalline calcite environment, whereas the broader peak shown in the CPMAS spectrum (FWHM, 0.9 ppm) is assigned to interfacial carbonates. The two carbonate species are not in close proximity because the corresponding peak components have very different T_1 relaxation times. The crystalline calcite signal shows substantial $^{13}C\{^{15}N\}$ and $^{13}C\{^{31}P\}$ REDOR dephasing effects. The internuclear ^{13}C–^{31}P and $^{13}C-^{15}N$ distances were found to be 3.3 ± 0.2 Å and 2.3 ± 0.2 Å, respectively, based on the spin-pair approximation. These results suggest that nitrogen and phosphorus moieties are incorporated into the calcite crystallites without significant distortion of the lattice structure.[192] Clearly, these nitrogen and phosphorus species cannot be any sizable biomolecules. Indeed, very little lattice distortion has been observed when some nitrate ions are incorporated into calcite lattice.[193] On the other hand, no pronounced $^{13}C\{^{15}N\}$ and $^{13}C\{^{31}P\}$ CP-REDOR dephasing is found for the broader carbonate signal, implying the absence of nitrogen or phosphorus species in the vicinity of interfacial carbonates.[192]

5.3. Bone

Bones are highly complex biomaterials with multi-hierarchical levels of structure of different length scales ranging from 1 nm to >1 mm. Solid-state NMR is well suited to characterize the most fundamental structural

units of bones. It is obvious that ^{31}P and ^{1}H NMR are very useful in the study of bone samples. The most important findings on bone samples obtained by solid-state NMR up to year 2003 have been nicely summarized in a monograph.[2] Here, we just focus on some new findings in the past few years.

Because the phosphorus content in the organic matrix would give a very weak ^{31}P signal only, the $^{31}P\{^{1}H\}$ CPMAS spectra are usually dominated by the orthophosphate units of the inorganic phase of bone.[28,194] Consequently, it is not necessary to remove the organic content of bone samples by chemical treatment prior to the $^{31}P\{^{1}H\}$ solid-state NMR measurements. This advantage has been exploited in the quantification of the apatitic hydroxyl groups in human bone samples, where the OH content was estimated to be ca. 20% of that in stoichiometric HAp based on $^{31}P\{^{1}H\}$ HETCOR measurements.[28] This quantitative result has been later confirmed in another independent measurement based on the $^{1}H\{^{31}P\}$ CPMAS technique.[19] The $^{31}P\{^{1}H\}$ HETCOR spectra acquired for the bone samples of human,[28] bovine,[28,195] rat,[28,195], and horse[196] invariably show only one featureless resonance at ca. 3.0 ppm in the ^{31}P dimension, which correlates to three resonances in the ^{1}H dimension, *viz*. a sharp signal at approximately 0 ppm, a broad peak centring around 5 ppm, and a very broad peak in the region of 5–15 ppm. These three ^{1}H peaks are assigned to the apatitic OH^{-} group, the structural water near the crystallite surface, and the disordered orthophosphates, respectively. The presence of water signal in the $^{31}P\{^{1}H\}$ HETCOR spectrum suggests that the mobility of the surface water molecules is slow enough to warrant some residual $^{1}H-^{31}P$ dipolar interactions and the significant signal line width indicates the presence of multiple water adsorption sites on the surface.[28] Furthermore, the absence of spinning sidebands for the water signal implies that the molecules may possess rapid exchange among the adsorption sites on the surface. The water signal in the HETCOR spectrum of bone is usually more intense than that observed for synthetic HAp because of the larger surface area of bone apatite.[28]

By monitoring the ^{1}H MAS spectra, it has been suggested that the loss of water from bone tissue is an irreversible process under air drying conditions.[38] It has been shown that CP transfer within an isolated heteronuclear spin pair will exhibit a characteristic oscillation, from which the dipolar coupling constant can be accurately determined.[197] The technique of LG-CPMAS can probe this oscillation pattern due to a dominating $^{31}P–^{1}H$ interaction in a dipolar coupled network, if any. However, such oscillation is seldom observed in $^{31}P\{^{1}H\}$ CPMAS measurements of biominerals because of the damping effect of the homonuclear dipole–dipole interaction. Thus, it is rather remarkable that the buildup curve of $^{31}P\{^{1}H\}$ LG-CPMAS obtained for a sample of powdered femoral cortical bone, which is partially hydrated, shows a distinctive

oscillation pattern, from which a $^{31}P–^{1}H$ distance of 2.32 to 2.55 Å was determined.[38] Knowing that there is a significant reduction of apatitic OH^- ions in bone[28] and that the oscillation pattern is not observed for the completely dehydrated sample, it has been inferred that the results observed for the partially hydrated sample is due to the interaction between the phosphate ions and an ordered water layer on the crystallite surface.[38] On the other hand, such oscillation pattern is not observed for the fully hydrated sample, presumably due to the dynamic exchange of the adsorbed water molecules with the bulk water. It has thus been suggested that interstitial water, which occupies crystal vacancies, may stabilize defect-containing apatite crystals.[195] These water molecules are confined between the mineral and the collagenous matrix, mediating mineral–organic matrix interactions.

A series of $^{13}C\{^{31}P\}$ REDOR measurements have been carried out for bone, teeth, and mineralized cartilage samples of natural abundance,[40,126,183,184] which represent some very important solid-state NMR studies of biominerals in the past few years. In the biomineral samples, ^{13}C spins are mostly confined to the organic matrix, whereas ^{31}P spins are largely originated from the orthophosphates of the inorganic phase. Therefore, any observed $^{13}C–^{31}P$ REDOR dephasing would reveal the molecular structure at the organic–inorganic interface. The carboxylate group of glutamic acid, resonating in the ^{13}C NMR region of 180–185 ppm, shows a considerable dephasing effect, from which it has been deduced that a glutamate-containing protein interacts strongly with the mineral surface.[126] The most interesting finding, however, is that a significant REDOR dephasing is observed for a ^{13}C signal at 76 ppm. Because no common amino acid would give rise to a signal in this region, it has been subsequently assigned to the secondary alcohol carbons in pyranose sugars such as GAGs in proteoglycans.[184] The evidence is that quite a similar REDOR dephasing data were obtained for tissues containing substantial amount of sugar content. As another supporting evidence, Duer and co-workers have prepared some model compounds to illustrate that ChS molecules, one family of GAGs, can be bound to the surface of HAp.[185] This series of studies have initiated a new line of thinking that GAGs, in addition to proteins, may also play a key role in the organic–mineral interface in vertebrates. After the submission of this review, a very important paper has been published by Schmidt-Rohr and co-workers (doi:10.1073/pnas.1009219107), which shows that the C-13 signal at 76 ppm observed in bone sample should be assigned to citrate ions bound on the apatite surface.

Differential $^{31}P\{^{1}H\}$ CPMAS technique has been applied to study mineral crystals of calcium phosphate deposited during osteoblast calcification in cell culture.[198] The samples harvested after 8 days of culture represent the minerals formed at the very early stage of calcification, in

which apatitic phosphate groups with poor crystallinity have been identified. The presence of the HPO_4^{2-} group has also been confirmed by the DCP technique after the removal of organic matrix. Interestingly, the ^{31}P CSAs of the HPO_4^{2-} species found in the 8-day and 60-day samples are very similar to that observed in mature bone mineral.[198] Most importantly, no ^{31}P signals associated with brushite, OCP or other mineral phase of calcium phosphate have been detected.

An *in situ* detection of the dehydration effect on bovine cortical bone samples has been carried out using $^{13}C\{^1H\}$ CPMAS and ^1H MAS.[199] Figure 15 shows the dehydration process manifested in the NMR spectra. The dehydration-induced line broadening shown in the ^{13}C spectra has been attributed to a local conformational disorder of the bone matrix and to the slow dynamics of side chains of collagen.[200–202] Another interesting aspect is that the resolution of the ^1H MAS spectra is significantly better than what has been shown previously.[28] The first ^{43}Ca NMR study of bone samples of natural abundance has been carried out recently.[122] The ^{43}Ca spectrum of the sample exhibits only one featureless signal, whereas there are two resolved resonances observed for crystalline HAp.[122,124] The ^{43}Ca chemical shift data show that the Ca···O distance in bone is about 2.4–2.5 Å, which is quite similar to that of crystalline HAp. Previously, it has been demonstrated that Ca^{2+} is readily replaced by sodium ions in crystalline Na-substituted calcium phosphate.[76,114] Interestingly, it is

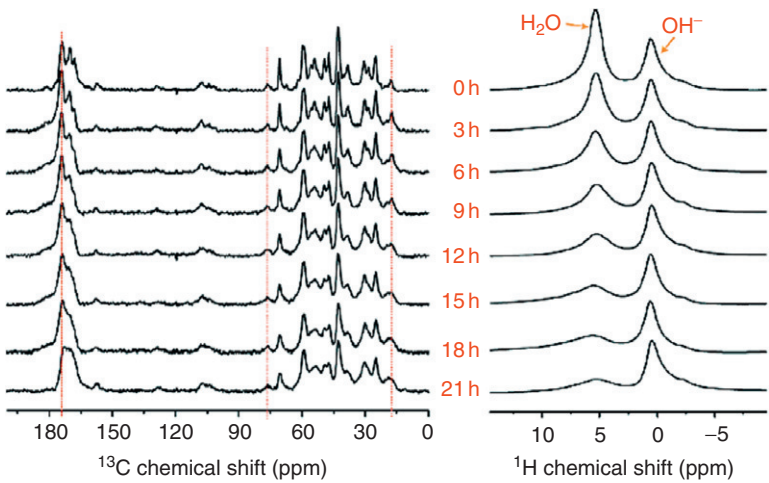

Figure 15 ^{13}C and ^1H MAS spectra of a fresh bovine cortical bone (0 h). Measurements were then carried out after successive 3 h intervals of dehydration (spectra labeled 3–21 h). The total acquisition times for each ^{13}C and ^1H spectrum were 3 h and 3 min, respectively. (Reprinted with permission from Ref. 199. © 2009 American Chemical Society.)

relatively easy to detect ^{23}Na signals in equine bone and bovine tooth.[122] Because of the intrinsic low crystallinity of biological apatites, there is a continuous distribution of the ^{23}Na chemical shift and quadrupolar parameters. The ^{23}Na{^{31}P} REDOR shows that all sodium ions in bone samples are close to phosphates. Measurements of ^{1}H{^{23}Na} R^{3}-HMQC spectra indicate that most sodium ions are located in the apatite phase of bone. Similar results were also obtained for the teeth samples.[122]

Recently, a detailed comparison of the ^{31}P{^{1}H} CPMAS spectra of normal bone samples and those affected by osteoarthritis have been carried out but there are no significant difference found in the NMR data. This suggests that osteoarthritis would not directly alter the mineral structure of bones.[196]

5.4. Bisphosphonate−bone interaction

Bisphosphonates are the major drugs for diseases associated with bone resorption.[203] There is an on-going effort to develop novel biomaterials for the delivery of bisphosphonates,[204–206] but a detailed discussion is beyond the scope of this review. Indeed, adsorption of bisphosphonates to bone is an important factor for their potency and therefore it is of great interest to study how bisphosphonates interact with bone.[207,208] The binding affinity of different bisphosphonates to human bone can be estimated from the corresponding signal intensities of the ^{31}P{^{1}H} CPMAS spectra measured for the bisphosphonate–bone samples.[207] The results have a good correlation with the retention times of the bisphosphonates on HAp obtained by column chromatography, suggesting that the binding of bisphosphonates to bone collagen is not significant.[207,209] In addition, by a quantitative analysis of the ^{31}P MAS signals of the pamidronate–bone samples as a function of the amount of pamidronate added, the surface area per pamidronate on bone is determined as 30−38 Å^{2} per molecule, implying a high coverage on the mineral surface of bone in a monolayer.[207] The binding behaviour can be described by the Langmuir-binding isotherm, which is the same as the statherin–HAp system.[178] However, the binding free energy of bisphosphonate–bone (–4.3 kcal/mol)[207] is lower than that of statherin–HAp (–7.9 kcal/mol).[178] The fact that high concentration of PO_4^{3-} ions is required to elute bisphophonates from HAp column suggests that chemisorptions is the major binding mechanism of bisphosphonates to bone.[209] As another supporting evidence for the chemisorptions mechanism, it has been shown that the ^{31}P CSAs of the bisphosphonates in free form and in bound state are quite similar. That is, there is no substantial motional averaging of CSA which would otherwise occur in a physisorption process.[207,210] By ^{13}C{^{15}N} transfer echo double resonance (TEDOR)[211] measurements, the conformation of the side chain C(1)–C(2)–C(3)–N of [$^{13}C_3$, ^{15}N]-pamidronate bound to bone was found to be close to *gauche*

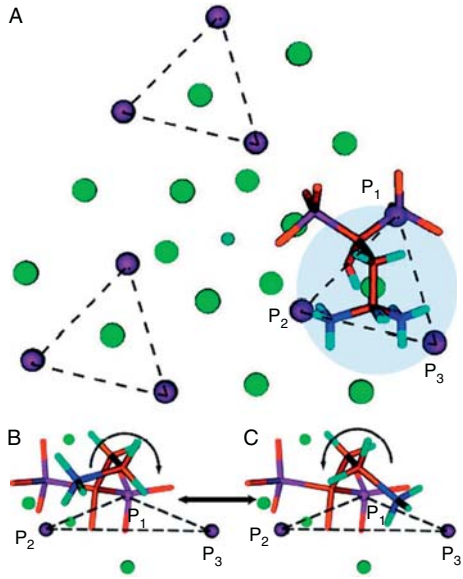

Figure 16 Molecular models for pamidronate–HAp interactions. (A) Top view of pamidronate bound to a "phosphorus-triangle" on HAp surface, where the PO_4^{3-} group at the P1 site was displaced by a phosphate group of the pamidronate. The OH group interacts with a neighbouring Ca^{2+} ion (green). Note that the two conformations of pamidronate, viz. *gauche*+ and *gauche*−, are superimposed on each other. (B, C) Two views of pamidronate (carbon in brown, oxygen in red, and hydrogen in cyan) with the side chain of NH_3^+ (dark blue) bound to P2 or P3 of the "phosphorus-triangle". (Reprinted with permission from Ref. 207. © 2008 American Chemical Society.)

backbone conformation, which would then maximizes the electrostatic interaction of pamidronate with the bone mineral surface.[207] The amine side chain of pamidronate was shown to be protonated by ^{15}N NMR. In addition, the side-chain mobility of bisphosphonates on bone has been characterized by ^{2}H NMR and the results suggest that the side chains of bisphosphonate undergo fast but restricted motions when bound to bone.[207] Figure 16 shows the molecular model constructed for pamidronate–bone interactions on the basis of the solid-state NMR data described above.

5.5. Dentin

There are three distinct biological minerals in an individual tooth, viz. enamel, dentin, and cementum. The chemical composition of dentin is quite similar to that of bone, containing 70 wt% of inorganic phase, 20 wt% of organic matrix and 10 wt% of water.[83] The inorganic phase of tooth

dentin was identified as calcium phosphate with an apatite structure.[132] Dentin is a hierarchical composite material comprising type-I collagen fibrils and nanocrystalline apatite.[212] The structure of dentin has as a feature the presence of dental tubules. Therefore, dentin can be categorized further into peritubular dentin (highly mineralized) and intertubular dentin (less mineralized). A recent TEM study shows that the intertubular mineral of age-induced transparent dentin contains apatite crystallites embedded in amorphous matrix.[213] Dentin samples of the incisor taken from Wistar rats of different ages were chosen for recent solid-state NMR studies.[16,33] Rat incisor is ''rootless'' in which the root canal is open and the tooth continues to grow indefinitely. The dentin sample was prepared by grinding the rat incisors into powder form after removing the enamel layer. To quantify the various ^{31}P species in dentin, a commercial HAp sample was used as the spin-counting standard. The contribution of the ^{31}P signal from the organic component is expected to be negligible.[2] To probe the ^{31}P species which are remote from any protons, the spin-echo technique incorporated with ^{1}H rotary resonance was employed. The ^{31}P signal intensities extrapolated at vanishing spin-echo delay reveals the data free from transverse relaxation effect. The acquired ^{31}P spectra invariably contain a single sharp peak at 3.2 ppm, with FWHM equal to 288 Hz (2.4 ppm). The relatively narrow FWHM indicates that the phosphorus species are of crystalline nature, which was subsequently assigned to HDAp, that is, OH-deficient apatite. The overall phosphate content decreases from the 3-week to the 24-month sample by 12%, which is mainly due to the decrease of the phosphorus content in the amorphous phase. The relative amounts of the HAp and ACP components were determined by measurement of a series of $^{31}P\{^{1}H\}$ HETCOR with different contact times.[16] The ^{31}P NMR data show that the phosphorus species in the amorphous phase account for more than 50% of the total phosphorus amount in rat dentin. After explicitly taking HO–H$\cdots$O–PO_3^{3-} and HPO_4^{2-} into account, it has been shown that 19% of the apatite crystallites in our dentin samples contain hydroxyl groups, which is quite similar to the result reported for bone minerals.[28] Furthermore, the total amount of HO–H$\cdots$O–PO_3^{3-} and HPO_4^{2-} decreases as rat dentins mature with age, consistent with the earlier FT-IR results of bone.[214] Because of their disorder nature, it is very difficult to separately quantify the amounts of HO–H$\cdots$O–PO_3^{3-} and HPO_4^{2-} in the amorphous phase. Nevertheless, the τ_{CP} data have led to the conclusion that in the 24-month sample the amount of HO–H$\cdots$O–PO_3^{3-} is significantly less than that of HPO_4^{2-}.[16]

Using the pulse sequences shown in Figure 4, the spin diffusion rate between two inorganic phases such as HAp/HDAp can be estimated. The results show that the ^{31}P spin diffusion rates of HAp/HDAP and ACP/HDAp are approximately the same, whereas the rate of HAp/ACP is considerably smaller. In other words, ACP and HDAp are in close proximity,

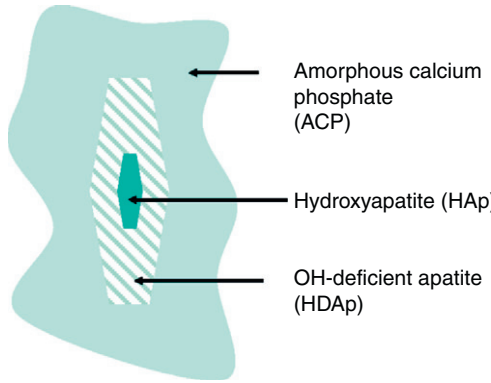

Figure 17 Structural model of rat dentin based on the ^{31}P solid-state NMR measurements. (Reprinted with permission from Ref. 33. © 2009 American Chemical Society.)

and so are HAp and HDAp. Because the phases of HAp and ACP are spatially more remote, the ''average'' structure of Wistar rat dentin is constructed as shown in Figure 17. Note that the phase of HDAp has a wide range of levels of hydroxyl deficiency. One may attempt to deduce the dimension of the apatite crystallites from the spin diffusion data. However, it is not easy to take into account the effect of ^{1}H–^{31}P dipole–dipole interaction, which is relatively strong in ACP, on the spin diffusion rate. In any case, the faster spin diffusion rate for ACP/HDAp indicates that such effect would not affect our major conclusion, that is, HAp constitutes the core of an apatite crystallite. The most intriguing aspect of our model is that the core of each apatite crystallite consists of HAp. During the dentinogenesis, the highly phosphorylated protein, dentin phosphoprotein, would induce the precipitation of calcium phosphate in the organic matrix to trigger the mineralization of dentin at the mineralization front.[215] The mechanism of the initiation of biological mineralization has been under debate for many years.[216] The major dispute is whether a non-apatitic phase such as ACP is the nucleating phase for *in vivo* biological apatite, or the biomineralization process proceeds via poorly crystalline apatitic mineral. Although the NMR data cannot directly address the issue concerning the role of ACP in the incipient formation of the apatitic phase, the results are indeed consistent with the scenario that ACP provides the nucleation sites for the formation of non-stoichiometric apatite crystallites (HDAp), which may then slowly transform to HAp as driven by thermodynamics.

5.6. Mineralized cartilage and others

Cartilage is an important connective tissue in the joints between bones and other parts of the endoskeleton of animals. The process of cartilage mineralization is closely related to bone formation.[77] The ^{31}P MAS spectra

measured for the calcified cartilage of the epiphyseal growth plate and for the mineralized articular cartilage are quite similar to the spectrum of bone, which exhibits a single broad and featureless peak.[40,214] As in the case of bone, the $^{13}C\{^1H\}$ CPMAS spectrum of mineralized cartilage is dominated by signals of collagen.[40] Using the $^1H \rightarrow ^{31}P \rightarrow ^1H$ strategy, the high-resolution ^1H spectrum of mineralized cartilage contains three ^1H signals at 0.2, 5.2, and 10.2 ppm, corresponding to the hydroxyl ions, bound water, and surface HPO_4^{2-} ions, respectively.[40] On the basis of $^{13}C\{^{31}P\}$ REDOR measurements, not only has the contact between GAGs and the mineral surface been inferred but also the proteins containing γ-carboxyglutamic acid have been suggested as possible mediators at the organic−mineral interface.[40]

Biominerals formed via pathological calcifications have received less attention in the literature of solid-state NMR. Nevertheless, a good understanding of the formation mechanisms of urinary stones, dental calculus, plaques, etc., is clearly an important issue in medical science. Duer and co-workers have shown that the organic–inorganic interface of plaques is quite similar to that of bones.[217] Using ^{13}C and ^{31}P MAS NMR, it has been found that uric acid and calcium oxalate are the major inorganic species found in renal calculi.[80] By comparison with a series of model crystalline compounds, the inorganic phosphates present in various types of urinary and bladder stones have been distinguished and quantified.[80] In another study, $^{13}C\{^1H\}$ CPMAS has been applied to study gall bladder stones and some preliminary spectral markers have been observed for the gallstones associated with different pathological conditions.[218]

6. OUTLOOK

We have reviewed the recent solid-state NMR studies of biomineralization. Thanks to the advancement of hardware and methodology in NMR, a great deal of progress has been achieved regarding our understanding of the structure of biominerals. In the coming decades, ^{31}P and ^{13}C most likely would remain popular options in the NMR studies of biomineralization. In the past few years, ^{43}Ca NMR on natural abundance samples has proved to be a feasible technique. Because the natural abundance of ^{25}Mg is significantly higher than that of ^{43}Ca, ^{25}Mg NMR may be another interesting possibility in the studies of biominerals. ^{17}O NMR, on the other hand, should be very useful in isotopically enriched *in vitro* model systems. Currently, ^{17}O NMR works on systems related to biomineralization are very scarce in the literature. Nonetheless, given the significant progress of ^{17}O NMR in other research fields,[219] it is worthy to pursue its applications in apatitic systems. For NMR works of low-gamma half-integer quadrupole nuclei such as ^{43}Ca, ^{25}Mg, and ^{17}O, sensitivity is an

important issue. Applications in biomineralization studies would present some stringent tests on any novel techniques for the signal enhancement of the central transitions. Furthermore, dynamic nuclear polarization (DNP)[220] is an exciting option for signal enhancement in the NMR studies of biominerals. In any case, judicious sample preparations would be the key to make a real progress in the field of biomineralization.

The NMR parameters of selected model compounds have been compiled in this review. The list of model compounds, however, is far from complete. Inclusion of some other interesting model compounds such as biological whitlockites ($(Ca, Mg)_3(PO_4)_2$) and calcium pyrophosphate dehydrate ($Ca_2P_2O_7 \cdot 2H_2O$) would be advantageous for the studies of related pathologically calcified tissues. Furthermore, theoretical calculations of the chemical shifts of model compounds are very important for the data interpretation of NMR spectra acquired for biominerals. This point has been well recognized by several research groups.[73,121,221,222]

ACKNOWLEDGEMENTS

This work was supported by the National Science Council of Taiwan. We thank Dr Yao-Hung Tseng for initiating our studies in biomineralization. The fruitful collaborations with Profs Chung-Yuan Mou, Chun-Pin Lin, and Yuan-Ling Lee are gratefully acknowledged.

REFERENCES

1. H. A. Lowenstam and S. Weiner, *On Biomineralization*. Oxford University Press, New York, 1989.
2. W. Kolodziejski, *in*: New Techniques in Solid-State NMR, (J. Klinowski ed.), Vol. 246, 2004, pp. 235–270.
3. A. Iuga, C. Ader, C. Groger and E. Brunner, *in*: Annual Reports on NMR Spectroscopy, (G. A. Webb ed.), Vol. 60, Academic Press, London, 2007, pp. 145–189.
4. C. Groger, K. Lutz and E. Brunner, *Prog. Nucl. Magn. Reson. Spectrosc.*, 2009, **54,** 54–68.
5. G. P. Drobny, J. R. Long, T. Karlsson, W. Shaw, J. Popham, N. Oyler, P. Bower, J. Stringer, D. Gregory, M. Mehta and P. S. Stayton, *Annu. Rev. Phys. Chem.*, 2003, **54,** 531–571.
6. P. S. Stayton, G. P. Drobny, W. J. Shaw, J. R. Long and M. Gilbert, *Crit. Rev. Oral Biol. Med.*, 2003, **14,** 370–376.
7. G. Goobes, R. Goobes, W. J. Shaw, J. M. Gibson, J. R. Long, V. Raghunathan, O. Schueler-Furman, J. M. Popham, D. Baker, C. T. Campbell, P. S. Stayton and G. P. Drobny, *Magn. Reson. Chem.*, 2007, **45,** S32–S47.
8. G. Goobes, P. S. Stayton and G. P. Drobny, *Prog. Nucl. Magn. Reson. Spectrosc.*, 2007, **50,** 71–85.
9. J. V. Hanna and M. E. Smith, *Solid State Nucl. Magn. Reson.*, 2010, **38,** 1–18.
10. J. P. Amoureux, J. Trebosc, L. Delevoye, O. Lafon, B. Hu and Q. Wang, *Solid State Nucl. Magn. Reson.*, 2009, **35,** 12–18.
11. M. Eden, *Solid State Nucl. Magn. Reson.*, 2009, **36,** 1–10.
12. V. Ladizhansky, *Solid State Nucl. Magn. Reson.*, 2009, **36,** 119–128.
13. P. K. Madhu, *Solid State Nucl. Magn. Reson.*, 2009, **35,** 2–11.

14. G. L. Turner, K. A. Smith, R. J. Kirkpatrick and E. Oldfield, *J. Magn. Reson.*, 1986, **70,** 408–415.
15. A. Kaflak-Hachulska, A. Samoson and W. Kolodziejski, *Calcif. Tissue Int.*, 2003, **73,** 476–486.
16. Y. H. Tseng, Y. L. Tsai, T. W. T. Tsai, J. C. H. Chao, C. P. Lin, S. H. Huang, C. Y. Mou and J. C. C. Chan, *Chem. Mater.*, 2007, **19,** 6088–6094.
17. A. Kaflak and W. Kolodziejski, *Magn. Reson. Chem.*, 2008, **46,** 335–341.
18. W. P. Rothwell, J. S. Waugh and J. P. Yesinowski, *J. Am. Chem. Soc.*, 1980, **102,** 2637–2643.
19. J. Kolmas and W. Kolodziejski, *Chem. Commun.*, 4390–4392.
20. W. Kolodziejski and J. Klinowski, *Chem. Rev.*, 2002, **102,** 613–628.
21. D. Laurencin, A. Wong, J. V. Hanna, R. Dupree and M. E. Smith, *J. Am. Chem. Soc.*, 2008, **130,** 2412–2413.
22. A. J. Vega, *J. Magn. Reson.*, 1992, **96,** 50–68.
23. R. G. Bryant, S. Ganapathy and S. D. Kennedy, *J. Magn. Reson.*, 1987, **72,** 376–378.
24. R. A. Santos, R. A. Wind and C. E. Bronnimann, *J. Magn. Reson. Ser. B*, 1994, **105,** 183–187.
25. B. J. van Rossum, C. P. de Groot, V. Ladizhansky, S. Vega and H. J. M. de Groot, *J. Am. Chem. Soc.*, 2000, **122,** 3465–3472.
26. V. Ladizhansky and S. Vega, *J. Chem. Phys.*, 2000, **112,** 7158–7168.
27. Y. T. Wu, J. L. Ackerman, H. M. Kim, C. Rey, A. Barroug and M. J. Glimcher, *J. Bone Miner Res.*, 2002, **17,** 472–480.
28. G. Y. Cho, Y. T. Wu and J. L. Ackerman, *Science*, 2003, **300,** 1123–1127.
29. A. Wong, D. Laurencin, R. Dupree and M. E. Smith, *Solid State Nucl. Magn. Reson.*, 2009, **35,** 32–35.
30. Y. T. Wu, M. J. Glimcher, C. Rey and J. L. Ackerman, *J. Mol. Biol.*, 1994, **244,** 423–435.
31. W. P. Aue, A. H. Roufosse, M. J. Glimcher and R. G. Griffin, *Biochemistry*, 1984, **23,** 6110–6114.
32. T. Gullion and J. Schaefer, *J. Magn. Reson.*, 1989, **81,** 196–200.
33. S. J. Huang, Y. L. Tsai, Y. L. Lee, C. P. Lin and J. C. C. Chan, *Chem. Mater.*, 2009, **21,** 2583–2585.
34. C. P. Jaroniec, C. Filip and R. G. Griffin, *J. Am. Chem. Soc.*, 2002, **124,** 10728–10742.
35. S. J. Huang, Y. H. Tseng, Y. Mou, S. B. Liu, S. H. Huang, C. P. Lin and J. C. C. Chan, *Solid State Nucl. Magn. Reson.*, 2006, **29,** 272–277.
36. J. P. Yesinowski and H. Eckert, *J. Am. Chem. Soc.*, 1987, **109,** 6274–6282.
37. M. M. Maricq and J. S. Waugh, *J. Chem. Phys.*, 1979, **70,** 3300–3316.
38. E. E. Wilson, A. Awonusi, M. D. Morris, D. H. Kohn, M. M. Tecklenburg and L. W. Beck, *J. Bone Miner Res.*, 2005, **20,** 625–634.
39. S. Maltsev and C. Jager, *Solid State Nucl. Magn. Reson.*, 2008, **34,** 175–179.
40. M. J. Duer, T. Friscic, R. C. Murray, D. G. Reid and E. R. Wise, *Biophys. J.*, 2009, **96,** 3372–3378.
41. K. Schmidt-Rohr, A. Rawal and X. W. Fang, *J. Chem. Phys.*, 2007, **126,** 16.
42. J. C. C. Chan, *Chem. Phys. Lett.*, 2001, **335,** 289–297.
43. J. C. C. Chan and H. Eckert, *J. Chem. Phys.*, 2001, **115,** 6095–6105.
44. M. Roming, C. Feldmann, Y. S. Avadhut and J. Gunne, *Chem. Mater.*, 2008, **20,** 5787–5795.
45. R. Tycko and G. Dabbagh, *Chem. Phys. Lett.*, 1990, **173,** 461–465.
46. M. Baldus, *Prog. Nucl. Magn. Reson. Spectrosc.*, 2002, **41,** 1–47.
47. S. Luca, H. Heise and M. Baldus, *Acc. Chem. Res.*, 2003, **36,** 858–865.
48. I. Schnell, *Prog. Nucl. Magn. Reson. Spectrosc.*, 2004, **45,** 145–207.
49. Y. K. Lee, N. D. Kurur, M. Helmle, O. G. Johannessen, N. C. Nielsen and M. H. Levitt, *Chem. Phys. Lett.*, 1995, **242,** 304–309.

50. M. Carravetta, M. Eden, X. Zhao, A. Brinkmann and M. H. Levitt, *Chem. Phys. Lett.*, 2000, **321,** 205–215.
51. A. Brinkmann, M. Eden, M. H. Levitt and J. Chem, *Phys.*, 2000, **112,** 8539–8554.
52. A. Brinkmann and M. H. Levitt, *J. Chem. Phys.*, 2001, **115,** 357–384.
53. M. H. Levitt, *in*: Encyclopedia in Nuclear Magnetic Resonance, D. M. Grant and R. K. Harris (eds.), Vol. 9, Wiley, Chichester, 2002.
54. M. H. Levitt, *J. Chem. Phys.*, 2008, **128,** 052205.
55. Y. Ishii, *J. Chem. Phys.*, 2001, **114,** 8473–8483.
56. N. A. Oyler and R. Tycko, J. Phys. Chem. *B*, 2002, **106,** 8382–8389.
57. A. Abragam, *Principles of Nuclear Magnetism*. Clarendon Press, Oxford, UK, 1961.
58. M. Bertmer and H. Eckert, *Solid State Nucl. Magn. Reson.*, 1999, **15,** 139–152.
59. J. Günne and H. Eckert, *Chem. Eur. J.*, 1998, **4,** 1762–1767.
60. M. Engelsberg and R. E. Norberg, *Phys. Rev. B*, 1972, **5,** 3395.
61. J. Günne, *J. Magn. Reson.*, 2006, **180,** 186–196.
62. E. R. de Azevedo, W. G. Hu, T. J. Bonagamba and K. Schmidt-Rohr, *J. Chem. Phys.*, 2000, **112,** 8988–9001.
63. D. Reichert, T. J. Bonagamba and K. Schmidt-Rohr, *J. Magn. Reson.*, 2001, **151,** 129–135.
64. E. R. de Azevedo, W. G. Hu, T. J. Bonagamba and K. Schmidt-Rohr, *J. Am. Chem. Soc.*, 1999, **121,** 8411–8412.
65. M. Kanapathipillai, Y. Yusufoglu, A. Rawal, Y. Y. Hu, C. T. Lo, P. Thiyaigarajan, Y. E. Kalay, M. Akinc, S. Mallapragada and K. Schmidt-Rohr, *Chem. Mater.*, 2008, **20,** 5922–5932.
66. A. Medek, J. S. Harwood and L. Frydman, *J. Am. Chem. Soc.*, 1995, **117,** 12779–12787.
67. J. P. Amoureux, C. Fernandez and S. Steuernagel, *J. Magn. Reson. Ser. A*, 1996, **123,** 116–118.
68. K. Shimoda, Y. Tobu, Y. Shimoikeda, T. Nemoto and K. Saito, *J. Magn. Reson.*, 2007, **186,** 156–159.
69. K. Shimoda, Y. Tobu, K. Kanehashi, K. Saito and T. Nemoto, *Solid State Nucl. Magn. Reson.*, 2006, **30,** 198–202.
70. S. V. Dorozhkin, *Materials*, 2009, **2,** 399–498.
71. L. J. Wang and G. H. Nancollas, *Chem. Rev.*, 2008, **108,** 4628–4669.
72. E. Brunner and U. Sternberg, *Prog. Nucl. Magn. Reson. Spectrosc.*, 1998, **32,** 21–57.
73. F. Pourpoint, C. Gervais, L. Bonhomme-Coury, T. Azais, C. Coelho, F. Mauri, B. Alonso, F. Babonneau and C. Bonhomme, *Appl. Magn. Reson.*, 2007, **32,** 435–457.
74. J. Feng, Y. J. Lee, R. J. Reeder and B. L. Phillips, *Am. Mineral.*, 2006, **91,** 957–960.
75. D. Stueber, A. M. Orendt, J. C. Facelli, R. W. Parry and D. M. Grant, *Solid State Nucl. Magn. Reson.*, 2002, **22,** 29–49.
76. H. E. Mason, A. Kozlowski and B. L. Phillips, *Chem. Mater.*, 2008, **20,** 294–302.
77. S. V. Dorozhkin and M. Epple, *Angew. Chem. Int. Ed.*, 2002, **41,** 3130–3146.
78. L. W. Schroeder, E. Prince and B. Dickens, *Acta Crystallogr., Sect. B: Struct. Sci.*, 1975, **B 31,** 9–12.
79. A. P. Legrand, H. Sfihi, N. Lequeux and J. Lemaitre, *J. Biomed. Mater. Res. Part B*, 2009, **91B,** 46–54.
80. M. Bak, J. K. Thomsen, H. J. Jakobsen, S. E. Petersen, T. E. Petersen and N. C. Nielsen, *J. Urol.*, 2000, **164,** 856–863.
81. N. A. Curry and D. W. Jones, *J. Chem. Soc. A*, 3725.
82. A. Kaflak-Hachulska, A. Slosarczyk and W. Kolodziejski, *Solid State Nucl. Magn. Reson.*, 2000, **15,** 237–238.
83. R. Z. LeGeros, *Calcium Phosphates in Oral Biology and Medicine*. Karger, Basel, 1991.
84. C. Jager, T. Welzel, W. Meyer-Zaika and M. Epple, *Magn. Reson. Chem.*, 2006, **44,** 573–580.

85. Y. H. Tseng, Y. Mou, C. Y. Mou and J. C. C. Chan, *Solid State Nucl. Magn. Reson.*, 2005, **27,** 266–270.
86. D. G. A. Nelson and J. D. B. Featherstone, *Calcif. Tissue Int.*, 1982, **34,** S69–S81.
87. J. C. Elliott, *in*: Phosphates: Geochemical, Geobiological, and Materials Importance, M. J. Kohn, J. Rakovan, and J. M. Hughes (eds.), **Vol.48,** Mineralogical Society of America, 2002, pp. 427–453.
88. K. Beshah, C. Rey, M. J. Glimcher, M. Schimizu and R. G. Griffin, *J. Solid State Chem.*, 1990, **84,** 71–81.
89. R. M. Wilson, S. E. P. Dowker and J. C. Elliott, *Biomaterials*, 2006, **27,** 4682–4692.
90. F. Babonneau, C. Bonhomme, S. Hayakawa and A. Osaka, in: Magnetic Resonance in Material Science, 2007, pp. 0984-MM0906–0905, Warrendale, PA.
91. N. Nassif, F. Martineau, O. Syzgantseva, F. Gobeaux, M. Willinger, T. Coradin, S. Cassaignon, T. Azais and M. M. Giraud-Guille, *Chem. Mater.*, 2010, **22,** 3653–3663.
92. N. Nassif, N. Pinna, N. Gehrke, M. Antonietti, C. Jager and H. Colfen, *Proc. Natl. Acad. Sci. USA*, 2005, **102,** 12653–12655.
93. J. Miller, *Prog. Nucl. Magn. Reson. Spectrosc.*, 1996, **28,** 255–281.
94. H. U. V. Gerth, T. Dammaschke, E. Schafer and H. Zuchner, *Dent. Mater.*, 2007, **23,** 1521–1528.
95. Y. Pan, *Solid State Nucl. Magn. Reson.*, 1995, **5,** 263–268.
96. P. Regnier, A. C. Lasaga, R. A. Berner, O. H. Han and K. W. Zilm, *Am. Mineral.*, 1994, **79,** 809–818.
97. H. E. Mason, F. M. McCubbin, A. Smirnov and B. L. Phillips, *Am. Mineral.*, 2009, **94,** 507–516.
98. W. E. Brown, *Clin. Orthop. Relat. Res.*, 1966, **44,** 205–220.
99. W. E. Brown, *Nature*, 1962, **196,** 1048–1050.
100. M. I. Kay, R. A. Young and A. S. Posner, *Nature*, 1964, **204,** 1050–1052.
101. M. Mathew, W. E. Brown, L. W. Schroeder and B. Dickens, *J. Crystallogr. Spectrosc. Res.*, 1988, **18,** 235–250.
102. Y. H. Tseng, J. H. Zhan, K. S. K. Lin, C. Y. Mou and J. C. C. Chan, *Solid State Nucl. Magn. Reson.*, 2004, **26,** 99–104.
103. K. S. K. Lin, Y. H. Tseng, Y. Mou, Y. C. Hsu, C. M. Yang and J. C. C. Chan, *Chem. Mater.*, 2005, **17,** 4493–4501.
104. Y. H. Tseng, C. Y. Mou and J. C. C. Chan, *J. Am. Chem. Soc.*, 2006, **128,** 6909–6918.
105. C. Rey, C. Combes, C. Drouet and M. J. Glimcher, *Osteoporosis Int.*, 2009, **20,** 1013–1021.
106. M. Iijima, D. G. A. Nelson, Y. Pan, A. T. Kreinbrink, M. Adachi, T. Goto and Y. Moriwaki, *Calcif. Tissue Int.*, 1996, **59,** 377–384.
107. Y. Wu, J. L. Ackerman, E. S. Strawich, C. Rey, H. M. Kim and M. J. Glimcher, *Calcif. Tissue Int.*, 2003, **72,** 610–626.
108. J. E. Roberts, L. C. Bonar, R. G. Griffin and M. J. Glimcher, *Calcif. Tissue Int.*, 1992, **50,** 42–48.
109. J. Tropp, N. C. Blumenthal and J. S. Waugh, *J. Am. Chem. Soc.*, 1983, **105,** 22–26.
110. M. Mathew, L. W. Schroeder, B. Dickens and W. E. Brown, Acta Crystallogr. *Sect. B Struct. Commun.*, 1977, **33,** 1325–1333.
111. M. Bohner, J. Lemaitre, A. P. Legrand, J. B. D. delaCaillerie and P. Belgrand, *J. Mater. Sci. Mater. Med.*, 1996, **7,** 457–463.
112. B. Dickens, L. W. Schroede and W. E. Brown, *J. Solid State Chem.*, 1974, **10,** 232–248.
113. M. Yashima, A. Sakai, T. Kamiyama and A. Hoshikawa, *J. Solid State Chem.*, 2003, **175,** 272–277.
114. L. Obadia, P. Deniard, B. Alonso, T. Rouillon, S. Jobic, J. Guicheux, M. Julien, D. Massiot, B. Bujoli and J. M. Bouler, *Chem. Mater.*, 2006, **18,** 1425–1433.
115. R. J. B. Jakeman, A. K. Cheetham, N. J. Clayden and C. M. Dobson, *J. Solid State Chem.*, 1989, **78,** 23–34.

116. J. Mason, *Solid State Nucl. Magn. Reson.*, 1993, **2,** 285–288.
117. R. Dupree, A. P. Howes and S. C. Kohn, *Chem. Phys. Lett.*, 1997, **276,** 399–404.
118. Z. J. Lin, M. E. Smith, F. E. Sowrey and R. J. Newport, *Phys. Rev. B*, 2004, **69,** 7.
119. A. Wong, A. P. Howes, R. Dupree and M. E. Smith, *Chem. Phys. Lett.*, 2006, **427,** 201–205.
120. F. Angeli, M. Gaillard, P. Jollivet and T. Charpentier, *Chem. Phys. Lett.*, 2007, **440,** 324–328.
121. C. Gervais, D. Laurencin, A. Wong, F. Pourpoint, J. Labram, B. Woodward, A. P. Howes, K. J. Pike, R. Dupree, F. Mauri, C. Bonhomme and M. E. Smith, *Chem. Phys. Lett.*, 2008, **464,** 42–48.
122. D. Laurencin, A. Wong, W. Chrzanowski, J. C. Knowles, D. Qiu, D. M. Pickup, R. J. Newport, Z. H. Gan, M. J. Duer and M. E. Smith, *Phys. Chem. Chem. Phys.*, 2010, **12,** 1081–1091.
123. D. L. Bryce, E. B. Bultz and D. Aebi, *J. Am. Chem. Soc.*, 2008, **130,** 9282–9292.
124. D. Laurencin, A. Wong, R. Dupree and M. E. Smith, *Magn. Reson. Chem.*, 2008, **46,** 347–350.
125. M. Ndao, J. T. Ash, P. S. Stayton and G. P. Drobny, *Surf. Sci.*, 2010, **604,** L39–L42.
126. C. Jaeger, N. S. Groom, E. A. Bowe, A. Horner, M. E. Davies, R. C. Murray and M. J. Duer, *Chem. Mater.*, 2005, **17,** 3059–3061.
127. G. Goobes, V. Raghunathan, E. A. Louie, J. M. Gibson, G. L. Olsen and G. P. Drobny, *Solid State Nucl. Magn. Reson.*, 2006, **29,** 242–250.
128. V. Raghunathan, J. M. Gibson, G. Goobes, J. M. Popham, E. A. Louie, P. S. Stayton and G. P. Drobny, J. Phys. Chem.. *B*, 2006, **110,** 9324–9332.
129. M. Ndao, J. T. Ash, N. F. Breen, G. Goobes, P. S. Stayton and G. P. Drobny, *Langmuir*, 2009, **25,** 12136–12143.
130. D. Laurencin, C. Gervais, A. Wong, C. Coelho, F. Mauri, D. Massiot, M. E. Smith and C. Bonhomme, *J. Am. Chem. Soc.*, 2009, **131,** 13430–13440.
131. C. P. Grey and A. J. Vega, *J. Am. Chem. Soc.*, 1995, **117,** 8232–8242.
132. S. Mann, Biomineralization—Principles and Concepts in Bioinorganic Materials Chemistry. Oxford University Press, New York, 2001.
133. M. Iijima and J. Moradian-Oldak, *J. Mater. Chem.*, 2004, **14,** 2189–2199.
134. J. Zhan, Y. H. Tseng, J. C. C. Chan and C. Y. Mou, *Adv. Funct. Mater.*, 2005, **15,** 2005–2010.
135. W. E. Brown, L. W. Schroeder and J. S. Ferris, *J. Phys. Chem.*, 1979, **83,** 1385–1388.
136. P. Bodier-Houlle, P. Steuer, J. C. Voegel and F. J. G. Cuisinier, Acta Crystallogr. *D*, 1998, **54,** 1377–1381.
137. M. Iijima, H. Tohda and Y. Moriwaki, *J. Cryst. Growth*, 1992, **116,** 319–326.
138. J. W. Greenawalt, C. S. Rossi and A. L. Lehninger, *J. Cell Biol.*, 1964, **23,** 21–38.
139. M. Markovic, B. O. Fowler and W. E. Brown, *Chem. Mater.*, 1993, **5,** 1401–1405.
140. L. Addadi and S. Weiner, *Proc. Natl. Acad. Sci. USA*, 1985, **82,** 4110–4114.
141. H. Monma and M. Goto, *Bull. Chem. Soc. Jpn.*, 1983, **56,** 3843–3844.
142. K. Sakamoto, S. Yamaguchi, M. Kaneno, I. Fujihara, K. Satoh and Y. Tsunawaki, *Thin Solid Films*, 2008, **517,** 1354–1357.
143. T. W. T. Tsai, F. C. Chou, Y. H. Tseng and J. C. C. Chan, *Phys. Chem. Chem. Phys.*, 2010, **12,** 6692–6697.
144. B. L. Phillips, Y. J. Lee and R. J. Reeder, *Environ. Sci. Technol.*, 2005, **39,** 4533–4539.
145. S. Weiner and L. Addadi, *J. Mater. Chem.*, 1997, **7,** 689–702.
146. S. I. Stupp and P. V. Braun, *Science*, 1997, **277,** 1242–1248.
147. S. H. Yu and H. Colfen, *J. Mater. Chem.*, 2004, **14,** 2124–2147.
148. F. C. Meldrum, *Int. Mater. Rev.*, 2003, **48,** 187–224.
149. L. Addadi, S. Raz and S. Weiner, *Adv. Mater.*, 2003, **15,** 959–970.
150. L. A. Estroff and A. D. Hamilton, *Chem. Mater.*, 2001, **13,** 3227–3235.
151. R. Gonzalez-McQuire, J. Y. Chane-Ching, E. Vignaud, A. Lebugle and S. Mann, *J. Mater. Chem.*, 2004, **14,** 2277–2281.

152. T. Matsumoto, M. Okazaki, M. Inoue, Y. Hamada, M. Taira and J. Takahashi, *Biomaterials*, 2002, **23,** 2241–2247.
153. H. G. Zhang, Q. S. Zhu and Y. Wang, *Chem. Mater.*, 2005, **17,** 5824–5830.
154. D. Walsh, J. L. Kingston, B. R. Heywood and S. Mann, *Growth*, 1993, **133,** 1–12.
155. J. Donners, R. J. M. Nolte and N. Sommerdijk, *Adv. Mater.*, 2003, **15,** 313–316.
156. L. Yan, Y. D. Li, Z. X. Deng, J. Zhuang and X. M. Sun, *Int. J. Inorg. Mater.*, 2001, **3,** 633–637.
157. S. Sarda, M. Heughebaert and A. Lebugle, *Chem. Mater.*, 1999, **11,** 2722–2727.
158. X. Wang, J. Zhuang, Q. Peng and Y. D. Li, *Adv. Mater.*, 2006, **18,** 2031.
159. M. H. Cao, Y. H. Wang, C. X. Guo, Y. J. Qi and C. W. Hu, *Langmuir*, 2004, **20,** 4784–4786.
160. Y. H. Tseng, Y. Mou, P. H. Chen, T. W. T. Tsai, C. I. Hsieh, C. Y. Mou and J. C. C. Chan, *Magn. Reson. Chem.*, 2008, **46,** 330–334.
161. A. Bielecki, A. C. Kolbert, H. J. M. de Groot, R. G. Griffin and M. H. Levitt, *Adv. Magn. Reson.*, 1990, **14,** 111–124.
162. D. Fukegawa, S. Hayakawa, Y. Yoshida, K. Suzuki, A. Osaka, B. Van Meerbeek and J. Dent, *Res.*, 2006, **85,** 941–944.
163. J. Aizenberg, A. J. Black and G. M. Whitesides, *Nature*, 1999, **398,** 495–498.
164. J. D. Hartgerink, E. Beniash and S. I. Stupp, *Science*, 2001, **294,** 1684–1688.
165. S. R. Whaley, D. S. English, E. L. Hu, P. F. Barbara and A. M. Belcher, *Nature*, 2000, **405,** 665–668.
166. S. Mann, *J. Chem. Soc. Dalton Trans.*, 3953–3961.
167. G. K. Hunter, J. O'Young, B. Grohe, M. Karttunen and H. A. Goldberg, *Langmuir*, . doi: 10.1021/la100401r.
168. J. P. Gorski, *Calcif. Tissue Int.*, 1992, **50,** 391–396.
169. V. L. Fernandez, J. A. Reimer and M. M. Denn, *J. Am. Chem. Soc.*, 1992, **114,** 9634–9642.
170. J. M. Gibson, V. Raghunathan, J. M. Popham, P. S. Stayton and G. P. Drobny, *J. Am. Chem. Soc.*, 2005, **127,** 9350–9351.
171. J. M. Gibson, J. M. Popham, V. Raghunathan, P. S. Stayton and G. P. Drobny, *J. Am. Chem. Soc.*, 2006, **128,** 5364–5370.
172. I. Ben Shir, S. Kababya, T. Amitay-Rosen, Y. S. Balazs and A. Schmidt, *J. Phys. Chem. B*, 2010, **114,** 5989–5996.
173. R. Goobes, G. Goobes, C. T. Campbell and P. S. Stayton, *Biochemistry*, 2006, **45,** 5576–5586.
174. P. H. Chen, Y. H. Tseng, Y. Mou, Y. L. Tsai, S. M. Guo, S. J. Huang, S. S. F. Yu and J. C. C. Chan, *J. Am. Chem. Soc.*, 2008, **130,** 2862–2868.
175. P. A. Raj, M. Johnsson, M. J. Levine and G. H. Nancollas, *J. Biol. Chem.*, 1992, **267,** 5968–5976.
176. D. S. Wishart, C. G. Bigam, J. Yao, F. Abildgaard, H. J. Dyson, E. Oldfield, J. L. Markley and B. D. Sykes, *J. Biomol. NMR*, 1995, **6,** 135–140.
177. A. T. Petkova and R. Tycko, *J. Magn. Reson.*, 2002, **155,** 293–299.
178. R. Goobes, G. Goobes, W. J. Shaw, G. P. Drobny, C. T. Campbell and P. S. Stayton, *Biochemistry*, 2007, **46,** 4725–4733.
179. W. J. Shaw, J. R. Long, A. A. Campbell, P. S. Stayton and G. P. Drobny, *J. Am. Chem. Soc.*, 2000, **122,** 7118–7119.
180. J. J. Gray, *Curr. Opin. Struct. Biol.*, 2004, **14,** 110–115.
181. K. Makrodimitris, D. L. Masica, E. T. Kim and J. J. Gray, *J. Am. Chem. Soc.*, 2007, **129,** 13713–13722.
182. D. L. Masica and J. J. Gray, *Biophys. J.*, 2009, **96,** 3082–3091.
183. D. G. Reid, M. J. Duer, R. C. Murray and E. R. Wise, *Chem. Mater.*, 2008, **20,** 3549–3550.
184. E. R. Wise, S. Maltsev, M. E. Davies, M. J. Duer, C. Jaeger, N. Loveridge, R. C. Murray and D. G. Reid, *Chem. Mater.*, 2007, **19,** 5055–5057.

185. S. M. Best, M. J. Duer, D. G. Reid, E. R. Wise and S. Zou, *Magn. Reson. Chem.*, 2008, **46,** 323–329.
186. J. D. Xu, P. X. Zhu, Z. H. Gan, N. Sahar, M. Tecklenburg, M. D. Morris, D. H. Kohn and A. Ramamoorthy, *J. Am. Chem. Soc.*, 2010, **132,** 11504–11509.
187. A. Wong, D. Laurencin, G. Wu, R. Dupree, M. E. Smith and J. Phys, Chem. *A*, 2008, **112,** 9807–9813.
188. C. M. Zaremba, A. M. Belcher, M. Fritz, Y. L. Li, S. Mann, P. K. Hansma, D. E. Morse, J. S. Speck and G. D. Stucky, *Chem. Mater.*, 1996, **8,** 679–690.
189. S. Weiner and W. Traub, *FEBS Lett.*, 1980, **111,** 311–316.
190. K. Takahashi, H. Yamamoto, A. Onoda, M. Doi, T. Inaba, M. Chiba, A. Kobayashi, T. Taguchi, T. Okamura and N. Ueyama, *Chem. Commun.*, 996–997.
191. C. Jager and H. Colfen, *Crystengcomm*, 2007, **9,** 1237–1244.
192. R. Gertman, I. Ben Shir, S. Kababya and A. Schmidt, *J. Am. Chem. Soc.*, 2008, **130,** 13425–13432.
193. J. Kontrec, D. Kralj, L. Brecevic, G. Falini, S. Fermani, V. Noethig-Laslo and K. Mirosavljevic, *Eur. J. Inorg. Chem.*, 2004, 4579–4585.
194. A. Kaflak, D. Chmielewski, A. Gorecki and W. Kolodziejski, *Solid State Nucl. Magn. Reson.*, 1998, **10,** 191–195.
195. E. E. Wilson, A. Awonusi, M. D. Morris, D. H. Kohn, M. M. J. Tecklenburg and L. W. Beck, *Biophys. J.*, 2006, **90,** 3722–3731.
196. S. Maltsev, M. J. Duer, R. C. Murray and C. Jaeger, *J. Mater. Sci.*, 2007, **42,** 8804–8810.
197. M. Mehring, High Resolution NMR Spectroscopy in Solids. 2nd ed. Springer Verlag, Berlin, 1983.
198. L. T. Kuhn, M. D. Grynpas, C. C. Rey, Y. Wu, J. L. Ackerman and M. J. Glimcher, *Calcif. Tissue Int.*, 2008, **83,** 146–154.
199. P. Z. Zhu, J. D. Xu, N. Sahar, M. D. Morris, D. H. Kohn and A. Ramamoorthy, *J. Am. Chem. Soc.*, 2009, **131,** 17064–17065.
200. H. Saito, R. Tabeta, A. Shoji, T. Ozaki, I. Ando and T. Miyata, *Biopolymers*, 1984, **23,** 2279–2297.
201. H. Saito and M. Yokoi, *J. Biochem.*, 1992, **111,** 376–382.
202. A. Naito, S. Tuzi and H. Saito, *Eur. J. Biochem.*, 1994, **224,** 729–734.
203. G. H. Nancollas, R. Tang, R. J. Phipps, Z. Henneman, S. Gulde, W. Wu, A. Mangood, R. G. G. Russell and F. H. Ebetino, *Bone*, 2006, **38,** 617–627.
204. S. Josse, C. Faucheux, A. Soueidan, G. Grimandi, D. Massiot, B. Alonso, P. Janvier, S. Laib, O. Gauthier, G. Daculsi, J. Guicheux, B. Bujoli and J. M. Bouler, *Adv. Mater.*, 2004, **16,** 1423–1427.
205. S. Josse, C. Faucheux, A. Soueldan, G. Grimandi, D. Massiot, B. Alonso, P. Janvier, S. Laib, P. Pilet, O. Gauthier, G. Daculsi, J. Guicheux, B. Bujoli and J. M. Bouler, *Biomaterials*, 2005, **26,** 2073–2080.
206. H. Roussiere, F. Fayon, B. Alonso, T. Rouillon, V. Schnitzler, E. Verron, J. Guicheux, M. Petit, D. Massiot, P. Janvier, J. M. Bouler and B. Bujoli, *Chem. Mater.*, 2008, **20,** 182–191.
207. S. Mukherjee, Y. C. Song and E. Oldfield, *J. Am. Chem. Soc.*, 2008, **130,** 1264–1273.
208. S. Mukherjee, C. C. Huang, F. Guerra, K. Wang and E. Oldfield, *J. Am. Chem. Soc.*, 2009, **131,** 8374–8375.
209. M. A. Lawson, J. T. Triffitt, F. H. Ebetino, B. L. Barnett, R. J. Phipps, R. M. Locklin and R. G. G. Russell, *J. Bone Miner Res.*, 2005, **20,** S396–S.
210. Y. Zhang and E. Oldfield, *J. Phys. Chem. B*, 2006, **110,** 579–586.
211. A. W. Hing, S. Vega and J. Schaefer, *J. Magn. Reson. Ser. A*, 1993, **103,** 151–162.
212. R. M. Frank and J. Nalbandian, in: A. Oksche and L. Vollrath, (eds.), Teeth. Springer, Berlin, 1989, pp. 75–171.

213. A. E. Porter, R. K. Nalla, A. Minor, J. R. Jinschek, C. Kisielowski, V. Radmilovic, J. H. Kinney, A. P. Tomsia and R. O. Ritchie, *Biomaterials*, 2005, **26,** 7650–7660.
214. C. Rey, K. Beshah, R. Griffin and M. J. Glimcher, *J. Bone Miner Res.*, 1991, **6,** 515–525.
215. W. T. Butler and H. Ritchie, *Int. J. Dev. Biol.*, 1995, **39,** 169–179.
216. M. D. Grynpas, *Bone*, 2007, **41,** 162–164.
217. M. J. Duer, T. Friscic, D. Proudfoot, D. G. Reid, M. Schoppet, C. M. Shanahan, J. N. Skepper and E. R. Wise, *Arterioscler. Thromb. Vasc. Biol.*, 2008, **28,** 2030–2034.
218. K. Jayalakshmi, K. Sonkar, A. Behari, V. K. Kapoor and N. Sinha, *Solid State Nucl. Magn. Reson.*, 2009, **36,** 60–65.
219. G. Wu, *Prog. Nucl. Magn. Reson. Spectrosc.*, 2008, **52,** 118–169.
220. R. G. Griffin and T. F. Prisner, *Phys. Chem. Chem. Phys*., 2010, **12,** 5737–5740.
221. F. Pourpoint, A. Kolassiba, C. Gervais, T. Azais, L. Bonhomme-Coury, C. Bonhomme and F. Mauri, *Chem. Mater*., 2007, **19,** 6367–6369.
222. H. Chappell, M. Duer, N. Groom, C. Pickard and P. Bristowe, *Phys. Chem. Chem. Phys.*, 2008, **10,** 600–606.
223. J. L. Miquel, L. Facchini, A. P. Legrand, C. Rey and J. Lemaitre, *Colloids Surf.*, 1990, **45,** 427–433.
224. C. A. Shand, G. Coutts, S. Hillier, D. G. Lumsdon and A. Chudek, *Environ. Sci. Technol.*, 2005, **39,** 9205–9210.
225. M. C. Connaway-Wagner, W. G. Klemperer and J. F. Young, *A Comparative Study of Magnesia-Orthophosphate and Magnesia-Tripolyphosphate Cement*. The American Ceramic Society, Inc., Waterville, OH, 1991.
226. S. N. Scrimgour, J. A. Chudek and C. H. Lloyd, *Dent. Mater*., 2007, **23,** 415–424.
227. S. Hunger, H. Cho, J. T. Sims and D. L. Sparks, *Environ. Sci. Technol*., 2004, **38,** 674–681.
228. M. A. Aramendia, V. Borau, C. Jimenez, J. M. Marinas, F. J. Romero and J. R. Ruiz, *J. Solid State Chem.*, 1998, **135,** 96–102.
229. A. R. Grimmer and U. Haubenreisser, *Chem. Phys. Lett.*, 1983, **99,** 487–490.
230. T. M. Duncan and D. C. Douglass, *Chem. Phys.*, 1984, **87,** 339–349.
231. M. Feike, R. Graf, I. Schnell, C. Jager and H. W. Spiess, *J. Am. Chem. Soc.*, 1996, **118,** 9631–9634.

CHAPTER 2

Recent Advances in the NMR Spectroscopy of Chlorine, Bromine and Iodine

Bradley J. Butler,* **James M. Hook,**[†,1] and **Jason B. Harper***[,1]

Contents

Abstract

This review is a comprehensive overview of the advances in the nuclear magnetic resonance spectroscopy of chlorine, bromine and iodine nuclei, with the former two being focused upon. A recent review specifically dealing with the solid state nuclear magnetic resonance (SS NMR) of these halogens was published in 2006 [D. Bryce and G. Sward, *Magn. Reson. Chem.*, 2006, **44,** 409–450.], with an update in 2009 [C. M. Widdifield, R. P. Chapman and D. L. Bryce, *Annu. Rep. NMR Spectrosc.*, 2009, **66,** 195–326.]. This review will cover

* School of Chemistry, University of New South Wales, Sydney, New South Wales, Australia
† Mark Wainwright Analytical Centre, University of New South Wales, Sydney, New South Wales, Australia
[1] Corresponding author.

Annual Reports on NMR Spectroscopy, Volume 73
ISSN 0066-4103, DOI: 10.1016/B978-0-08-097074-5.00002-5

work in this area subsequent to the material already presented, including all work up until and including September 2010. In addition, the use of chlorine, bromine and iodine NMR spectroscopy in the solution state over the past 10 years is covered with emphases on its development and application. Recent advancements in instrumental and analytical techniques are analysed in order to view their impact on the use of these particular halogens in NMR spectroscopy.

Key Words: NMR, SS NMR, Halogen NMR, Chlorine-35, Chlorine-37, Bromine-79, Bromine-81, Iodine-127.

ABBREVIATIONS

CPMG	Carr–Purcell–Meiboom–Gill
C_Q	nuclear quadrupolar coupling constant
D^P	receptivity relative to ^1H
EFG	electric field gradient
I	nuclear spin quantum number
MAS	magic-angle spinning
MAS NMR	magic-angle spinning nuclear magnetic resonance
mb	10^{-31} m^2
NMR	nuclear magnetic resonance
NQR	nuclear quadrupolar resonance
Q	quadrupolar moment
QCPMG	quadrupolar Carr–Purcell–Meiboom–Gill
QI	quadrupolar interaction
SS NMR	solid state nuclear magnetic resonance
T	relaxation time
T_1	spin–lattice relaxation time
T_2	spin–spin relaxation time
γ	magnetogyric ratio
δ	chemical shift
δ_{iso}	chemical shift tensor value
η_Q	quadrupolar asymmetry parameter
Ξ	frequency ratio

1. INTRODUCTION

Chlorine, bromine and iodine are elements that are widely distributed naturally and form part of a range of processes, everything from biological through industrial. Each has at least one isotope that is nuclear magnetic resonance (NMR) active, and hence there is the opportunity to

TABLE 1 Selected NMR properties of the NMR active quadrupolar halogen nuclei

^{A}X	Natural abundance (%)	I	γ (10^7 rad T^{-1} s^{-1})	Ξ (%)	D^P	Q (mb)[a]
^{35}Cl	75.8	3/2	2.62	9.98	3.58×10^{-3}	−81.7
^{37}Cl	24.2	3/2	2.18	8.16	6.59×10^{-4}	−64.4
^{79}Br	50.7	3/2	6.73	25.1	4.03×10^{-2}	313
^{81}Br	49.3	3/2	7.25	27.0	4.91×10^{-2}	262
^{127}I	100	5/2	5.39	20.0	9.54×10^{-2}	−696

Data adapted from Harris et al.[1] and adjusted to three significant figures.
[a] Updated values from Pyykko et al.[2]

use NMR spectroscopy of the heavier halogens to obtain information about a given system. However, the ability to utilise the quadrupolar halogens in NMR spectroscopy greatly depends on the magnetic and electrical properties of the halogen nuclei, which are summarised in Table 1.

Both major isotopes of chlorine are NMR active with ^{35}Cl having a higher natural abundance than ^{37}Cl by a factor of around 3:1 which, along with the higher magnetogyric ratio, results in a higher sensitivity relative to ^{1}H NMR spectroscopy. For this reason, ^{35}Cl is more commonly used.

Much like chlorine, both of the major isotopes of bromine, ^{79}Br and ^{81}Br, may be used for NMR experiments. The sensitivity for the ^{81}Br nucleus is slightly better, and a smaller quadrupole moment leads to reduced linewidth; however, ^{79}Br is more commonly used. This is most likely due to the fact that the frequency of ^{79}Br is very close to that of ^{13}C so minimal adjustments to existing equipment need to be performed.[3] Due to the much higher quadrupolar moment relative to chlorine, the linewidths of resulting signals tend to be much broader. As a result, the use of bromine NMR spectroscopy is not currently as widespread as chlorine NMR spectroscopy.

Although ^{127}I is an NMR active nucleus with 100% abundance and comparative sensitivity to chlorine and bromine, its large quadrupolar moment make for very broad signals and low intensity spectra; it is therefore rarely used.[1]

Of the obstructions preventing the everyday use of NMR spectroscopy of chlorine, bromine and iodine, line broadening (as mentioned briefly above) is arguably the most significant. This broadening is due to the fact that when a nucleus with $I > 1$ is subject to a non-zero electric field, the electric field gradient (EFG) may couple with the quadrupole moment.[4] This interaction between the EFG and Q is known as the quadrupole interaction. If the quadrupolar interaction (QI) is too great, the resulting

signals will be very broad; this is particularly a problem when the nucleus is in an asymmetric electronic environment[5] and for nuclei with large Q such as the heavier halogens.[1]

However, such drawbacks may be exploited in some cases. For example, the sensitivity of the signal broadening to the environment means that the environment may be determined, and followed if changing, using halogen NMR spectroscopy. This has potential application in following the kinetics of ion exchange and obtaining structural data. In the extreme case, the fact that only nuclei in certain environments give rise to observable signals results in very simple spectra appropriate for a range of applications; several examples of such will be discussed further later in the text.

Outlined in this review are the developments in the field of NMR spectroscopy as applied to chlorine, bromine and iodine; these developments are both technical (in terms of improving the information gained) and practical (in terms of applying the information gained, often to new systems). It is hoped that the reader gains an appreciation not only for how NMR spectroscopy of the quadrupolar halogens can be used, but also the potential areas for development and exploitation in the future.

2. SOLID STATE NMR SPECTROSCOPY

It is useful to emphasise from the outset that alternative techniques for investigating solid samples, other than NMR spectroscopy of the quadrupolar halogen nuclei, tend to be considered first; this is likely due to the (perceived) difficulty of the technique and may be related to the issues of sensitivity and line broadening mentioned above. However, the information gained is often complementary, and hence solid state nuclear magnetic resonance (SS NMR) spectroscopy is primarily used when it can provide unique insight unavailable with other techniques.

Whilst diffraction techniques immediately spring to mind for solid samples, the quadrupolar nature of the heavier halogen nuclei means that a principle technique related to SS NMR spectroscopy is nuclear quadrupole resonance spectroscopy.[6] For systems with a quadrupole moment, an EFG generates two energy states in the absence of an applied magnetic field.[a,7] It is appropriate to start by considering illustrative cases in which SS NMR spectroscopy provides information that the closely related nuclear quadrupolar resonance (NQR) technique does not.

First and foremost, NMR spectroscopy is transferable from the solid state to solution phase; this is not the case for NQR spectroscopy as it is

[a] The fact that an applied magnetic field is not required distinguishes this from NMR spectroscopy.

limited to solids.[4] Hence, NMR spectroscopy has advantages over NQR spectroscopy in that the same technique can be used to obtain data in both solution and solid phases. This is particularly relevant if both phases are present and even more so if a transition between the two occurs; this will be discussed with respect to halogen NMR spectroscopy later in this review.[8]

Another advantage of NMR spectroscopy over NQR spectroscopy is that detailed structural information may be obtained with a smaller sample size. This is exemplified by recent work in which Widdifield et al.[9] showed that $^{79/81}$Br NMR measurements of non-cubic inorganic solids were able to provide detailed data regarding local structure of the crystals. The information gathered is similar to that available using NQR spectroscopy; however, NMR spectroscopy allowed it to be obtained without the need for either gram quantities of sample or large single crystals.

Recently, SS NMR spectroscopy of the heavier halogens has been used to gather data on QIs, EFGs, chemical shifts and relaxation times; each of which have, in turn, been translated to information related to nature of the sample.

2.1. The use of QIs and symmetry

QIs are often used to determine both intramolecular and intermolecular interactions. One example of the use of NMR spectroscopy of chlorine and bromine nuclei has been exploited to determine the difference in the interactions between components of room temperature ionic liquids[b] in the solid state and in other organic ionic solids.[8,11]

Gordon et al.[11] used both experimental and simulated ^{35}Cl SS NMR spectroscopic data to calculate coupling constants (C_Q), quadrupolar asymmetry parameters (η_Q) and chemical shift tensor values (δ_{iso}) for ionic liquids based on either an imidazolium or a pyridinium cation. The values for C_Q found for the solid forms of the ionic liquids studied were shown to fall between 0.8 and 1.5 MHz. These values lie well within the range for typical organic and inorganic solid salts of 0–9.0 MHz.[12–14] Further, the δ_{iso} values determined were in a relatively narrow range of 61–92 ppm, compared to various solid organic halides that have δ_{iso} values ranging from 10 to 120 ppm.[12,15] These indicate that, despite their low melting points, the ionic liquids considered have structures in the solid state that do not differ markedly from 'typical' salts.

[b] Room temperature ionic liquids are defined as salts that melt below 100 °C.[10] Since these systems often contain halogens, halogen NMR spectroscopy has been used extensively in recent years in ionic liquids.

In the case above,[11] because the chlorine atoms are neither chemically bound to any other atoms nor in close proximity to other anions, the NMR parameters are dependent on the spatial distribution of the cations. This can be extended to other related systems, such as in *n*-alkyltrimethylammonium bromide crystals; Alonso et al.[16] used ^{81}Br parameters to study the effects of altering the alkyl chain length in such systems and to correlate any changes to the structure of the crystals. To increase the accuracy of the data obtained, magic-angle spinning NMR (MAS NMR) was performed. MAS NMR was used to generate values for C_Q and η_Q at four different frequencies; no effect of the MAS frequency (0–30 kHz) was observed, and the averaged values are shown below in Table 2.

In these systems, the primary influence on the ^{81}Br NMR parameters is the spatial distributions of the tetraalkylammonium cations around the bromide anions. Both C_Q and η_Q increase with alkyl chain length as shown below in Figure 1. The increase in C_Q is consistent with a decrease in the distance between the polar N head group and the Br^- ion, whilst the change in η_Q could be accounted for by a decrease in symmetry. Each of these was compared with crystal structure data and found to be the case. The sensitivity of the ^{81}Br NMR parameters to the change in alkyl length in the crystal led to the conclusion that ^{81}Br has potential as a probe for monitoring the geometries of local sites of polar head groups and their corresponding counteranions.

As noted previously, the NMR active quadrupolar halogen nuclei have generally been studied in systems with little to no asymmetry in order to avoid QI affecting the spectra. Whilst this is less of a factor for chlorine due to its lower Q, it is significant for bromine. Widdifield et al.[9] recently investigated a series of group II bromides and there corresponding hydrates using $^{79/81}$Br SS NMR. The group II bromides were chosen as they are able to provide up to four unique magnetic sites with a range of bromine QI in order to demonstrate the ability to obtain spectra on asymmetric systems. The metal halides were used to show

TABLE 2 ^{81}Br NMR parameters of *n*-alkyltrimethylammonium bromide salts averaged over a range of MAS frequencies[16]

	C_Q (MHz)	η_Q
$CH_3(CH_3)_3N^+Br^-$	6.030 ± 0.002	0.02 ± 0.01
$C_{12}H_{25}(CH_3)_3N^+Br^-$	7.39 ± 0.10	0.11 ± 0.02
$C_{14}H_{29}(CH_3)_3N^+Br^-$	7.74 ± 0.17	0.16 ± 0.03
$C_{16}H_{33}(CH_3)_3N^+Br^-$	8.03 ± 0.03	0.18 ± 0.02
$C_{18}H_{37}(CH_3)_3N^+Br^-$	8.08 ± 0.07	0.19 ± 0.01

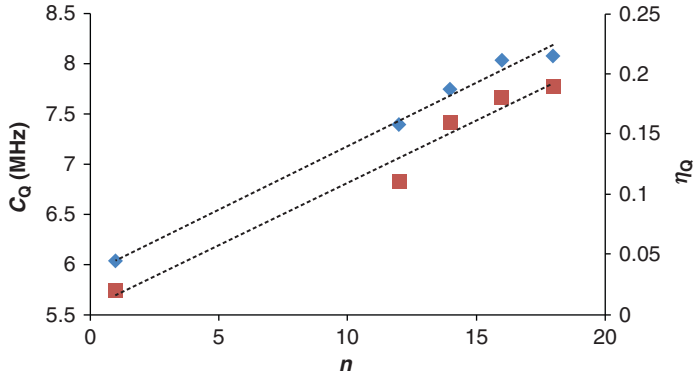

Figure 1 Variation of C_Q and η_Q as a function of alkyl chain length (n) in n-alkyltrimethylammonium bromides ($C_nH_{2n+1}(CH_3)_3N^+Br^-$).[16]

TABLE 3 Experimental $^{79/81}$Br NMR parameters for some group II bromides

	Br site label	C_Q (^{81}Br) (MHz)	C_Q (^{79}Br) (MHz)	η_Q	δ_{iso} (ppm)
$SrBr_2$	1	10.3	12.3	0.07	422
	2	18.1	21.7	0.03	410
	3	25.6	30.6	0.695	320
	4	53.7	64.2	0.33	300
$BaBr_2$	1	23.5	28.1	0.17	280
	2	27.2	32.5	0.070	480
$SrBr_2 \cdot 6H_2O$	–	27.7	33.2	<0.01	95
$BaBr_2 \cdot 2H_2O$	–	7.32	8.74	0.76	218

Adapted from Widdlefield et al.[9]

any relationship between $^{79/81}$Br SS NMR parameters and pseudopolymorphism. All relevant data referred to are presented in Table 3.

Strontium bromide was used to demonstrate the difference between symmetric and asymmetric bromine sites in a crystal. As Table 3 shows, two bromine sites have near 0 η_Q (labelled as sites 1 and 2) and two have significant η_Q (labelled as sites 3 and 4; represented in Figure 2). When a large frequency range scan was performed, four distinct signals were observed with the symmetric sites (1, 2) having similar δ_{iso} of 422 and 410 ppm and the two asymmetric sites (3, 4) being at lower values of δ_{iso}. Hence, strontium bromide was used to demonstrate the ability of Br SS NMR to resolve both symmetric and asymmetric sites.

The C_Q for the bromine signals in the bromide salts of barium and strontium and their corresponding hydrates were used to show the effect

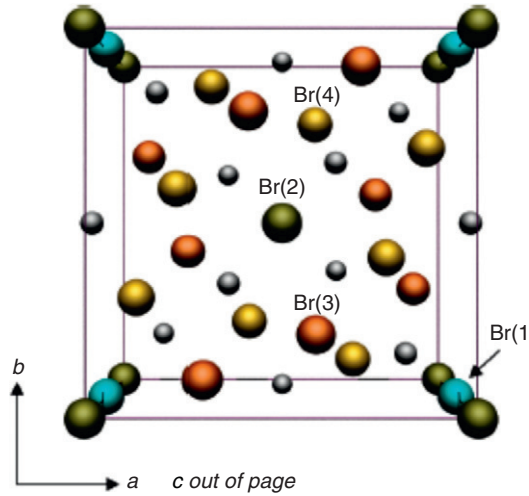

Figure 2 The unit cell of strontium bromide. From Widdlefield et al.[9]

of hydration on the NMR parameters. As Table 3 shows, there is a marked difference in the C_Q and in the number of signals observed. This demonstrates that bromine SS NMR spectroscopy may provide an effective technique for detecting the presence of hydrates and analysing the effect of water on structure in such samples.

2.2. Relaxation times, chemical shifts and linewidths

Other parameters derived using NMR spectroscopy that can provide information are the chemical shift (δ) of the signal and the spin relaxation times ($T_{1,2}$) of the nuclei. One feature of both δ[17] and $T_{1,2}$[18] is their temperature dependence; this has been considered for the ^{79}Br signals by Thurber et al.[19] for potassium bromide. Both T_1 and δ vary greatly with temperature change with T_1 becoming less dependent at high temperatures (>320 K) and δ having a linear relationship with temperature ($40\ \text{K} < \delta < 320\ \text{K}$) (Figure 3).

Whilst both are potentially useful, the sensitivity of relaxation time measurements at low temperatures is a distinct advantage. Although this sensitivity is decreased at temperatures above room temperature, the spin-lattice relaxation time is very fast which allows for rapid data acquisition and hence a high signal-to-noise ratio. The temperature dependence of the relaxation time measurements was shown to be independent of magnetic interactions above 20 K. This increases the utility of the system since, as a result, small magnetic impurities in the potassium bromide would not affect the values obtained. Combine this

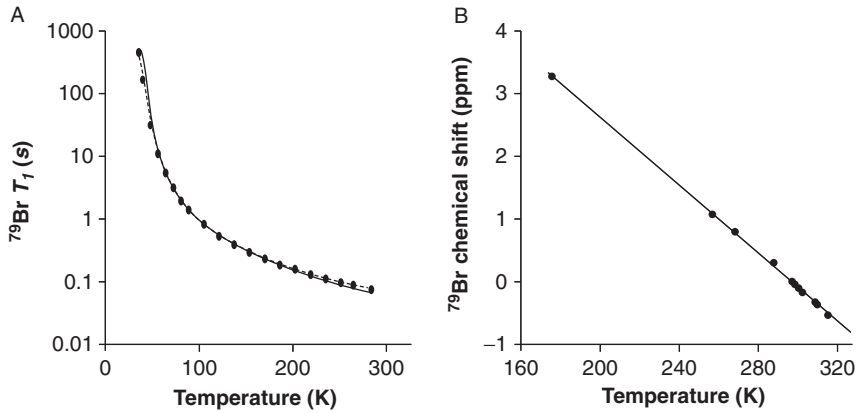

Figure 3 (A) Temperature dependence of ^{79}Br spin-lattice relaxation time T_1 and (B) temperature dependence of ^{79}Br chemical shift in samples of potassium bromide (from Thurber et al.[19]).

with the low toxicity of potassium bromide,[20] the similarity of the ^{79}Br and ^{13}C NMR frequencies as discussed above and the short relaxation times of ^{79}Br NMR signals (and hence short acquisition times), and the result is a highly practical *in situ* thermometer with all the advantages such have over *ex situ* equivalents.[19]

The examination of linewidths and relaxation times can be extended to iodine NMR spectroscopy where both can be used to show a change in crystallographic structure; this was demonstrated recently by Pecher et al.[21] This work is significant as it utilised the large quadrupolar moment of iodine in order to show a change in the crystallographic position of the iodine atoms in $Li_{7-x}PS_{6-x}I_x$. As noted above, in symmetric environments, values of QI approach zero and high-resolution spectra are easier to obtain relative to asymmetric environments. The temperature dependence of the NMR parameters of the iodine nucleus was analysed and both the linewidth and the relaxation time reduce dramatically at 180 K, indicating a change from an asymmetric to a symmetric environment.

Before concluding the discussion of SS NMR spectroscopy of the quadrupolar halogens, it is worth noting two points. Firstly, since the previous reviews[22,23] there has been only one[8] report using iodine NMR spectroscopy to study solids; this is perhaps not surprising given the large quadrupole moment of iodine. Secondly, as access to computing power becomes more readily available, simulation of spectral data is becoming the norm and is useful in both comparative and predictive senses. In many of the examples above, previous NQR data was used in order to generate reference NMR spectra in order to aid analysis.[9,24,25]

3. SOLUTION PHASE NMR SPECTROSCOPY

A drawcard of NMR spectroscopy is that it can be used to obtain information on systems in both solid and solution phase. Arguably, this is an area in which NMR spectroscopy of chlorine, bromine and iodine has been underutilised because of the limitations associated with the quadrupolar nature of the nuclei. However, recently, it has shown wide potential application particularly as a tool for quantifying halide content in samples and for following reaction progress.

3.1. Quantifying halide content

To demonstrate the accuracy and precision of NMR spectroscopy for quantifying solution concentrations, consider the work by Lim et al. using ^{35}Cl NMR spectroscopy as a quantitative procedure for solutions containing chloride ions.[26] Figure 4 shows the increase in signal intensity with increasing chloride concentration. The detection limit found in these experiments using 0.01–0.05 M reference and 512 scans was 20 ppm. Although this value is higher than other analytical techniques such as ion chromatography (0.01 ppm),[27] it was postulated that if lower detection limits were required the limit could easily be reduced through a combination of a lower concentration of reference material and a higher number of scans.

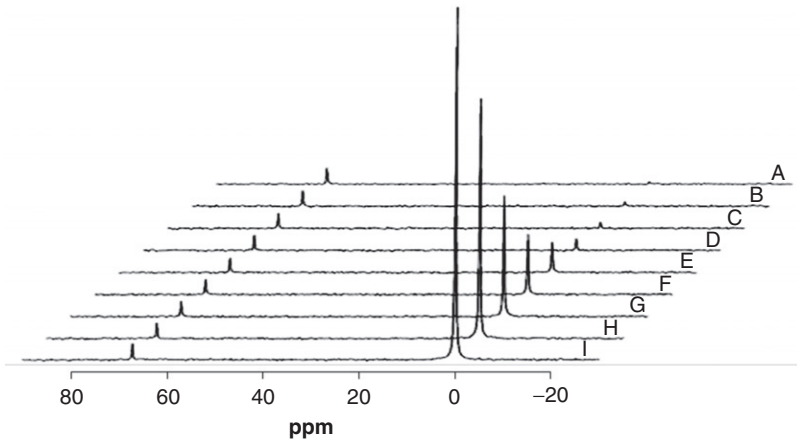

Figure 4 A series of stacked plots demonstrating the increase in signal ($\delta = \sim 0$) due to chloride (from sodium chloride) in DMSO-d_6 with increasing chloride concentration (20–3000 ppm). The signal at δ ca. 70 is chlorine from tetraethylammonium chloride. Reproduced from Lim et al.[26]

3.2. Following reaction progress

An important feature of solution phase measurements is the ability to record data while the reaction is progressing. *In situ* NMR spectroscopy has been a mainstay for popular forms such as ^{1}H NMR spectroscopy for many years, but in recent years, it has been demonstrated that it is also possible for the quadrupolar halogens.[28–31]

As shown above, NMR spectroscopy can be a useful technique for quantitative analysis, even with the quadrupolar halogens. A further application of NMR spectroscopy for the quadrupolar halogens may be the ability to quantitatively follow a reaction as it is progressing. This is possible due to the asymmetrical environment about a quadrupolar halogen nucleus in organohalides. In an asymmetric environment, no signal is observed for the halogen nuclei.[5] As such, processes that involve reaction of an organohalide to generate a halide anion may be followed by observing the appearance of a signal in the halogen NMR spectrum due to the symmetric anion produced (this is solution dependent as discussed later in the text). Since solvents do not typically contain the halide ion of interest, or any other nuclei likely to give rise to a signal, the resulting spectra are simple and easy to interpret.

This has been demonstrated for ^{35}Cl NMR spectroscopy following the methanolysis of an organochloride as outlined in Scheme 1 and Figure 5.[28] Importantly, only this method could be used to follow the reaction progress as other spectroscopic methods (such as ^{1}H NMR spectroscopy) proved ineffective, and methods involving isolation of the organic products were hampered by the ionic liquid present in the reaction mixture. The general applicability of the method over a range of temperatures was subsequently demonstrated in experiments designed to determine activation parameters.[29]

The ability to follow a reaction *in situ* is not restricted to the formation of chloride ions and has recently been demonstrated for ^{79}Br by Chan et al.[30] The linewidth of the signals in such spectra is significantly larger than the chlorine example, due to higher QI. However, as only a single signal was present, as expected, this was not a significant issue in and of

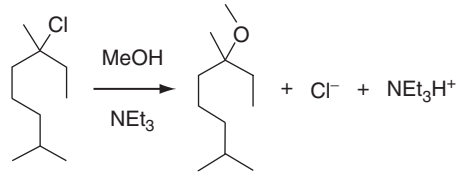

Scheme 1 Solvolysis of 3-chloro-3,7-dimethyloctane studied in mixtures of methanol and 1-butyl-3-methylimidazolium *bis*(trifluoromethanesulfonyl)imide as was studied using ^{35}C^{1} NMR spectroscopy. Adapted from Man et al.[28]

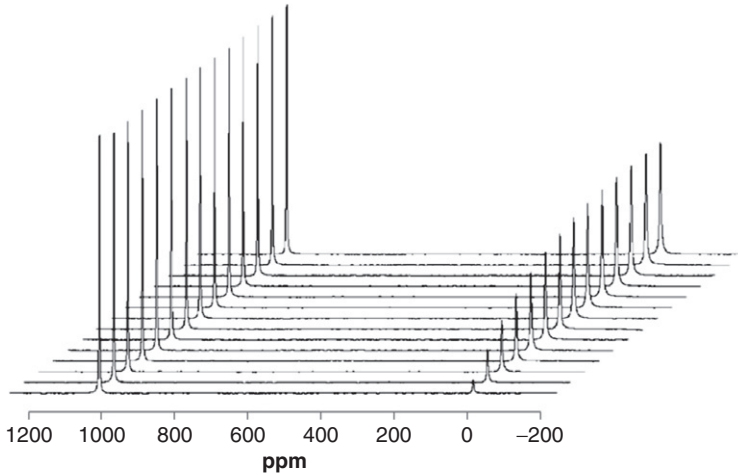

Figure 5 Stacked plots of ^{35}Cl NMR spectra of the solvolysis outlined in Scheme 1. The signal at ca. δ 0 corresponds to chloride and the signal at ca. δ 1000 to sodium perchlorate, an external standard. Adapted from Man et al.[28]

itself, though the effect of the solvent is an important consideration. The change in the linewidth of the ^{79}Br NMR signal as the solvent was varied was used to demonstrate how the solvent may either hinder or improve the probability of high-resolution spectra. Although there were differences in viscosity between the solvents used, this was ruled out as a source of the major line broadening. Rather, it was shown that some solvents dielectric properties affect the electrical symmetry of the bromide ions with solvents such as acetonitrile preserving symmetry and methanol disrupting symmetry[32]; this effect on symmetry greatly effects the linewidths.

The reaction shown in Scheme 2 can be used to show the ability of ^{79}Br NMR spectroscopy to follow the formation of a bromide ion and to compare this to using ^{1}H NMR spectroscopy. As Figure 6 demonstrates, due to the simplicity of the spectra in the bromine case, the ^{79}Br integration data is much more precise than the corresponding ^{1}H data; in the complex ^{1}H NMR spectrum, signal overlap becomes significant due to the complexity of the reaction mixture. Hence, although ^{1}H NMR spectroscopy is more widely used, this shows that ^{79}Br NMR spectroscopy is as good, if not better, for following reactions in solution under appropriate conditions.

It is worth noting that, like SS NMR spectroscopy and likely for the same reasons, little work has been performed on iodine systems in solution. However, preliminary work in our own group has demonstrated that it is possible to use ^{127}I NMR spectroscopy for kinetic measurements.[31]

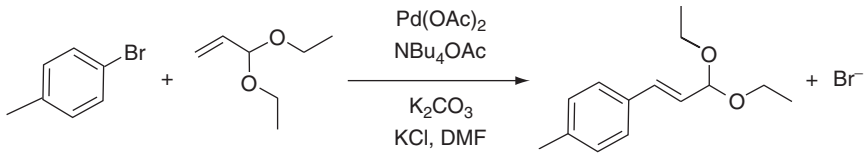

Scheme 2 The Heck reaction of 4-bromotoluene with acrolein diethyl acetal as followed using ^{79}Br NMR spectroscopy. Adapted from Chan et al.[30]

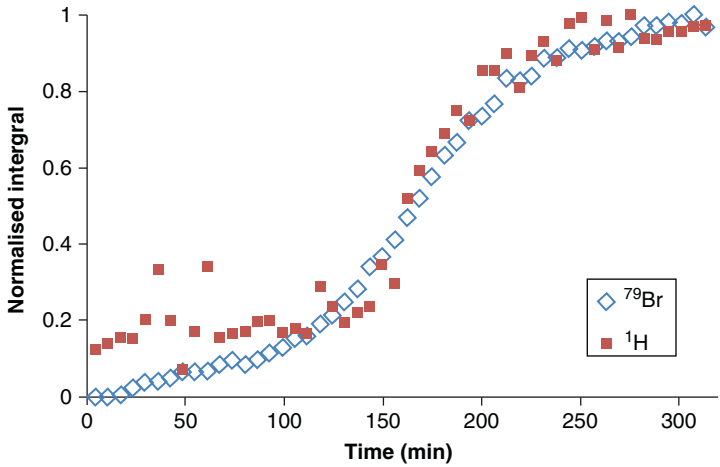

Figure 6 Comparison of ^{1}H NMR and ^{79}Br NMR spectroscopies for following the reaction outlined in Scheme 2. The integrations are for the signal corresponding to δ_H 5.25 for the ^{1}H NMR signal and the ^{79}Br signal at δ_{Br} 97. Adapted from Chan et al.[30]

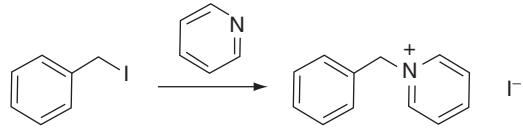

Scheme 3 Menschutkin reaction of pyridine with benzyl iodide in acetonitrile followed using ^{127}I NMR spectroscopy.[31]

The reaction that was chosen is outlined in Scheme 3; this is one that we have used to demonstrate the utility of ^{79}Br NMR spectroscopy for the corresponding bromides; and a series of representative spectra are shown in Figure 7. The large linewidth inherent to iodine NMR spectra was not a limiting factor in this case as it does not hinder the measuring of the rate of appearance of the iodide ion.

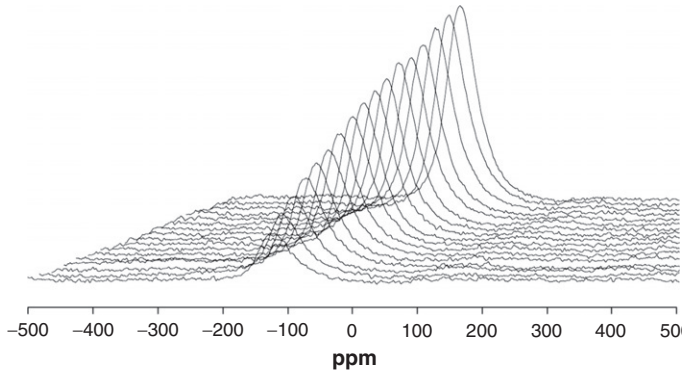

Figure 7 Stacked ^{127}I NMR spectra for the reaction shown in Scheme 3 as it progresses.[31]

3.3. Chemical shift

In addition to the integration of the signals in chlorine, bromine and iodine NMR spectroscopy, the chemical shift can be used to determine the chemical environment of a nucleus in solution. Particularly, this is useful in qualitatively assessing intramolecular forces such as hydrogen bonding.

Remsing et al.[33] used the change in $^{35/37}$Cl chemical shift to demonstrate hydrogen bonding in neat 1-butyl-3-methylimidazolium chloride, an ionic liquid. Deuteration of the cation resulted in a change in the chemical shift of the signal corresponding to the chloride counterion; this change resulted after deuteration of both the C-2 and C-4/5 positions (Figure 8). This was used as evidence for the presence of hydrogen bonding in the ionic liquid and demonstrates it occurs with each of the protons on the imidazolium cation.

3.4. Relaxation times and linewidth

Relaxation times of quadrupolar halogen nuclei may also be used to obtain sample information. One application of relaxation time measurements in the solution states is the ability to probe the level of ordering present in a solution, and it is of particular interest when compared directly to the solid state, an advantage of NMR spectroscopy highlighted earlier.

As mentioned above, Gordon et al. investigated the structure of the solid forms of imidazolium chloride ionic liquids.[11] The same group has used relaxation time measurements in ^{35}Cl and ^{79}Br NMR spectroscopy in an attempt to see if any solution state ordering is present in various room temperature ionic liquids.[8] The ratio of the spin-lattice to the spin–spin relaxation times was found to be close to unity, suggesting little to no ordering in these systems.

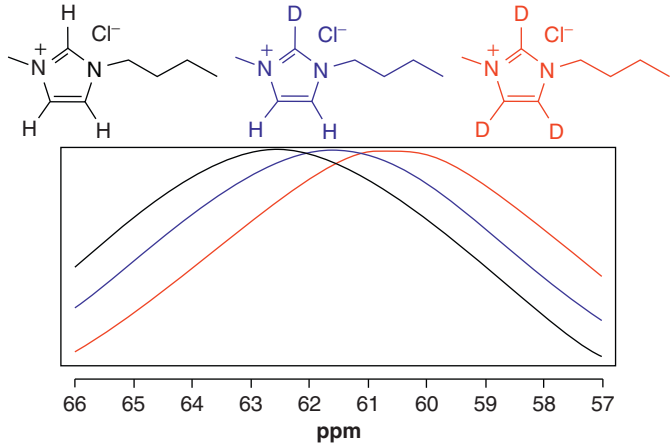

Figure 8 The change in ^{35}Cl NMR chemical shift with increasing levels of deuteration of the imidazolium cations in the appropriate imidazolium chloride. Adapted from Remsing et al.[33]

Relaxation times of $^{35/37}$Cl were also considered by Remsing et al. to investigate the dissolution of cellulose in a 1-butyl-3-methylimidazolium chloride solution.[34] The values of such were observed to vary greatly with cellobiose concentration (Figure 9), indicating a strong interaction between the anion and cellulose. This supported the proposal that such interactions play an important role in the dissolution of carbohydrates in ionic liquids, through interaction of chloride ions with the hydroxyl groups on the carbohydrate (effectively breaking the hydrogen bonding between cation and anion).[35] Further analysis of the line width of the signals indicated a 1:1 stoichiometry of chloride and hydroxyl groups in the interaction.

Another use of relaxation times is to characterise interaction of ions in solution with solids, such as occurs in a suspension. Yu et al.[36] used relaxation times from ^{35}Cl NMR spectroscopy to investigate how chloride ions in a cement suspension interact with the cement particles. Given that, for all forms of cement considered, only a single ^{35}Cl signal was observed (corresponding to chloride ions in solution) and there was no observed signal for surface adsorbed chloride; it was concluded that all the chloride ions are in a solution environment and in rapid exchange. The relaxation times for three cement samples were then used to analyse the chloride surface binding affinity in each case and demonstrated variation between the sample types used.

Another use of relaxation times is to provide insight into mobility and diffusion as shown by Nagata et al. where ^{35}Cl NMR was used to analyse the effect of temperature on sodium chloride mobility in crab meat.[37]

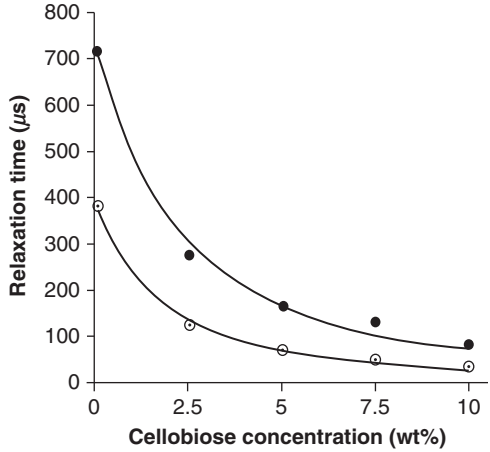

Figure 9 $^{35/37}$Cl relaxation times with changing cellobiose concentration in 1-butyl-3-methylimidazolium chloride. ●, T_1; ○, T_2. Adapted from Remsing et al.[34]

To measure the T_1 times for ^{35}Cl, an inversion relaxation pulse sequence was used where the spins are flipped to 180° and T measured repeatedly until equilibrium allowing, T_1 to be calculated and the mobility of the chloride anions inferred. Importantly, these studies indicated distinct chloride states with differing mobilities. The effect of various heat treatments on the crab meat to the mobility of the chloride ions was investigated. It was shown that with high heat treatment, the T_1 times greatly decreased indicating decreased mobility of the chloride ions. This change in mobility was then discussed in relation to the effect of the heat treatment on the diffusion of sodium chloride in the crab meat, with the heat-treated meats having more chloride ions in the free state rather than in a bound state, increasing the saltiness of the meat.

Relaxation times of ^{81}Br NMR signals were used recently by Balevicius et al. in order to analyse solvent effects on the local environment for an ionic liquid.[38] As noted previously,[33] hydrogen bonding to halide ions in imidazolium chloride ionic liquids can have significant effects on the chemical shift in halogen NMR spectra. This is further built upon using solutions of imidazolium bromide ionic liquids with a range of both hydrogen bonding and non-hydrogen bonding solvents, as well as the corresponding neat ionic liquids. In these studies, both systems containing the hydrogen bonding solvents and the neat solution demonstrated much broader linewidths and longer relaxation times relative to the non-hydrogen bonding solutions. For the solution cases, this is discussed as being due to the hydrogen bonding decreasing the mobility of the

bromide ions, thus increasing relaxation times and broadening the signals. For the neat ionic liquid, it was postulated, based on the highly complex, temperature-dependent ^{81}Br NMR spectra, that supramolecular structures were being formed, reducing mobility. Note that no discussion of the effect of symmetry at the bromine nucleus, and the potential effects on linewidth, is included.

4. FURTHER ADVANCES IN HALOGEN NMR SPECTROSCOPY

Having discussed the recent work in the areas of chlorine, bromine and iodine NMR spectroscopy, it is also worthwhile to consider the advancements being made in NMR spectroscopy in general and how they might be specifically applied to overcome the inherent limitations present in examining NMR spectra of the quadrupolar nuclei.

Increasing the magnetic field strength will provide higher resolution NMR spectra for quadrupolar nuclei.[39] Hence, perhaps the most important advancement is the development of ultra-high magnetic fields for SS NMR equipment using hybrid magnets (HM).[40–42] With field strengths of up to 30 T,[41] there is the potential for high-resolution spectra of the quadrupolar halogens; this has already been demonstrated for solid potassium bromide.[42]

As QIs present in the halogen nuclei often cause the resulting spectra to be very broad, much of the data may be lost due to instrumental noise. Although chlorine has the smallest QI relative to the other quadrupolar halogens, the ^{35}Cl NMR signals have been estimated from NQR data to be up to 1–3 MHz in breadth in systems such as cyclopentadienyltitanium (III) chloride.[43,44] By modifying the pulse programme, as with the quadrupolar Carr–Purcell–Meiboom–Gill (QCPMG) protocol, higher signal-to-noise ratios can be obtained.[45] This has been shown to be an effective technique to increase the sensitivity of NMR spectroscopy of the quadrupolar halogens in SS NMR.[24,25,46] Hung et al. recently analysed the practicality of QCPMG NMR for quadrupolar nuclei, including ^{35}Cl, and summarised that it is a highly useful technique for analysing wideline spectra, providing a list of guidelines for its application.[46] This technique may be highly useful for both covalently bound systems and iodine NMR spectroscopy in general as these systems tend to yield broad spectra. The former is demonstrated by the recent work of Rossini et al.[25] in which the QCPMG sequence was used and the first practical ^{35}Cl NMR data for covalently bonded chlorine atoms obtained; in this case, the chlorine NMR spectra were of organometallic species of group IV transition metals. There is significant potential for this technique to be applied to multiple systems, particularly, organohalides.

5. CONCLUDING COMMENTS

The use of the NMR active quadrupolar halogens as a valuable and viable source of NMR data makes it an increasingly important technique. As we have shown in this review, the range of systems that can potentially be analysed and the information gained using halogen NMR techniques is very broad, ranging from solid state crystallographic data to following solution phase reactions *in situ*. This increased usage may be attributed to the developing understanding of the properties of these nuclei and the refinement of NMR instrumentation and techniques. The exploitation of what was once a hindrance in the inability to qualitatively obtain spectra, that being signal broadening for nuclei in asymmetric electrical environments, is now being exploited to analyse the local environment of the halogen in both the solid and solution states. In solution state, it has been shown that NMR spectra of the quadrupolar halogens can be used to follow reaction progress in cases that might otherwise not be readily monitored, and it is likely that this will become more widely applied now the technique has been demonstrated.

Previous limitations to the use of chlorine, bromine and iodine NMR spectroscopy are gradually being overcome. The recent advancements in NMR instrumentation, such as the increase in field strengths available, are allowing analysis of halogen nuclei with QIs that were previously too large to analyse using lower field strengths; this greatly increases the range of samples that can be analysed. The application of advanced analytical techniques such as QCPMG further allows analysis of spectra previously considered to have a signal-to-noise ratio too low to provide reliable data. It is the opinion of the authors that the combination of these factors will be a driving force in the increased use of chlorine, bromine and iodine NMR spectroscopy both in areas where it has previously not been applied along with those described above.

REFERENCES

1. R. K. Harris, E. D. Becker, S. M. C. de Menezes, R. Goodfellow and P. Granger, *Pure Appl. Chem.*, 2001, **73,** 1795–1818.
2. P. Pyykko, *Mol. Phys.*, 2008, **106,** 1965–1974.
3. B. Lindman and S. Forsén, Chlorine, Bromine, and Iodine NMR: Physico-Chemical and Biological Applications. Springer-Verlag, Berlin, 1976.
4. R. V. Pound, *Phys. Rev.*, 1950, **79,** 685–702.
5. I. P. Gerothanassis and C. G. Tsanaktsidis, *Concepts Magn. Reson. A*, 1996, **8,** 63–74.
6. G. P. Wulfsberg, Nuclear Quadrupole Resonance (NQR) Spectroscopy. *in*: Encyclopedia of Inorganic Chemistry, 2nd edn, (R. B. King ed.), John Wiley & Sons, Ltd., Chichester, UK, 2008.
7. J. A. S. Smith, *J. Chem. Educ.*, 1971, **48,** 39–48.
8. P. G. Gordon, D. H. Brouwer and J. A. Ripmeester, *Chemphyschem*, 2010, **11,** 260–268.

9. C. Widdifield and D. Bryce, *J. Phys. Chem. A*, 2010, **114,** 2102–2116.
10. S. Z. E. Abedin and F. Endres, *Acc. Chem. Res.*, 2007, **40,** 1106–1113.
11. P. G. Gordon, D. H. Brouwer and J. A. Ripmeester, *J. Phys. Chem. A*, 2008, **112,** 12527–12529.
12. R. Chapman and D. Bryce, *Phys. Chem. Chem. Phys.*, 2007, **9,** 6219–6230.
13. S. Hayashi and K. Hayamizu, *Bull. Chem. Soc. Jpn.*, 1990, **63,** 913–919.
14. T. Weeding and W. Veeman, *J. Chem. Soc. Chem. Commun.*, 1989, 946–948.
15. T. Sandland, L. Du, J. Stebbins and J. Webster, *Geochim. Cosmochim. Acta*, 2004, **68,** 5059–5069.
16. B. Alonso, D. Massiot, P. Florian, H. Paradies, P. Gaveau and T. Mineva, *J. Phys. Chem. B*, 2009, **113,** 11906–11920.
17. N. J. Baxter and M. P. Williamson, *J. Biomol. NMR*, 1997, **9,** 359–369.
18. D. E. Woessner and J. R. Zimmerman, *J. Phys. Chem.*, 1963, **67,** 1590–1600.
19. K. R. Thurber and R. Tycko, *J. Magn. Reson.*, 2009, **196,** 84–87.
20. Potassium Bromide, MSDS No. P5587 [Online], J. T. Baker, Phillipsburg, NJ, August 20, 2008, http://www.jtbaker.com/msds/englishhtml/p5587.htm (October 1, 2010).
21. O. Pecher, S.-T. Kong, T. Goebel, V. Nickel, K. Weichert, C. Reiner, H.-J. Deiseroth, J. Maier, F. Haarmann and D. Zahn, *Chem. Eur. J.*, 2010, **16,** 8347–8354.
22. D. Bryce and G. Sward, *Magn. Reson. Chem.*, 2006, **44,** 409–450.
23. C. M. Widdifield, R. P. Chapman and D. L. Bryce, *Annu. Rep. NMR Spectrosc.*, 2009, **66,** 195–326.
24. R. P. Chapman and D. L. Bryce, *Phys. Chem. Chem. Phys.*, 2009, **11,** 6987–6998.
25. A. J. Rossini, R. W. Mills, G. A. Briscoe, E. L. Norton, S. J. Geier, I. Hung, S. Zheng, J. Autschbach and R. W. Schurko, *J. Am. Chem. Soc.*, 2009, **131,** 3317–3330.
26. H.-S. Lim and S.-G. Lee, *Bull. Korean Chem. Soc.*, 2006, **27,** 972–973.
27. B. W. Smee, G. E. M. Hall and D. J. Koop, *J. Geochem. Explor.*, 1978, **10,** 245–258.
28. B. Y. W. Man, J. M. Hook and J. B. Harper, *Tetrahedron Lett.*, 2005, **46,** 7641–7645.
29. H. M. Yau, S. A. Barnes, J. M. Hook, T. G. A. Youngs, A. K. Croft and J. B. Harper, *Chem. Commun.*, 2008, 3576–3578.
30. S. J. Chan, A. G. Howe, J. M. Hook and J. B. Harper, *Magn. Reson. Chem.*, 2009, **47,** 342–347.
31. H. M. Yau, J. B. Harper and J. M. Hook, Unpublished results, 2009.
32. R. Ayala, J. M. Martinez, R. R. Pappalardo and E. Sanchez Marcos, *J. Phys. Chem. A*, 2000, **104,** 2799–2807.
33. R. Remsing, J. Wildin, A. Rapp and G. Moyna, *J. Phys. Chem. B*, 2007, **111,** 11619–11621.
34. R. Remsing, R. Swatloski, R. Rogers and G. Moyna, *Chem. Commun.*, 2006, **2006,** 1271–1273.
35. R. P. Swatloski, S. K. Spear, J. D. Holbrey and R. D. Rogers, *J. Am. Chem. Soc.*, 2002, **124,** 4974–4975.
36. P. Yu and R. Kirkpatrick, *Cem. Concr. Res.*, 2001, **31,** 1479–1485.
37. T. Nagata, Y. Chuda, X. Yan, M. Suzuki and K.-I. Kawasaki, *J. Sci. Food Agric.*, 2000, **80,** 1151–1154.
38. V. Balevicius, Z. Gdaniec, K. Aidas and J. Tamuliene, *J. Phys. Chem. A*, 2010, **114,** 5365–5371.
39. Z. Gan, P. Gor'kov, T. A. Cross, A. Samoson and D. Massiot, *J. Am. Chem. Soc.*, 2002, **124,** 5634–5635.
40. K. Hashi, T. Shimizu, T. Fujito, A. Goto, S. Ohki, T. Asano and S. Nimori, *Jpn. J. Appl. Phys.*, 2009, **48,** 010220.
41. K. Hashi, T. Shimizu, A. Goto, T. Iijima and S. Ohki, *Jpn. J. Appl. Phys.*, 2005, **44,** 4194–4199.
42. K. Hashi, T. Shimizu, T. Fujito, A. Goto and S. Ohki, *J. Low Temp. Phys.*, 2010, **159,** 288–291.

43. E. V. Bryukhova, G. K. Semin, I. M. Alimov, A. N. Nesmeyanov, O. V. Nogina, V. A. Dubovitsky and S. I. Kuznetsov, *J. Organomet. Chem.*, 1974, **81,** 195–199.
44. S. I. Kuznetsov, E. V. Bryukhova, T. L. Khotsyanova and G. K. Semin, *Z. Naturforsch. A Phys. Sci.*, 1994, **49,** 627–629.
45. F. H. Larsen, H. J. Jakobsen, P. D. Ellis and N. C. Nielsen, *J. Phys. Chem. A*, 1997, **101,** 8597–8606.
46. I. Hung and Z. Gan, *J. Magn. Reson.*, 2010, **204,** 256–265.

CHAPTER 3

Solution-State Dynamic Nuclear Polarization

Mark D. Lingwood and **Songi Han**[1]

Contents

Abstract

Solution-state dynamic nuclear polarization (DNP) is an increasingly popular method of enhancing nuclear spin polarization that has many applications in nuclear magnetic resonance (NMR) and magnetic resonance imaging (MRI). The theory, methods and applications of DNP in the solution state using the Overhauser effect are distinctly different from those of solid-state DNP or what is known as dissolution DNP. This review discusses the theory and recent experimental advances of Overhauser DNP techniques in the

Department of Chemistry and Biochemistry, University of California, Santa Barbara, California, USA
[1] Corresponding author.

Annual Reports on NMR Spectroscopy, Volume 73
ISSN 0066-4103, DOI: 10.1016/B978-0-08-097074-5.00003-7

solution state at various field strengths ranging from the earth's magnetic field to 9.2 T, covering the literature from 1986 to late 2010. Most of the focus in this review is on spectroscopy applications of DNP, although proton–electron double resonance imaging (PEDRI) and remotely enhanced liquids for imaging contrast (RELIC) applications are briefly covered.

Key Words: Dynamic nuclear polarization, DNP, Overhauser effect, Hyperpolarization, Sensitivity enhancement, Hydration dynamics, Portable NMR, PEDRI, Overhauser MRI, RELIC.

1. INTRODUCTION

Magnetic resonance techniques have found many key applications in a diverse range of fields from structural identification to medical imaging, owing to the wealth of available information at the molecular level and the non-invasive nature of the technique. However, while nuclear magnetic resonance (NMR) and magnetic resonance imaging (MRI) are powerful approaches, they are also inherently insensitive. The small energy splitting between nuclear spin states even in a strong magnetic field results in low thermal polarization of the nuclei (due to Boltzmann statistics), and only a fraction of the nuclei contribute to the observed signal. This problem is compounded for elements that have a low natural abundance of magnetically active nuclei, such as the biologically important ^{13}C and ^{15}N.

One way to overcome the insensitivity of NMR and MRI is to increase the applied magnetic field, as the Zeeman splitting of the nuclear spin states increases with magnetic field. Currently, the highest commercially available magnet for NMR is 23.5 T, but even this very high field strength only gives ^{1}H nuclear polarizations of 0.008% at room temperature. High magnetic fields also do not solve another difficulty of magnetic resonance, namely the often very limited contrast between the signal of interest and the background signal. This is especially true for MRI, where for some applications, the naturally available signal contrast is not sufficient for image interpretation, and therefore external contrast agents must be added to the sample.

These limitations of sensitivity and contrast have led researchers to develop hyperpolarization methods, where the nuclear polarization is greatly increased by the manipulation of spin states. Currently, the most general and popular hyperpolarization method is dynamic nuclear polarization (DNP), where the much higher polarization of an unpaired electron is transferred to the nuclei of interest. DNP was originally

predicted in 1953 by Albert Overhauser for conduction electrons,[1] and was soon experimentally verified by Carver and Slichter.[2] Further investigation found that DNP was not only effective for metals, but could also be applied to diamagnetic crystals and paramagnetic molecules in solution.[3] DNP experiments can be performed in the liquid state through the Overhauser effect[1,4] or in the solid state through the solid effect,[5] thermal mixing[5,6] or cross effect.[7] Solid-state DNP can give very large enhancements at cryogenic temperatures, and the combination of DNP at 1.2 K and rapid sample dissolution to ambient temperatures (which is known as dissolution DNP) can give up to 10,000-fold signal enhancement for molecules in solution.[8] The recent commercial availability of dissolution DNP equipment has helped to spur the general growth of all DNP approaches.

There are several distinct advantages to performing DNP directly in the solution state. While the achievable enhancements in liquids are smaller than what is possible through dissolution DNP, the equipment is often much simpler and the sample does not have to undergo a freeze–thaw process. Most importantly, many applications do not depend on the ultimate signal gain but instead draw information from the contrast provided by the electron–nuclear interaction, and thus provide unique information about molecular properties, interactions and interfaces, giving insight into materials and biological systems and presenting new opportunities. The enhancement levels available with Overhauser DNP are still significant and can enhance detection sensitivity, allow the observation of previously undetectable species and enable faster signal acquisition.

In this review, we focus on solution-state DNP studies utilizing the Overhauser effect. Solid-state DNP is not included in this review,[9,10] nor are experiments where the hyperpolarization is performed in the solid state before melting[11,12] or dissolving[8,13,14] the sample into solution. Chemically induced DNP (CIDNP)[15–17] and the Overhauser effect of conduction electrons[18,19] are also excluded, and the interested reader is referred to the cited papers for more information. The principles and prospects of proton–electron double resonance imaging (PEDRI) are briefly included, as a thorough coverage of this research area is out of the scope of this document.

This review attempts to include all solution-state DNP papers from 1986 to late 2010. While solution-state DNP has been reviewed as recently as 1993,[20] we chose to cover a slightly larger time frame as it encompasses the modern renaissance of DNP. For earlier papers, the reader is referred to a number of excellent reviews.[4,20–22] Interestingly, the number of papers discussing solution-state DNP has dramatically increased even during the past 3 years, as can be seen in Figure 1. This chart implies that solution-state DNP is a rapidly expanding field with a strong future ahead.

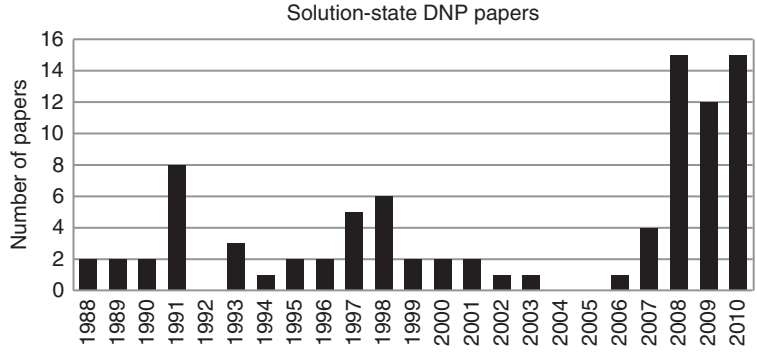

Figure 1 Experimental solution-state DNP papers cited in this work, displayed by the year of publication. Papers with PEDRI results are not included in this chart because only selected PEDRI papers are cited in this review.

2. THEORETICAL BACKGROUND

The Overhauser effect has been widely employed as an NMR analysis method in many disciplines ranging from medical to chemical sciences, and broadly refers to the motion-mediated transfer of spin polarization from a species with a higher gyromagnetic ratio (γ) to one with a lower gyromagnetic ratio. Because molecular motion is critical for efficient transfer, the Overhauser effect is most commonly observed in liquid samples. The Overhauser effect can be divided into two categories: the nuclear Overhauser effect (NOE), where both species are nuclear spins, and Overhauser DNP, where the higher γ spin is an unpaired electron. As Overhauser DNP is the focus of this review, some of the terminology and equations are specific to the Overhauser DNP effect.

2.1. NMR signal enhancement through the Overhauser effect

The Hamiltonian for a system of two coupled spin 1/2 species I and S in a magnetic field is given by[4]

$$\mathcal{H} = \hbar\gamma_S(\mathbf{S}\cdot\mathbf{B}_0) + \hbar\gamma_I(\mathbf{I}\cdot\mathbf{B}_0) + \mathcal{H}_\mathrm{S} + \mathcal{H}_\mathrm{D}. \quad (1)$$

The first and second terms describe the electron and nuclear Zeeman interactions, where γ_S and γ_I are the gyromagnetic ratios of the electron and nucleus, respectively, and $\mathbf{B}_0$ is the externally applied magnetic field. This description of the electron Zeeman interaction is appropriate for a free electron or organic radical, but for metal ions or semiconductors it should be rewritten as $g\mu_\mathrm{B}(\mathbf{S}\cdot\mathbf{B}_0)$ where g is the g-factor of the unpaired electron and μ_B is the Bohr magnetron. The terms $\mathcal{H}_\mathrm{S}$ and $\mathcal{H}_\mathrm{D}$ in

Equation (1) represent, respectively, the scalar and dipolar interactions between the electron and nucleus and are given by

$$\mathcal{H}_S = \frac{\gamma_S \gamma_I \hbar^2 8\pi}{3} |\psi(0)|^2 (\mathbf{I}\cdot\mathbf{S}) \tag{2a}$$

$$\mathcal{H}_D = \gamma_S \gamma_I \hbar^2 \left[\frac{\mathbf{I}\cdot\mathbf{S}}{r^3} - \frac{3(\mathbf{I}\cdot\mathbf{r})(\mathbf{S}\cdot\mathbf{r})}{r^5} \right] \tag{2b}$$

The scalar interaction is proportional to the square of the unpaired electron's wavefunction at the nucleus, $|\psi(0)|^2$. In general, this quantity is not known or cannot be determined, making the scalar interaction difficult to predict except in certain and simple situations.[4] The dipolar term is heavily dependent on the distance r between the two spins, leading to the distance (and time) dependence of the Overhauser effect. Further discussions of the dipolar interaction term are available in the literature.[23]

At fields above ~100 mT, the scalar and dipolar terms are small relative to the Zeeman terms and they can be treated as perturbations to describe the system with the four-level energy diagram shown in Figure 2. Saturation of the electron spin resonance (ESR) transition p will create a non-equilibrium population distribution in the system if cross-relaxation occurs through the transitions w_0 and w_2. This causes the nuclear spin polarization to be increased, as long as $w_0 \neq w_2$. In the limit of pure dipolar coupling, relaxation through w_2 is six times greater than

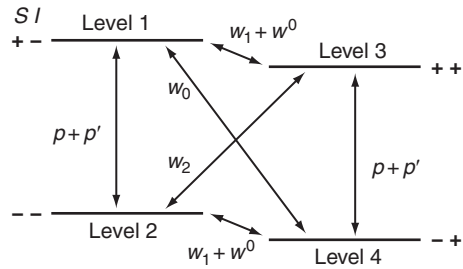

Figure 2 The four-level diagram for a system of two interacting spins, in this case an electron (S) and nucleus with a positive gyromagnetic ratio (I). The intrinsic electron and nuclear spin relaxation are given by p and w^0, respectively, and the dipolar and/or scalar interactions between the electron and nuclear spin are represented by p', w_0, w_1 and w_2. The transition w_0 is known as the zero-quantum transition, while w_1 is the single-quantum transition and w_2 is the double-quantum transition. Nuclear and electronic relaxation through mechanisms other than scalar or dipolar coupling are denoted with $w^0 = 1/T_{1n}$ and $p = 1/T_{1e}$, where T_{1n} and T_{1e} are the longitudinal relaxation times of the nucleus and electron in the absence of any coupling between them. Since much stronger relaxation mechanisms are available to the electron spin, the assumption $p \gg p'$ can be safely made. Adapted with permission from Ref. [24].

that through w_0,[25] which results in an increased population of the higher energy nuclear spin state giving an enhanced NMR signal that is in the opposite phase as the non-enhanced signal. Pure scalar coupling occurs if the relaxation is exclusively through w_0, and produces an enhanced NMR peak in the same phase as the thermally polarized signal. The mutual spin relaxation transitions w_0 and w_2 require an exchange of energy with the lattice, and thus these transitions are effective only if the dipolar and scalar terms in the Hamiltonian are time dependent on a timescale comparable to the inverse of the electron Larmor frequency, which is ~100 ps (1/10 GHz) at 0.35 T.[6] Either translational or rotational motion can satisfy this time dependence; for example, the translational motion of two colliding small molecules in a liquid is characterized by correlation times on the order of 100 ps,[26] while the rotational motion of a complex of two small molecules can have correlation times on the order of 10 ps.[26,27]

The mathematical formulation for Overhauser DNP comes from the differential equation for population changes of the nuclear spin state I, from the initial value I_0 to the excited value $\langle I_z \rangle$, originally described by Solomon[28]:

$$\frac{\mathrm{d}\langle I_z\rangle}{\mathrm{d}t} = -\left(w_0 + 2w_1 + w_2 + w^0\right)\left(\langle I_z\rangle - I_0\right) - \left(w_2 - w_0\right)\left(\langle S_z\rangle - S_0\right) \tag{3}$$

There is a similar equation for the electron spin S, but it can be ignored in this context due to the more powerful intrinsic relaxation processes of an electron spin. Since we want to know the steady state populations of the detected nuclear spin I, $\mathrm{d}\langle I_z\rangle/\mathrm{d}t$ can be set to zero and solved, giving Equation (4)

$$\frac{\langle I_z\rangle}{I_0} = 1 + \frac{w_2 - w_0}{w_0 + 2w_1 + w_2} \cdot \frac{w_0 + 2w_1 + w_2}{w_0 + 2w_1 + w_2 + w^0} \cdot \frac{S_0 - \langle S_z\rangle}{S_0} \cdot \frac{S_0}{I_0}. \tag{4}$$

Equation (4) is written in a form that best presents the physical parameters that describe DNP enhancements. The following definitions:

$$\rho = \frac{w_2 - w_0}{w_0 + 2w_1 + w_2} \tag{5a}$$

$$f = \frac{w_0 + 2w_1 + w_2}{w_0 + 2w_1 + w_2 + w^0} \tag{5b}$$

$$s = \frac{S_0 - \langle S_z\rangle}{S_0} \tag{5c}$$

are used in order to rewrite Equation (4) to give the primary equation describing DNP enhancement,

$$E = \frac{\langle I_z\rangle}{I_0} = 1 - \rho f s \frac{|\gamma_S|}{\gamma_I}. \tag{6}$$

In Equations (4) and (6), E is the observed signal enhancement obtained from the signal integral before and after electron spin saturation, ρ is the coupling factor, f is the leakage factor and s is the saturation factor. In Equation (6), the negative gyromagnetic ratio of the electron is factored out to give a negative sign in front of the second term. Note that some authors use Equation (6) but replace the symbol E with ε,[29,30] while other authors instead use the equation $(\langle I_z\rangle - I_0)/I_0 = -\rho f s|\gamma_S|/\gamma_I$ and set $(\langle I_z\rangle - I_0)/I_0$ equal to the symbols P,[4] G,[31,32] A,[33,34] ε,[35] DNPF[36] and even E.[37] Following Lurie et al.[38] and other authors,[39,40] we chose to use the expression for E because this quantity is easily measured experimentally. Also, while many authors represent the coupling factor with ρ,[33,39,40] some authors use the symbols ξ,[4,35,41–43] σ[37] or k[44] for the coupling factor with the same meaning as defined for ρ in Equation (5a). Other authors and much of the NOE community define $\sigma = w_2 - w_0$ and $\rho = w_0 + 2w_1 + w_2$.[28,45,46] In the following discussions, we will use E and ρ as defined in Equations (5a) and (6) and translate literature values into E and ρ to provide consistency. Therefore, the numerical enhancement value found in a particular cited reference and the value given here might be different, due to the conversion between the different variables (e.g. $E = A + 1$).

2.2. DNP parameters

The coupling factor is the most relevant parameter for DNP, as it is the difference of the transitions that cause polarization enhancement (w_2 and w_0) relative to all nuclear spin transitions caused by relaxation through the electron spin. In the extreme narrowing limit ($\omega\tau_t \to 0$), the upper limit of ρ is 0.5 if cross relaxation is of exclusively dipolar nature, and the lower limit of $\rho = -1$ is reached if scalar relaxation is the only pathway. As discussed below, the coupling factor sensitively depends on the timescale modulating the electron–nuclear spin interaction at a given magnetic field and thus is related to molecular diffusion and the distance between the two spins. This provides the opportunity to measure molecular dynamics and structure through DNP (and NOE), and thus makes the determination of the coupling factor an important experimental goal.

The leakage factor f quantifies the fraction of nuclear spin relaxation caused from coupling to the electron spin, as it is defined as the ratio of the sum of dipolar and scalar transitions over all possible nuclear relaxation pathways. A leakage factor of $f = 1$ means that all nuclear spin relaxation is caused by coupling to the electron, while $f = 0$ shows that no nuclear relaxation is caused by the electron spin. The leakage factor is easy to experimentally determine by measuring the longitudinal relaxation time of the sample with radicals (T_1) and without radicals (T_{10}) and using the relation

$$f = 1 - \frac{T_1}{T_{10}}. \tag{7}$$

The leakage factor depends on radical concentration through T_1. Assuming that the electron spin concentration is dilute relative to the nuclei, Equation (7) can be rewritten as

$$f = \frac{kCT_{10}}{1 + kCT_{10}} \tag{8}$$

where k is the relaxivity constant of the radical species and C is the concentration of the radicals.

The saturation factor gives the degree to which the applied radio-frequency (RF) field saturates the electron transition of all radicals in the sample and can range from 0 to 1. The saturation factor can be written as a function of the applied radiation power P,

$$s = \frac{\alpha P}{1 + \alpha P} \tag{9}$$

where α is a constant related to the electron spin longitudinal and transverse relaxation times, T_{1e} and T_{2e}, as well as the properties of the ESR coil or cavity that is used to excite the sample.[4]

From here, the saturation factor requires further discussion. Equation (9) is correct for radicals with a single ESR transition; however, the picture becomes more complicated for radicals with more than one transition due to hyperfine splitting. The nitroxide radicals commonly used for ESR and DNP fall into this category,[47,48] as the unpaired electron in these molecules partially resides on a nitrogen nucleus with spin 1 (^{14}N) or spin 1/2 (^{15}N) giving three or two hyperfine lines, respectively. For the more common ^{14}N nitroxide radicals, at low concentrations in aqueous solutions the right side of Equation (9) is multiplied by a factor of 1/3, as only one hyperfine line can be saturated at a time.[49] However, two processes can serve to mix the hyperfine lines and increase the saturation factor in the limit of infinite power (s_{max}) of nitroxide radicals well beyond $s_{max} = 1/3$.

For systems where molecular collisions between radicals occur rapidly compared to T_{1e}, Heisenberg electron spin exchange will mix the hyperfine lines.[31,50] This is a process where two colliding radicals with opposite electron spin states exchange their electron spins, and if the nitrogen nuclei on the two radicals are in different spin states then the hyperfine lines are mixed as a result. Through efficient electron spin exchange, the maximum possible saturation factor can reach $s_{max} \approx 1$ at nitroxide radical concentrations in water from tens of millimolars up to 100 mM concentrations, as reported by Armstrong and Han and Franck et al.[50,51] A recent report by Höfer et al. gives another demonstration of electron

spin exchange, as the authors investigated the concurrent saturation of both ESR lines of ^{15}N,^{16}D-4-oxo-TEMPO (where TEMPO is the nitroxide radical most commonly used for DNP, 2,2,6,6-tetramethylpiperidine-1-oxyl) and noticed no difference in the DNP-amplified signal between saturating a single line and saturating both hyperfine lines.

Another process that can mix nitroxide hyperfine lines is fast nitrogen nuclear spin relaxation,[50] which can be extremely efficient when the rotational mobility of the nitroxide radical is restricted.[52] If the relaxation of the nitrogen nucleus is faster than that of the nitroxide's electron spin, the electron 'sees' more nitrogen spin states while being irradiated, and thus the hyperfine lines are mixed (i.e. all hyperfine lines can be effectively saturated) while irradiating only one of the hyperfine resonances. Because nitrogen nuclear spin relaxation begins to affect DNP when nitroxide motion is restricted,[52] nitroxides tethered to solid matrices, macromolecules, proteins or even unstructured proteins and smaller peptide oligomers can easily reach $s_{\max} = 1$, even though adjacent radicals do not frequently come close enough to undergo collision-driven Heisenberg spin exchange. This has been experimentally demonstrated by observations that immobilized ^{14}N and ^{15}N nitroxide radicals give the same enhancement in the limit of infinite power, even with different numbers of hyperfine lines.[53]

These descriptions of the saturation factor are based solely on classical T_1 relaxation dynamics of the electron populations and do not include electron–nitrogen spin–spin (T_2) relaxation effects due to spin coherences. To include electron–nitrogen T_2 effects into the saturation factor, semi-classical relaxation theory[25,54] can be used, and a recent paper by Sezer et al. presents a formalism to include these effects.[55]

The isolation of the coupling factor is very important to gaining the desired information from an experiment. The first step towards isolating the coupling factor is to measure signal enhancement as a function of ESR saturation power and extrapolate to infinite power.[26,50] This determines the maximum enhancement, $E_{\max}$, where

$$E_{\max} = 1 - \rho f s_{\max} \frac{|\gamma_S|}{\gamma_I}. \tag{10}$$

Since the leakage factor can be easily calculated from T_1 relaxation data, and γ_S/γ_I is constant, that only leaves the determination of $s_{\max}$ before the coupling factor can be directly accessed. For solutions of radicals where Heisenberg exchange is prominent, $E_{\max}$ must be measured as a function of concentration and extrapolated to infinite concentration where $s_{\max} = 1$.[26,50] For immobilized or tethered radicals, nitrogen nuclear spin relaxation effectively mixes the hyperfine states in virtually all cases (small peptides may be an exception) and $s_{\max} \approx 1$ can safely be assumed.[53,56] Alternately, the determination of $s_{\max}$ can be avoided

entirely, and instead NMR T_1 relaxation dispersion (NMRD) is used to extract the coupling factors; this approach is discussed in Section 3.1.

It should be noted that additional considerations need to be made when working with nuclei other than hydrogen. First, while ^{1}H nuclei display almost exclusively dipolar coupling to electron spins,[21,26,57,58] other nuclei (such as ^{13}C) can show pure dipolar enhancement or a mix of scalar and dipolar effects, depending on the molecule.[24,58–60] For carbon, scalar coupling is often observed for ^{13}C atoms close to the large electron cloud of a halogen atom[46,58,60] or for systems where the radical and nuclei are held in close contact,[24,27] as scalar coupling requires an overlap of the electron and nuclear wavefunctions to be effective (from the $|\psi(0)|^2$ term in Equation (2a)). Also, for DNP with nuclei other than hydrogen, the three-spin effect needs to be considered. First described by Hausser and Reinbold in 1962,[61] the three-spin effect describes DNP in a system with a radical and two nuclear spins that are coupled to each other. Using ^{13}C and ^{1}H as an example, the ^{13}C can be enhanced either through direct contact from the radical or through the NOE from nearby protons that have also been hyperpolarized by the radical. This leads to a modification of the enhancement equation (Equation (6)) to give

$$E_2 = 1 + \rho_2^S f_2^S s \frac{\gamma_S}{\gamma_{I_2}} + \rho_2^1 f_2^1 \frac{\gamma_{I_1}}{\gamma_{I_2}} (1 - E_1) \tag{11}$$

where the detected species (i.e. carbon) is nuclear spin 2 and third species (hydrogen) is nuclear spin 1. The symbol ρ_2^S indicates the coupling factor of spin 2 due to its interaction with the electron spin S (DNP), and ρ_2^1 is the coupling factor between carbon and hydrogen (NOE). Note that the negative sign of the electron's gyromagnetic ratio has not been factored out in Equation (11) as it was in Equation (6). A few papers in the recent literature have discussed the three-spin effect.[24,62,63]

In an idealized scenario, the largest possible enhancement through Overhauser DNP can be found for the case of exclusive dipolar coupling by using Equation (6) with $\rho = 0.5, f = 1, s = 1$ and the value of $|\gamma_S|/\gamma_I$ for the specific electron–nuclear spin pair (658 for ^{1}H, 2618 for ^{13}C and -6494 for ^{15}N, assuming $g = 2$). This gives the largest enhancements of $E = -328$ for ^{1}H, $E = -1308$ for ^{13}C and $E = 3248$ for ^{15}N. For the case of exclusively scalar coupling, $\rho = -1$ and the largest enhancements are $E = 659$ for ^{1}H, $E = 2619$ for ^{13}C and $E = -6493$ for ^{15}N.

2.3. Modelling the coupling factor

After the coupling factor has been determined, models of molecular interactions can be used to calculate the correlation time, τ_c, which describes the dynamics of the system. The process of calculating τ_c from

ρ is simplified when the assumption can be made that coupling is dominated by dipolar interactions. While mixed scalar and dipolar models can be employed,[4] previous studies have shown that ^{1}H DNP of nitroxide radicals dissolved in water is almost exclusively dipolar,[21,57,58] thus making this a fair assumption since most recent Overhauser DNP experiments in liquids utilize nitroxides and water molecules. In addition, it is assumed that the electron spin relaxation time constants T_{1e} and T_{2e} are much greater than τ_c, which is the case for nitroxide radicals where T_{1e} and T_{2e} are typically tens to hundreds of nanoseconds, while τ_c is usually tens to hundreds of picoseconds. This allows us to use a single spectral density function $j(\omega, \tau_c)$ to describe the coupling factor as[4]

$$\rho = \frac{6j(\omega_S + \omega_I, \tau_c) - j(\omega_S - \omega_I, \tau_c)}{6j(\omega_S + \omega_I, \tau_c) + 3j(\omega_I, \tau_c) + j(\omega_S - \omega_I, \tau_c)} \tag{12}$$

where ω_S and ω_I are the electron and nuclear Larmor frequencies, respectively. Selecting or developing the suitable spectral density function assuming a suitable dynamic model is the first step of extracting dynamics information from the coupling factor.

For systems where translational motion best describes the dynamics at timescales relevant to DNP, a number of different spectral density functions have been used to investigate the coupling factor.[4,26,41,64] Here, we describe the force-free hard sphere (FFHS) model developed by Hwang and Freed[65,66] because it has been widely used in recent work,[26,41,67] and there are no other obvious models for obtaining an analytical expression for the spectral density function that have clear benefits over the FFHS model while providing similar versatility. The FFHS model describes translational Brownian diffusion where the spins are centered on hard spheres (whose excluded volume can be taken into account) with no forces acting between them. If we assume that the overall correlation time is the translational correlation time, $\tau_c = \tau_t$, and again assume that T_{1e} and T_{2e} are much greater than τ_t, a single reduced spectral density function can be written for all dipolar transition rates[65]:

$$j(\omega, \tau_t) = \frac{1 + (5\sqrt{2}/8)(\omega\tau_t)^{1/2} + (\omega\tau_t/4)}{1 + (2\omega\tau_t)^{1/2} + \omega\tau_t + (\sqrt{2}/3)(\omega\tau_t)^{3/2} + (16/81)(\omega\tau_t)^2 + (4\sqrt{2}/81)(\omega\tau_t)^{5/2} + \left((\omega\tau_t)^3/81\right)}. \tag{13}$$

Equations (12) and (13) give a link between the coupling factor measured from a DNP experiment and the translational correlation time τ_t. This relationship is shown by the solid line in Figure 3, where the coupling factor is plotted as a function of the product of the electron Larmor frequency and the translational correlation time.

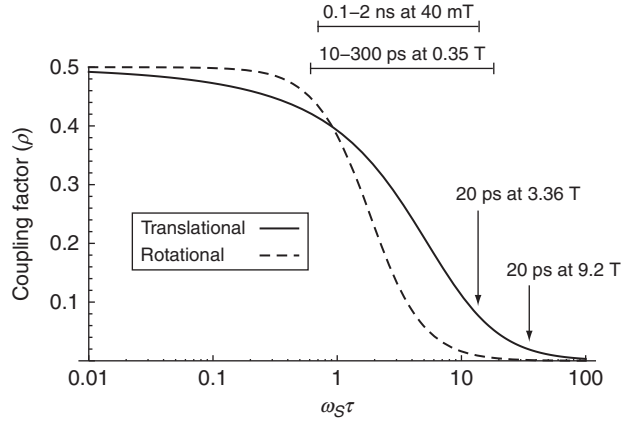

Figure 3 Plot of the coupling factor as a function of the electron Larmor frequency ω_S times the translational correlation time τ_t using the spectral density functions of Equations (13) and (15). Marked on the graph are regions or points pertaining to recently published reports. Experiments concerning changes in DNP for different systems are most effective where the small changes in correlation times will give appreciable changes in the coupling factor, and these regions are marked for 40 mT[68] and 0.35 T.[67,69,70] Experiments at higher magnetic fields have been more concerned with the amount of enhancement possible at these fields, and the correlation time given by the authors for nitroxide radicals dissolved in water is indicated at 3.36[41,71] and 9.2 T.[72]

The translational correlation time can also be related to the molecular diffusion coefficients through the relation[65]

$$\tau_t = \frac{d^2}{D_I + D_S} \tag{14}$$

where d is the distance of closest approach between the radical and nuclei, and D_I and D_S are the diffusion coefficients of the nuclei and radical, respectively. Equation (14) is important because for systems where translational motion can be assumed, the results of a DNP experiment can give the values for the local diffusion coefficient of the two molecules at the point of interaction if the distance of closest approach is known, or at a given distance of closest approach. Separate experiments have shown that, for nitroxide radicals dissolved in water, the dynamics can be safely described using only translational motion.[26,41,57] After d is calibrated through calculations or a reference experiment, the local diffusion coefficient of water interacting with a bound radical spin label can be found at the determined distance of closest approach d. Here, it is important to note that recent experiments show minimal differences in the coupling factors, and thus the distances of closest approaches, of chemically

different nitroxide radicals.[73] This process has recently been used to estimate local diffusion of water within ~10 Å of the nitroxide radical on the surface of lipid vesicles,[67] inside polyelectrolyte coacervates[69] and on the surface of proteins.[56]

Some systems cannot be well described by translational motion, so instead they require a model based on rotational diffusion. The commonly used model is one where the nuclei and radical form a bound complex, then this complex rotates to modulate dipolar coupling.[74] Here, the overall correlation time consists of the rotational correlation time of the solvent complex, τ_r, and the exchange rate of molecules in and out of the complex, τ_m, where $1/\tau_c = 1/\tau_r + 1/\tau_m$. The form of this spectral density function is simpler[4,25]:

$$j(\omega, \tau_c) = \frac{\tau_c}{1 + \omega^2 {\tau_c}^2} \tag{15}$$

Although the lifetime of the bound complex needs to be accounted for, it is often the case that $\tau_r \gg \tau_m$ so that τ_m can be ignored. A plot of the coupling factor versus magnetic field and the rotational correlation time is given by the dashed line in Figure 3.

These same models are also used to interpret NMRD measurements. NMRD is the measurement of relaxation rates $1/T_1$ as a function of magnetic field, and the data from such an experiment can be fit to a model to extract the coupling factor.[4,26,41] Both DNP and NMRD can, in principle, give access to the same coupling factor and correlation times. DNP can directly measure the coupling factor without employing a model for molecular dynamics (and the spectral density function) if the saturation and leakage factors are known or can be determined (through Equation (10)),[26] but a model is required to calculate the correlation times from ρ (Equations (12) and (13)). NMRD data provide both the coupling factor and correlation times, but the determination of either quantity requires the use of an appropriate model. A more complete description of the models used for NMRD can be found in the literature.[26,74–78]

While these models match experimental data reasonably well at lower fields, recent experiments at higher magnetic fields of 3.4 and 9.2 T show enhancement values that are much higher than predicted with the currently employed theory.[41,72,79] At these higher fields, the timescale of molecular interactions that give rise to Overhauser DNP effects is much shorter (sub-picoseconds to picoseconds) and thus should be more sensitive to the rotational diffusion dynamics of water, closely related to the atomistic details of the radical and solvent, instead of translational diffusion dynamics. These atomistic details are not accurately represented in the FFHS or rotational models (Equations (13) and (15)), implying that further work needs to be done to develop more accurate models.

Due to the imperfections of the FFHS and other models at high magnetic fields, molecular dynamics (MD) simulations have recently been proposed to calculate the coupling factor,[35] eliminating the need for explicitly translational or rotational models in an ideal scenario. In this approach, the MD simulations are used to calculate correlation functions for the electron–nuclear dynamics. The correlation functions are then related to the computed spectral density functions that are connected to the coupling factor as discussed above. While the first efforts in this direction show promising results that come closer to explaining experimental results at high magnetic fields, further development of theory and computational approaches is needed for MD simulations to become a reliable and generally usable tool for computing the coupling factor.

3. EXPERIMENTAL RESULTS

The details, outlook and potential of a DNP experiment depend on the choice of the external magnetic field, through the dependence of the electron Larmor frequency on field. The hardware required for the experiment varies dramatically between the different frequencies and field regimes. Also, the type of studies that are feasible vary with field as well, due to the quality of the thermally polarized signal, the maximum sample size for the different ESR frequencies and the accessible dynamic timescales. Most importantly, the coupling factor decreases with increasing field leading to further restrictions on the systems available for study at different field strengths. Therefore, this section is divided into parts dedicated to the different field regimes used for DNP studies.

3.1. Measuring the coupling factor

Before investigating each individual field regime, it is illustrative to discuss recent attempts to accurately measure the coupling factor. A DNP experiment can measure $E_{\max}$ (by extrapolating enhancement values to infinite power), but $E_{\max}$ is related to the product of ρ, f, $s_{\max}$ and γ_S/γ_I, as shown in Equation (10). As f can be measured separately and γ_S/γ_I is a constant, determining the coupling factor ρ from maximum enhancement measurements only requires separating the coupling factor from the maximum saturation factor $s_{\max}$. For radicals with a single hyperfine line, $s_{\max} = 1$ and the coupling factor is easy to determine.[80,81] For nitroxide radicals with two or three hyperfine lines, the determination of $s_{\max}$ values needs further careful consideration.[26,50,71]

Many authors have published reports comparing the DNP performance of different radicals but have in the past given conflicting or occasionally unphysical values for the coupling factor. Grucker et al.

measured DNP performance and calculated the coupling factor of multiple nitroxide radicals in buffer solutions with 1 mM nitroxide radical concentrations, but assumed that $s_{max} = 1/3$ at 6.85 mT.[37] Benial et al. also assumed that $s_{max} = 1/3$ for ^{14}N nitroxides and $s_{max} = 1/2$ for ^{15}N nitroxides between 0.45 and 5 mM and measured coupling factors at ~6 mT of 0.45 and 0.46 for ^{14}N and ^{15}N nitroxides, respectively.[39] Nicholson et al. measured the DNP of 4-oxo-TEMPO with the assumption that $1/n$, where n is the number of hyperfine lines of the sample.[49] The authors assumed that n must be greater than 3 due to the additional ESR transitions that become allowed at low magnetic fields, and this assumption was required to explain their data which would give a coupling factor of larger than 0.5 at 10 mT if $n = 3$.

In 1977, Bates and Drozdoski showed that Heisenberg electron spin exchange would affect DNP enhancements by increasing s_{max} with increasing radical concentrations from $s_{max} = 1/3$ to a limit of $s_{max} \approx 1$.[31] Recent experiments have shown that, indeed, electron spin exchange critically affects DNP experiments with radical concentrations above 0.5 mM,[50] thus encompassing the bulk of commonly performed DNP experiments. Despite this, Bates and Drozdoski's work went unnoticed by much of the DNP community except for a few authors who mentioned electron spin exchange in their DNP papers but did not take the step of calculating coupling factors with this consideration.[62,82,83] Armstrong and Han revived the discussion of the coupling and saturation factors in the literature on the coupling factor by using Heisenberg electron spin exchange to describe their DNP enhancement data from nitroxide radicals in water.[50] This renewed the focus on electron spin exchange, as demonstrated by Armstrong et al.[26] and Garcia et al.,[68] where coupling factors were calculated by measuring E_{max} as a function of concentration and extrapolating to infinite concentration. At infinite concentration, it can be assumed that $s_{max} = 1$ (experimentally achievable high nitroxide concentrations on the order of ~100 mM closely approach this limit[51]), allowing for the measurement of coupling factors. In a separate paper, Armstrong et al. used this method to calculate the coupling factors of pyrroline and piperidine ring radicals (five- and six-membered rings, respectively) and compared these results with MD simulations of several key parameters for these two radicals, finding that there were no differences in any of the parameters that affect DNP.[73] This allows for the accurate comparison of DNP results between the pyrroline rings, commonly used to label proteins, and piperidine ring radicals, commonly used in small molecule DNP work.

A recent advance in the quantification of DNP came with the inclusion of nitrogen nuclear relaxation into the saturation factor. Inspired by the measurement of nitrogen spin–lattice relaxation times over a wide range of correlation times by Robinson et al.,[52] Armstrong and Han developed a

formalism to allow for the mixing of nitroxide radical hyperfine states by taking both Heisenberg electron spin exchange and nitrogen nuclear relaxation into account.[50] This included an explicit formula for s_{max} in terms of the electron spin exchange rate, electron spin relaxation rate and nitrogen nuclear spin relaxation rate. An interesting outcome of this model is that $s_{max} \approx 1$ for nitroxides with slow motion/long correlation times, such as spin labels bound to larger molecules (including peptide oligomers or disordered proteins with high protein mobility[56]) or immobilized to solid supports. This was shown experimentally with immobilized ^{14}N and ^{15}N nitroxide radicals that had nearly identical E_{max} values,[53] and with spin-labelled tau proteins that only provided reasonable E_{max} values when $s_{max} \approx 1$ is assumed.[56] The tau proteins also gave E_{max} values that did not change when the freely dissolved proteins aggregated to form immobilized fibres that significantly broadened the ESR spectrum of the spin label, indicating that the monomeric (freely dissolved) tau protein's mobility is already sufficiently hindering the nitroxide radical motion to fulfil the condition of $s_{max} \approx 1$.

Other authors, when faced with the determination of s_{max} before calculating a coupling factor, have opted to not calculate a coupling factor from DNP data, but instead use NMRD on the same system to compute the coupling factor. As mentioned above, NMRD data can be fit to give a coupling factor by using the same models and spectral density functions used for DNP (i.e. Equations (12) and (13)). This method was initially proposed by Hausser and Stehlik[4] and first demonstrated by Höfer et al.,[29,41,77] where the NMRD curves for 4-hydroxy-TEMPO are fit to provide a correlation time of $\tau = 15$–20 ps. This correlation time gave a coupling factor of $\rho = 0.36$ at 0.34 T and $\rho = 0.06$ at 3.36 T, which was compared to the observed DNP enhancements of $E = -100$ and $E = -20$ at 0.34 and 3.36 T, respectively.

Shortly after the study by Höfer et al., Armstrong and Han demonstrated that the maximum saturation factor can be experimentally determined directly through DNP experiments, achieving good agreement between theoretical and experimental s_{max} values for 4-oxo-TEMPO.[26] The coupling factor can then be determined with the calculated value of s_{max} by measuring E_{max} as a function of radical concentration then extrapolating to infinite concentration. The coupling factor of $\rho = 0.22$ determined in this manner gave a translational correlation time of $\tau = 76$ ps, which is higher than the NMRD value. Armstrong and Han confirmed the previous NMRD finding through independent relaxation measurements carried out in collaboration with S. Stapf and C. Mattea, showing that there is indeed a disagreement between DNP and NMRD calculations of the coupling factor and dynamics on the example 4-oxo-TEMPO, where the NMRD fit values gave $\tau = 24$ ps and $\rho = 0.36$ at 0.35 T. The authors suggested in 2009 that the disagreement in the methods is due to the

limitations of the available models for describing the spin dynamics interactions. However, more recent measurements by Türke et al.[71] and Franck et al.[51] show that the coupling factor determined through DNP measurements can approach higher values, much closer to the NMRD values of $\rho \approx 0.30$–0.35, depending on the choice of instrumental and experimental conditions (such as sample heating and the quality factor of the microwave resonator). This conclusion is contrary to the previous finding by Armstrong et al. of $\rho = 0.22$,[26] and a discussion of this discrepancy is forthcoming.[51]

To reach this conclusion, Türke et al. investigated the experimental parameters that should affect the evaluation of DNP enhancement and found a condition where they believed complete saturation of the ESR line occurred with no sample heating for ^{15}N,^{16}D-4-oxo-TEMPO.[71] From there, they measured actual enhancements of $E = -170$ at 0.35 T, yielding a coupling factor of $\rho \leq 0.34$ at 27 °C. This experimental DNP data more closely approaches the NMRD data in the accompanying paper by Bennati et al., where a coupling factor of $\rho = 0.35$ was determined at 25 °C, which corresponds to a maximum predicted DNP signal enhancement of $E_{max} = -218$.[76] Electron–electron double resonance (ELDOR) experiments led the authors to assume $s_{max} = 0.8$ for the given sample and instrumental setting, in which case, the actual enhancement E from the DNP experiments and E_{max} from NMRD are in good agreement. The authors did not present DNP measurements as function of power, instead stating that they had achieved maximum saturation in a single measurement.

The Han group's most recent experimental results,[51] however, show that extrapolation to infinite power can lead to higher s_{max} and E_{max} values, thus experimentally achieving the limit predicted by NMRD data ($\rho = 0.36$ at 0.35 T) with DNP measurements. While the values of the coupling factor previously published by the Han group will need revisiting, their prior key conclusions, that one can operate under experimental conditions where $s_{max} \approx 1$ and that the coupling factors can be obtained with this model-free approach using optimized instrumental settings, are still valid. This is especially true now that the previous discrepancies between different research groups and between NMRD and DNP data have been resolved. This conclusion has significant implications because Overhauser DNP is inherently much more sensitive than NMRD measurements as it relies on large signal enhancements rather than signal decay, and also because time-resolved hydration dynamics measurements are potentially viable with Overhauser DNP but not with NMRD methods. Although corrections to previously published absolute ρ values need to be made, note that relative ρ values, and thus changes in correlation times (τ), measured with the same instrumental and experimental settings remain correct. Therefore, for example, the findings by

Kausik et al.,[67] Pavlova et al.[56] and Ortony et al.[84] that the translational diffusion of hydration water on a given protein, macromolecule or lipid vesicle surface is two- to four-fold slower compared to bulk water is still valid.

Besides Overhauser DNP and NMRD, a third method to determine the saturation and coupling factor that relies on MD simulations has been demonstrated by Sezer et al.[35,55] As mentioned previously, MD simulations are used to calculate correlation functions for the electron–nuclear interactions, which were used to compute spectral density functions, yielding a coupling factor of around 0.3 at 0.35 T. This number is slightly lower than the values determined from DNP and NMRD, but still in reasonable agreement. To calculate the saturation factor, the effects of electron–nuclear spin–spin (T_2) relaxation effects due to spin coherences were included with semiclassical relaxation theory[25,54]. The saturation factor was combined with the previously calculated coupling factor to produce enhancement values, which compared well with experimentally determined values at 9.2 T. It should be mentioned that this treatment of the saturation factor by Sezer et al. included the effects of rapid mixing of the nitroxide's hyperfine states through fast nitrogen nuclear spin relaxation, and showed that these effects do increase the saturation factor, as predicted by Armstrong and Han.[50] However, this effect is small for the particular example of nitroxide radicals freely dissolved in solution, unlike the case of tethered nitroxide labels.

As the discussion in this section shows, there remains somewhat conflicting reports on the proper way to measure the coupling factor and maximum saturation factor for nitroxide radicals. While this is not a concern for radicals (such as trityl) with only one hyperfine line, nitroxide radicals have been shown to give generally better DNP signal enhancements for solution-state systems than water-soluble trityl radicals at both 0.34 and 3.3 T.[41] Because of the importance of nitroxide radicals, further work needs to be done to resolve all discrepancies. However, the most recent results show that theory and various experimental reports are closer in agreement than ever before.

3.2. Low magnetic fields: Below 0.1 T

DNP at very low magnetic fields is attractive for two reasons. First, the electron saturation frequency at low fields is in the radiofrequency range, where it is much easier to obtain high-power radiation sources, amplifiers and transmission equipment. In fact, the first experimental verifications of the Overhauser effect were conducted between 1 and 5 mT,[2,85,86] likely due to the ease of constructing a suitable magnet and equipment to perform ESR saturation. The second reason for adding DNP to a low-field system is to help overcome the limited thermal polarization at low

fields, which is especially important for portable NMR applications using simple magnet designs or the earth's magnetic field.

One consideration that needs to be made for low-field DNP studies is the unique behavior of nitroxide radicals at very low magnetic fields, affecting the optimal frequency for ESR saturation. At fields of ~0.1 T and higher, the electron spin and nitroxide nitrogen spin are coupled only through the hyperfine interaction, leading to the familiar three ESR transitions for ^{14}N nitroxides or two ESR transitions for ^{15}N nitroxides. However, at lower fields, the electron and nitrogen spins are strongly coupled, leading to unequal intensities and spacing of the hyperfine lines below 0.1 T and additional allowed transitions that become significant below 3 mT. To visualize this effect, Figure 4 shows the simulated DNP-detected ESR spectrum at X-band (0.35 T) and a low field value of 1.5 mT (chosen because of recent studies at 1.5 mT[32,87,89]). The detailed theory of DNP with nitroxides in low fields has been thoroughly described by other authors,[36,87,88,90–94] so it will not be reproduced here.

The beauty of low-field DNP is the simple and versatile hardware that can be employed for experiments. Magnetic fields under 40 mT are experimentally easy to generate with electromagnets,[87,88,95,96] permanent magnets,[68] the fringe field of a superconducting magnet[97] or even the earth's magnetic field.[98] Any number of coil designs can be used for ESR saturation and NMR detection, depending on the frequencies required. Usually two separate coils are used[36,87,99]; however, a special double-resonant single-coil probe was designed and demonstrated at 2.7 mT by TonThat et al.[95] The radiofrequency electronics are also much easier to acquire and build than those needed for higher frequencies. An example of a recently described experimental system for DNP at 1.5 mT is shown in Figure 5.

Many reports of low-field DNP are focused on expanding the knowledge base of the type and magnitude of signal enhancements observed in

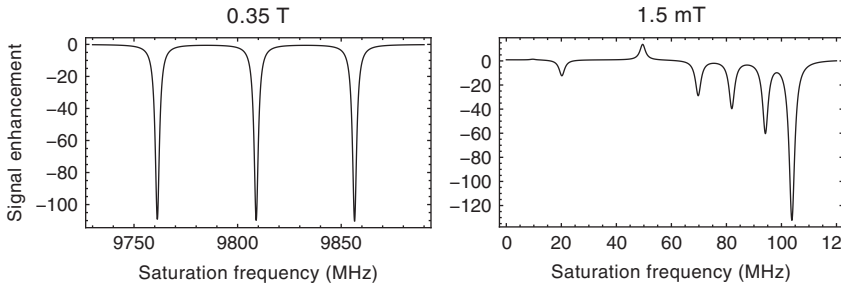

Figure 4 Plots of the DNP-detected ESR spectra of a ^{14}N nitroxide radical at 0.35 T and 1.5 mT. The low-field spectra includes both π and σ transitions. The reader is referred to the literature for further details.[32,36,87,88]

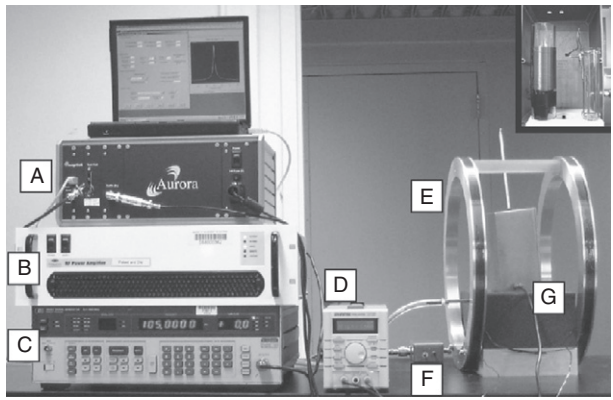

Figure 5 Photograph of a recently published 1.5 mT DNP–NMR system. Labelled in the photograph are the (A) NMR spectrometer, (B) ESR saturation amplifier, (C) signal generator for ESR saturation, (D) magnet power supply, (E) electromagnet, (F) home-built LC tuning circuit and (G) sample RF shielding box. The inset in the upper right shows the inside of the RF shielding box, with the NMR coil on the left and a birdcage coil for ESR saturation on the right. During operation, the ESR coil is placed coaxially inside the NMR coil. Adapted with permission from Ref. [87].

different chemical systems. Sapunov and Chirkov investigated an aromatic nitroxide radical (4,4′-di(*tert*-butyldiphenyl)-*N*-oxyl) in hexane, decane and dimethylformamide (DMF) at 1.17 mT.[100] They found that the DNP interaction is mostly dipolar, and also determined electron spin exchange rate constants. Tregubenkov and Baldin derived analytical expressions for the ^{15}N nitroxide radical at fields comparable to the hyperfine interaction and then recorded a DNP-detected ESR spectrum at 1.8 mT.[101] In addition to presenting the seminal formulation of low-field DNP theory, Guiberteau and Grucker reported field-cycled DNP data to support their theory with NMR detection at 6.8 mT and ESR saturation between 4.5–9[88] and 0–4 mT.[36] Polyon et al. gave a larger set of field-cycled DNP data for both ^{14}N and ^{15}N nitroxides with ESR saturation from 0 to 8 mT and NMR detection at 59 mT.[93] Interestingly, TonThat et al. showed the only recent example of solution-state DNP experiments where the electron spin source is provided by a dissolved paramagnetic ion ($MnCl_2/H_2O$) in their paper that was aimed solely towards demonstrating a new double-resonant single-coil probe design.[95]

A few papers have dealt with the effects of Heisenberg electron spin exchange on low-field DNP behavior. Bates and Drozdoski's initial description of spin exchange effects on DNP was tested against data collected at 7 mT,[31] and further work by Bates showed the changes in the DNP-detected ESR spectra at 5–9.5 mT as radical concentration was increased.[92] Tregubenkov et al. presented the calculated effects of spin

exchange on DNP at low fields, but did not provide any experimental data.[102] The most recent work on spin exchange in low-field DNP was published by Lingwood et al. using an addition to Guiberteau and Grucker's theory to allow for spin exchange at 1.5 mT, where additional allowed nitroxide transitions lead to more than three ESR hyperfine lines.[87]

While low-field imaging experiments are discussed in Section 3.6, some reports have been published on low-field DNP spectroscopy with the aim of benefiting PEDRI experiments. The first is by Lurie et al., where they described the theory of field-cycled DNP in low magnetic fields and showed experimental results to help advance their ongoing imaging experiments with ESR saturation at 0.1–12 mT and NMR detection at 10 mT.[99] A similar study investigated the potential of DNP using pulsed electron saturation to reduce heating in large biological samples, with both ESR saturation and NMR detection occurring at 10 mT.[103] In another experiment, Grucker et al. measured the DNP signal enhancement at 6.85 mT using 18 different nitroxide radical species in sodium phosphate buffer solutions, and also investigated the DNP efficiency of many of these radicals in albumin solutions, serum, red blood cell suspensions and whole blood with the aim of developing radicals for *in vivo* DNP applications.[37] The largest measured enhancement was $E_{max} = -40.6$ for 1 mM 2,2,4,4-tetramethyloxazolidine-*N*-oxyl dissolved in sodium phosphate buffer. In a similar study, Ardenkjær-Larsen et al. demonstrated the ESR and DNP properties of three different trityl radicals dissolved in water, saline, plasma and blood at 9.5 mT, obtaining DNP enhancements of up to $E_{max} = -277$ (at extrapolated infinite concentration, which corresponds to $\rho = 0.42$) with deuterated hydroxyl trityl dissolved in water.[64] Their experiments were aimed towards identifying optimal radical species for *in vivo* DNP and PEDRI studies. In addition to DNP experiments, the authors used NMRD to measure the correlation times of their samples, obtaining $\tau = 166$ ps for their system that gave the highest DNP enhancement. This correlation time for trityl radicals is much higher than the $\tau = 15$–25 ps that is measured with NMRD for nitroxide radicals, likely due to the larger distance of closest approach between the water molecules and the unpaired electron on the trityl radical. This provides further evidence that while the single ESR transitions of trityl radicals are easier to saturate, nitroxide radicals are generally a better agent for DNP due to lower correlation times (and shorter distances of closest approach, d) and thus yield larger coupling factors.

Another interesting application motivated by medicine is the use of the three-spin effect to determine lithium concentration solely through ^{1}H DNP measurements. In a proof of principle study by Zeghib et al., an increased concentration of ^{7}LiOH in aqueous solution with trityl radicals resulted in a decreased ^{1}H DNP enhancement at 6.8 mT due to a competing three-spin effect.[96] This was proposed to allow lithium monitoring

in vivo. However, the method suffers from the requirement for concentrations of lithium far exceeding biological values, as lithium concentrations of 0.5–2 M were measured in the study while the greatest biological values do not exceed 2 mM.

The simpler equipment design of low-field DNP systems has allowed researchers to move beyond developing the technique to investigating various chemical systems. A team at Hacettepe University built a 1.5-mT DNP system and performed multiple investigations on the low-field DNP properties of nitroxide radicals in various solvents and mixtures of solvents. Nitroxide radicals have been measured in methanol,[104] ethanol, tetrahydrofuran (THF) and dimethyl sulphoxide (DMSO)[105] and in soybean oil mixtures.[106] DNP enhancement through both π and σ transitions was measured with nitroxides in water and phosphate buffer.[32] Their most recent study recorded DNP and DNP-detected ESR spectra as a function of viscosity of water/glycerol solutions using 4-hydroxy-TEMPO, confirming that increased viscosity resulted in decreased signal enhancement due to the restriction of the translational motion of the molecules.[83]

Researchers at Uludağ University also have published DNP studies at 1.5 mT,[107] focusing on chemicals extracted from asphalt and highly fluorinated solutions. The chemical from asphalt, asphaltene, intrinsically contains unpaired electrons which can be used for DNP analysis, and the study by Çimenoğlu measured DNP enhancement of asphaltene suspended in numerous solvents.[108] In this report, dipolar enhancement was observed for hydrocarbon solvents, and the enhancement values increased with the addition of CS_2 to the mixture, due to the action of CS_2 to disperse asphaltene micelles and decrease the viscosity of the medium. The addition of CCl_4 had mixed effects depending on the other cosolvent in the mixture. Aydoğdu et al. also observed dipolar enhancement for asphaltene suspended in various xylene isomers.[109] Ersözlü et al. saw dipolar enhancement for asphaltene suspended in pure and mixed chlorobenzene and pyridine; the enhancement increased with chlorobenzene concentration and uniformly increased with temperature.[110] In a different study, Peksoz et al. tested the ^{19}F DNP enhancement of the α,γ-bisdiphenylene-β-phenyl allyl (BDPA) radical in multiple fluorinated solvents and observed that the aliphatic solvents gave dipolar enhancement while the aromatic solvents gave scalar enhancement.[80] The scalar enhancement was interpreted as an effect of the delocalized electron in BDPA and stacking between the planar BDPA and the aromatic ^{19}F solvent molecules creating electron spin density at the solvent nuclei. A follow-up study showed that when the BDPA radical was replaced with a galvinoxyl radical, the effect reversed somewhat due to the different radical structure: the aromatic solvents had large dipolar enhancements and the aliphatic solvents displayed a greater scalar character while still

having a mostly positive coupling factor.[81] A study by Ovalioğlu et al. investigated the ^{19}F DNP-detected ESR spectra of galvinoxyl dissolved in *N*-methyl-bis-trifluoroacetamide (MBFA) and octafluorotoluene (OFT) and saw hyperfine structure in the MFBA spectrum that indicates a hyperfine interaction between the galvinoxyl radical and the nitrogen atom on the MFBA, indicating bond or complex formation between galvinoxyl radicals and MFBA.[89] In another study by the same authors, the ^{19}F DNP-detected ESR spectra of BDPA in some highly fluorinated solvents were obtained, noticing that the intensity of the ESR peaks decreased at higher temperatures, while not discussing the dipolar or scalar nature of the enhancement.[111]

Low-field DNP has also been used to study aqueous char suspensions at 11.7 mT in a series of papers by Odintsov, Clarkson and co-workers. After designing and testing the system with nitroxide radicals and the solvated electron of hexamethylphosphorous amide,[42] the initial report of ^{1}H DNP signal enhancement from the intrinsic free electrons contained in chars found that the hardwood char suspensions gave $E_{max} = +17.4$ and softwood char suspensions gave $E_{max} = -27.6$.[112] The dominantly ^{1}H scalar enhancement of the hardwood chars was notable and was explained to be due to hydrogen bonding or chemisorption of the water onto the surface of the char followed by a slower molecular exchange process with the bulk water. The sign of enhancement for hardwood char suspensions was found to change with temperature, due to the delicate balance between the translationally mediated dipolar enhancement and the scalar enhancement/molecular exchange process; a plot showing this result is reproduced in Figure 6.[34] The biological applications of this work were described in another paper, where imaging experiments were conducted that showed the feasibility of measuring dissolved oxygen concentration using aqueous char suspensions and PEDRI methods, owing to the changes in the ESR linewidth (and thus achievable ESR saturation) and leakage factor of the chars as the oxygen concentration varies.[113] Changing the oxygen concentration from 0% to 4% resulted in obvious differences in the PEDRI images with fructose chars. Finally, DNP enhancements of various char samples were compared to pulsed-field gradient (PFG) diffusion measurements of the water inside the porous structure of the chars, showing that the short-range nuclear–electronic interactions inside the pores have the dominant effect on DNP enhancements.[114]

DNP can also easily be performed in the earth's magnetic field. Halse and Callaghan recently demonstrated DNP with detection in the earth's field and hyperpolarization of the ^{1}H NMR signal of water with and without field cycling, using a modified commercial earth-field MRI system.[98] Both methods of performing DNP gave enhanced magnetization greater than what would be feasibly possible with prepolarization in a

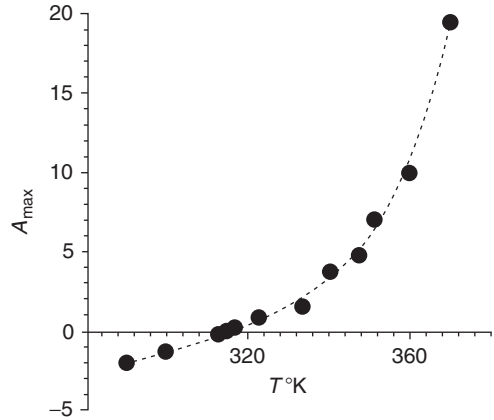

Figure 6 Temperature dependence of the DNP enhancement of water protons in an aqueous suspension of hardwood char. The dramatic change with temperature is due to the interplay between translational motion and the exchange rates of water tightly bound to the char. $A_{max} = E_{max} + 1$. Reproduced with permission from Ref. [34].

higher magnetic field. A 2D ^{19}F–^{1}H correlation spectroscopy spectrum of 2,2,2-trifluoroethanol doped with TEMPO was presented as the motivation and outlook for 2D NMR techniques in the earth's magnetic field. In addition to spectroscopy, earth's field DNP can also be used to create new devices, such as a sensitive magnetometer using DNP to measure small changes in the earth's magnetic field.[115]

In the discussion of their 1.5 mT DNP system, Lingwood et al.[87] compared the enhanced signal possible at 1.5 mT to that reported by Halse and Callaghan.[98] The higher theoretical enhancement in the earth's magnetic field is outweighed by low thermal polarization, and the DNP-enhanced signal intensities are comparable in the earth's field and at 1.5 mT. However, the signal-to-noise ratio (SNR) of DNP-enhanced signal at 1.5 mT is expected to be 380 times larger than in the earth's field because the SNR of a magnetic resonance experiment increases with the proton detection frequency by an additional factor of $\omega_H{}^{3/4}$, given equal polarization.[116] This shows that the SNR will be greater at low fields such as 1.5 mT than in the earth's magnetic field. However, the earth's field will be superior for some applications (such as 2D spectroscopy) due to the natural homogeneity of the earth's magnetic field, which is difficult to reproduce with a portable magnet system.

Garcia et al. describe the design of an L-band DNP spectrometer at 40 mT, employing an ESR frequency of 1.1 GHz, and report a coupling factor for 4-oxo-TEMPO dissolved in water of $\rho = 0.39$.[68] This coupling factor corresponds to a translational correlation time of $\tau = 150$ ps, which implies that the actual coupling factor at 40 mT should be higher to yield

correlation times similar to the $\tau = \sim 20$ ps measured at 0.35 T for the dissolved nitroxide–water system. The discrepancy may come from the fact that the quality factor of the loop-gap resonator is low, so that ESR saturation close to s_{max} could not be achieved. This discussion shows that DNP instrumentation needs to be perfectly optimized and calibrated to provide absolute values for molecular dynamics. In any case, a key benefit of DNP at 40 mT is the sensitivity to changes in the molecular dynamics of systems with correlation times on the order of 0.1–10 ns, that is, longer timescales that are assessable at ~0.3 T fields. Therefore, dynamics that are similar to or up to 10 times slower than bulk water (with τ_t on the order of 20 ps) are more sensitively detected at 0.35 T, while the dynamics of significantly hindered or entrapped water, or even the structural water of proteins, can be more sensitively detected at 40 mT.

In addition, multiple researchers have used polarization at low magnetic fields strengths (10–54 mT) followed by flowing or shuttling the sample to higher fields (4.7–7 T).[97,117–121] Since these experiments involve changing magnetic field strengths, they are discussed in further detail in Section 3.5.

3.3. Magnetic fields corresponding to X-band ESR: 0.3–0.35 T

Moderate magnetic fields are well suited for solution-state DNP. Interestingly, the only published solution-state DNP experiments between 0.1 and 1 T have been performed at the magnetic fields corresponding to X-band ESR, due to the commercial availability of X-band ESR systems operating at 0.3–0.35 T. The higher field increases the detection sensitivity for both the unenhanced and enhanced signal, while the coupling factor at 0.35 T is in an ideal range for studying solution dynamics of the disordered and highly dynamic hydration water that solvates macromolecules, as the solution dynamics are typically by a factor of 2–10 slower than bulk water.

The equipment and hardware for X-band DNP experiments are more complex than at the lower fields discussed so far. The higher field strength of the magnet cannot be produced with simple solenoids; instead, complex superconducting magnets,[24] electromagnets[29,50] or permanent magnet arrays[122,123] must be used. Electron saturation frequencies are in the microwave region (8.4–9.8 GHz) and are more difficult to generate, amplify and transmit to the sample than radiofrequency signals. Coils cannot be used to achieve ESR saturation of the sample; instead, resonant cavity structures[24,29,124] or horn antennas are required. However, these frequencies are still low enough that they will penetrate a small aqueous sample up to ~1 mm thickness.[71] If a commercial X-band ESR system is used, NMR detection can be included through small radiofrequency NMR probes inserted into the microwave cavity[24] or by use of an electron–nuclear double resonance (ENDOR) cavity with an added

home-built tuning circuit.[29] The output of the ESR system can be directly used for electron saturation,[29,50] or higher power microwave sources can be installed.[71,122] With some hardware modifications, these systems allow for concurrent ESR and DNP experiments, which have several practical advantages.

Much of the recent development of theory and methods for measuring the coupling factor has been performed with X-band DNP.[26,29,41,50,71,73] Since these studies were discussed earlier in Section 3.1, they are not included here and instead this section covers recent applications for DNP carried out at this field.

One of the main focuses of recent work at moderate fields has been the development of X-band DNP for the investigation of soft matter systems through the measurement of translational dynamics of hydration water interacting with molecular and material surfaces. The first work in this area involved the ^{1}H enhancement of water using spin-labelled fatty acids (the radical is bound to the fatty acid molecule). McCarney et al. showed that DNP enhancement of water is larger inside spin-labelled stearic acid micelles and smaller within vesicle bilayers assembled of spin-labelled stearic acid and stearate.[70,125,126] This is due to the different water accessibility of the fatty acid hydrocarbon tail within these structures, likely owing to different curvature and packing density of the assemblies. This result is reproduced in Figure 7. Kausik and Han extended this work to the quantification of local diffusion coefficients of water within 10 Å distances of the lipid vesicle surface, which encompasses up to approximately three water layers (also referred to as hydration water or outer sphere water).[67] They reproduced the findings of theory and quasi-elastic neutron scattering studies that the local diffusion coefficients of hydration water are impeded compared to bulk water diffusion by about two- to four-fold. This approach is unique in that local and interfacial information can be obtained in the complete presence of bulk water, and that such dilute concentrations (<1 mM) and small sample volumes (<10 µl) can be used. For these applications, the enhanced signal comes solely from the interaction of water with the spin label within molecular distances of up to $\sim$10 Å. The fast exchange of water compared to the timescale of the ^{1}H T_1 relaxation leads to polarization build-up of the bulk water signal that is modulated only due to these local interactions. Overhauser DNP has also been used to investigate the local water dynamics of coacervating polyelectrolyte systems, where the diffusion coefficients of the water interacting with the spin-labelled polymers were found to decrease by an order of magnitude when the polyelectrolytes assemble into a dense liquid coacervate phase suspended in a dilute solvent phase.[69] Dollman et al. synthesized thermoresponsive spin-labelled hydrogels which spontaneously collapsed as the temperature was increased, with the intent to polarize molecules inside the gel matrix and subsequently expel the polarized

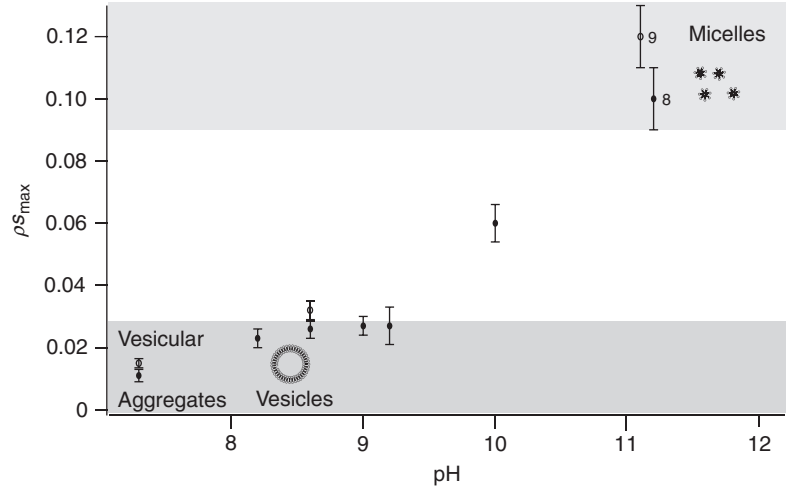

Figure 7 Plot of the change in the product of the coupling and maximum saturation factors as a function of macromolecular structure. At lower pH values, the spin-labelled lipids are present as vesicles and vesicular aggregates, while at higher pH values, micelles are formed. The higher ρs_{max} values for the micelles imply greater water accessibility to the radical site. The solid circles represent 16-DS (16-doxyl stearic acid, spin-labelled at the end of the lipid tail) while the open circles represent 5-DS (5-doxyl stearic acid, spin-labelled near the polar head group). Reproduced with permission from Ref. [70].

molecules from the gel through heat-induced collapse.[127] This study was performed with imaging applications in mind, where the hyperpolarized solvent would no longer be in close contact with the radicals after the heat-induced collapse, giving enhanced signal with a longer T_1 relaxation time. These gels gave -26-fold enhancement of water before heating, and the enhancement decreased with increasing temperature due to the gradual collapse of the gel. McCarney and Han[53] and Lingwood et al.,[124] on the other hand, measured the 0.35 T DNP enhancement of immobilized radicals for flow imaging applications, finding that TEMPO directly immobilized onto Sepharose beads gave $E_{max} = -46$, while TEMPO bound to a polyvinylimidazole polyelectrolyte linker which was then bound to Sepharose beads gave $E_{max} = -122$. While these systems are discussed in more detail in Section 3.5, it is appropriate to note here that spin-labelled polyelectrolytes have been observed to give the highest enhancements of all currently reported tethered nitroxide radical systems, with enhancement values approaching that of nitroxide radicals freely dissolved in solution.

This X-band Overhauser DNP technique has also been developed to study proteins and their interactions with site-specific resolution, employing site-directed mutagenesis and spin-labelling methods[128] to

introduce the spin label specifically at chosen protein sites. Pavlova et al. used tau proteins spin labelled at specific positions to demonstrate the utility of Overhauser DNP to monitor early protein aggregation events and observed the decrease of signal enhancement over the course of aggregation as the water was gradually slowed and ultimately excluded as protein monomers formed oligomers and eventually protein fibres.[56,84]

The majority of recent solution-state DNP studies at X-band have been focused on the hyperpolarization of ^{1}H signal. However, a recent report by Lingwood and Han described DNP signal enhancement of ^{13}C-labelled small molecules dissolved in aqueous solution.[24] The authors measured varying levels of signal enhancement from several small molecules and investigated the influence of the three-spin effect between the radical, the water proton and the ^{13}C nuclei. They found that the relative levels of scalar and dipolar coupling are hard to predict for ^{13}C, and showed that the three-spin effect can either increase or diminish the overall signal enhancement depending on whether scalar or dipolar enhancement is dominant. The authors concluded that the amount of DNP signal enhancement is more dependent on the distance of closest approach and the relative amounts of scalar and dipolar coupling, and not as dependent on the diffusion of the ^{13}C-containing molecule.

Recently, reports on portable DNP instrumentation operating at X-band have appeared in the literature, made possible by recent advances in permanent magnet design and efficient solid-state X-band microwave amplifiers. Armstrong et al. described a portable system with a custom-built microwave amplifier array capable of achieving greater than −100-fold DNP enhancement with 4-oxo-TEMPO radicals in water.[122] When combined with a variable-field Halbach magnet (∼0.3 T) and a portable NMR spectrometer, the whole system fit easily onto a small cart. Lingwood et al. developed a portable DNP system using this microwave amplifier that was transported to a clinical MRI facility to perform DNP-enhanced flow imaging.[124] Münnemann et al. separately developed a mobile DNP system using a variable-field Halbach magnet at 0.30 T equipped with a cryostat and high-power travelling wave tube (TWT) microwave amplifier, which produced −50-fold enhancement using a spin-labelled cationic polyelectrolyte dissolved in a glycerol–water mixture.[123]

Another report to mention is that of Toda et al., where they place an NMR coil directly above the microwave cavity of an X-band ESR system and shuttle the sample between the center of the microwave cavity and the NMR coil.[30] They observed −19-fold enhancement with toluene and the BDPA radical at 0.40 T. Since their research program is focused on developing gyrotrons for high-field DNP, they did not further pursue X-band DNP experiments.

Finally, the application of optimal control theory to DNP studies needs to be discussed. Optimal control theory is a means to systematically design and optimize pulse sequences to maximize the efficiency of transfer between spin states. While this method was initially introduced to benefit high-resolution NMR studies, it has recently been adapted to improve the electron–nuclear polarization transfer in DNP applications by considering simple two- or three-spin systems.[129–131] While no experimental implementation of DNP pulse sequences designed by optimal control methods has been reported, these methods have the great potential to enhance DNP performance at X-band, due to the powerful pulsed ESR hardware that is commercially available at these frequencies.

3.4. High magnetic fields: Above 1 T

The reasons for performing DNP at higher magnetic fields are the same reasons why most conventional NMR studies benefit from higher fields: greater chemical shift resolution and higher (thermal) signal sensitivity. However, DNP at these fields suffers from the difficulty of generating, amplifying and efficiently transmitting the high ESR Larmor frequencies of tens and hundreds of gigahertz and from the high dielectric loss of electromagnetic radiation in liquid samples over this frequency regime. In spite of these difficulties, many researchers are pursuing DNP at fields above 1 T motivated by the great potential benefits of the technique.

The hardware required for DNP at high magnetic fields critically depends on the frequency required for ESR saturation. As the size of microwave resonators decreases with increasing frequency, simple resonant cavities like those used at X-band are not feasible at higher frequencies. Several microwave transmission systems have been reported: a horn and reflector at 40 GHz,[40] a high-Q non-radiative dielectric resonator[132] and commercial ENDOR probes[41,133] at 95 GHz, an open waveguide and reflector at 140 GHz,[46] a helical cavity at 260 GHz[134] and a tapered waveguide and mirror at 300 GHz.[30] Microwave sources employed for solution-state DNP also vary, including solid-state sources with TWT amplifiers at 40 GHz,[40] unamplified[41,132] and amplified[133] W-band bridges at 95 GHz, solid-state sources at 260 GHz[134] and gyrotrons with frequency outputs ranging from 140 to 980 GHz.[30,46,135–138] Gyrotrons provide the highest power output by far of all sources listed here. Nearly all experimental systems in this range of fields utilize superconducting magnets.

Wind and Ardenkjær-Larsen reported the development of a 1.4 T DNP system using a horn and reflector system to transmit the 40 GHz radiation with a screening coil placed around the sample to reduce heating.[40] Using a symmetric trityl radical, −9-fold enhancement of the water signal was measured in their report. In a second experiment, Wind et al. used the

same equipment to observe DNP with BDPA radicals dissolved in supercritical ethylene pressurized between 60 and 300 bar at room temperature.[139] Scalar ^{1}H Overhauser enhancements of up to $E = 55$ were observed, caused by interactions between supercritical ethylene and undissolved BDPA, as BDPA was not appreciably soluble in supercritical ethylene. Also visible were small contributions from the solid/thermal mixing effect, implying that portions of ethylene were adsorbed to the solid radical surface for a prolonged time.

Several research groups have developed systems for DNP at 3.4 T based on W-band ESR equipment operating at 95 GHz. Annino et al. presented a novel double resonance structure for concurrent ESR saturation and NMR detection based on a high-Q non-radiative dielectric resonator with an integrated miniaturized radiofrequency coil.[132] With this design, an enhancement of $E = -16$ was measured for TEMPO dissolved in a mixture of water and dioxane with only 70 mW of microwave power. Villanueva-Garibay et al. used the same system to measure the DNP of TEMPO solutions in nanoliter volumes and observed even higher enhancements of up to $E = -65$ for 4-hydroxy-TEMPO dissolved in water.[43] This is much greater enhancement than expected at 95 GHz, based on theory and previous observations, and is likely due to the very high resonator quality factor and lossless penetration of radiation through the minute sample volume. Kryukov et al. developed a DNP spectrometer by using a commercial W-band ESR instrument with an ENDOR probe and inserting a high-power extended interaction klystron (EIK) amplifier into the system.[133] They measured −49-fold enhancements for toluene and 4-hydroxy-TEMPO, and performed extensive temperature dependence measurements to investigate the molecular motions in the system. Höfer et al. used an unmodified commercial ESR spectrometer and ENDOR cavity to carry out W-band DNP studies, and observed $E = -20$ for 4-hydroxy-TEMPO in water and $E = -4$ for a trityl radical.[41] Türke et al. used the same system with a power upgrade module (400 mW) and found $E = -43$ for ^{15}N,^{16}D-4-oxo-TEMPO in water. Based on NMRD data from an accompanying paper, the authors give the coupling factor as $\rho = 0.11$.[76] As it is apparent from this paragraph, DNP enhancement values and coupling factors measured at 95 GHz, even for the same radical and water system, widely diverge between different groups or experimental settings, while the same discussions for solution-state DNP at X-band are nearing to a close agreement.

DNP in liquids has also been reported at higher fields of 5 T (140 GHz electron frequency) by Loening et al.[46] In this report, the chemical systems were specifically selected to optimize scalar coupling, as the decrease in the coupling factor with increasing field is less dramatic for scalar-coupled species.[4] Enhancements of $E = 181$ for ^{31}P triphenylphospine, $E = 41$ for ^{13}C carbon tetrachloride, $E = -35$ for ^{15}N aniline and $E = 9.4$

for ^{19}F hexafluorobenzene were reported with BDPA employed as the radical. Note that the negative enhancements for ^{15}N are still due to scalar coupling, as the sign of enhancement is reversed due to the negative gyromagnetic ratio of ^{15}N.

Thus far, only one high-field DNP system operating at 9.2 T and 260 GHz has been reported to experimentally realize DNP enhancements of solution-state systems. The spectrometer design and ESR spectra were presented by Denysenkov et al.,[134] and the first DNP data were presented by Prandolini et al.[79] This system gave $E = -3.0$ for 4-hydroxy-TEMPO in water, and the enhancement was confirmed to be due to the Overhauser effect with dipolar coupling. From here, the authors were able to achieve enhancements of $E = -9.4$ for water by improving microwave stability, increasing power to 45 mW from the previous 22 mW and by using ^{15}N-Fremy's salt as a radical with higher DNP efficiency due to its narrower ESR linewidths.[72] Gafurov et al. investigated the biradical bis-TEMPO–bis-ketal, finding that the solution-state DNP enhancement of this radical at 9.2 T was entirely due to the Overhauser effect and that the -2- to -3-fold enhancements from the biradical were similar to standard TEMPO radicals.[140] This instrument was also used to measure DNP enhancement as a function of microwave frequency, to compare with the results of the models developed by Sezer et al.[55] Most recently, the microwave source was replaced with a high-power gyrotron source (20 W) that led to a DNP enhancement of $E = -28$ for aqueous ^{15}N-Fremy's salt at 60 °C.[135]

The work of researchers at the University of Fukui on developing high-power gyrotrons for DNP should be noted. They have recently reported the development of gyrotron microwave sources operating at 394 and 980 GHz and planned to apply these sources to DNP experiments at high fields.[136–138] DNP at 10.7 T and 300 GHz has also been attempted by the same authors, but the BDPA and toluene system completely evaporated due to sample heating before any NMR signal enhancement could be observed.[30]

Even though only a small number of reports have been published, it appears that the enhancement values measured so far at high magnetic fields are greater than what is predicted to be possible with existing theoretical models. Using the FFHS model and the reported translational correlation times for nitroxide radicals and water of $\tau_t = 20$ ps,[76] a coupling factor of 0.022 is derived for 260 GHz, which gives a maximum theoretical enhancement of $E_{max} = -13.3$ (Equation (10) with $f = 1$ and $s_{max} = 1$). This value is distinctly lower than the experimentally observed $E = -28$,[135] suggesting that different or new models may need to be considered and developed. For example, the rotational diffusion of individual water molecules with correlation times on the order of 1 ps may play a role.[141] These discrepancies were the motivation for the development of MD simulations to calculate the coupling factor by Sezer et al.[35,55]

However, it is clear overall that further detailed experimental studies and development of theory are necessary to enhance the current understanding of solution-state DNP at high magnetic fields.

3.5. DNP with flowing or shuttling between fields

One of the difficulties of designing a DNP experiment is simultaneously optimizing for high ESR saturation and sensitive NMR detection; however this can be partially overcome by hyperpolarizing and performing NMR detection at separate fields and rapidly transporting samples between the two locations and fields. This allows for the ESR saturation to be performed at a lower frequency to avoid the sample size restrictions found at higher irradiation frequencies and to avoid the complications of building NMR detection capabilities into a resonant microwave cavity. The NMR experiment can be performed at a higher field in a system designed for that purpose, offering greater sensitivity and often narrower NMR linewidths due to the presence of shim systems and the absence of bulky metal microwave components distorting the field homogeneity.

The downside of hyperpolarizing and detecting separately is that the enhanced signal decays with the T_1 value of the nuclei, and thus signal is lost during the shuttling process. This effect is dramatically increased if the radicals are left in contact with the sample during flow or shuttling, as an aqueous solution of radicals can easily have a $T_1 < 500$ ms for ^{1}H nuclei. In the case of ^{13}C or other nuclei such as ^{15}N or ^{29}Si, the transfer time should not be as significant due to the longer T_1 of those species. Alternately, immobilized radicals can be used for DNP, then filtered from the sample,[53,142,143] but previously described immobilized radical systems give lower DNP performance than radicals freely dissolved in solution.[53,63,127,143] However, a recent report describes the use of immobilized spin-labelled polyvinylimidazole for DNP studies, showing that this system gives DNP enhancement values approaching that of freely dissolved nitroxides with larger than -100-fold measured enhancements.[124]

The idea of using flowing liquids with polarization highly amplified by Overhauser DNP was pioneered and developed by the Dorn group. In the first demonstration of the technique, the NMR coil was placed just below the microwave cavity in a commercial X-band ESR instrument; both hyperpolarization and detection were performed at 0.33 T and signal enhancements of approximately $E = -64$ were observed for benzene with the 2,4,6-tri-*t*-butylphenoxide radical.[33] This experimental system was also used to demonstrate the feasibility of using immobilized radicals to hyperpolarize a flowing liquid by enhancing the signal of benzene flowing over spin-labelled silica gel.[143]

The Dorn group then built a system to perform DNP at 0.33 T and detect NMR in a separate, higher field 4.7 T magnet,[144] allowing for NMR

chemical shift resolution of the enhanced species. These low to high magnetic field transfer experiments necessitated the formulation of a new model for maximum enhancements by Tsai et al.,[62] which included the effects of incomplete polarization build-up due to fast flow through the microwave cavity and the relaxation decay between hyperpolarization and NMR detection. Using this 0.33–4.7 T DNP system, different samples were investigated. In another paper by Tsai et al., dissolved TEMPO was used to enhance the ^{29}Si NMR signal of hexamethyldisiloxane.[82] Here, enhancement values of +13-fold were observed, which correspond to predominantly dipolar enhancement because the negative gyromagnetic ratio of ^{29}Si changes the sign of the enhanced signal. Dorn et al. investigated ^{13}C DNP by using immobilized radicals to enhance benzene and chloroform, and noted a large (+63) scalar-dominated enhancement of chloroform.[63] ^{13}C DNP was also performed on fullerenes (C_{60}) dissolved in benzene using TEMPO radicals with the aim of describing collision dynamics in solution, where the enhancement for 20% ^{13}C-labelled fullerenes was found to be dominated by dipolar coupling and mediated by mostly rotational motion.[145] Stevenson et al. further developed the flow-DNP technique as a detector for continuous-flow on-line chromatography, demonstrating greatly improved sensitivity for on-line ^{13}C NMR detection after a chromatographic separation of several chlorinated and fluorinated organic molecules.[60] DNP was also shown to improve recycled-flow NMR experiments (the flowing sample brings new molecules into the NMR probe to shorten repetition times), where the DNP-enhanced experiments provided an increase in sensitivity over traditional, unenhanced recycled-flow NMR.[146] Most recently, Russ et al. used DNP, NMR contact shift measurements and density functional theory (DFT) calculations to investigate the collision dynamics of acetonitrile and acetamide using TEMPO radicals, finding that both molecules displayed dipolar and scalar coupling to the electron at different sites.[27]

Reese, Krahn and co-workers have developed a shuttling system that allows for polarization at 0.34 T and NMR detection at 14.09 T. Their first design placed a 0.34 T permanent magnet directly above a 14 T superconducting magnet, employing a pneumatic shuttle system to transfer the sample in 115 ms. In the initial report, ^{1}H enhancements of −0.41-fold (relative to thermal polarization at 14 T) were obtained with water and 4-hydroxy-TEMPO radicals.[147] The system was then optimized to provide enhancements of −2.6 for water and +15 for ^{13}C chloroform, employing ^{15}N,^{16}D-4-oxo-TEMPO radicals.[148] The second design of the shuttle system used ferromagnetic shims to modify the fringe field of the same 14 T magnet, thus allowing the placement of the hyperpolarization location inside the magnet bore and reducing the shuttle time to 40 ms.[149] With this system, ^{1}H enhancements of −3.7 were measured for water using ^{15}N,^{16}D-4-oxo-TEMPO. Most importantly, the shorter shuttling time

allowed for the enhancement of molecules that were not detected with their earlier shuttling system because of rapid magnetization decay, including larger molecules. This finding was demonstrated with enhancements between −1.4 and −2.8 for the different protons of glucose.

The Han group has developed the hardware and techniques to enhance water at 0.35 T under continuous-flow, then subsequently image this hyperpolarized water either at 0.35 T or in higher fields, such as a 1.5 T. This technique, named remotely enhanced liquids for imaging contrast (RELIC), was first demonstrated by conducting both DNP and imaging experiments within a 0.35-T electromagnet.[150] The flow dispersion path of enhanced water could clearly be visualized as it travelled through unenhanced bulk water—a phenomenon that cannot be visualized otherwise unless tracer molecules are used. As the hydrophilic, agarose gel-based immobilized radical systems were of a new design, they were described and characterized more thoroughly in a later report, with a maximum enhancement of $E_{max} = -46$.[53] This work was extended to a clinical setting, where efficient DNP enhancement was achieved in the 0.35 T location in the fringe field of a 1.5 T clinical MRI magnet that was modified to present sufficient field homogeneities using resistive shims.[124] The images at 1.5 T showed ^{1}H signal with −7-fold enhancement (relative to thermal polarization at 1.5 T), permitting direct visualization and tracing of enhanced water flow through a bulk water system. This is shown in Figure 8, where the trajectory of hyperpolarized water can easily be seen upon injection into a phantom filled with unenhanced water. While the fringe field of a 1.5 T magnet was used in this study, the authors note that the fringe field of non-actively shielded magnets up to ∼4.7 T could be used, as the homogeneity requirements for DNP are much less than what is required for spectroscopy. This paper also includes the first report of an immobilized radical system that gives

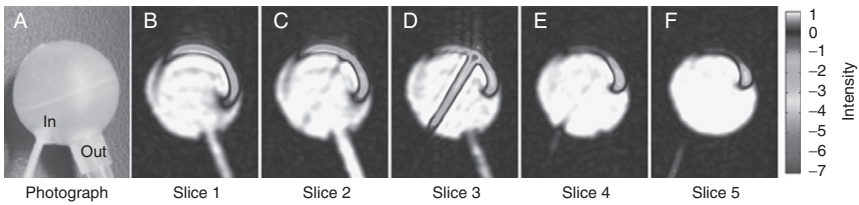

Figure 8 Photograph and MR images of a phantom for demonstrating the remotely enhanced liquids for imaging contrast (RELIC) technique. Water is hyperpolarized in the 0.35 T location in the fringe field then transferred into the center of the same magnet for imaging. (A) Photograph of the phantom; the water enters from the bottom left and exits through the bottom right. (B)–(F) Slices of the MR image with hyperpolarized water, clearly showing the jet of hyperpolarized water as it flows through unenhanced water. Adapted with permission from the full-color images in Ref. [124].

DNP enhancement approaching that of freely dissolved radicals, with the measured maximum enhancement of $E_{max} = -122$ for immobilized spin-labelled polyvinylimidazole.

DNP has been performed in flowing systems to compare with CIDNP and stimulated nuclear polarization (SNP) experiments on radical reaction products. Here, the transfer from lower to higher fields was used for experimental convenience and was not the point of the work. Bagryanskaya et al. used polarization between 0 and 6 mT with detection at 4.7 T to study the mechanism of the photo-induced reactions of quinines[117] and the *trans–cis* isomerization of fumaronitrile.[118] Ananchenko et al. used the same system except with detection at 7 T to investigate the low-field transitions of the photolysis of 2,4,6-trimethylbenzoylphosphonic acid dimethyl ester.[119] These experiments were expanded by the work of Gorelik et al., where the theoretical basis of stationary and time-resolved DNP of reaction products was extended to include degenerated electron spin exchange, and the theory was compared with experiments.[120] Yamakage et al. utilized polarization at 0.33 T and detection at 2.35 T to investigate the photochemical reaction of benzaldehyde with time-resolved DNP, and describe a theoretical model suitable for these systems.[151] Most recently, Bagryanskaya et al. measured DNP and CIDNP of multiple radical reactions with polarization at 54 mT and 0.33 T accompanied with NMR detection at 7 T, and described the interplay of DNP, CIDNP and SNP that must be taken into account when investigating these systems.[121] The use of DNP to study radical reaction products in solution is a broad research area with many promising applications; however, a more thorough discussion is out of the scope of this review since this area has more in common with CIDNP (which employs a different mechanism) than conventional Overhauser DNP experiments where the goal is NMR signal enhancement.

The recent report of Korchak et al. describes a field-cycling DNP system which hyperpolarizes at either 10 or 49.6 mT with NMR detection at 7 T.[97] This paper is notable because the DNP was performed in the fringe field of the 7 T magnet. The aim of this report was to develop the theory for pulsed ESR saturation and optimize the experimental conditions such as pulse length, duty cycle, inter-pulse delay and applied power to give the greatest levels of DNP enhancement. By using pulsed ESR saturation, the authors were able to reduce applied ESR saturation power levels by a factor of 10 while only reducing observed enhancements by less than a factor of 2.

3.6. Proton–electron double resonance imaging

PEDRI (also known as Overhauser MRI) integrates the principles of Overhauser DNP with MRI to provide information on the spatial distribution of free radicals within the system of interest. Much work has been done to

develop PEDRI as an imaging modality, especially for *in vivo* applications; however, a complete collection of the large volume of PEDRI papers is out of the scope of this review. Instead, we describe the technical capabilities and recent applications of PEDRI and refer the reader to a number of recent reviews for further details.[44,152–157]

PEDRI was first demonstrated by Lurie et al. in 1988[158] with phantom images at 40 mT (1.12 GHz electron saturation). This initial report was quickly followed by the introduction of field-cycled PEDRI.[159] Because of the dielectric losses of biological samples, the magnetic field strengths used for electron saturation are limited to roughly 20 mT (~560 MHz ESR frequency),[160] with the optimum field value being somewhat lower.[161] To avoid the low SNRs that occur when detecting nuclear signals at these low fields, field-cycling is now commonly combined with PEDRI experiments allowing for ESR saturation at lower fields and NMR/MRI detection at higher fields.[159,162–165] Thus far, the most advanced system reported in the literature performs ESR saturation at 5 mT and NMR detection at 450 mT.[166]

PEDRI has been used for a number of different applications both *in vitro* and *in vivo*, where the *in vivo* experiments have thus only included animal models. The simplest example application is to monitor the distribution and clearance of the radical species in the body[160,167,168] or isolated organs[169] by comparing the amount of signal enhancement at different spatial locations, as shown in Figure 9. A common application of PEDRI is oximetry, where the amount of dissolved oxygen *in vivo* can be detected through the effects of paramagnetic oxygen on reducing observed DNP enhancements, due to reductions in the leakage factor and the lowering of ESR saturation of a broader ESR line.[156,170–174] Acidity can be measured *in situ* through pH-sensitive hyperfine ESR splittings of certain nitroxide radicals, where the DNP-detected ESR spectrum can easily be measured using field-cycled PEDRI instrumentation and recording signal enhancement as a function of magnetic field during electron saturation.[164,175,176] The progress of reduction/oxidation (redox) reactions can also be monitored with PEDRI through the consumption and regeneration of the unpaired electron (usually PROXYL radicals, 2,2,5,5-tetramethylpyrrolidine-*N*-oxyl) in the redox reaction, leading to the modulation of the DNP-enhanced ^{1}H NMR signal.[177–180] Proteolysis (protein degradation) information can be obtained with PEDRI through the use of spin-labelled proteins; when the spin-labelled protein is broken into small pieces during proteolysis, the nitroxide correlation time decreases and the DNP enhancement increases.[181] Finally, systems have been developed to use Overhauser enhancements to assist with needle and catheter placement during interventional MRI,[182] including a self-contained 'marker' carrying a radical solution and coaxial transmission line for ESR saturation that can be inserted into tissue for locating the marker's enhanced signal with unmodified MRI equipment.[183,184]

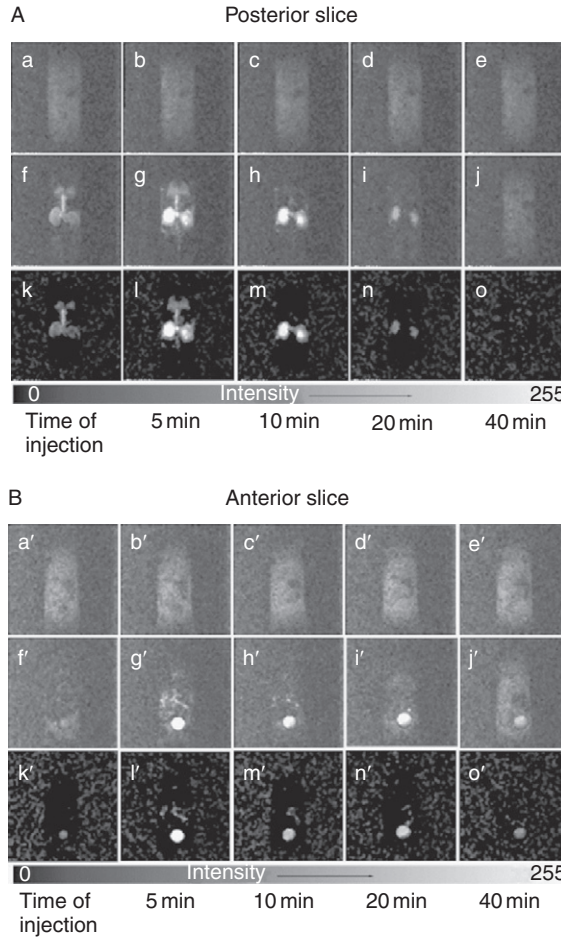

Figure 9 Time-dependent PEDRI images of a living mouse with an intravenous infusion of 2,2,5,5-tetramethyl-3-carboxylpyrrolidine-*N*-oxyl (PCA) radical. (A) The posterior slice: (a–e) no ESR irradiation, (f–j) 12 W of ESR irradiation and (k–o) the subtraction of ESR on and off images. (B) The anterior slice: (a′–e′) no ESR irradiation, (f′–j′) 12 W of ESR irradiation and (k′–o′) the subtraction of ESR on and off images. The posterior images show that PCA is initially distributed in the heart, lungs, kidneys and major vessels, while the anterior images show that PCA is collected in the bladder over time. Adapted with permission from Ref. [160].

PEDRI is still an evolving field. In addition to application-oriented research, much emphasis is also being placed on improving the technique itself. Examples include the development of new field-cycling magnets,[152,165] improved ESR saturation equipment[185,186] and expanding the technique to include ^{19}F detection.[187,188] Other new developments include

a real-time spectral analysis and visualization program,[189] fast-imaging pulse sequences adapted to field-cycled PEDRI[190] and the implementation of intermolecular double-quantum coherence imaging.[191] As all these applications critically depend on the DNP performance of the radical species, some recent reports have focused on the characterization of existing radicals[39] and the synthesis and DNP analysis of isotopically labelled radicals.[192] In addition to biological and *in vivo* studies, PEDRI has also been used to investigate the formation of hydrogels as a function of time[193] and to monitor free radicals in sediment samples.[194] The wide range of information accessible with PEDRI and the wide interest of the magnetic resonance community imply that much further research will be done in this area.

4. CONCLUSION

As has been presented in this review, there are many different applications and an exciting outlook for solution-state DNP techniques. While the Overhauser effect was first predicted over 50 years ago, DNP is still a young field due to the need for complex hardware and theory development. Much of the published work in this area has focused on developing the equipment and techniques and gaining an understanding of what is possible, rather than exploring or demonstrating applications and outcomes. The amount of interest in solution-state DNP has greatly increased over the past few years, and this is indicative of the great potential of the technique. Signal enhancement as the end goal is useful in portable and low-field applications, where the signal is difficult to detect without hyperpolarization. At higher fields, the contrast that is available through DNP is unique and specific to the local interactions between the radical and the solvent, and applications that exploit this specific contrast will provide insights in areas ranging from medical imaging to molecular interactions and interfaces. Reports of useful applications of Overhauser DNP methods have started to increase in the literature, many of which point towards the future of these techniques. If DNP is to transition from a curiosity into a mainstream experimental method, the information gained by DNP must be quantitative and made relevant to a broader scientific community. While there is still much work to be done, the great potential of solution-state Overhauser DNP indicates that these methods have a bright and promising future.

REFERENCES

1. A. W. Overhauser, *Phys. Rev.*, 1953, **92,** 411.
2. T. R. Carver and C. P. Slichter, *Phys. Rev.*, 1953, **92,** 212.
3. A. Abragam, *Phys. Rev.*, 1955, **98,** 1729.
4. K. H. Hausser and D. Stehlik, *Adv. Magn. Reson.*, 1968, **3,** 79.

5. A. Abragam and M. Goldman, *Rep. Prog. Phys.*, 1978, **41,** 395.
6. R. A. Wind, M. J. Duijvestijn, C. van der Lugt, A. Manenschijn and J. Vriend, *Prog. Nucl. Magn. Reson. Spectrosc.*, 1985, **17,** 33.
7. C. T. Farrar, D. A. Hall, G. J. Gerfen, S. J. Inati and R. G. Griffin, *J. Chem. Phys.*, 2001, **114,** 4922.
8. J. H. Ardenkjær-Larsen, B. Fridlund, A. Gram, G. Hansson, L. Hansson, M. H. Lerche, R. Servin, M. Thaning and K. Golman, *Proc. Natl. Acad. Sci. USA*, 2003, **100,** 10158.
9. A. B. Barnes, G. De Paëpe, P. C. A. van der Wel, K. N. Hu, C. G. Joo, V. S. Bajaj, M. L. Mak-Jurkauskas, J. R. Sirigiri, J. Herzfeld, R. J. Temkin and R. G. Griffin, *Appl. Magn. Reson.*, 2008, **34,** 237.
10. T. Maly, G. T. Debelouchina, V. S. Bajaj, K.-N. Hu, C.-G. Joo, M. L. MakJurkauskas, J. R. Sirigiri, P. C. A. van der Wel, J. Herzfeld, R. J. Temkin and R. G. Griffin, *J. Chem. Phys.*, 2008, **128,** 052211.
11. C. G. Joo, A. Casey, C. J. Turner and R. G. Griffin, *J. Am. Chem. Soc.*, 2009, **131,** 12.
12. C.-G. Joo, K.-N. Hu, J. A. Bryant and R. G. Griffin, *J. Am. Chem. Soc.*, 2006, **128,** 9428.
13. F. A. Gallagher, M. I. Kettunen and K. M. Brindle, *Prog. Nucl. Magn. Reson. Spectrosc.*, 2009, **55,** 285.
14. K. Golman and J. S. Petersson, *Acad. Radiol.*, 2006, **13,** 932.
15. J. R. Woodward, *Prog. React. Kinet. Mech.*, 2002, **27,** 165.
16. M. Goez, Photo-CIDNP spectroscopy. *in*: Annual Reports on NMR Spectroscopy, (G. A. Webb ed.). Academic Press, London, 2009, **66,** pp. 77–147.
17. J. Matysik, A. Diller, E. Roy and A. Alia, *Photosynth. Res.*, 2009, **102,** 427.
18. G. Kaur and G. Denninger, *Appl. Magn. Reson.*, 2010, **39,** 185.
19. S. B. Orlinskii, J. Schmidt, P. G. Baranov, C. d. M. Donegá and A. Meijerink, *Phys. Rev. B*, 2009, **79,** 165316.
20. R. D. Bates, *Magn. Reson. Rev.*, 1993, **16,** 237.
21. W. Müller-Warmuth and K. Meise-Gresch, *Adv. Magn. Reson.*, 1983, **11,** 1.
22. J. Potenza, *Adv. Mol. Relax. Process*, 1972, **4,** 229.
23. C. P. Slichter, Principles of Magnetic Resonance. Springer-Verlag, Berlin, 1990.
24. M. D. Lingwood and S. Han, *J. Magn. Reson.*, 2009, **201,** 137.
25. A. Abragam, The Principles of Nuclear Magnetism. Clarendon Press, Oxford, 1961.
26. B. D. Armstrong and S. Han, *J. Am. Chem. Soc.*, 2009, **131,** 4641.
27. J. L. Russ, J. Gu, K.-H. Tsai, T. Glass, J. C. Duchamp and H. C. Dorn, *J. Am. Chem. Soc.*, 2007, **129,** 7018.
28. I. Solomon, *Phys. Rev.*, 1955, **99,** 559.
29. P. Höfer, P. Carl, G. Guthausen, T. Prisner, M. Reese, T. Carlomagno, C. Griesinger and M. Bennati, *Appl. Magn. Reson.*, 2008, **34,** 393.
30. M. Toda, Y. Fujii, S. Mitsudo, I. Ogawa, T. Idehara, T. Saito, H. Ito and M. Chiba, *Appl. Magn. Reson.*, 2008, **34,** 277.
31. R. D. Bates and W. S. Drozdoski, *J. Chem. Phys.*, 1977, **67,** 4038.
32. A. O. Salman, M. M. Sünnetçioğlu, R. Sungur and G. Bingöl, *J. Magn. Reson.*, 1998, **134,** 1.
33. H. C. Dorn, J. Wang, L. Allen, D. Sweeney and T. E. Glass, *J. Magn. Reson.*, 1988, **79,** 404.
34. B. M. Odintsov, R. L. Belford, P. J. Ceroke, A. B. Odintsov and R. B. Clarkson, *Surf. Sci.*, 1997, **393,** 162.
35. D. Sezer, M. J. Prandolini and T. F. Prisner, *Phys. Chem. Chem. Phys.*, 2009, **11,** 6626.
36. T. Guiberteau and D. Grucker, *J. Magn. Reson. B*, 1996, **110,** 47.
37. D. Grucker, T. Guiberteau, B. Eclancher, J. Chambron, R. Chiarelli, A. Rassat, G. Subra and B. Gallez, *J. Magn. Reson. B*, 1995, **106,** 101.
38. D. J. Lurie, I. Nicholson and J. R. Mallard, *J. Magn. Reson.*, 1991, **94,** 197.
39. A. M. F. Benial, K. Ichikawa, R. Murugesan, K. I. Yamada and H. Utsumi, *J. Magn. Reson.*, 2006, **182,** 273.
40. R. A. Wind and J.-H. Ardenkjær-Larsen, *J. Magn. Reson.*, 1999, **141,** 347.

41. P. Höfer, G. Parigi, C. Luchinat, P. Carl, G. Guthausen, M. Reese, T. Carlomagno, C. Griesinger and M. Bennati, *J. Am. Chem. Soc.*, 2008, **130,** 3254.
42. B. M. Odintsov, R. L. Belford and R. B. Clarkson, *J. Phys. Chem. A*, 1997, **101,** 116.
43. J. A. Villanueva-Garibay, G. Annino, P. J. M. van Bentum and A. P. M. Kentgens, *Phys. Chem. Chem. Phys.*, 2010, **12,** 5846.
44. K. Golman, I. Leunbach, J. H. Ardenkjær-Larsen, G. J. Ehnholm, L. G. Wistrand, J. S. Petersson, A. Järvi and S. Vahasalo, *Acta Radiol.*, 1998, **39,** 10.
45. D. Neuhaus and M. P. Williamson, The Nuclear Overhauser Effect in Structural and Conformational Analysis. Wiley-VCH, New York, 2000.
46. N. M. Loening, M. Rosay, V. Weis and R. G. Griffin, *J. Am. Chem. Soc.*, 2002, **124,** 8808.
47. O. H. Griffith, D. W. Cornell and H. M. McConnell, *J. Chem. Phys.*, 1965, **43,** 2909.
48. T. J. Stone, T. Buckman, P. L. Nordio and H. M. McConnell, *Proc. Natl. Acad. Sci. USA*, 1965, **54,** 1010.
49. I. Nicholson, D. J. Lurie and F. J. L. Robb, *J. Magn. Reson. B*, 1994, **104,** 250.
50. B. D. Armstrong and S. Han, *J. Chem. Phys.*, 2007, **127,** 104508.
51. J. M. Franck, A. Pavlova and S. Han, *Prog. Nucl. Magn. Reson. Spectrosc.*, (in preparation).
52. B. H. Robinson, D. A. Haas and C. Mailer, *Science*, 1994, **263,** 490.
53. E. R. McCarney and S. Han, *J. Magn. Reson.*, 2008, **190,** 307.
54. M. Goldman, *J. Magn. Reson.*, 2001, **149,** 160.
55. D. Sezer, M. Gafurov, M. J. Prandolini, V. P. Denysenkov and T. F. Prisner, *Phys. Chem. Chem. Phys.*, 2009, **11,** 6638.
56. A. Pavlova, E. R. McCarney, D. W. Peterson, F. W. Dahlquist, J. Lew and S. Han, *Phys. Chem. Chem. Phys.*, 2009, **11,** 6833.
57. B. Borah and R. G. Bryant, *J. Chem. Phys.*, 1981, **75,** 3297.
58. W. Müller-Warmuth, R. Vilhjalmsson, P. A. M. Gerlof, J. Smidt and J. Trommel, *Mol. Phys.*, 1976, **31,** 1055.
59. H. Brunner and K. H. Hausser, *J. Magn. Reson.*, 1972, **6,** 605.
60. S. Stevenson and H. C. Dorn, *Anal. Chem.*, 1994, **66,** 2993.
61. K. H. Hausser and F. Reinbold, *Phys. Lett.*, 1962, **2,** 53.
62. K. H. Tsai and H. C. Dorn, *Appl. Magn. Reson.*, 1990, **1,** 231.
63. H. Dorn, T. Glass, R. Gitti and K. Tsai, *Appl. Magn. Reson.*, 1991, **2,** 9.
64. J. H. Ardenkjær-Larsen, I. Laursen, I. Leunbach, G. Ehnholm, L. G. Wistrand, J. S. Petersson and K. Golman, *J. Magn. Reson.*, 1998, **133,** 1.
65. J. H. Freed, *J. Chem. Phys.*, 1978, **68,** 4034.
66. L.-P. Hwang and J. H. Freed, *J. Chem. Phys.*, 1975, **63,** 4017.
67. R. Kausik and S. Han, *J. Am. Chem. Soc.*, 2009, **131,** 18254.
68. S. Garcia, J. H. Walton, B. Armstrong, S. Han and M. J. McCarthy, *J. Magn. Reson.*, 2010, **203,** 138.
69. R. Kausik, A. Srivastava, P. A. Korevaar, G. Stucky, J. H. Waite and S. Han, *Macromolecules*, 2009, **42,** 7404.
70. E. R. McCarney, B. D. Armstrong, R. Kausik and S. Han, *Langmuir*, 2008, **24,** 10062.
71. M. T. Türke, I. Tkach, M. Reese, P. Höfer and M. Bennati, *Phys. Chem. Chem. Phys.*, 2010, **12,** 5893.
72. M. J. Prandolini, V. P. Denysenkov, M. Gafurov, B. Endeward and T. F. Prisner, *J. Am. Chem. Soc.*, 2009, **131,** 6090.
73. B. D. Armstrong, P. Soto, J.-E. Shea and S. Han, *J. Magn. Reson.*, 2009, **200,** 137.
74. É. Tóth, L. Helm and A. Merbach, Relaxivity of MRI contrast agents. *in*: Contrast Agents I, (W. Krause ed.). Springer, Berlin/Heidelberg, 2002.
75. M. W. Hodges, D. S. Cafiso, C. F. Polnaszek, C. C. Lester and R. G. Bryant, *Biophys. J.*, 1997, **73,** 2575.
76. M. Bennati, C. Luchinat, G. Parigi and M. T. Türke, *Phys. Chem. Chem. Phys.*, 2010, **12,** 5902.

77. C. Luchinat and G. Parigi, *Appl. Magn. Reson.*, 2008, **34,** 379.
78. B. Halle, *J. Chem. Phys.*, 2009, **131,** 224507.
79. M. J. Prandolini, V. P. Denysenkov, M. Gafurov, S. Lyubenova, B. Endeward, M. Bennati and T. F. Prisner, *Appl. Magn. Reson.*, 2008, **34,** 399.
80. A. Peksoz, M. A. Çimenoğlu and A. Yalçiner, *J. Disper. Sci. Technol.*, 2008, **29,** 40.
81. A. Peksoz, A. Yalçiner and M. A. Çimenoğlu, *Z. Naturforsch. A*, 2009, **64,** 477.
82. K. H. Tsai, T. E. Glass and H. C. Dorn, *J. Magn. Reson.*, 1990, **89,** 362.
83. I. Sert, M. M. Sünnetçioğlu, R. Sungur and G. Bingöl, *Z. Naturforsch. A*, 2000, **55,** 682.
84. J. H. Ortony, C.-Y. Cheng, J. M. Franck, R. Kausik, A. Pavlova, J. Hunt and S. Han, *New J. Phys.*, 2011, **13,** 015006.
85. T. R. Carver and C. P. Slichter, *Phys. Rev.*, 1956, **102,** 975.
86. L. H. Bennett and H. C. Torrey, *Phys. Rev.*, 1957, **108,** 499.
87. M. D. Lingwood, I. A. Ivanov, A. R. Cote and S. Han, *J. Magn. Reson.*, 2010, **204,** 56.
88. T. Guiberteau and D. Grucker, *J. Magn. Reson. A*, 1993, **105,** 98.
89. H. Ovalioğlu, A. Peksoz, H. E. Kırımlı and A. Yalçiner, *Z. Naturforsch. A*, 2010, **65,** 254.
90. G. Breit and I. I. Rabi, *Phys. Rev.*, 1931, **38,** 2082.
91. V. W. Müller-Warmuth, *Z. Naturforsch.*, 1960, **15a,** 927.
92. R. D. Bates, *J. Magn. Reson.*, 1982, **48,** 111.
93. C. Polyon, D. J. Lurie, W. Youngdee, C. Thomas and I. Thomas, *J. Phys. D*, 2007, **40,** 5527.
94. M. Fedin, S. Shakirov, P. Purtov and E. Bagryanskaya, *Russ. Chem. Bull.*, 2006, **55,** 1703.
95. D. M. TonThat, M. P. Augustine, A. Pines and J. Clarke, *Rev. Sci. Instrum.*, 1997, **68,** 1527.
96. N. Zeghib and D. Grucker, *Phys. Med. Biol.*, 2001, **46,** 2371.
97. S. E. Korchak, A. S. Kiryutin, K. L. Ivanov, A. V. Yurkovskaya, Y. A. Grishin, H. Zimmermann and H. M. Vieth, *Appl. Magn. Reson.*, 2010, **37,** 515.
98. M. E. Halse and P. T. Callaghan, *J. Magn. Reson.*, 2008, **195,** 162.
99. D. J. Lurie, I. Nicholson and J. R. Mallard, *J. Magn. Reson.*, 1991, **95,** 405.
100. V. A. Sapunov and A. K. Chirkov, *Sov. J. Chem. Phys.*, 1991, **7,** 1447.
101. A. Y. Tregubenkov and V. I. Baldin, *Sov. J. Chem. Phys.*, 1991, **7,** 1238.
102. A. Y. Tregubenkov, V. I. Baldin and S. P. Dovgopol, *Teor. Eksp. Khim.*, 1991, **27,** 1.
103. M. Alecci and D. J. Lurie, *J. Magn. Reson.*, 1999, **138,** 313.
104. M. Sünnetçioğlu, G. Bingöl and R. Sungur, *Z. Naturforsch. A*, 1991, **46,** 976.
105. R. Sungur, *Doga Turk. Fiz. Astrofiz. Derg.*, 1991, **15,** 63.
106. N. Horasan, M. M. Sünnetçioğlu, R. Sungur and G. Bingöl, *Z. Naturforsch. A*, 1997, **52,** 485.
107. C. Akay and A. Yalçiner, *Z. Naturforsch. A*, 1995, **50,** 177.
108. M. A. Çimenoğlu, *Fuel*, 2001, **80,** 2041.
109. D. Aydoğdu, M. A. Çimenoğlu and A. Yalçiner, *J. Disper. Sci. Technol.*, 2006, **27,** 955.
110. N. U. Ersözlü, A. Peksöz, H. Ovalıoğlu, H. E. Kırımlı, M. A. Çimenoğlu and A. Yalçiner, *J. Disper. Sci. Technol.*, 2008, **29,** 899.
111. H. Ovalioğlu, A. Peksoz, H. E. Kırımlı and A. Yalçiner, *J. Disper. Sci. Technol.*, 2010, **31,** 332.
112. B. M. Odintsov, R. L. Belford, P. J. Ceroke and R. B. Clarkson, *J. Am. Chem. Soc.*, 1998, **120,** 1076.
113. R. B. Clarkson, B. M. Odintsov, P. J. Ceroke, J. H. Ardenkjær-Larsen, M. Fruianu and R. L. Belford, *Phys. Med. Biol.*, 1907, **1998,** 43.
114. B. M. Odintsov, R. L. Belford, P. J. Ceroke, Z. S. Idiyatullin, R. S. Kashaev, I. V. Kuriashkin, V. S. Rukhlov, A. N. Temnikov and R. B. Clarkson, *J. Magn. Reson.*, 1998, **135,** 435.
115. N. Kernevez and H. Glénat, *IEEE Trans. Magn.*, 1991, **27,** 5402.
116. D. I. Hoult and R. E. Richards, *J. Magn. Reson.*, 1976, **24,** 71.
117. E. G. Bagryanskaya, Y. A. Grishin, N. I. Avdievitch, R. Z. Sagdeev and Y. N. Molin, *Chem. Phys. Lett.*, 1986, **128,** 162.

118. E. G. Bagryanskaya, N. I. Avdievich, Y. A. Grishin and R. Z. Sagdeev, *Chem. Phys.*, 1989, **135,** 123.
119. G. S. Ananchenko, E. G. Bagryanskaya and R. Z. Sagdeev, *Chem. Phys. Lett.*, 1998, **282,** 450.
120. V. R. Gorelik, E. G. Bagryanskaya, N. N. Lukzen, I. V. Koptyug, V. V. Perov and R. Z. Sagdeev, *J. Phys. Chem.*, 1996, **100,** 5800.
121. E. G. Bagryanskaya, G. S. Ananchenko, T. Nagashima, K. Maeda, S. Milikisyants and H. Paul, *J. Phys. Chem. A*, 1999, **103,** 11271.
122. B. D. Armstrong, M. D. Lingwood, E. R. McCarney, E. R. Brown, P. Blümler and S. Han, *J. Magn. Reson.*, 2008, **191,** 273.
123. K. Münnemann, C. Bauer, J. Schmiedeskamp, H. W. Spiess, W. G. Schreiber and D. Hinderberger, *Appl. Magn. Reson.*, 2008, **34,** 321.
124. M. D. Lingwood, T. A. Siaw, N. Sailasuta, B. D. Ross, P. Bhattacharya and S. Han, *J. Magn. Reson.*, 2010, **205,** 247.
125. S. Han, E. R. McCarney and B. D. Armstrong, *Appl. Magn. Reson.*, 2008, **34,** 439.
126. S. Han, E. R. McCarney, B. D. Armstrong and M. D. Lingwood, Dynamic nuclear polarization-enhanced magnetic resonance analysis at X-band using amplified ^{1}H water signal. *in*: Magnetic Resonance Microscopy, S. L. Codd and J. D. Seymour (eds.), . Wiley-VCH, Weinheim, 2009.
127. B. C. Dollmann, M. J. N. Junk, M. Drechsler, H. W. Spiess, D. Hinderberger and K. Münnemann, *Phys. Chem. Chem. Phys.*, 2010, **12,** 5879.
128. W. L. Hubbell and C. Altenbach, *Curr. Opin. Struct. Biol.*, 1994, **4,** 566.
129. N. Pomplun, B. Heitmann, N. Khaneja and S. J. Glaser, *Appl. Magn. Reson.*, 2008, **34,** 331.
130. N. Pomplun and S. J. Glaser, *Phys. Chem. Chem. Phys.*, 2010, **12,** 5791.
131. I. I. Maximov, Z. Tošner and N. C. Nielsen, *J. Chem. Phys.*, 2008, **128,** 184505.
132. G. Annino, J. A. Villanueva-Garibay, P. J. M. van Bentum, A. A. K. Klaassen and A. P. M. Kentgens, *Appl. Magn. Reson.*, 2010, **37,** 851.
133. E. V. Kryukov, M. E. Newton, K. J. Pike, D. R. Bolton, R. M. Kowalczyk, A. P. Howes, M. E. Smith and R. Dupree, *Phys. Chem. Chem. Phys.*, 2010, **12,** 5757.
134. V. P. Denysenkov, M. J. Prandolini, A. Krahn, M. Gafurov, B. Endeward and T. F. Prisner, *Appl. Magn. Reson.*, 2008, **34,** 289.
135. V. Denysenkov, M. J. Prandolini, M. Gafurov, D. Sezer, B. Endeward and T. F. Prisner, *Phys. Chem. Chem. Phys.*, 2010, **12,** 5786.
136. T. Idehara, K. Kosuga, L. Agusu, R. Ikeda, I. Ogawa, T. Saito, Y. Matsuki, K. Ueda and T. Fujiwara, *J. Infrared Millim. Te.*, 2010, **31,** 775.
137. T. Idehara, T. Saito, I. Ogawa, S. Mitsudo, Y. Tatematsu, L. Agusu, H. Mori and S. Kobayashi, *Appl. Magn. Reson.*, 2009, **34,** 265.
138. S. P. Sabchevski and T. Idehara, *J. Infrared Millim. Te.*, 2010, **31,** 934.
139. R. A. Wind, S. Bai, J. Z. Hu, M. S. Solum, P. D. Ellis, D. M. Grant, R. J. Pugmire, C. M. V. Taylor and C. R. Yonker, *J. Magn. Reson.*, 2000, **143,** 233.
140. M. Gafurov, S. Lyubenova, V. Denysenkov, O. Ouari, H. Karoui, F. Le Moigne, P. Tordo and T. Prisner, *Appl. Magn. Reson.*, 2010, **37,** 505.
141. B. Halle and L. Nilsson, *J. Phys. Chem. B*, 2009, **113,** 8210.
142. H. H. Fischer, M. Seiler, T. S. Ertl, U. Eberhardinger, H. Bertagnolli, H. Schmitt-Willich and K. Albert, *J. Phys. Chem. B*, 2003, **107,** 4879.
143. R. Gitti, C. Wild, C. Tsiao, K. Zimmer, T. E. Glass and H. C. Dorn, *J. Am. Chem. Soc.*, 1988, **110,** 2294.
144. H. C. Dorn, R. Gitti, K. H. Tsai and T. E. Glass, *Chem. Phys. Lett.*, 1989, **155,** 227.
145. H. C. Dorn, J. Gu, D. S. Bethune, R. D. Johnson and C. S. Yannoni, *Chem. Phys. Lett.*, 1993, **203,** 549.
146. S. Stevenson, T. Glass and H. C. Dorn, *Anal. Chem.*, 1998, **70,** 2623.

147. M. Reese, D. Lennartz, T. Marquardsen, P. Höfer, A. Tavernier, P. Carl, T. Schippmann, M. Bennati, T. Carlomagno, F. Engelke and C. Griesinger, *Appl. Magn. Reson.*, 2008, **34,** 301.
148. M. Reese, M.-T. Türke, I. Tkach, G. Parigi, C. Luchinat, T. Marquardsen, A. Tavernier, P. Höfer, F. Engelke, C. Griesinger and M. Bennati, *J. Am. Chem. Soc.*, 2009, **131,** 15086.
149. A. Krahn, P. Lottmann, T. Marquardsen, A. Tavernier, M. T. Türke, M. Reese, A. Leonov, M. Bennati, P. Hoefer, F. Engelke and C. Griesinger, *Phys. Chem. Chem. Phys.*, 2010, **12,** 5830.
150. E. R. McCarney, B. D. Armstrong, M. D. Lingwood and S. Han, *Proc. Natl. Acad. Sci. USA*, 2007, **104,** 1754.
151. Y. Yamakage, K. Maeda and T. Azumi, *Mol. Phys.*, 1997, **90,** 431.
152. D. J. Lurie, S. Aime, S. Baroni, N. A. Booth, L. M. Broche, C. H. Choi, G. R. Davies, S. Ismail, D. O. hÓgáin and K. J. Pine, *C. R. Phys.*, 2010, **11,** 136.
153. K. I. Matsumoto, S. Subramanian, R. Murugesan, J. B. Mitchell and M. C. Krishna, *Antioxid. Redox Signal.*, 2007, **9,** 1125.
154. D. J. Lurie and K. Mäder, *Adv. Drug Deliv. Rev.*, 2005, **57,** 1171.
155. B. Gallez, C. Baudelet and B. F. Jordan, *NMR Biomed.*, 2004, **17,** 240.
156. M. C. Krishna, S. Subramanian, P. Kuppusamy and J. B. Mitchell, *Semin. Radiat. Oncol.*, 2001, **11,** 58.
157. D. Grucker, *Prog. Nucl. Magn. Reson. Spectrosc.*, 2000, **36,** 241.
158. D. J. Lurie, D. M. Bussell, L. H. Bell and J. R. Mallard, *J. Magn. Reson.*, 1988, **76,** 366.
159. D. J. Lurie, J. M. S. Hutchison, L. H. Bell, I. Nicholson, D. M. Bussell and J. R. Mallard, *J. Magn. Reson.*, 1989, **84,** 431.
160. H. Li, G. He, Y. Deng, P. Kuppusamy and J. L. Zweier, *Magn. Reson. Med.*, 2006, **55,** 669.
161. W. Youngdee, G. Planinšič and D. J. Lurie, *Phys. Med. Biol.*, 2001, **46,** 2531.
162. G. Planinšič, T. Guiberteau and D. Grucker, *J. Magn. Reson. B*, 1996, **110,** 205.
163. T. Claasen-Vujčić, H. Borsboom, E. Konijnenburg, D. Korbee, J. Trommel and T. Mehlkopf, *Phys. Med. Biol.*, 1863, **1998,** 43.
164. V. V. Khramtsov, G. L. Caia, K. Shet, E. Kesselring, S. Petryakov, J. L. Zweier and A. Samouilov, *J. Magn. Reson.*, 2010, **202,** 267.
165. K. Shet, G. L. Caia, E. Kesselring, A. Samouilov, S. Petryakov, D. J. Lurie and J. L. Zweier, *J. Magn. Reson.*, 2010, **205,** 202.
166. D. J. Lurie, G. R. Davies, M. A. Foster and J. M. S. Hutchison, *Magn. Reson. Imaging*, 2005, **23,** 175.
167. H. Li, Y. Deng, G. He, P. Kuppusamy, D. J. Lurie and J. L. Zweier, *Magn. Reson. Med.*, 2002, **48,** 530.
168. K. Golman, I. Leunbach, J. S. Petersson, D. Holz and J. Overweg, *Acad. Radiol.*, 2002, **9,** S104.
169. T. Liebgott, H. Li, Y. Deng and J. L. Zweier, *Magn. Reson. Med.*, 2003, **50,** 391.
170. S. Matsumoto, H. Yasui, S. Batra, Y. Kinoshita, M. Bernardo, J. P. Munasinghe, H. Utsumi, R. Choudhuri, N. Devasahayam, S. Subramanian, J. B. Mitchell and M. C. Krishna, *Proc. Natl. Acad. Sci. USA*, 2009, **106,** 17898.
171. S. Matsumoto, H. Utsumi, T. Aravalluvan, K. Matsumoto, A. Matsumoto, N. Devasahayam, A. L. Sowers, J. B. Mitchell, S. Subramanian and M. C. Krishna, *Magn. Reson. Med.*, 2005, **54,** 213.
172. S. Subramanian, K.-i. Matsumoto, J. B. Mitchell and M. C. Krishna, *NMR Biomed.*, 2004, **17,** 263.
173. M. C. Krishna, S. English, K. Yamada, J. Yoo, R. Murugesan, D. Nallathamby, J. A. Cook, K. Golman, J. H. Ardenkjaer-Larsen, S. Subramanian and J. B. Mitchell, *Proc. Natl. Acad. Sci. USA*, 2002, **99,** 2216.
174. K. Golman, J. S. Petersson, J.-H. Ardenkjær-Larsen, I. Leunbach, L.-G. Wistrand, G. Ehnholm and K. Liu, *J. Magn. Reson. Imaging*, 2000, **12,** 929.

175. D. I. Potapenko, M. A. Foster, D. J. Lurie, I. A. Kirilyuk, J. M. S. Hutchison, I. A. Grigor'ev, E. G. Bagryanskaya and V. V. Khramtsov, *J. Magn. Reson.*, 2006, **182,** 1.
176. M. A. Foster, I. A. Grigor'ev, D. J. Lurie, V. V. Khramtsov, S. McCallum, I. Panagiotelis, J. M. S. Hutchison, A. Koptioug and I. Nicholson, *Magn. Reson. Med.*, 2003, **49,** 558.
177. A. M. F. Benial, H. Utsumi, K. Ichikawa, R. Murugesan, K.-i. Yamada, Y. Kinoshita, T. Naganuma and M. Kato, *J. Magn. Reson.*, 2010, **204,** 131.
178. M. Yamato, T. Shiba, K. Yamada, T. Watanabe and H. Utsumi, *J. Cereb. Blood Flow Met.*, 2009, **29,** 1655.
179. F. Hyodo, R. Murugesan, K.-i. Matsumoto, E. Hyodo, S. Subramanian, J. B. Mitchell and M. C. Krishna, *J. Magn. Reson.*, 2008, **190,** 105.
180. H. Utsumi, K. Yamada, K. Ichikawa, K. Sakai, Y. Kinoshita, S. Matsumoto and M. Nagai, *Proc. Natl. Acad. Sci. USA*, 2006, **103,** 1463.
181. P. Mellet, P. Massot, G. Madelin, S. R. A. Marque, E. Harte, J. M. Franconi and E. Thiaudière, *PLoS ONE*, 2009, **4,** 9.
182. E. Vahala, M. Ylihautala, G. Ehnholm, N. Etelä, I. Young, K. Golman and I. Leunbach, *J. Magn. Reson.*, 2002, **157,** 298.
183. R. P. Joensuu, R. E. Sepponen, A. E. Lamminen and C.-G. M. Standertskjöld-Nordenstam, *Magn. Reson. Med.*, 2000, **43,** 139.
184. R. P. J. Joensuu, R. E. Sepponen, A. E. Lamminen and C.-G. M. Standertskjöld-Nordenstam, *Acta Radiol.*, 1997, **38,** 43.
185. S. Matsumoto, K. Yamada, H. Hirata, K. Yasukawa, F. Hyodo, K. Ichikawa and H. Utsumi, *Magn. Reson. Med.*, 2007, **57,** 806.
186. S. Petryakov, A. Samouilov, M. Roytenberg, H. H. Li and J. L. Zweier, *Magn. Reson. Med.*, 2006, **56,** 654.
187. A. Modica, D. J. Lurie and M. Alecci, *Phys. Med. Biol.*, 2006, **51,** N39.
188. R. Murugesan, S. English, K. Reijnders, K.-i. Yamada, J. A. Cook, J. B. Mitchell, S. Subramanian and M. C. Krishna, *Magn. Reson. Med.*, 2002, **48,** 523.
189. Y. Deng, K. Shet, H. Li, P. Kuppusamy and J. L. Zweier, *Comput. Methods Programs Biomed.*, 2006, **82,** 67.
190. W. Youngdee, D. J. Lurie and M. A. Foster, *Phys. Med. Biol.*, 2002, **47,** 1091.
191. W. Barros, P. L. de Sousa and M. Engelsberg, *J. Magn. Reson.*, 2003, **165,** 175.
192. K. I. Yamada, Y. Kinoshita, T. Yamasaki, H. Sadasue, F. Mito, M. Nagai, S. Matsumoto, M. Aso, H. Suemune, K. Sakai and H. Utsumi, *Arch. Pharm.*, 2008, **341,** 548.
193. J. W. Barros and M. Engelsberg, *J. Magn. Reson.*, 2007, **184,** 101.
194. N. Nestle, K. Shet and D. J. Lurie, *Magn. Reson. Imaging*, 2005, **23,** 183.

CHAPTER 4

Solid-State NMR of Membrane Proteins: Moving Towards Greater Complexity

Lynmarie K. Thompson

Contents

Abstract

Membrane proteins represent an important and challenging frontier in structural biology: they mediate fundamental and medically important processes but are challenging targets for structure/function studies. Magic angle spinning solid-state NMR methods for structure determination of proteins have developed rapidly in

Department of Chemistry, University of Massachusetts Amherst, Massachusetts, USA

Annual Reports on NMR Spectroscopy, Volume 73
ISSN 0066-4103, DOI: 10.1016/B978-0-08-097074-5.00004-9

recent years and are now being employed to determine complete structures of small (<100 residue) membrane proteins. NMR studies of larger systems have measured selected distances to map active sites, test structural models and investigate mechanisms. What is possible between complete structure determination of small membrane proteins and single distance measurements within large membrane proteins and complexes? This review explores this middle ground, and presents several approaches for focusing NMR experiments on a region of interest in an extensively labelled protein in order to simultaneously measure many constraints. Creative application of emerging NMR methods promises to make solid-state NMR a versatile tool that can provide key structural and mechanistic insights on functional states of large membrane proteins and complexes.

Key Words: Solid-state NMR, Membrane proteins, Magic angle spinning.

1. INTRODUCTION

Membrane proteins mediate key life processes: cells employ membrane proteins to harness energy, sense the environment and import molecules. Understanding the mechanisms of these critical processes, as well as designing pharmaceuticals targeting membrane proteins to treat diseases, is limited by the challenging nature of membrane protein studies. Although membrane proteins are common (about 20–30% of all proteins), they are quite under-represented in the Protein Data Bank (about 1% of all known structures). There is recent excitement in the field[1,2] due to advances in expression, stabilization, crystallization and NMR methods that have fuelled an exponential growth in the numbers of structures being solved, principally by X-ray crystallography, and also by electron diffraction, solution NMR and solid-state NMR. As in the early years of structural biology of soluble proteins, some of the best understood thus far are likely to be the ''well-behaved'' cases: membrane proteins that are plentiful, stable, small or rigid, for example. Full understanding of the mechanisms of action of many membrane proteins is likely to require watching them function in multiple states, in complexes and in the lipid bilayer. Solid-state NMR, which has the potential to measure detailed structure in membrane proteins in their native environments, states and complexes, is poised to provide key insights into the mechanisms of membrane proteins and advance this critical frontier in biology.

Recent advances have made it possible to determine complete structures of a number of globular proteins and of small membrane proteins by

magic angle spinning solid-state NMR.[3] These studies have also yielded extensive spectral assignments for some medium size membrane proteins, in preparation for structure determination. Oriented sample NMR[4,5] has yielded structures for a number of small membrane proteins as well. It is exciting to see the growing list of membrane protein structures (http://www.drorlist.com/nmr/MPNMR.html) determined by solution NMR and by oriented sample and magic angle spinning solid-state NMR. The use of multiple methods makes it possible to examine protein structures in multiple environments: for example, the influenza M2 proton channel structure has been solved by X-ray crystallography and solution NMR in detergent micelles, and by magic angle spinning and oriented sample solid-state NMR in lipid bilayers, yielding different structures in all cases (see Ref. 6 and references therein).

The focus of this review is to explore the recent progress and promise of magic angle spinning solid-state NMR for membrane proteins and their complexes that are out of reach for complete structure determination (at least currently). Oriented sample solid-state NMR is a promising complementary approach as well, but is beyond the scope of this review. Selected distances measured on such systems via magic angle spinning experiments have provided important information: ligand–ligand or ligand–protein distances have mapped active sites; site-directed protein–protein distances elsewhere have tested structural models and investigated mechanisms. What is possible between complete structure determination of small proteins and single distance measurements within large proteins and complexes? Complete structure determination requires resolving and assigning all residues, which becomes challenging for large proteins (that have too many residues) and for functional states or complexes (that may not have narrow linewidths). One approach to make such cases experimentally tractable is an NMR experiment that is somehow limited to a subset of the protein resonances and yet can efficiently provide multiple structural constraints. This is valuable for the many membrane proteins for which there is incomplete structural information: structural constraints measured by solid-state NMR can connect domains or subunits of known structure into the structure of the active protein or complex, or determine how key regions in a state of known structure change during a catalytic cycle.

Figure 1 makes a visual comparison between the M2 channel, a small membrane protein whose structure has been solved by magic angle spinning solid-state NMR, and the bacterial chemotaxis receptor, a large membrane protein which functions in complexes with two binding partners (one of which is shown). Structural biology of the M2 channel has advanced rapidly in recent years, with structures being solved by multiple methods (crystallography,[8] solution NMR,[9] magic angle spinning[7] and oriented sample[10] solid-state NMR) and in different states modulated

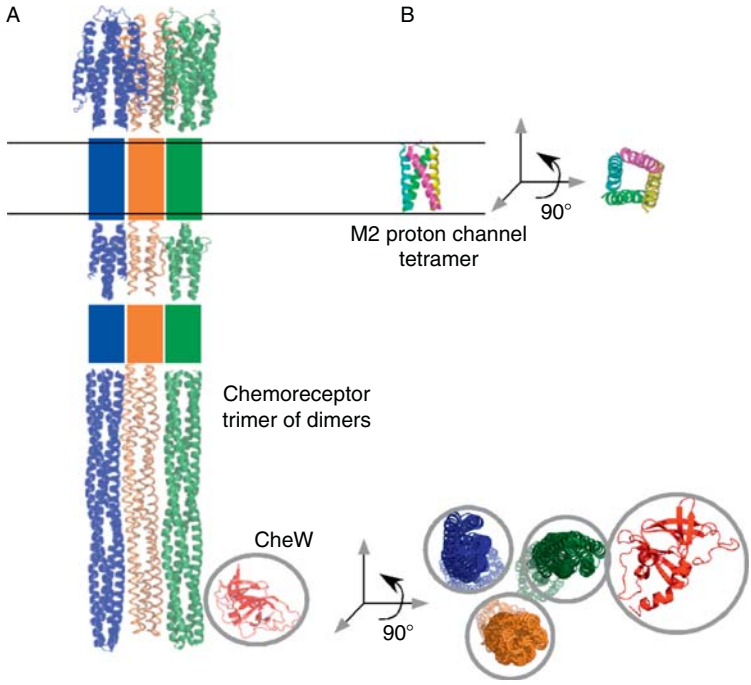

Figure 1 Scale comparison of a membrane protein target for complete structure determination with a target for focused structural analysis by solid-state NMR. Both are shown in lateral view (left) and end-on view from below (right). (A) Chemotaxis receptors function in hexagonal arrays that are thought to be organized as receptor trimers of dimers (as shown, 6 × 60 kDa) in complex with CheW (2ho9, 18 kDa) and CheA (not shown, 70 kDa). Boxes represent helical connectors missing from high-resolution structures of the other domains of the receptor (1vlt, 2asw, 1qu7); grey circles highlight some of the docking interactions (between receptor dimers and between the receptor and CheW) for which there is no high-resolution structural information. (B) The structure shown for the tetrameric M2 proton channel transmembrane domain (2kqt, 11 kDa total) was solved by solid-state NMR by Hong and co-workers.[7]

by pH and inhibitor binding. These structures can address both important fundamental questions such as the mechanism of pH gating of an ion channel[11–13] and critical medical questions such as the basis of resistance to antiviral drugs. The chemotaxis receptor is representative of the many larger membrane proteins and their complexes that are beyond the current reach of complete structure determination methodology. This system is of interest for probing the fundamental mechanism of transmembrane signalling and for gaining insights into other membrane receptors that are the targets of the majority of current drugs. This review discusses how magic angle spinning solid-state NMR methods in use and under

development for complete structure determination of proteins such as the M2 channel can be applied to measure local structure and probe mechanisms of larger membrane proteins and complexes. Section 2 describes promising approaches for focused structural analysis of such systems by solid-state NMR, and Section 3 describes recent applications of magic angle spinning solid-state NMR to provide insights into mechanisms of membrane proteins and their complexes.

2. STRATEGIES FOR OVERCOMING COMPLEXITY AND FOCUSING ON SITES OF INTEREST

The goal is to generalize emerging solid-state NMR tools to make it possible to expand applications from proteins with small numbers of resonances to large intact systems and complexes, and from sample conditions optimized to observe the narrowest linewidths to conditions optimized to observe particular functional states. This is being achieved through a combination of labelling schemes and NMR experiments that enable selection of a subset of resonances. These both become especially powerful when they also direct the experiment to sites of interest within the protein, and when they are combined with biochemical approaches to prepare functional states and with novel NMR techniques that enhance sensitivity or extend distance measurement limits. An ideal strategy would be to combine emerging methods for complete structure determination with methods for directing these to a subset of the protein or complex, particularly in regions of structural and mechanistic interest. The following sections describe strategies for simplifying NMR spectra, for focusing on sites and properties of interest, and for investigating functional states and complexes. Such strategies make it possible to cope with cases that are not ideal for NMR, to observe and characterize membrane proteins at work.

2.1. Simplifying NMR spectra

Efficient determination of multiple structural constraints requires extensive isotopic labelling and simultaneous measurement of multiple distances. It is known that uniform ^{13}C labelling can be problematic for solid-state NMR, even of small proteins, because dipolar truncation makes it difficult to measure weak dipolar couplings (the long distances most valuable to structure determination) in the presence of strong dipolar couplings (the short distances between directly bonded nuclei). This can be reduced (but not eliminated)[14] by metabolic labelling schemes that reduce ^{13}C pairs, such as the complementary alternating carbon labelling achieved by LeMaster and Kushlan through growth on 1,3-$^{13}C_2$-glycerol

or 2-^{13}C-glycerol.[15] Such a labelling scheme was used to aid in obtaining assignments and distance restraints to determine the global fold of a microcrystalline SH3 domain,[16] and general assignment strategies have been developed for proteins labelled with these schemes.[17] Furthermore, new extensive labelling patterns can be achieved by taking advantage of other metabolic pathways. For example, backbone carbonyl labelling of half the amino acids was achieved via glucose metabolism by the Entner–Doudoroff pathway in *Pseudomonas aeruginosa*, and it should be possible to obtain this labelling pattern in *Escherichia coli* grown on gluconate.[18]

Reverse-labelling strategies can further reduce spectral congestion by including strategically chosen unlabelled amino acids. For example, Hong and Jakes simplified the spectrum of a membrane protein by labelling with 2-^{13}C-glycerol and including 10 unlabelled amino acids (hydrophilic amino acids of the citric acid cycle); the resulting spectra contained resonances from only selected carbons of the other 10 predominantly hydrophobic amino acids.[19] The best amino acids for the reverse labelling depend on the composition of the protein and the goal of the experiment: a few dominant amino acids can be chosen to dramatically reduce the number of resonances in the spectrum. For example, reverse labelling of four amino acids corresponding to 34% of the sequence of sensory rhodopsin (SR) dramatically simplified the spectrum to enable extensive assignments of residues of an otherwise uniformly ^{13}C-labelled membrane protein sample (see Section 3 below).[20]

Another means of simplifying the spectrum is to isotopically label one subunit of a complex or one domain of a protein. Labelling one domain of a protein can be achieved by using segmental labelling protocols or by reassembling split protein constructs. Methods for segmental labelling of proteins for solution NMR applications have been recently reviewed[21]; application of such approaches for production of solid-state NMR samples would greatly simplify spectra of large proteins. A biochemically simpler approach has been introduced by Polenova and co-workers who separately expressed two differently labelled fragments of thioredoxin and then reassembled the protein for solid-state NMR analysis.[22] This should be applicable to membrane proteins that can be expressed as two fragments and reassembled into a functional complex, which include bacteriorhodopsin, lac permease and several G protein-coupled receptors (GPCRs).[23] Differential labelling of two subunits of a complex is straightforward, and such samples can be used to interrogate the subunit interface. An extensive labelling approach with ^{13}C labelling of one subunit and ^{15}N labelling of the other is described in Section 2.4. More limited subunit labelling schemes include differential ^{13}C labelling of methyl groups, for example, Leu/Val on one subunit and Ile on the other, as has been suggested for mapping homodimer interface contacts in solution NMR.[24] If combined with an efficient strategy for making assignments,

the ≈10 ppm chemical shift difference between these would make it possible to use such labelling schemes for solid-state NMR studies of protein interfaces as well. A number of reviews of labelling schemes useful for NMR are found in a recent collection.[25]

Cell-free expression provides another important approach for preparing a variety of desired isotopic labelling patterns, which has been widely applied to soluble proteins. In addition to avoiding problems with cell toxicity and label scrambling, cell-free expression makes it possible to achieve certain selective labelling patterns that are otherwise metabolically impossible or prohibitively expensive. In recent years, cell-free expression of membrane proteins has also been successful. Membrane proteins are either produced as insoluble precipitates or incorporated directly into added detergents or liposomes. Yields sufficient for structural studies have been achieved for membrane proteins expressed as precipitates or expressed into detergent micelles,[26] and a recent study combined cell-free expression with paramagnetic distance restraints for rapid solution NMR determination of backbone structures of three membrane proteins.[27] Solid-state NMR should also benefit from this labelling methodology,[28] and thus far, it has been used for the MscL channel[29] and EmrE transporter.[30]

Sometimes residue-specific labelling is the key to addressing a question of interest, as in the case of the multidrug resistance transporter EmrE, to investigate the role of the conserved Glu14 in the transport mechanism. Two groups took different approaches to the fact that residue-specific labelling of Glu is not possible due to scrambling. Glaubitz and co-workers used cell-free expression to incorporate uniform ^{13}C-Glu, and demonstrated there was no detectable scrambling to other residues. They also removed the only other Glu residue in this small protein by mutagenesis, and performed transport assays on proteoliposomes reconstituted with the E25A mutant to demonstrate that it retained function. NMR and parallel control studies of the ^{13}C-Glu E25A EmrE samples demonstrated convincingly that Glu14 in EmrE homodimers is asymmetric and interacts with substrate.[30] Reif and co-workers instead employed a REDOR filter on a uniform ^{13}C,^{15}N EmrE sample to selectively detect the Asp and Glu carboxyl side chain carbons (carbonyl carbons with no directly bonded nitrogen).[31] This approach was first used by Jaroniec et al. to measure distances between the protonated Schiff base and two Asp residues in the retinal-binding pocket of bacteriorhodopsin.[32]

In summary, depending on the protein and question of interest, one can choose from a variety of labelling schemes and strategies to reduce the number of NMR resonances and obtain interpretable spectra for even large membrane proteins and complexes. The remainder of Section 2 describes how such labelling can be combined with various NMR methods to focus on sites of interest, with the ultimate goal of addressing key aspects of the structure and mechanism of the system.

2.2. Focusing on sites of interest: Ligands and cofactors

Early solid-state NMR experiments on membrane proteins focused on the active site by introducing isotopic labels in a ligand or cofactor. Chemical shifts and later distances involving ^{13}C and/or ^{15}N retinal in bacteriorhodopsin were used in pioneering experiments by Griffin and co-workers to deduce the conformations of the retinal chromophore in various states of the photocycle.[33–46] More recent studies have exploited the unique retinal chemical shifts to focus the NMR experiment in a uniform ^{13}C,^{15}N-bacteriorhodopsin sample. Building on extensive previous work that has assigned these chromophore resonances, Bajaj et al. transferred polarization from the retinal Schiff base nitrogen selectively to either the retinal chain or the covalently attached Lys chain in a cryotrapped state, and based on the observed chemical shifts determined the mixture of photocycle intermediates present.[47] Such experiments provide important information for deducing the connectivity between intermediates in the photocycle mechanism in bacteriorhodopsin. This approach for focusing the experiment on the ligand site within a uniformly labelled sample is applicable to ligands that contain a unique chemical shift. The sensitivity limitations of such an experiment, limited by both the mixture of states present and the sequential polarization transfers, were overcome by using dynamic nuclear polarization (DNP) at 90 K, with an amazing 90-fold total signal enhancement. The DNP methodology opens the door to experiments in which sensitivity is limited either by the complexity of the NMR experiment, or by small sample amounts, or both, as in this application.

Magic angle spinning solid-state NMR has been used to investigate ligands of membrane receptors, channels and transporters. For efficient determination of the structure of a ligand bound to its membrane protein target, it is desirable to perform NMR measurements on a single sample containing uniformly labelled ligand. Watts and co-workers employed such an approach to determine the structure of acetylcholine bound to the nicotinic acetylcholine receptor. Multiple rotational resonance experiments were performed to measure the ^{13}C to ^{13}C distances in uniform ^{13}C-acetylcholine bound to the receptor.[48] Studies of larger ligands of this receptor employed two-dimensional (2D) spectra to resolve the resonances: Krabben et al. assigned many of the resonances of the 61-residue neurotoxin II bound to the nicotinic acetylcholine receptor using neurotoxin ligands labelled via incorporation of uniform ^{15}N and uniform ^{13}C-glycerol, 1,3-^{13}C-glycerol or 2-^{13}C-glycerol. Large (>0.5 ppm) chemical shift changes between the solution and bound states of this ligand were used to deduce the interaction surface between neurotoxin and the receptor.[49] The conformation of the 52-residue phospholamban bound to the Ca^{2+}-ATPase that it regulates has been investigated by magic angle

spinning solid-state NMR on both specific and extensively labelled phospholamban. Pairwise rotational resonance and REDOR distance measurements revealed a conformational change upon binding to the ATPase.[50] Further studies of uniform ^{13}C,^{15}N-phospholamban along with reverse-labelled and selectively labelled samples yielded chemical shift-based deductions of the secondary structure when bound to the ATPase.[51]

Ligand-focused solid-state NMR experiments have also begun to contribute insights into the study of GPCRs, a large class of proteins of significant pharmaceutical importance. Studies of uniformly or extensively labelled peptide ligands bound to their target GPCRs have employed double-quantum filtering or 2D spectra to suppress the huge natural abundance signals of the receptor and detect chemical shifts that reveal the backbone structures of the hexapeptide fragment of the 13-residue neurotensin bound to its receptor in proteoliposomes[52] and the nine-residue peptide hormone bradykinin bound to its receptor in detergent solution.[53] Chemical shifts of various $^{13}C_2$-labelled retinals incorporated into rhodopsin phototrapped in the bathorhodopsin state have yielded insights into how energy is stored in this first intermediate of the photocycle.[54] Similar approaches have been used to show that histamine binds to its GPCR in two different protonation states.[55] In summary, structural models for ligands bound to large membrane proteins have been deduced through a few pairwise distances and/or a more extensive set of chemical shifts, and the latter can also reveal the interaction surface between the ligand and the membrane protein.

Studies of transporters have addressed the challenge of detection of weakly bound ligands in the presence of excess unbound ligand. The strategy is to perform cross-polarization experiments on unfrozen proteoliposome samples: cross-polarization enhances the resonances of the immobilized bound ligand relative to the mobile unbound ligand, because the mobility of the latter reduces the cross-polarization efficiency. This technique has been applied to a number of transporters (see Ref. 56 and references therein) in both native membranes and reconstituted proteoliposomes. A recent study by Middleton and co-workers measured ligand to protein distances between glucose substrate and Trp residues of the sugar transporter GalP. The weak binding of this ligand made it necessary to find an optimum lower temperature with reduced dynamics of the bound ligand without immobilizing the free ligand. Ligand to Trp contacts in the binding pocket were then measured using dipolar-assisted rotational resonance (DARR). Control experiments with the inhibitor forskolin were used to demonstrate that glucose resonances and glucose–Trp crosspeaks were due to glucose bound to GalP, and not due to the protein impurities or the unbound glucose also present.[57]

2.3. Focusing on sites of interest: Generalizing to elsewhere in the protein

One means of directing the NMR experiment within a large biosynthetically produced membrane protein is to take advantage of unique dipeptides within the native protein sequence. If there is only one instance in the protein sequence of the dipeptide sequence XY, then incorporation of 1-^{13}C-X and ^{15}N-Y will create a single ^{13}C–^{15}N peptide bond at XY within the protein, which can be detected in a ^{13}C{^{15}N} REDOR ΔS spectrum of the protein. The ΔS spectrum consists of both the dipeptide XY and a natural abundance contribution which can become large when X or Y occurs frequently in the sequence: intensity = 1 XY + 0.011(n_Y) + 0.0036 (n_X), where n_X and n_Y are the number of occurrences of X and Y, respectively. This strategy has been used to deduce secondary structure at a few positions in a domain of the influenza hemagglutinin protein in cells, inclusion bodies and membranes.[58] A similar approach used ^{13}C/^{15}N double cross-polarization of a ^{13}C-Val/^{15}N-Ile proteorhodopsin sample to identify one of the 21 Val that occurs in the only Val-Ile dipeptide in the protein.[59] Resonances of unique YP and PT dipeptides were assigned in 2D spectra of a U-^{13}C,^{15}N-Y,P,T-labelled ABC transporter.[60] However, this approach depends on the fortuitous occurrence of unique dipeptides at locations of interest and becomes impractical for large proteins due to the diminished number of unique dipeptides and the large natural abundance contribution.

Our laboratory has developed a general approach for targeting single NMR distance measurements to any site of interest in a protein and has applied this approach to measure helix–helix distances testing proposed structures and conformational changes in bacterial chemoreceptors.[61–63] The strategy is applicable in cases where a good structural model is available to guide the design of the experiment. The model is used to choose a pair of nuclei for distance measurement that satisfies the following criteria: (1) it addresses the question of interest, (2) it is measurable by NMR (e.g. $\leq$5 Å for ^{13}C{^{15}N} REDOR, $\leq$6 Å for ^{13}C^{13}C rotational resonance and $\leq$10 Å for ^{13}C{^{19}F} REDOR) and (3) it involves one rare residue (x) and one mutatable residue (y). A unique amino acid is introduced at site y via site-directed mutagenesis and the activity of the mutant protein is measured to determine whether it tolerates the substitution. Cysteine is a convenient choice for the unique amino acid: because of its low frequency of occurrence in native sequences and its utility for protein labelling via thiol substitution, Cys-less constructs and biochemically characterized single-Cys mutants are available for many proteins. The active single-Cys mutant is labelled biosynthetically by using an expression medium containing 18 unlabelled amino acids as well as appropriately labelled versions of Cys and of amino acid x; after purification, the

protein will contain an isolated spin pair for the NMR distance measurement. This is a powerful approach for selected distance measurements within large membrane proteins and their complexes, because it is applicable to systems that are not crystallizable and it measures distances with a precision that is not possible with EPR or FRET.

Experiments that detect resonances within a region of interest to simultaneously measure multiple chemical shifts or distances would provide a more efficient means to measure local structure. The remainder of Sections 2.3–2.5 describe several promising approaches; three of these are shown schematically in Figure 2.

Rienstra and co-workers have developed such an experiment that combines REDOR with 2D ^{15}N–^{13}C correlation spectra to measure multiple distances and correlations in a single sample.[64] The FRESH experiment (^{19}F REdor SHift) was demonstrated on the model protein GB1, with

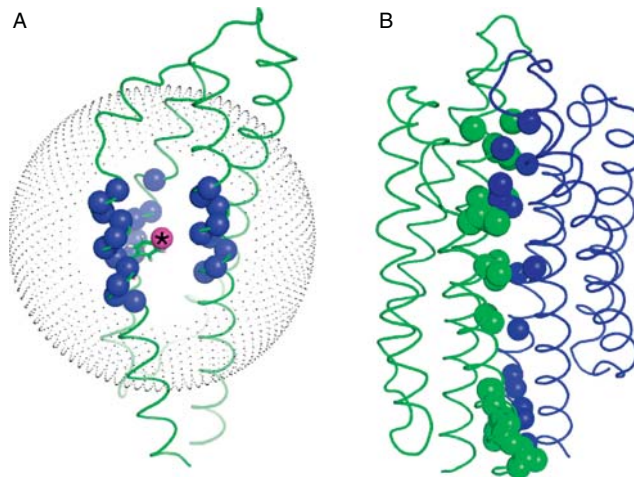

Figure 2 Illustration of schemes for selective detection of regions of proteins. (A) One 16 kDa monomer unit of a dimeric protein is shown (the periplasmic domain of a model for the *E. coli* Ser receptor). The FRESH method[64] detects nitrogens (spacefill) within 9 Å of a fluorine nucleus (*) incorporated as p-F-Phe. If the * was the site of an unpaired electron (a unique Cys labelled with either a nitroxide spin label or an EDTA-chelated copper), it would alter linewidths of resonances within the 20 Å radius sphere shown.[65,66] FRESH would select 19 resonances within the monomer as shown; the paramagnetic effect sphere contains 137 nitrogens and extends into the other subunit (not shown) of the dimer. (B) The same protein is shown as a dimer to illustrate selective detection of protein–protein interface residues: 34 carbons (light grey/green) on the left subunit within 5 Å of 16 nitrogens (dark grey/blue) on the right subunit would be detected.

^{19}F labelling of its single Trp and uniform ^{13}C,^{15}N labelling. The experiment begins with proton to nitrogen cross-polarization, followed by ^{19}F REDOR dephasing pulses and ^{15}N chemical shift evolution during t_1, SPECIFIC CP transfer to Cα (or CO) and ^{13}C chemical shift evolution during t_2. Subtraction of the 2D ^{15}N–^{13}C correlation spectra for different REDOR dephasing times ($S_t - S_0$) yields 2D ΔS spectra containing signals of only the ^{13}C that are correlated with ^{15}N close to the fluorine; analysis of signal intensity versus dephasing time yields ^{19}F to ^{15}N distances within ±20% of the crystal structure distances for multiple sites in GB1 up to 9 Å away (and much more precise for two short (<5 Å) distances). This experiment provides a new approach for obtaining long-distance constraints for protein structure determination.[64]

The FRESH experiment provides a promising means for measuring multiple distances around a site of interest in a large protein. The ΔS spectrum is limited to nitrogens within 9 Å of the fluorine, making it possible to resolve and identify resonances near the site of interest in a 2D spectrum of a uniformly ^{13}C,^{15}N-labelled protein, as long as sufficient ^{13}C correlations are available to assign these resonances. This focus should make it possible to overcome spectral crowding in highly labelled samples of functional states of large membrane proteins. The fluorine can be introduced biosynthetically, typically on aromatic amino acids, or chemically, via incorporation of a trifluoromethyl group on a unique cysteine. Most proteins will have multiple copies of each aromatic amino acid, so special strategies for labelling a specific site may be required; such a strategy is available for labelling a single Phe with p-F-Phe.[67] Furthermore, mutagenesis can be used to introduce an aromatic amino acid at a desired site, or to remove additional copies at other sites, subject of course to testing the mutants with a functional assay. As illustrated in Figure 2A, the FRESH experiment can then target any region in which an (ideally unique) aromatic amino acid or Cys is present or can be introduced within a large protein.

The Jaroniec lab has developed an exciting approach using paramagnetic ions to measure multiple longer distance restraints. Paramagnetic relaxation enhancement (PRE) measurements have become a useful source of long distances for solution NMR structure determination,[68–70] but are not yet widely used in solid-state NMR experiments. Jaroniec and co-workers initially used site-directed spin labelling with nitroxides at unique Cys residues to show altered crosspeak intensities for sites within 20 Å of the nitroxide in solid-state 2D ^{15}N–^{13}Cα spectra of GB1.[65] More recently they have instead incorporated an EDTA–metal complex at the unique Cys and compared the effects of metals with different electron relaxation properties to show that EDTA–Cu^{2+} specifically enhances longitudinal relaxation rates and provides distance restraints for ^{15}N nuclei up to 20 Å away.[66] Nitrogen is chosen for this experiment because

its weak dipolar couplings reduce spin diffusion that is expected to rapidly equalize proton or carbon relaxation rates across the sample. Reif and co-workers have shown that with perdeuteration of the protein sample spin diffusion is no longer a problem, and soluble Cu–EDTA enhancement of amide proton longitudinal relaxation rates can be used as a measure of surface accessibility.[71]

In addition to significantly extending the range of measurable distances, these paramagnetic effects should make it possible to obtain spectra focused on a region of interest within a large protein. The paramagnetic enhancement of the ^{15}N longitudinal relaxation rate could be exploited to obtain difference spectra containing only fast-relaxing resonances, for example, within 20 Å of the Cys-EDTA-Cu^{2+}, as a means of simplifying a complex spectrum. Distances from the paramagnet to this subset of resonances would measure local structure in the region of interest, providing a powerful tool applicable to large proteins (see Figure 2A). Alternatively, for perdeuterated protein samples with soluble Cu–EDTA, short recycle delays could be used to obtain spectra containing only the fast-relaxing surface-proximal amides.

Several other recent studies have demonstrated important additional uses for paramagnetic effects in solid-state NMR that will likely also benefit studies of large membrane proteins and their complexes. Bertini et al. used paramagnetic pseudocontact shifts to aid in solving the structure of a cobalt-substituted 17.6 kDa matrix metalloprotease, the largest protein structure solved to date by solid-state NMR.[72] This is a significant step forward: the next largest monomer unit structures solved by solid-state NMR are in the 9–9.5 kDa range (ubiquitin and Crh). Solid-state NMR will also be advantageous for the study of paramagnetic proteins that have been challenging for solution NMR, because paramagnetic broadening is smaller for the ^{13}C and ^{15}N typically detected in solid-state experiments than for the ^{1}H detected in solution NMR experiments. This was demonstrated in a study of oxidized superoxide dismutase that achieved extensive assignments of solid-state NMR spectra of this 32 kDa homodimeric protein.[73]

Another exciting development is the use of PRE to decrease NMR experiment times. Sensitivity has been a barrier for applications to large membrane proteins and complexes, because total amounts of the protein of interest are limited by both the size of the protein and the need to include the lipid bilayer and/or protein partners within the NMR sample. The experiment time is dominated ($\geq$95%) by long recycle delays between scans ($\geq$1 s), which are needed to allow for ^{1}H relaxation and to avoid sample heating and/or probe damage by the high-power radio-frequency pulses. Ishii and co-workers demonstrated a method to decrease experiment times by 5- to 20-fold: doping samples with Cu(II)–EDTA was used to shorten the proton $T_1 \approx$ fivefold without perturbing

chemical shifts or linewidths, and very fast magic angle spinning (40 kHz) was used to average the NMR interactions such that high-resolution spectra could be achieved with low-power pulses.[74] Reif and co-workers demonstrated an alternate approach for achieving similar sensitivity enhancements with Cu(II)–EDTA doping: highly deuterated samples back exchanged into 10% H_2O have narrow linewidths with only low-power (2 kHz) proton decoupling and 24 kHz magic angle spinning.[75] An alternative means of incorporating copper in a membrane protein sample is the use of a copper-chelated lipid.[76] Finally, such schemes for faster data acquisition can be applied to proteins site specifically tagged with EDTA–Cu(II) for rapid measurement of long paramagnetic distance restraints.[77] Sensitivity enhancement via paramagnetic relaxation or DNP is likely to be a key element of strategies for expanding applications of solid-state NMR to large membrane proteins and their complexes.

2.4. Focusing on sites of interest: Protein–protein interfaces

Tools for defining the structure of protein–protein interfaces will be quite valuable for many systems in which the structures of the protein partners are known but it is not known how they are assembled into the active complex, or how that complex changes to carry out its function.

Differential labelling of protein-binding partners has been used by several groups to identify contacts at protein interfaces. Baldus, Böckmann and co-workers investigated the Crh dimer interface in a ^{13}C:^{15}N sample (U-^{13}C-Crh plus U-^{15}N-Crh) using NHHC polarization transfer.[78] The resulting 2D spectra contain crosspeaks for a significant fraction of the interface residues with H to H distances of up to 4.5 Å. This approach is especially suitable when resonance assignments are available for at least one protein partner. Polenova and co-workers developed a suite of experiments for a ^{13}C:^{15}N,^{13}C labelling scheme, with the advantage that both detection of interface contacts and the assignment and structural analysis of the ^{15}N,^{13}C-labelled protein partner can be performed within the same sample.[79] This approach was demonstrated on reassembled split thioredoxin (U-^{13}C,^{15}N-fragment 1–73 plus U-^{15}N-fragment 74–108). Interface detection is performed with a REDOR–PAINCP experiment: after proton to nitrogen cross-polarization, ^{13}C REDOR dephasing pulses are used to remove magnetization from nitrogen that is directly bonded to ^{13}C in the ^{13}C,^{15}N-labelled protein in the sample. This is followed by nitrogen chemical shift evolution during t_1 and PAINCP transfer across the protein interface to carbon for detection of ^{13}C close to ^{15}N at the protein–protein interface.

As illustrated in Figure 2B, these interface detection schemes provide a means of obtaining simplified spectra containing only resonances of interface residues within a large membrane protein complex, to obtain

constraints for assembling the structure of the complex. Sensitivity is a serious limitation however: the NHHC transfer efficiency is 5–10% of a direct CP signal[78]; the efficiency is increased with PAINCP (particularly for long range transfer), but the REDOR dephasing time results in a 15–20% signal loss.[79] Furthermore, the crosspeak intensities cannot be interpreted as quantitative distances. Despite these limitations, NHHC polarization transfer on a ^{13}C:^{15}N sample was used to identify intermolecular contacts as part of the solid-state NMR structure determination of amyloid fibrils of the HET-s prion protein core domain.[80]

2.5. Focusing on properties of interest

Another means of reducing congestion in spectra of extensively labelled large membrane proteins is to employ NMR experiments that selectively detect a subset of resonances from nuclei with a shared property such as mobility or exchange with water protons. These properties in turn can provide insights into structure and dynamics of the protein.

One approach is to obtain complementary NMR 2D spectra containing resonances from the mobile versus the rigid portions of the protein. As demonstrated in a study of phospholamban,[81] the mobile cytoplasmic N-terminal domain can be detected using polarization transfer schemes that are mediated by through-bond J couplings (e.g. TOBSY-based methods for homonuclear transfers[82] and INEPT-based methods for heteronuclear transfers) and the rigid transmembrane domain can be detected using polarization transfer mediated by through-space dipolar couplings. In addition to the spectral simplification achieved by these experiments, it may be of interest to focus on the mobile portions of the protein for various structure/function studies.

Water-edited spectra provide additional information and another means of spectral simplification: only nuclei within a short distance of mobile water are detected. This experiment relies on an initial relaxation-based selection of mobile water proton magnetization (its longer T_2 survives a relaxation filter), followed by a longitudinal spin diffusion time before cross-polarization to the heteronucleus for observation. A related early experiment (with no spin diffusion time) demonstrated that the protonated Schiff base in bacteriorhodopsin is in fast exchange with water protons, providing insight into the pathway for proton pumping by this protein.[83] Spectra obtained with various spin diffusion times have been used to measure depths of groups within the membrane in colicin E1[84] and gramicidin.[85] A related experiment used spin diffusion from the mobile lipid methyl tail rather than from surface water to measure topology of colicin Ia in the membrane.[86] Recent applications have employed a short spin diffusion time prior to 2D correlation experiments to identify water-exposed groups in membrane proteins, helping to position the SR

structure within the bilayer[20] and monitoring the pH-induced opening of the KcsA potassium channel.[87] Implementation of these techniques will benefit from recognition of the different NMR properties of distinct water pools in the sample, to better optimize the relaxation filter for selection of the pool that exchanges polarization with the protein on the timescale of the NMR experiment.[88]

Finally, NMR spectra of the lipid can provide insights into the overall hydration of a membrane protein without tackling the complexities of the protein spectrum. In a study of rhodopsin by Gawrisch and co-workers, molecular dynamics simulations suggested a significant increase in internal hydration of rhodopsin in the meta I-intermediate; this was verified by proton NMR experiments demonstrating increased water to protein to lipid magnetization transfer specifically for native membranes containing the meta I state of rhodopsin.[89]

2.6. Investigating functional states and complexes

The use of techniques that focus on a subset of resonances make it possible to do productive NMR experiments on systems that do not have the narrowest possible linewidths, and thus to investigate more challenging proteins or to optimize sample conditions for a particular functional state rather than for the narrowest resonances. However, since the information content of the NMR experiment depends on the number of resolvable resonances, which depends on their linewidths, it is critical to seek conditions that minimize the linewidths while preserving functionality. The membrane protein system of interest will dictate which sample types are possible and which conditions preserve functionality: Table 1 documents membrane protein linewidths that have been observed in a variety of sample types including nanocrystals, 2D crystals, detergent micelles, proteoliposomes and nanodisks.

The choice of sample temperature is complex. In some systems, there is an increase in signal intensity at lower temperatures, due to better cross-polarization upon rigidification of the protein (and sometimes also to improved probe tuning and favourable Boltzmann factor). However, narrower resonances are also often observed in unfrozen samples, most likely because this avoids freeze-trapping multiple states and allows motional averaging. Finally, the temperature of the cooling gas is typically reported (but this is not always clear). The actual sample temperature is often significantly higher due to warming effects of frictional heating by the spinning, radiofrequency pulsing and room temperature spinning gases. Because the degree of heating depends on multiple factors, including the gas flow rates, spinning speed and sample composition, a single calibration is not sufficient to know the sample temperature in all experiments.

TABLE 1 Linewidths of various membrane proteins under study by solid-state NMR

Membrane protein	Sample type	Linewidth[a]	Temperature[b]	Notes
MSP1 (200 residue lipid-binding domain of human apolipoprotein A1)[90]	PEG precipitate of nanodiscs	0.3–0.5 ppm	263 K gas ≈ 283 K sample	Signals broaden at lower temperatures
CYP3A4 (cytochrome P450)[91]	PEG precipitate of nanodiscs	0.5–0.7 ppm	248 K gas temperature	Broader lines at 233 K
Cytochrome bo_3 oxidase[92]	Proteoliposome pellets	0.2–0.5 ppm	223 K gas temperature (lower signal intensity at higher temperatures)	No reconstitution: protein retained native lipids through dialysis
Sensory rhodopsin (SRII[20] and SRII/HtrII[93])	Proteoliposome pellets	0.7 ppm	228–278 K	Reconstituted with native lipids
DAGK (diacyl glycerol kinase)[94]	Nanocrystals	0.3 ppm ^{15}N (deconvolution of Leu spectrum[c])	268 K	Protein retained native lipids
DAGK (diacyl glycerol kinase)[94]	Proteoliposome pellets	0.5 ppm ^{15}N (deconvolution of Leu spectrum[c])	248 K	Protein:lipid = 1:100 shown to retain maximal activity
OmpG (outer membrane protein G)[95]	2D crystals	0.5–0.8 ppm	262–280 K (broader when frozen, 240 K)	Broader in proteoliposomes
DsbB (disulfide bond forming enzyme)[96]	Detergent solubilized, then dialyzed and pelleted	0.5 ppm	223–273 K (cooling gas temperature)	Linewidths decreased with increasing temperature to 263 K
Proteorhodopsin[97]	2D crystals	0.5–0.8 ppm ^{13}C and ^{15}N	280 K	Good CP unfrozen (unlike reconstituted sample); sample washing important

(*continued*)

TABLE 1 (*continued*)

Membrane protein	Sample type	Linewidth[a]	Temperature[b]	Notes
Proteorhodopsin[98,99]	DMPC/DMPA proteoliposome pellets	0.5–0.6 ppm ^{13}C; 0.7 ppm ^{15}N	278 K	Linewidths increase below 273 K
KcsA potassium channel[100]	PEG precipitate of detergent micelles	0.4 ppm	250 K gas ≈ 270 K sample	
KcsA potassium channel[101]	DOPE/DOPS proteoliposome pellets	0.3–0.5 ppm	240 K gas ≈ 280 K sample	Hydration (excess water) essential to observation of one state
KcsA-Kv1.3 chimeric potassium channel[102]	Proteoliposome pellets	0.7 ppm ^{13}C; 1.5 ppm ^{15}N	253–285 K	
ArtMP[60]	2D crystals	0.9 ppm K	285 K	Screened by transmission electron microscopy

[a] ^{13}C linewidth unless specified. Linewidth is typically reported for one or more resolved peaks, so it does not necessarily reflect the linewidths throughout the protein.
[b] Although not always stated, reported temperatures are typically the cooling gas temperature. The sample temperature is likely to be significantly higher (e.g. 15–25 K higher)[90] due to sample heating by magic angle spinning and radiofrequency pulsing.
[c] ^{15}N-Leu labelling has been suggested as an economical approach for initial assessment of linewidths, since it is about 25-fold less expensive than uniform or extensive labelling.[94]

A key contribution of solid-state NMR is the ability to make detailed structural measurements of membrane proteins in their native environment, the lipid bilayer. This can make it possible to do correlated structure/function studies on membrane proteins under the same sample conditions, for example, to examine the structural differences between functional states of a protein. A number of bilayer-like environments have been introduced that confer different advantages appropriate for particular membrane proteins or experiments. Three such media are discussed below as potential alternatives to reconstituting membrane proteins in proteoliposomes: bicelles, nanodiscs and templating vesicles.

Bicelles (reviewed in Refs. [5,103]) are bilayers composed of long-chain lipids with edges stabilized by short-chain lipids or detergents. Bicelles have a complex morphology that is often pictured as bilayer discs but is more likely to be a ''swiss cheese'' bilayer with the short lipid or detergent lining the holes. Due to their tendency to spontaneously orient in magnetic fields, bicelles have been used extensively for both solution NMR and oriented sample solid-state NMR applications. Bicelles also provide a favourable medium for magic angle spinning experiments: ^{1}H and ^{15}N linewidths of lipid, peptide and protein resonances can be narrower for bicelles than for liposomes[104] or multilamellar vesicle samples.[105] Bicelles provide a bilayer environment for a membrane protein that is more likely than detergent micelles to preserve function and stability of the protein. Bicelles, unlike liposome preparations, also provide full access to both sides of the membrane, which is often important for assays of membrane protein activity. Although bicelles may not support activity for all membrane proteins, they have been used for successful reconstitution or stabilization of GPCRs.[106,107] An additional challenge is that bicelle formation requires a narrow window of lipid composition and temperature; however, Park and Opella have recently demonstrated that bicelles formed with the detergent Triton X-100 are more robust to changes in temperature.[108]

Nanodiscs[109] are $\approx$10 nm diameter lipid bilayer discs that can form when the hydrophobic membrane edges are stabilized by the amphipathic membrane scaffold protein (which is related to the primary component of high-density lipoproteins). Like bicelles, nanodiscs provide a bilayer environment and access to both sides of the membrane, but appear to have better defined morphology and to be compatible with a range of lipid compositions. Several membrane proteins have been shown to be functional upon reconstitution into nanodiscs, and NMR studies of the membrane scaffold protein[90] and cytochrome P450[91] (solid-state NMR) as well as the VDAC-1 channel[110] (solution NMR) suggest that nanodisc samples have favourable NMR properties, including narrow linewidths.

Templating vesicles provide a means of facilitating the assembly of membrane-associated functional complexes.[111] The kinase and methylation

activities of bacterial chemoreceptors appear to require the organization of the membrane, since they are lost when the intact receptor is solubilized in detergent or when the cytoplasmic domain is expressed as a soluble fragment. Weis and co-workers developed templating vesicles for assembling the cytoplasmic fragment with its partners into active signalling arrays, restoring both kinase and methylation activity.[111] This method employs vesicles with nickel-chelating head groups that bind the His-tagged cytoplasmic fragment. Advantages of this method, which should be generally applicable to the water-exposed domains of other membrane proteins, include the ability to restore activity to a smaller fragment of the membrane protein and the ease of working primarily with soluble proteins that are then assembled into active membrane-bound complexes.

NMR studies of functional complexes require optimizing conditions to obtain ≈100% complex and to retain functionality in the face of the freezing and RF heating of the NMR experiment. Assembly of maximal chemoreceptor signalling complexes was achieved by titrating the proteins to maximize kinase activity. The complex prepared with the original template assembly conditions did not retain activity after the NMR experiment, most likely because of the presence of a low freezing point ''cryoprotectant'' that prevented complete freezing of the sample, leading to increased heating.[63] A number of recent studies have addressed the heating issue, especially through the design of single-coil or crossed-coil probes with demonstrated reduced sample heating.[112–121] An alternative is to address the issue through the sample conditions, particularly if conditions can be found that both prevent heat damage and retain protein activity. It was found that addition of PEG8000 protected the chemoreceptor protein complex against freezing damage and heating damage: the sample retained 100% activity after the NMR experiment. Fortuitously, the PEG sample conditions were also found to promote assembly of a functional complex with no requirement for the templating vesicle. This study[63] illustrates the importance of integrating functional analysis with NMR experiments in order to assemble and preserve a functional complex for NMR measurements of structural constraints.

Sample conditions that maintain membrane protein stability over the course of the experiments are critical to a successful investigation of a functional and homogeneous membrane protein. It is interesting to note that gentle purification conditions can be important to enable the protein to retain native lipids. For example, in a study of cytochrome bo_3 oxidase, Rienstra and co-workers found that samples purified via a single step of Ni^{2+} affinity chromatography yielded better NMR spectra than those subjected to a second anion exchange chromatography step. The latter showed similar activity but a twofold decrease in the lipid to protein ratio and a significant reduction in CP signal intensities in 1D ^{15}N NMR spectra.[92] The retention of native lipids may have rigidified the protein

or improved its stability. These observations are consistent with a growing body of evidence that bound lipids can be critical for the structure, function, or stability of membrane proteins and their complexes.[122]

Finally, it is worth keeping in mind that the protein may be perturbed reversibly by the conditions of the NMR experiment. For example, a recent study demonstrated that removal of the bulk buffer that typically separates from the sample during magic angle spinning reversibly altered the conformation of the selectivity filter of the KcsA potassium channel: addition of buffer to the rotor restored the conformation.[101] Based on this observation of a hydration-induced shift in conformation, it seems prudent to maintain high hydration levels for NMR studies of proteins in general.

3. SOLID-STATE NMR SNAPSHOTS OF MEMBRANE PROTEINS AT WORK

The above NMR methods and labelling strategies can be applied to large membrane proteins and their complexes (systems beyond the <100 amino acid size typical for targets of complete structure determination) to yield structural and mechanistic information. Selected examples are discussed below to illustrate how solid-state NMR can test proposed models for structures and mechanisms in complex membrane protein systems.

Recent studies of potassium channels by solid-state NMR have probed both the well-studied KscA channel and a KcsA–Kv1.1 chimeric channel that has a high-affinity binding site for scorpion toxins. Although spectra of these proteins are highly congested due to the helical structure, the resonances of the selectivity filter, one of the most mechanistically interesting regions, are more easily resolved and assigned due to its nonhelical conformation. Baldus and co-workers[102] have assigned 59% of the 160 residues of KcsA–Kv1.1 in proteoliposome samples by using a reverse-labelled protein (reverse labelled at four residues corresponding to 29% of the sequence) to obtain less congested spectra that complement the NMR spectra of the uniform $^{13}C,^{15}N$-labelled protein. The chemical shifts and some proton–proton distance information from proton-driven spin diffusion spectra suggest the structure is similar to the crystal structure of KcsA. In a parallel study,[123] this group used electrophysiology experiments to show that the KcsA–Kv1.1 channel enters an inactivated state at pH 4.0 and used NMR to identify conformational changes localized to the selectivity filter, gating hinge and inner helix bundle. The NMR data suggest that either pH 4.0 or a porphyrin channel blocker induces a ''non-conductive'' selectivity filter conformation similar to a previously reported crystal structure of KcsA at low-K^+ concentrations. A recent

extensive study[124] examined the effects of pH, [K+] and ligands (porphyrin and kaliotoxin) on chemical shifts within and beyond the selectivity filter to deduce the protonation states of various Glu residues and the conformation of gates on both ends of the channel, yielding insights into the coupling between the gates and the mechanistic cycle of the channel.

A careful study by McDermott and co-workers of the high-K^+ and low-K^+ states of the KcsA channel has focused exclusively on the selectivity filter.[101] They discovered that low K^+ also induces the ''non-conductive'' or ''collapsed'' structure of the selectivity filter at neutral pH, but only if the sample remains well hydrated: this state is lost if the bulk buffer is removed from the NMR rotor after spinning. Comparison of the measured chemical shifts with predictions by the SHIFTX and SPARTA programs identified the crystal structures that are most consistent with the selectivity filter conformations in the high-K^+ and low-K^+ proteoliposome samples. Titrations of the chemical shift changes were used to measure site-specific affinities for K^+. Based on the slow exchange rate between these conformations ($<500\ s^{-1}$), the authors suggest that the low-K^+ conformation is relevant to channel inactivation rather than to conduction.[101]

Several recent solid-state NMR studies have focused on proteorhodopsin, a eubacterial 27 kDa light-driven proton pump of unknown structure related to the well-studied archaebacterial bacteriorhodopsin. Ladizhansky and co-workers assigned 64% of the residues in experiments on uniform ^{13}C,^{15}N-labelled and two reverse-labelled samples. With these assignments, chemical shifts were used to deduce secondary structure and compare to the structure of bacteriorhodopsin, to identify similarities and differences and to deduce the protonation state of various Asp and Glu side chains that may be involved in the proton transfer pathway.[98,99] NMR experiments by Glaubitz and co-workers[59,125] measured chemical shifts of retinal and the Schiff base nitrogen in the wild-type and mutant proteins to deduce retinal conformation and to suggest possible interactions of a key residue H75, which is conserved in proteorhodopsins but missing in bacteriorhodopsin.

Baldus and co-workers have investigated SRII in proteoliposomes, alone[20] and in complex with its transducer (HtrII).[93] Strategies for spectral simplification are critical for NMR studies of this large system (249 amino acids of SRII + 157 amino acids of HtrII construct) even with its favourable 0.7 ppm linewidths. Labelling strategies used to relieve spectral congestion in spectra of these U-^{13}C,^{15}N proteins included labelling individual proteins (SRII or HtrII) and protein fragments (HAMP domain of HtrII), and reverse labelling of dominant residues (e.g. four residues corresponding to 34% of SRII sequence). NMR strategies for simplification and focus included selective detection of (1) rigid, water-exposed protein regions, (2) mobile regions and (3) SRII residues near the HtrII

interface. These approaches simplified the spectra sufficiently to make a significant number of sequential assignments and to demonstrate that some of the loop and tail resonances are missing due to mobility.[20] Then comparison of spectra of SRII and SRII/HtrII complexes was used to identify residues that undergo changes in conformation or dynamics upon complex formation (residues highlighted on the left SRII in the complex shown in Figure 3). Further studies of the SRII/HtrII complex used difference spectra between the ground state and freeze-trapped photo-excited state to identify chemical shift changes that support one of two proposed models for the light-induced conformational change (residues highlighted on the right SRII in the complex shown in Figure 3).[93] This use of extensive labelling with simplification of spectra via NMR selection experiments enabled the assignment (including different stated levels of confidence) of resonances corresponding to about 40% of SRII,[20] providing a powerful tool for investigating changes in structure and dynamics throughout the protein and their role in the mechanism.

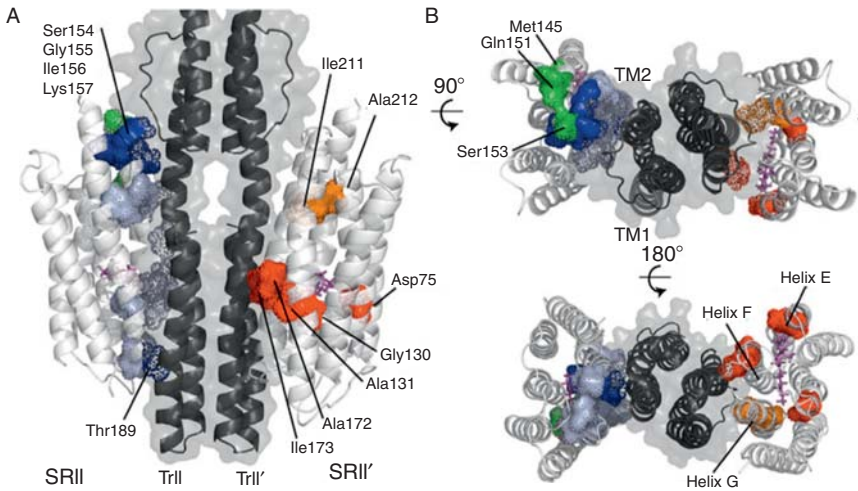

Figure 3 NMR-detected changes in sensory rhodopsin upon complex formation or light activation (adapted with permission from Ref. 93). Protein backbones are represented as ribbons (grey=SRII, black=TRII); retinal in stick representation (purple) is most visible in the right SRII of (B). Residues undergoing changes detected by NMR are highlighted by spacefill representation. Residues highlighted and identified on the left SRII in (A) (lateral view) and (B) (end-on view) undergo changes upon complex formation in either mobility (green) or chemical shift (dark blue/light blue indicate identified/likely residues). Residues highlighted and identified on the right SRII in (A) and (B) undergo changes in chemical shift upon light activation (red/orange indicate identified/likely residues).

Magic angle spinning NMR studies of rhodopsin (44 kDa) by Smith and co-workers have revealed conformational changes that occur during the photocycle to provide key insights into the mechanism of this GPCR.[126] Spectral simplification is achieved in these studies through incorporation of specific labelled amino acids and/or retinal. NMR experiments then focus on resonances that change upon light activation: 1D difference spectra report on changes in chemical shift; crosspeak positions or intensities in 2D ^{13}C DARR spectra report on changes in chemical shift or distance, respectively. For example, a recent study[127] describes the following NMR evidence for displacement of extracellular loop 2 upon light activation: light activation leads to chemical shift changes of resonances of several residues of this loop and loss of contact (DARR crosspeaks) between these residues and various retinal carbons. Assignments (e.g. which Ser in the $^{13}C\beta$-Ser labelled protein) were made using either mutant proteins (based on disappearance of the resonance in the spectrum of the mutant) or using proximity to specific retinal carbons that are within 6 Å in the crystal structure of the dark state (crosspeaks in 2D DARR spectra of appropriately labelled samples). Crosspeak intensities gave qualitative measures of the distance (≤ 4, ≤ 5 or ≤ 6 Å for strong, medium or weak crosspeaks, respectively) that are consistent with the crystal structure of the dark state. Disappearance of crosspeaks indicates that the separation between extracellular loop 2 and retinal increases to over 6 Å in the meta II state. Figure 4 shows some of the evidence for this movement: Cys 187 on extracellular loop 2 displays both chemical shift changes (Figure 4A) and disappearance of DARR crosspeaks to retinal carbons (Figure 4B). Further studies of the hydrogen-bonding network of this loop yielded insights into the coupling between retinal isomerization and conformational changes that activate rhodopsin. The authors suggest that this extracellular loop controls access to the retinal-binding site and may control access of ligands to other GPCRs. This example is one of a series of solid-state NMR studies of rhodopsin that have measured chemical shift and distance changes for selected amino acids and retinal positions to provide insights into the signalling mechanism of this receptor.[126]

A study by Oschkinat and co-workers of the ABC transporter ArtMP (222 residue ArtM + 240 residue ArtP) illustrates the need for focused NMR experiments to investigate mechanisms in complex membrane proteins.[60] In spite of using carefully optimized 2D crystalline samples that yielded spectra with narrow linewidths (0.9 ppm), and using limited amino acid specific labelling (U-^{13}C,^{15}N-Tyr, Pro and Thr), spectral overlap is still significant for the complete transporter ArtMP. This challenge was overcome by obtaining assignments in a simplified system, 3D crystals of the soluble nucleotide-binding domain ArtP, which could then be transferred by comparison to spectra of the ArtMP complex. The Tyr, Pro and Thr labels are well chosen for probing the mechanism of this

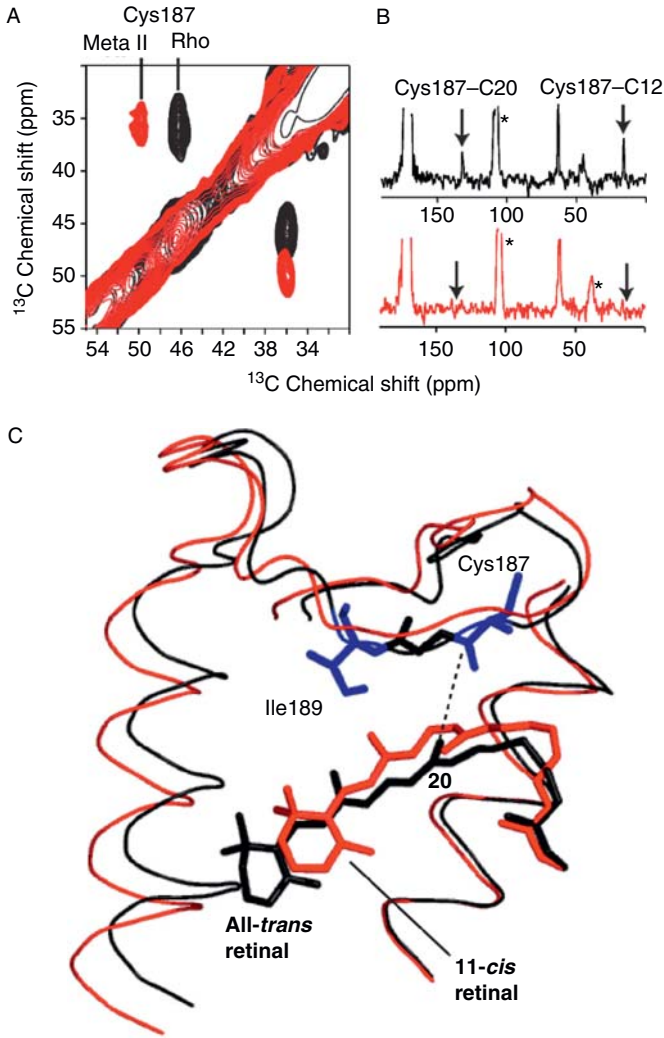

Figure 4 Chemical shift and dipolar coupling evidence for displacement of extracellular loop 2 upon light activation of rhodopsin (adapted from Refs. 127 and 126, with permission). (A) 2D ^{13}C DARR spectra of rhodopsin ground state (black) and meta II state (grey, red in colour version) show the loop residue Cys187 Cβ chemical shift changes from 46 to 50 ppm. (B) 1D slices of 2D DARR spectra measure dipolar couplings in rhodopsin ground state (top) and meta II state (bottom). Cys187 to retinal contacts present in the ground state are lost in the meta II state. (C) Light-induced structural change between the rhodopsin ground state (black, crystal structure) and meta II state (red, model based on NMR measurements and MD simulations) includes the displacement of extracellular loop 2 from the retinal-binding pocket.

transporter because they enable the specific detection and assignment of two unique dipeptides, YP and PT, that are located in the ATP-binding site and nucleotide-binding domain dimer interface. An initial comparison of resonances in samples ±ATP and ±transmembrane domain revealed some changes and demonstrates the feasibility of using NMR to probe differences between states in the transport cycle.

Our laboratory has used a site-directed distance measurement approach on bacterial chemotaxis receptors to test proposals for the signalling mechanism and for the structural contacts in receptor signalling arrays. As discussed above, these experiments are directed to the site of interest by introducing a unique Cys residue. We used $^{13}C\{^{19}F\}$ REDOR[61] and ^{13}C–^{13}C rotational resonance[62] to measure helix–helix distances in periplasmic and transmembrane domains of the intact Ser receptor (551 amino acids) bound to native membrane vesicles (sites 1 and 2 in Figure 5A). We measured a small ligand-induced distance change consistent with the proposed[128] ''piston'' displacement of one helix that is thought to initiate the transmembrane signal (Figure 5B). Study of the full signalling properties of this receptor requires the assembly of signalling arrays which include the receptor and two binding partners, CheA and CheW. We assembled functional complexes of the receptor cytoplasmic domain (30 kDa) with these partners (70 and 18 kDa) and used $^{13}C\{^{19}F\}$ REDOR to measure receptor–receptor distances testing packing interactions proposed based on crystal structures of the receptor domain alone.[63] Surprisingly, our NMR data refuted the prevailing model[129] for the receptor packing interactions (Figure 5C). The chemoreceptor work illustrates the use of solid-state NMR to provide high-resolution distance measurements on a large functional membrane protein and its complexes to test models based on crystal structures of fragments and/or biochemical studies of the system.

Several strategies emerge from these studies. For the first three cases (16 kDa KcsA, 27 kDa proteorhodopsin and 26 kDa SR), NMR studies have achieved ≈40–60% assignments: this will enable widespread monitoring of changes in structure and dynamics. These studies also focus on system-specific properties that are both mechanistically interesting and spectroscopically advantageous: the nonhelical selectivity filter in KcsA, the retinal in proteorhodopsin and the protein interface in SRII/HtrII. Studies of multisubunit complexes such as SRII/HtrII (and ArtMP below) can take advantage of the ability to compare spectra of the individual and complexed proteins. An alternate strategy that is especially important for larger systems is to employ specific residue labels; this approach was chosen for the studies of the 44 kDa rhodopsin, 46 kDa ArtMP and 60 kDa chemoreceptor and its >118 kDa complexes. Using different tools for focusing on sites of interest (proximity to retinal, unique dipeptides and site-directed Cys mutants), these studies are measuring

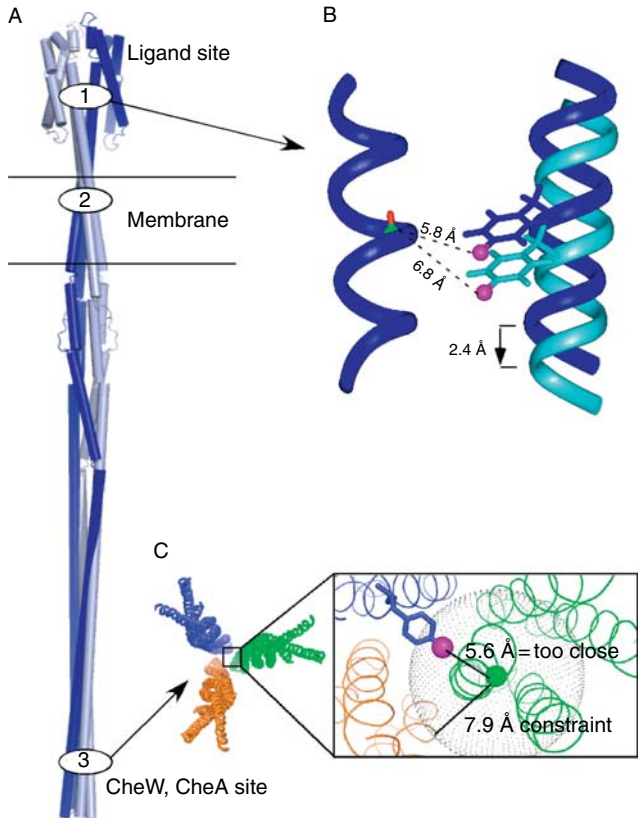

Figure 5 Site-directed distance measurements probing structure and mechanism in bacterial chemotaxis receptors and their complexes. (A) Cartoon representation of an intact, transmembrane receptor dimer, indicating sites of NMR distance measurements by $^{13}C\{^{19}F\}$ REDOR (sites 1 and 3) and ^{13}C rotational resonance (site 2). All measurements involved a unique Cys residue introduced by mutagenesis. (B) Comparison of an inter-helix distance at site 1 with or without ligand bound provided the first high-resolution measurement of the ligand-induced conformational change in the intact, membrane-bound receptor.[61] The NMR measurement is consistent with the proposed ligand-induced piston of helix 4. (C) This end-on (from above) view of receptors organized as trimers of dimers (pdb code 1qu7) illustrates the distance measurement at site 3, which was performed on the cytoplasmic fragment of the receptor assembled into kinase-active complexes with its partner proteins CheA and CheW (not shown). NMR results refuted the proposed dimer–dimer contact and provided a distance constraint for the structure of the receptor trimer of dimers.[63]

structure and structural changes important to understanding mechanisms of these membrane proteins. Choice of strategy will continue to depend on both the questions of interest and the complexity of the system for NMR (size, dynamics, linewidths). As complete structure determination

methodology continues to advance, the size of proteins that can be investigated will also increase. Creative application of these key developments to even larger proteins will make solid-state NMR a versatile tool that can provide key structural and mechanistic insights on large proteins and complexes.

4. CONCLUSIONS

The time is ripe for solid-state NMR to provide structural constraints and mechanistic insights on large membrane proteins and their complexes. To illustrate this, I have highlighted some recent magic angle spinning studies of large membrane proteins as well as some techniques that appear promising for focusing structural measurements on a subset or region of interest within such proteins. Combining such focus with the powerful solid-state NMR techniques being developed for complete structure determination of smaller systems should yield multiple constraints for membrane proteins in various functional states to provide insights into their mechanisms. Although not covered in this review, many solid-state NMR studies of oriented samples and of smaller membrane peptide systems provide important complementary techniques and insights applicable to large membrane proteins. Together with other biophysical and biochemical approaches, solid-state NMR is poised to provide structural constraints that help reveal the mechanisms used by membrane proteins to perform fundamental life processes such as transmembrane sensing, signalling and transport.

ACKNOWLEDGEMENTS

I would like to thank Dr. Dan Fowler and Dr. Michael Harris for stimulating discussions and for helpful comments on the chapter. This research was supported by U.S. Public Health Service Grants GM47601 and GM085288, and by U.S. Army Research Office Grant W911NF-08-1-0412.

REFERENCES

1. H. J. Kim, S. C. Howell, W. D. Van Horn, Y. H. Jeon and C. R. Sanders, *Prog. Nucl. Magn. Reson. Spectrosc.*, 2009, **55,** 335.
2. C. G. Tate and R. C. Stevens, *Curr. Opin. Struct. Biol.*, 2010, **20,** 399.
3. A. McDermott, *Annu. Rev. Biophys.*, 2009, **38,** 385.
4. R. C. Page, C. Li, J. Hu, F. P. Gao and T. A. Cross, *Magn. Reson. Chem.*, 2007, **45,** S2.
5. A. Diller, C. Loudet, F. Aussenac, G. Raffard, S. Fournier, M. Laguerre, A. Grelard, S. J. Opella, F. M. Marassi and E. J. Dufourc, *Biochimie*, 2009, **91,** 744.
6. S. D. Cady, T. V. Mishanina and M. Hong, *J. Mol. Biol.*, 2009, **385,** 1127.

7. S. D. Cady, K. Schmidt-Rohr, J. Wang, C. S. Soto, W. F. Degrado and M. Hong, *Nature*, 2010, **463,** 689.
8. A. L. Stouffer, R. Acharya, D. Salom, A. S. Levine, L. Di Costanzo, C. S. Soto, V. Tereshko, V. Nanda, S. Stayrook and W. F. DeGrado, *Nature*, 2008, **451,** 596.
9. J. R. Schnell and J. J. Chou, *Nature*, 2008, **451,** 591.
10. J. Hu, T. Asbury, S. Achuthan, C. Li, R. Bertram, J. R. Quine, R. Fu and T. A. Cross, *Biophys. J.*, 2007, **92,** 4335.
11. G. Fiorin, V. Carnevale and W. F. DeGrado, *Science*, 2010, **330,** 456.
12. F. Hu, W. Luo and M. Hong, *Science*, 2010, **330,** 505.
13. M. Sharma, M. Yi, H. Dong, H. Qin, E. Peterson, D. D. Busath, H. X. Zhou and T. A. Cross, *Science*, 2010, **330,** 509.
14. M. J. Bayro, M. Huber, R. Ramachandran, T. C. Davenport, B. H. Meier, M. Ernst and R. G. Griffin, *J. Chem. Phys.*, 2009, **130,** 114506.
15. D. M. LeMaster and D. M. Kushlan, *J. Am. Chem. Soc.*, 1996, **118,** 9255.
16. F. Castellani, B. van Rossum, A. Diehl, M. Schubert, K. Rehbein and H. Oschkinat, *Nature*, 2002, **420,** 98.
17. V. A. Higman, J. Flinders, M. Hiller, S. Jehle, S. Markovic, S. Fiedler, B. J. van Rossum and H. Oschkinat, *J. Biomol. NMR*, 2009, **44,** 245.
18. A. Goldbourt, L. A. Day and A. E. McDermott, *J. Magn. Reson.*, 2007, **189,** 157.
19. M. Hong and K. Jakes, *J. Biomol. NMR*, 1999, **14,** 71.
20. M. Etzkorn, S. Martell, O. C. Andronesi, K. Seidel, M. Engelhard and M. Baldus, *Angew. Chem. Int. Ed. Engl.*, 2007, **46,** 459.
21. L. Skrisovska, M. Schubert and F. H. Allain, *J. Biomol. NMR*, 2010, **46,** 51.
22. D. Marulanda, M. L. Tasayco, A. McDermott, M. Cataldi, V. Arriaran and T. Polenova, *J. Am. Chem. Soc.*, 2004, **126,** 16608.
23. J. L. Popot and D. M. Engelman, *Annu. Rev. Biochem.*, 2000, **69,** 881.
24. N. J. Traaseth, R. Verardi and G. Veglia, *J. Am. Chem. Soc.*, 2008, **130,** 2400.
25. G. Wagner, *J. Biomol. NMR*, 2010, **46,** 1.
26. S. Sobhanifar, S. Reckel, F. Junge, D. Schwarz, L. Kai, M. Karbyshev, F. Lohr, F. Bernhard and V. Dotsch, *J. Biomol. NMR*, 2010, **46,** 33.
27. I. Maslennikov, C. Klammt, E. Hwang, G. Kefala, M. Okamura, L. Esquivies, K. Mors, C. Glaubitz, W. Kwiatkowski, Y. H. Jeon and S. Choe, *Proc. Natl. Acad. Sci. USA*, 2010, **107,** 10902.
28. A. Abdine, M. A. Verhoeven and D. E. Warschawski, *N. Biotechnol.* 2010, doi:101016/j.nbt.2010.07.014.
29. A. Abdine, M. A. Verhoeven, K. H. Park, A. Ghazi, E. Guittet, C. Berrier, C. Van Heijenoort and D. E. Warschawski, *J. Magn. Reson.*, 2010, **204,** 155.
30. I. Lehner, D. Basting, B. Meyer, W. Haase, T. Manolikas, C. Kaiser, M. Karas and C. Glaubitz, *J. Biol. Chem.*, 2008, **283,** 3281.
31. V. Agarwal, U. Fink, S. Schuldiner and B. Reif, *Biochim. Biophys. Acta*, 2007, **1768,** 3036.
32. C. P. Jaroniec, J. C. Lansing, B. A. Tounge, M. Belenky, J. Herzfeld and R. G. Griffin, *J. Am. Chem. Soc.*, 2001, **123,** 12929.
33. G. S. Harbison, J. Herzfeld and R. G. Griffin, *Biochemistry*, 1983, **22,** 1.
34. G. S. Harbison, S. O. Smith, J. A. Pardoen, P. P. Mulder, J. Lugtenburg, J. Herzfeld, R. Mathies and R. G. Griffin, *Biochemistry*, 1984, **23,** 2662.
35. G. S. Harbison, S. O. Smith, J. A. Pardoen, C. Winkel, J. Lugtenburg, J. Herzfeld, R. Mathies and R. G. Griffin, *Proc. Natl. Acad. Sci. USA*, 1984, **81,** 1706.
36. G. S. Harbison, S. O. Smith, J. A. Pardoen, J. M. Courtin, J. Lugtenburg, J. Herzfeld, R. A. Mathies and R. G. Griffin, *Biochemistry*, 1985, **24,** 6955.
37. S. O. Smith, J. Courtin, E. van den Berg, C. Winkel, J. Lugtenburg, J. Herzfeld and R. G. Griffin, *Biochemistry*, 1989, **28,** 237.
38. S. O. Smith, H. J. de Groot, R. Gebhard, J. M. Courtin, J. Lugtenburg, J. Herzfeld and R. G. Griffin, *Biochemistry*, 1989, **28,** 8897.

39. F. Creuzet, A. McDermott, R. Gebhard, K. van der Hoef, M. B. Spijker-Assink, J. Herzfeld, J. Lugtenburg, M. H. Levitt and R. G. Griffin, *Science*, 1991, **251,** 783.
40. L. K. Thompson, A. E. McDermott, J. Raap, C. M. van der Wielen, J. Lugtenburg, J. Herzfeld and R. G. Griffin, *Biochemistry*, 1992, **31,** 7931.
41. M. R. Farrar, K. V. Lakshmi, S. O. Smith, R. S. Brown, J. Raap, J. Lugtenburg, R. G. Griffin and J. Herzfeld, *Biophys. J.*, 1993, **65,** 310.
42. K. V. Lakshmi, M. Auger, J. Raap, J. Lugtenburg, R. G. Griffin and J. Herzfeld, *J. Am. Chem. Soc.*, 1993, **115,** 8515.
43. K. V. Lakshmi, M. R. Farrar, J. Raap, J. Lugtenburg, R. G. Griffin and J. Herzfeld, *Biochemistry*, 1994, **33,** 8853.
44. A. E. McDermott, F. Creuzet, R. Gebhard, K. van der Hoef, M. H. Levitt, J. Herzfeld, J. Lugtenburg and R. G. Griffin, *Biochemistry*, 1994, **33,** 6129.
45. J. G. Hu, B. Q. Sun, A. T. Petkova, R. G. Griffin and J. Herzfeld, *Biochemistry*, 1997, **36,** 9316.
46. J. G. Hu, B. Q. Sun, M. Bizounok, M. E. Hatcher, J. C. Lansing, J. Raap, P. J. Verdegem, J. Lugtenburg, R. G. Griffin and J. Herzfeld, *Biochemistry*, 1998, **37,** 8088.
47. V. S. Bajaj, M. L. Mak-Jurkauskas, M. Belenky, J. Herzfeld and R. G. Griffin, *Proc. Natl. Acad. Sci. USA*, 2009, **106,** 9244.
48. P. T. Williamson, A. Verhoeven, K. W. Miller, B. H. Meier and A. Watts, *Proc. Natl. Acad. Sci. USA*, 2007, **104,** 18031.
49. L. Krabben, B. J. van Rossum, S. Jehle, E. Bocharov, E. N. Lyukmanova, A. A. Schulga, A. Arseniev, F. Hucho and H. Oschkinat, *J. Mol. Biol.*, 2009, **390,** 662.
50. E. Hughes and D. A. Middleton, *J. Biol. Chem.*, 2003, **278,** 20835.
51. K. Seidel, O. C. Andronesi, J. Krebs, C. Griesinger, H. S. Young, S. Becker and M. Baldus, *Biochemistry*, 2008, **47,** 4369.
52. S. Luca, J. F. White, A. K. Sohal, D. V. Filippov, J. H. van Boom, R. Grisshammer and M. Baldus, *Proc. Natl. Acad. Sci. USA*, 2003, **100,** 10706.
53. J. J. Lopez, A. K. Shukla, C. Reinhart, H. Schwalbe, H. Michel and C. Glaubitz, *Angew. Chem. Int. Ed. Engl.*, 2008, **47,** 1668.
54. A. Gansmuller, M. Concistre, N. McLean, O. G. Johannessen, I. Marin-Montesinos, P. H. Bovee-Geurts, P. Verdegem, J. Lugtenburg, R. C. Brown, W. J. Degrip and M. H. Levitt, *Biochim. Biophys. Acta*, 2009, **1788,** 1350.
55. V. R. Ratnala, S. R. Kiihne, F. Buda, R. Leurs, H. J. de Groot and W. J. DeGrip, *J. Am. Chem. Soc.*, 2007, **129,** 867.
56. D. Basting, I. Lehner, M. Lorch and C. Glaubitz, *Naunyn Schmiedebergs Arch. Pharmacol.*, 2006, **372,** 451.
57. S. G. Patching, P. J. Henderson, R. B. Herbert and D. A. Middleton, *J. Am. Chem. Soc.*, 2008, **130,** 1236.
58. J. Curtis-Fisk, R. M. Spencer and D. P. Weliky, *J. Am. Chem. Soc.*, 2008, **130,** 12568.
59. N. Pfleger, A. C. Worner, J. Yang, S. Shastri, U. A. Hellmich, L. Aslimovska, M. S. Maier and C. Glaubitz, *Biochim. Biophys. Acta*, 2009, **1787,** 697.
60. V. Lange, J. Becker-Baldus, B. Kunert, B. J. van Rossum, F. Casagrande, A. Engel, Y. Roske, F. M. Scheffel, E. Schneider and H. Oschkinat, *Chembiochem*, 2010, **11,** 547.
61. O. J. Murphy, 3rd, F. A. Kovacs, E. L. Sicard and L. K. Thompson, *Biochemistry*, 2001, **40,** 1358.
62. B. Isaac, G. J. Gallagher, Y. S. Balazs and L. K. Thompson, *Biochemistry*, 2002, **41,** 3025.
63. D. J. Fowler, R. M. Weis and L. K. Thompson, *Biochemistry*, 2010, **49,** 1425.
64. D. T. Graesser, B. J. Wylie, A. J. Nieuwkoop, W. T. Franks and C. M. Rienstra, *Magn. Reson. Chem.*, 2007, **45**(1), S129.
65. P. S. Nadaud, J. J. Helmus, N. Hofer and C. P. Jaroniec, *J. Am. Chem. Soc.*, 2007, **129,** 7502.
66. P. S. Nadaud, J. J. Helmus, S. L. Kall and C. P. Jaroniec, *J. Am. Chem. Soc.*, 2009, **131,** 8108.
67. R. Furter, *Protein Sci.*, 1998, **7,** 419.

68. L. Banci, I. Bertini, C. Luchinat and M. Mori, *Prog. Nucl. Magn. Reson. Spectrosc.*, 2010, **56,** 247.
69. G. Otting, *Annu. Rev. Biophys.*, 2010, **39,** 387.
70. G. M. Clore, C. Tang and J. Iwahara, *Curr. Opin. Struct. Biol.*, 2007, **17,** 603.
71. R. Linser, U. Fink and B. Reif, *J. Am. Chem. Soc.*, 2009, **131,** 13703.
72. I. Bertini, A. Bhaumik, G. De Paepe, R. G. Griffin, M. Lelli, J. R. Lewandowski and C. Luchinat, *J. Am. Chem. Soc.*, 2010, **132,** 1032.
73. G. Pintacuda, N. Giraud, R. Pierattelli, A. Bockmann, I. Bertini and L. Emsley, *Angew. Chem. Int. Ed. Engl.*, 2007, **46,** 1079.
74. N. P. Wickramasinghe, S. Parthasarathy, C. R. Jones, C. Bhardwaj, F. Long, M. Kotecha, S. Mehboob, L. W. Fung, J. Past, A. Samoson and Y. Ishii, *Nat. Methods*, 2009, **6,** 215.
75. R. Linser, V. Chevelkov, A. Diehl and B. Reif, *J. Magn. Reson.*, 2007, **189,** 209.
76. K. Yamamoto, J. Xu, K. E. Kawulka, J. C. Vederas and A. Ramamoorthy, *J. Am. Chem. Soc.*, 2010, **132,** 6929.
77. P. S. Nadaud, J. J. Helmus, I. Sengupta and C. P. Jaroniec, *J. Am. Chem. Soc.*, 2010, **132,** 9561.
78. M. Etzkorn, A. Bockmann, A. Lange and M. Baldus, *J. Am. Chem. Soc.*, 2004, **126,** 14746.
79. J. Yang, M. L. Tasayco and T. Polenova, *J. Am. Chem. Soc.*, 2008, **130,** 5798.
80. C. Wasmer, A. Lange, H. Van Melckebeke, A. B. Siemer, R. Riek and B. H. Meier, *Science*, 2008, **319,** 1523.
81. O. C. Andronesi, S. Becker, K. Seidel, H. Heise, H. S. Young and M. Baldus, *J. Am. Chem. Soc.*, 2005, **127,** 12965.
82. M. Baldus and B. H. Meier, *J. Magn. Reson. A*, 1996, **121,** 65.
83. G. S. Harbison, J. E. Roberts, J. Herzfeld and R. G. Griffin, *J. Am. Chem. Soc.*, 1988, **110,** 7221.
84. K. K. Kumashiro, K. Schmidt-Rohr, O. J. Murphy, K. L. Ouellette, W. A. Cramer and L. K. Thompson, *J. Am. Chem. Soc.*, 1998, **120,** 5043.
85. G. J. Gallagher, M. Hong and L. K. Thompson, *Biochemistry*, 2004, **43,** 7899.
86. D. Huster, X. L. Yao and M. Hong, *J. Am. Chem. Soc.*, 2002, **124,** 874.
87. C. Ader, R. Schneider, K. Seidel, M. Etzkorn, S. Becker and M. Baldus, *J. Am. Chem. Soc.*, 2009, **131,** 170.
88. A. Bockmann, C. Gardiennet, R. Verel, A. Hunkeler, A. Loquet, G. Pintacuda, L. Emsley, B. H. Meier and A. Lesage, *J. Biomol. NMR*, 2009, **45,** 319.
89. A. Grossfield, M. C. Pitman, S. E. Feller, O. Soubias and K. Gawrisch, *J. Mol. Biol.*, 2008, **381,** 478.
90. Y. Li, A. Z. Kijac, S. G. Sligar and C. M. Rienstra, *Biophys. J.*, 2006, **91,** 3819.
91. A. Z. Kijac, Y. Li, S. G. Sligar and C. M. Rienstra, *Biochemistry*, 2007, **46,** 13696.
92. H. L. Frericks, D. H. Zhou, L. L. Yap, R. B. Gennis and C. M. Rienstra, *J. Biomol. NMR*, 2006, **36,** 55.
93. M. Etzkorn, K. Seidel, L. Li, S. Martell, M. Geyer, M. Engelhard and M. Baldus, *Structure*, 2010, **18,** 293.
94. M. Lorch, S. Faham, C. Kaiser, I. Weber, A. J. Mason, J. U. Bowie and C. Glaubitz, *Chembiochem*, 2005, **6,** 1693.
95. M. Hiller, L. Krabben, K. R. Vinothkumar, F. Castellani, B. J. van Rossum, W. Kuhlbrandt and H. Oschkinat, *Chembiochem*, 2005, **6,** 1679.
96. Y. Li, D. A. Berthold, H. L. Frericks, R. B. Gennis and C. M. Rienstra, *Chembiochem*, 2007, **8,** 434.
97. S. Shastri, J. Vonck, N. Pfleger, W. Haase, W. Kuehlbrandt and C. Glaubitz, *Biochim. Biophys. Acta*, 2007, **1768,** 3012.
98. L. Shi, M. A. Ahmed, W. Zhang, G. Whited, L. S. Brown and V. Ladizhansky, *J. Mol. Biol.*, 2009, **386,** 1078.
99. L. Shi, E. M. Lake, M. A. Ahmed, L. S. Brown and V. Ladizhansky, *Biochim. Biophys. Acta*, 2009, **1788,** 2563.

100. K. Varga, L. Tian and A. E. McDermott, *Biochim. Biophys. Acta*, 2007, **1774,** 1604.
101. M. P. Bhate, B. J. Wylie, L. Tian and A. E. McDermott, *J. Mol. Biol.*, 2010, **401,** 155.
102. R. Schneider, C. Ader, A. Lange, K. Giller, S. Hornig, O. Pongs, S. Becker and M. Baldus, *J. Am. Chem. Soc.*, 2008, **130,** 7427.
103. I. Marcotte and M. Auger, *Concepts Magn. Reson. A*, 2005, **24A,** 17.
104. C. Sizun, F. Aussenac, A. Grelard and E. J. Dufourc, *Magn. Reson. Chem.*, 2004, **42,** 180.
105. J. Xu, U. H. Durr, S. C. Im, Z. Gan, L. Waskell and A. Ramamoorthy, *Angew. Chem. Int. Ed. Engl.*, 2008, **47,** 7864.
106. P. Schmidt, C. Berger, H. A. Scheidt, S. Berndt, A. Bunge, A. G. Beck-Sickinger and D. Huster, *Biophys. Chem.*, 2010, **150,** 29.
107. C. McKibbin, N. A. Farmer, C. Jeans, P. J. Reeves, H. G. Khorana, B. A. Wallace, P. C. Edwards, C. Villa and P. J. Booth, *J. Mol. Biol.*, 2007, **374,** 1319.
108. S. H. Park and S. J. Opella, *J. Am. Chem. Soc.*, 2010, **132,** 12552.
109. T. H. Bayburt and S. G. Sligar, *FEBS Lett.*, 2010, **584,** 1721.
110. T. Raschle, S. Hiller, T. Y. Yu, A. J. Rice, T. Walz and G. Wagner, *J. Am. Chem. Soc.*, 2009, **131,** 17777.
111. A. L. Shrout, D. J. Montefusco and R. M. Weis, *Biochemistry*, 2003, **42,** 13379.
112. J. A. Stringer, C. E. Bronnimann, C. G. Mullen, D. H. Zhou, S. A. Stellfox, Y. Li, E. H. Williams and C. M. Rienstra, *J. Magn. Reson.*, 2005, **173,** 40.
113. S. A. McNeill, P. L. Gor'kov, K. Shetty, W. W. Brey and J. R. Long, *J. Magn. Reson.*, 2009, **197,** 135.
114. F. D. Doty, J. Kulkarni, C. Turner, G. Entzminger and A. Bielecki, *J. Magn. Reson.*, 2006, **182,** 239.
115. J. B. D. de Lacaillerie, B. Jarry, O. Pascui and D. Reichert, *Solid State Nucl. Magn. Reson.*, 2005, **28,** 225.
116. S. V. Dvinskikh, K. Yamamoto, U. H. N. Durr and A. Ramamoorthy, *J. Magn. Reson.*, 2007, **184,** 228.
117. B. Dillmann, K. Elbayed, H. Zeiger, M. C. Weingertner, M. Plotto and F. Engelke, *J. Magn. Reson.*, 2007, **187,** 10.
118. A. Krahn, U. Priller, L. Emsley and F. Engelke, *J. Magn. Reson.*, 2008, **191,** 78.
119. C. V. Grant, S. L. Sit, A. A. De Angelis, K. S. Khuong, C. H. Wu, L. A. Plesniak and S. J. Opella, *J. Magn. Reson.*, 2007, **188,** 279.
120. P. L. Gor'kov, E. Y. Chekmenev, C. G. Li, M. Cotten, J. J. Buffy, N. J. Traaseth, G. Veglia and W. W. Brey, *J. Magn. Reson.*, 2007, **185,** 77.
121. P. L. Gor'kov, R. Witter, E. Y. Chekmenev, F. Nozirov, R. Fu and W. W. Brey, *J. Magn. Reson.*, 2007, **189,** 182.
122. H. Palsdottir and C. Hunte, *Biochim. Biophys. Acta*, 2004, **1666,** 2.
123. C. Ader, R. Schneider, S. Hornig, P. Velisetty, E. M. Wilson, A. Lange, K. Giller, I. Ohmert, M. F. Martin-Eauclaire, D. Trauner, S. Becker O. Pongs, *et al.*, *Nat. Struct. Mol. Biol.*, 2008, **15,** 605.
124. C. Ader, R. Schneider, S. Hornig, P. Velisetty, V. Vardanyan, K. Giller, I. Ohmert, S. Becker, O. Pongs and M. Baldus, *EMBO J.*, 2009, **28,** 2825.
125. N. Pfleger, M. Lorch, A. C. Woerner, S. Shastri and C. Glaubitz, *J. Biomol. NMR*, 2008, **40,** 15.
126. J. A. Goncalves, S. Ahuja, S. Erfani, M. Eilers and S. O. Smith, *Prog. Nucl. Magn. Reson. Spectrosc.*, 2010, **57,** 159.
127. S. Ahuja, V. Hornak, E. C. Yan, N. Syrett, J. A. Goncalves, A. Hirshfeld, M. Ziliox, T. P. Sakmar, M. Sheves, P. J. Reeves, S. O. Smith and M. Eilers, *Nat. Struct. Mol. Biol.*, 2009, **16,** 168.
128. S. A. Chervitz and J. J. Falke, *Proc. Natl. Acad. Sci. USA*, 1996, **93,** 2545.
129. K. K. Kim, H. Yokota and S. H. Kim, *Nature*, 1999, **400,** 787.

CHAPTER 5

Chromatographic NMR

Stefano Caldarelli

Contents

Abstract

The principle of chromatographic NMR, a version of NMR diffusometry devised for a facilitated study of mixtures using the addition of a selectively retarding agent, is illustrated. The technical requirements for acquiring exploitable ^{1}H NMR diffusometry spectra for a heterogeneous solution/solid mix are described. Applications of the technique to test mixtures for several choices of solvents/interacting phase are reviewed.

Key Words: Mixtures, Porous materials, Diffusion, HRMAS, DOSY.

Aix Marseille Université, ISm2 UMR 6263, Campus de Saint Jérôme, Marseille, France

Annual Reports on NMR Spectroscopy, Volume 73
ISSN 0066-4103, DOI: 10.1016/B978-0-08-097074-5.00005-0

1. INTRODUCTION

The study of the composition of a mixture is an extremely common problem in analytical and bioanalytical chemistry. While chromatography and solvent extraction are commonly employed to simplify the analysis prior to characterization of the constituents, NMR has provided a series of tools that help in unravelling the components of complex samples, when a previous separation of the pure compounds is not feasible or complete. Thus, TOCSY, NMR diffusometry (DOSY, among all) and heteronuclear correlation experiments are widely used to this purpose, for example, for the characterization of small molecules in biologically relevant samples, such as in metabolomics,[1] plant extracts analysis,[2] food quality control,[3,4] to name a few cases.

Among these methods, DOSY analysis has the peculiarity of a somewhat reduced resolution with respect to the other mentioned NMR techniques. Indeed, while the resolution of multidimensional NMR is just limited by the signal lifetime (i.e. the relaxation rate), the one of DOSY and alike relies on mathematical algorithms,[5–12] the performance of which is put at strain in the presence of signal overlaps.[13] Moreover, the mathematical analysis that produces DOSY spectra (or any other processing approach of NMR diffusion data) is facilitated if the molecules in the mix have largely different mobilities. Chromatographic NMR is a procedure that aims at improving the resolution of DOSY experiments on mixtures, by expanding the range of molecular mobilities through selective interaction with an immobilized or slowly moving phase.[14] The namesake comes from the fact that its principle of action is borrowed from liquid chromatography, where effective separation of mixture components is achieved due to their different partition coefficient between a mobile and a solid phase. In this respect, chrom-NMR is a variation on the theme of affinity NMR,[15] which relies on large modifications of the mobility of a particular molecular probe to unveil the presence of intermolecular interactions among species with difference in molecular weight at least of one order of magnitude. Along these lines, differential solubility into micelles has been described already in 1994 as a valuable tool for resolving ^{1}H NMR spectra of mixtures.[16] The interest of tapping into chromatographic materials is that a very large selection of conditions (solid and mobile phase composition) exists in the literature and could serve of inspiration. In addition to the analytical aspects of the method, the evolution of the average observed diffusion coefficient due to the introduction of a chromatographic solid can provide insight on the mechanism of the chromatographic interaction. Indeed, a suspension of chromatographic phases in conjunction with high-resolution magic angle spinning (HRMAS) has been used to explore the interaction of specific analytes with the solids, mainly by saturation transfer or transferred nOe experiments.[17–22]

The first examples of the chromatographic NMR philosophy have been demonstrated in 2003,[14] with the addition of grafted and bare chromatographic phases in a DOSY experiment, under magic angle spinning (MAS) detection to achieve high resolution. Subsequently other declinations were proposed, without MAS[23] or using polymers,[24,25] for example, as the delaying phase and recently the use of micelles has been revived.[26,27] In the following, the basic underlining theoretical elements of NMR diffusometry will be exposed, and an outline of the principal findings to date of chromatographic NMR will be provided.

2. METHODS TO ACHIEVE HIGH-RESOLUTION NMR SPECTRA IN THE PRESENCE OF DELAYING MEDIA

The addition of a solid to the solution to analyse induces susceptibility broadening of the NMR proton signals, which can reach several tens of Hz. This effect, in conjunction with shortened T_2 relaxation for adsorbed species, may degrade the spectral resolution of ^{1}H NMR spectra beyond exploitation. As the latter effect cannot be countered by technological means, only susceptibility-broadening methods will be discussed in this section, but the reader should be aware that exclusively systems in which the solid phase, or any other matrix, does not induce severe relaxation broadening are suitable for chrom-NMR analysis.

2.1. MAS for magnetic susceptibility averaging

MAS at adequate frequencies is capable of attenuating and removing broadening of the NMR signal stemming from second order anisotropic corrections. This includes susceptibility broadening, an effect that can be represented as a coupling of the nuclei with the demagnetizing field. Satisfying line narrowing for heterogeneous samples (e.g. a wet solid) in a cylindrical container such as the typical MAS rotor can be achieved by moderate spinning rates.[28,29] The integration of MAS with a detection setup typical for liquids, that is, optimized for best ^{1}H spectra lineshape, provides a so-called HRMAS experiment.[30,31] However, the introduction of the mechanical rotation of the sample brings up some additional issues that need to be clarified, as the possible necessity of synchronizing the timing of the pulse sequences in HRMAS with the period of rotation. Although this point has been shown to be a sensitive one in experiments with spin-lock pulses, such as TOCSY,[32] no synchronization appears to be required in typical Pulse field gradients (PFG) diffusometry HRMAS. Conversely, convection has been a known source of imprecision in NMR diffusometry,[33,34] so that the introduction of MAS in this kind of analysis should be evaluated. Possible interferences of the motion induced by the

spinning with the measurement of the molecular displacement have been observed,[35] but they are most likely associated with turbulences due to the spinning of liquid or strongly mobile samples. At any rate, the effect due to the rotation can be contained if a reduced volume of analysis is used.[35,36]

2.2. Chrom-NMR without MAS

An alternative solution to reduce magnetic susceptibility broadenings in silica suspensions without resorting to MAS has been proposed in which these effects are countered by using a solvent that matches the silica gel susceptibility as closely as possible.[23] Common solvents do not have this property, but silica gel susceptibility matching can be achieved by using a composition of solvents, for example, $CDCl_3$ and CH_2I_2 or $CDBr_3$ in due proportions.[23] The best linewidth obtained by this scheme is of about 10 Hz, somewhat broader than the equivalent HRMAS experiment, but still providing an acceptable resolution for analysis of a few molecules in a mixture. In this experiment, best linewidth values degrade linearly with silica concentration. Fortunately, concentrations above 4 wt% in the solid gel do not produce appreciable improvements in the pseudo-chromatographic resolution, and thus the experiment can be carried on with acceptable resolution.

Another approach that is worth mentioning, although it has not yet been used for enhanced diffusometry, has been dubbed NMR wool tube. Here, an alternative method of putting in contact silica and a solution for NMR analysis has been proposed, in which a functionalized glass-wool was inserted in the NMR tube.[37]

Finally, it is noteworthy that susceptibility-broadening effects are not relevant in declinations of the method in which the retarding agent is soluble, a polymer or a micelle, for instance.

3. MOBILITY PFG

3.1. Diffusion NMR and its representation

In this section, we provide an outline of the theoretical and practical aspects of diffusometry NMR experiments that are the core of chrom-NMR. This issue has been reviewed at large[38,39] and thus only the key and most relevant aspects will be mentioned below. The displacement of a given molecular tracer is followed by a classical Stejskal–Tanner experiment. In this, pulses of magnetic field gradients are used to label the initial position of the tracer, and to follow its displacement along the direction of the gradient, Δz. Indeed, in a spin-echo experiment, any displacement corresponds to a reduction of the efficiency of the echo formation.

Recording a series of experiments with increasing echo time or gradient strength allows following and are typically studied by varying the intensity of the pulse field gradients (PFG).

This way the experiment has constant time duration over the series, and thus relaxation can be neglected to the first order, as it just provides a common scaling factor. Stimulated echo (STE)[40] is the most typical choice in the case of heterogeneous sample, as in this case the echo intensity is attenuated according to the slower longitudinal relaxation rate rather than by T_2 effects, which can be significantly effective in semi-solid environments. For Gaussian displacement propagators, the evolution of the STE intensity in such an experiment can be described in terms of the strength, g, and duration, δ, of the PFG along with the echo time delay, Δ, as[38]

$$I(g;\delta,\Delta) = S(g;\delta,\Delta)/S_{\text{ref}}(\delta,\Delta) = \exp[-Dq^2(\Delta - \delta/3)] \tag{1}$$

where S_{ref} is the echo intensity measured for null or, as most used in practical experiments, very weak PFG intensity. The use of a relative quantity allows eliding, to the first order, any effect due to the relaxation from the calculation. The variable q, with the dimension of an inverse distance, is equal to the product of the gradient pulse intensity, g, its duration, δ, and the nucleus the gyromagnetic ratio, γ. Gradient pulses short compared to the diffusion delay have been assumed. Finally, D is a quantity with the dimension of a diffusion constant defined by the average displacement along the gradient direction z', where the prime stress the fact that the gradient needs not to be parallel to the B_0 magnetic field direction

$$D = \frac{\left\langle z'^2(t) \right\rangle}{2\Delta} \tag{2}$$

In a solution, the diffusion constant D is described by Stokes–Einstein equation

$$D = \frac{kT}{6\pi\eta r_{\text{H}}} \tag{3}$$

with r_{H} the hydrodynamic ratio, T the temperature, k Boltzman constant, and η the medium viscosity. Diffusometry and its particular representation DOSY have inspired comparisons with chromatography, as the spectrum of molecules mixed in a solution with different D values can be separated spectrally by these methods, producing a layout resembling Thin Layer Chromatography (TLC). In the case of a mixture in a solution, significant differences in the diffusion coefficients are possible essentially due to variation of r_{H}, a parameter that is mainly linked to the molecular size.

The smaller differences in D distinguishable by NMR diffusometry depend on the quality of the mathematical treatment, but they hardly surpass a few percent in the most favourable cases.[41] Indeed, the presence in mixtures of overlapping signals requires an efficient inversion of a global version of Equation (1), the sum of several exponentially decaying trends, which is a mathematically challenging problem. The larger the difference in diffusion coefficients, the easier becomes this task, an observation that justifies the quest for methods capable of enhancing the spread of molecular mobility values in a mixture.

3.2. Diffusion in multiphasic environments

Addition to the mixture to analyse of a solid (e.g. a chromatographic phase, a porous glass, a zeolite) requires a specific theoretical framework for describing PFG NMR experiments in confined, heterogeneous environments.[42–44] A first aspect to take into account is that the several regions that constitute a multiphasic system are characterized by specific molecular mobilities. If the tracer under study evolves in such different environments, its average displacement will reflect the respective mobilities. As the displacement rate will vary along the measurement time, Δ, Equation (2) will measure rather an apparent diffusion coefficient, D_e, the description of which in physical terms may be not straightforward. The easiest cases to describe are the limit ones, in which the mass transport between the different phases is either extremely slow or extremely fast. Note that the timescale of the experiment, with respect to which the exchange rate should be compared, is again set by the delay Δ for diffusion encoding in the pulse sequence. In the case of slow or no exchange, molecules in different sections of the sample will change positions according to the local diffusion coefficients, and thus a multiexponential decay will be observed for the decay of the PFG STE intensity as a function of q. Conversely, an average apparent diffusion coefficient is characteristic of fast exchange

$$D_e = \sum_I x_i D_i \tag{4}$$

where x_i are the partition and D_i the diffusion coefficients of each environment. More complex functional forms are expected for apparent diffusion coefficients in the intermediate exchange regime.[42,45] For the purpose of chromatographic and pseudo-chromatographic experiments, the fast exchange regime is the only one that provides exploitable, reproducible outcomes. In the simplest situation, the tracer molecule is in a liquid- (L) or solid (S)-like phase and thus

$$D_e = x_L D_L + x_S D_S \tag{5}$$

In the approximation that diffusion of molecules adsorbed on the solid can be neglected to the first order, the measured diffusivity becomes an estimate of the partition of the tracer in the 'mobile phase', intended as the part of the sample in which high mobility is expected.

To summarize this section, a prerequisite for chromatographic NMR based on solid phases is a fast exchange kinetics among *slow* and *fast* diffusion environments of the tracer molecule. This is another analogy with liquid chromatography, where strongly bound molecules are a nuisance to the separation performance, as they tend to remain trapped behind.

Finally, a second aspect arising from the sample heterogeneity needs to be analysed. The magnetic susceptibility variation along the sample provides natural, internal magnetic field gradients that may interfere with the diffusometry measurement. Modification to the basic STE pulse sequence, such as the 13 pulses[46] or BPP-LED[47] acquisition schemes were devised to suppress this interference.

3.3. Specificity of diffusion PFG measurements in porous media

Additional care must be taken if the added solid has a porous structure. For instance, porous media add obstacles to the molecular movement as only the void space fraction, inside the pores and the between particles, is contributing to the transport. This is described typically by a parameter, the tortuosity factor, τ,[48] that illustrates the reduction of the space available with respect to the liquid phase as

$$D_e = \frac{D}{t} = D\varepsilon \tag{6}$$

where ε is the total porosity (the fraction of void space) of the sample.[43] For the present case, the tortuosity factor constitute merely a scaling factor, but one that could vary for different solids and should be taken into account if comparisons along a series of experiments are of interests.

It has been assumed in Equation (6) that the tracer can freely access all void space, be it intra- or interparticle. Note that if a barrier to this exchange exists instead, the possibility of the onset of anomalous diffusion should be considered.[42] In this case, the molecular displacement does not increase linearly as a function of the echo time, due to the physical threshold, which translates in an apparent reduction of the diffusion coefficients (till vanishing) for increasing Δ. Thus, the independence of D_e on the echo time must be controlled in order not to produce erratic experimental values.

4. EXAMPLES OF CHROM-NMR

4.1. Comparison with Liquid Chromatography (LC)

The first chronological demonstration of chrom-NMR is shown in Figure 1,[14] and consisted in testing an analogy of both inverse (naphthalene, ethanol and dec-1-ene in deuterated ethanol on a octadecylsilyl Octadecylsilane (ODS) phase) and direct (dichlorophenol, ethanol and heptane in deuterated cyclohexane over bare silica) chromatographic conditions. In these examples, a logical correspondence between the observed variation in mobility induced by the solid and the outcome expected on the basis of LC is confirmed. Thus, (Figure 1, top panels)

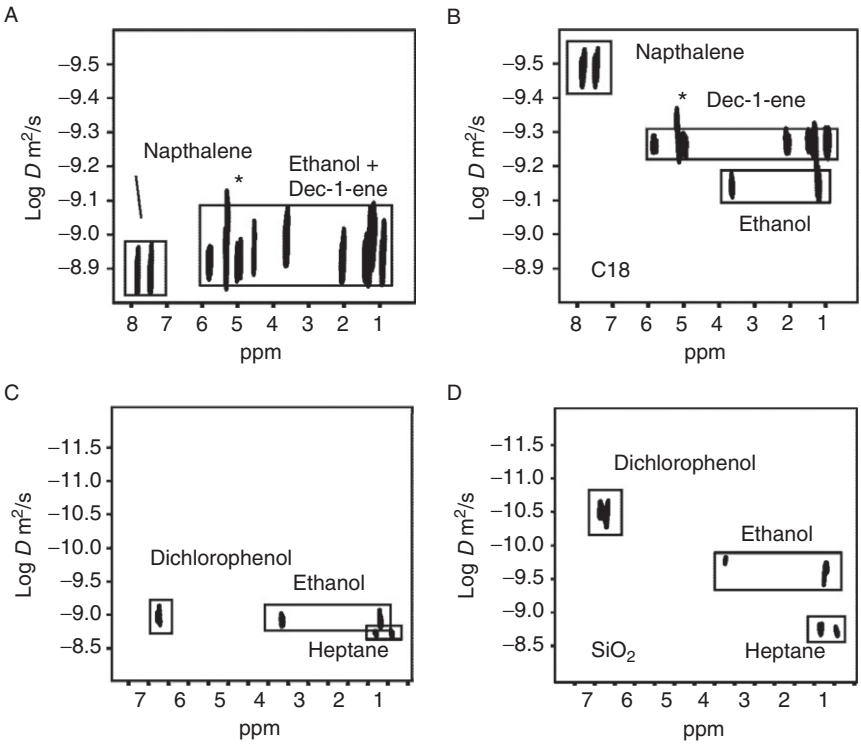

Figure 1 First chronological demonstration of the principle of chrom-NMR, on two pseudo-chromatographic setups. The top panels illustrate a DOSY layout for a mixture of naphthalene, ethanol and dec-1-ene in deuterated ethanol in pure solution (A) and upon addition of an ODS phase (B). A second set of DOSY experiments is shown in the bottom panels, for a mixture of dichlorophenol, ethanol and heptane in deuterated cyclohexane in pure solution (C) and upon addition of a bare porous silica phase (D). Adapted from Ref. 14. Copyright 2003 National Academy of Sciences, USA.

naphthalene, dec-1-ene and ethanol dissolved in deuterated ethanol have similar diffusivities in solution (Figure 1A), but they differ markedly once the chromatographic solid is added to the solution, the former molecule becoming less mobile (Figure 1B). Similarly, dichlorophenol, ethanol and heptane mixed in perdeuterated cyclohexane apparent diffusion coefficients are modified by the addition of a bare silica gel (Figure 1, bottom panels) according to their expected affinity for the solid, none for heptane, highest for the π-electron-rich diol. To recover resolution, the spectra are recorded under MAS, as explained above.

However, the analogy between LC and chrom-NMR is not strictly respected in all occurrences of the experiment. Indeed, significant variations have been highlighted. Figure 2 shows chrom-NMR spectra of a series of aromatic homologues (benzene, naphthalene, anthracene) in two sets of pseudo-chromatographic conditions.[49] The use of homologue molecules is a common practice in chromatographic characterization of interactions and partition effects. The top panels illustrate a typical LC separation for aromatic molecules, featuring an ODS phase and a mobile phase in isocratic conditions (left top panel) and its chrom-NMR counterpart (left bottom panel). Both techniques provide an excellent separation of the three components, physical for LC and purely spectral for chrom-NMR. The elution order of the aromatic molecules in the LC experiment (benzene, naphthalene, anthracene) reflects the expected partition coefficient, based on the growing number of carbons, and thus hydrophobicity, along the series. In perfect analogy, anthracene is found to be the slowest molecule of the set by NMR diffusometry, followed by naphthalene and benzene. The bottom panel represents a similar experiment, in which only the solid phase was changed, for a bare silica gel. With this choice of conditions, LC fails to separate the three compounds, while the outcome of the chrom-NMR experiment is as effective as in the precedent example.

The somewhat unexpected, and in this case superior, performance of chrom-NMR with respect to LC can be rationalized in terms of the different phase ratio used in the two experiments. Indeed, chromatographic columns have typically much larger volumes of the mobile than of the solid phase. Particularly, specific variations in the separation potential induced by a silica gel are observed if its pores are partially or completely filled. The broadest impact relevance of this aspect is under investigation. Note that in both chrom-NMR examples, benzene is found to diffuse faster than in pure solution. This apparently surprising effect is due to the high volatility of this specific tracer, which allows for vapour phase molecules to contribute to the average mass transport rate.[48,50,51] Following these results, it becomes interesting to explore if bare silica can act as a broad active adsorbent for chrom-NMR purposes.

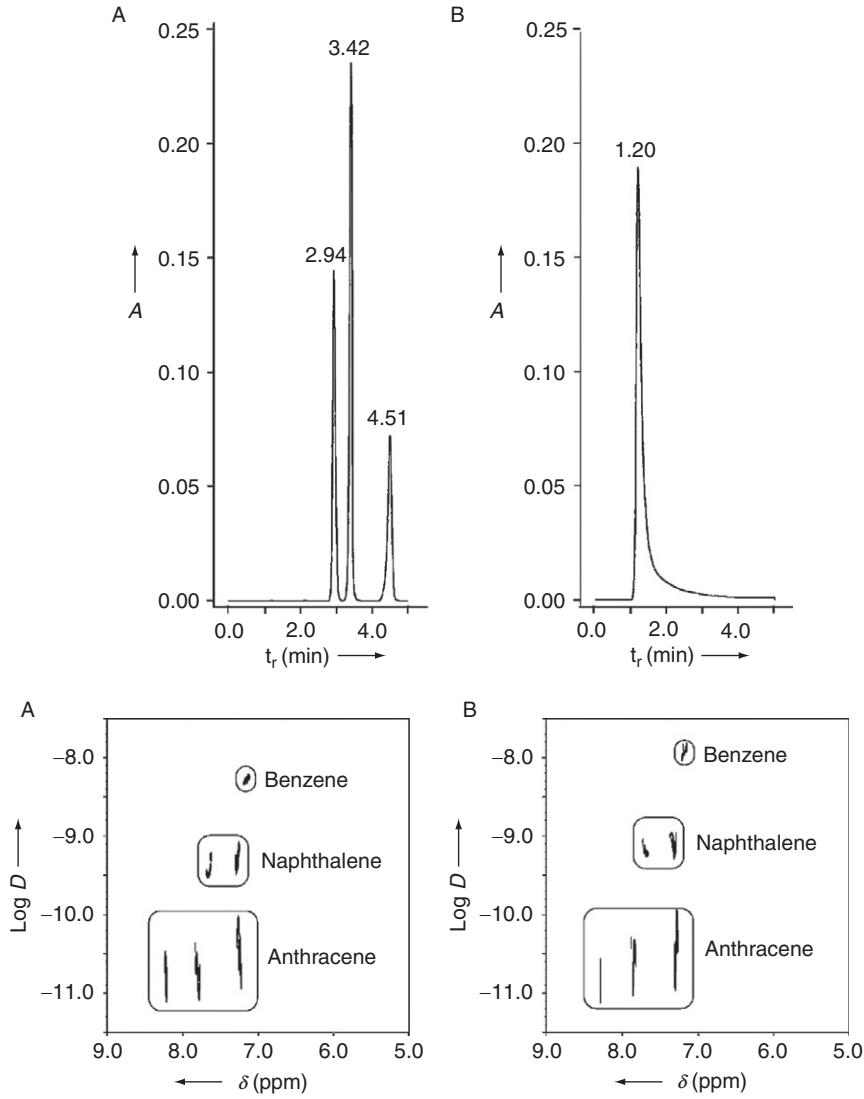

Figure 2 Comparison of HPLC (top panels) and chrom-NMR (bottom panels) for a series of homologous aromatic molecules, recorded under RPLC (left panels: ODS solid phase and water/acetonitrile mobile phase) and HILIC conditions (right panels: bare silica solid phase and water/acetonitrile mobile phase). From Ref. 49. Copyright 2006 Wiley-VCH Verlag GmbH & Co. KGaA, Weinheim.

4.2. Non-chromatographic mobile phases

The composition of the mobile phase plays a crucial role in determining the partition coefficient and it is thus a key aspect for separation in liquid chromatography. This parameter was observed to influence chromatographic NMR experiments as well, as summarized in Figure 3. Different solvent compositions, with a varying water/acetonitrile ratio, induced distinguishable diffusion constant for two series of homologue tracers, aromatic molecules and ketones.[52] In the case of the aromatic homologues, benzene is the most strongly affected by addition of an increased amount of water to acetonitrile, followed by naphthalene and anthracene. For the three compounds, an increase in mobility is observed.

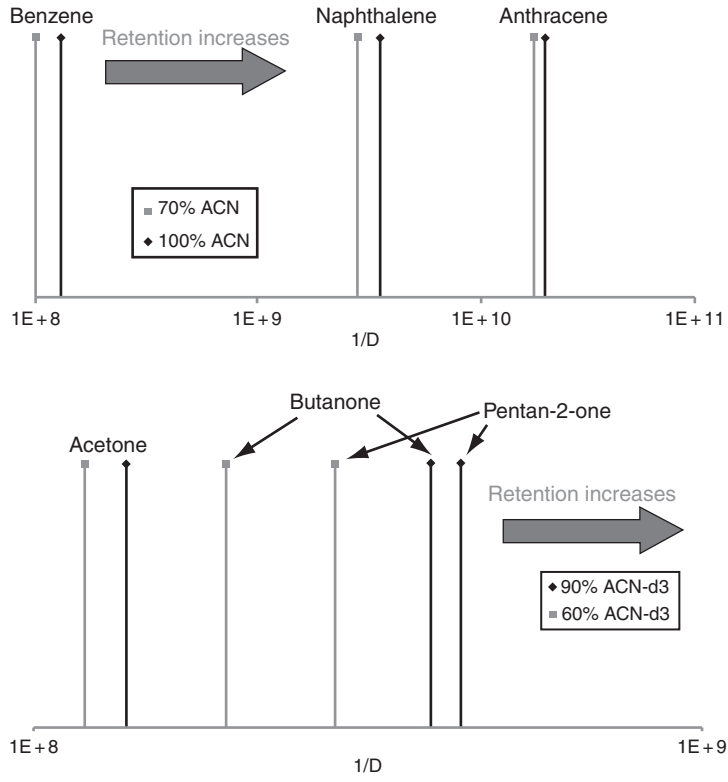

Figure 3 Impact of the mobile phase composition on the apparent diffusion constant on series of homologue molecules. *Top panel*: evolution of the reciprocal apparent diffusion constant for three aromatic homologue molecules for two compositions of the mobile phase. *Bottom panel*: representation of the variation of the reciprocal apparent diffusion constant for a series of ketones for two compositions of the mobile phase. Adapted with permission from Ref. 52. Copyright 2006 American Chemical Society.

A stronger impact on the apparent diffusion constants due to increasing the water addition is observed for the series of ketones. Among acetone, butanone and pentan-2-one, the two latter molecules mobilities are strongly influenced by water addition. Acetone diffusion constant, on the other hand, did not vary appreciably with the augmentation of the water ratio, consistently with its common role of inert in reverse phase liquid chromatography (RPLC). These results points towards a competitive effect of water, rather than a mere variation of the partition coefficient, although a more complete investigation would be required to accurately describe the relevance of the solvent composition on the tracer diffusivities.

Another aspect affecting the solvent choice in the case of ^{1}H NMR measurements is that deuterated solvents are the most convenient option.[53] In principle, the deuterated version of regular LC mobile phases could be used, as deuteration has been shown to have only a minor effect on the partition,[52] and they were applied in the studied outlined above.

However, the selection of commercially available deuterated molecules does not cover all the typical choices of LC studies, and it would be most practical to use the common selection of NMR solvents. The performance of chrom-NMR in two typical deuterated solvents, chloroform-d_3 and heavy water, is shown in Figure 4, using bare silica as the retarding solid phase.[53] The aromatic homologue series (benzene, naphthalene, anthracene) is well separated in the chloroform/silica DOSY (Figure 4, left panel). As an example of polar compounds, a series of alcohols (methanol, isopropanol, phenol, ethylene glycol) has been analysed by chrom-NMR. Figure 4 shows that this ensemble of molecules interacts with the solid phase proportionally to their ability at forming hydrogen bonds, with the exception of the phenol that can additionally interact with silica through its π-electron system.

Another example of the use of non-chromatographic solvents was mentioned above, as a mixture susceptibility matched to silica, and it is

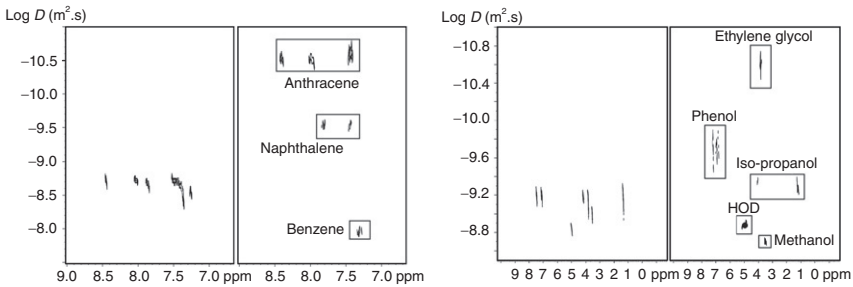

Figure 4 Example of the application of chrom-NMR/HRMAS with regular NMR solvents and bare silica as a solid phase. *Left panel*: aromatic molecule homologues in deuterated chloroform: benzene, naphthalene and anthracene. *Right panel*: alcohol mixture ethylene glycol, phenol, isopropanol in deuterated water. Adapted with permission from Ref. 53. Copyright 2008 Elsevier.

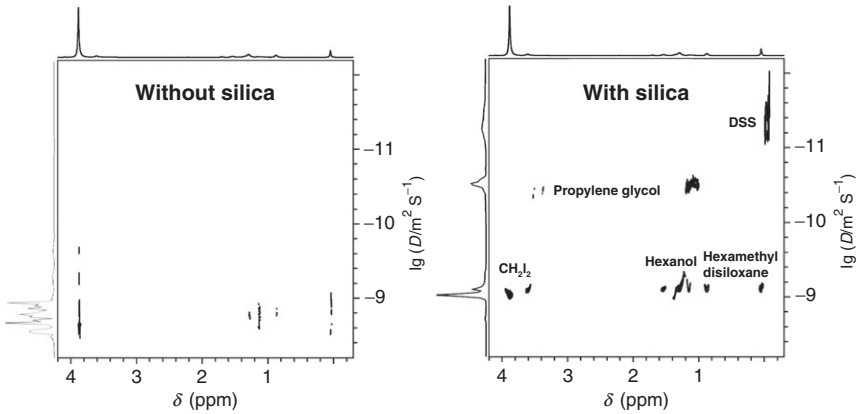

Figure 5 ^{1}H DOSY without (left panel) and with (right panel) the addition of silica illustrating chrom-NMR without HRMAS, as the mobile phase (a $CHCl_3/CH_2I_2$ mixture) is magnetic susceptibility matched to bare silica. Adapted with permission from Ref. 23. Copyright 2008 Elsevier.

exemplified in Figure 5, where the overlapping DOSY signal of hexanol and propylene glycol become resolved upon addition of a silica gel suspension in a solvent mix of $CHCl_3$ and CH_2I_2.[23]

Soluble polymers, such as polyvinylpyrrolidone (PVP) or polyethylene glycol (PEG) with an MW of the order of 10,000, constitute the most recent addition as a delaying agent in the chrom-NMR methodology.[24,25] Used in concentrations largely exceeding the one of the analytes, the soluble polymers provides an adequate and selective slow-diffusing moiety that can induce the pseudo-chromatographic effect in DOSY (Figure 6).

Finally, the use of micelles as a retarding agent, initially demonstrated in 1994,[16] is being reinvestigated in the perspective of chrom-NMR.[26,27]

5. CONCLUSIONS

Since its inception, the concept of chromatographic NMR, the introduction of a selectively delaying agent in a mixture to increase the spread of average mobility of its constituents to easy their identification, has been explored in several directions, borrowing from the vast literature of liquid chromatography on one hand, but also expanding along other directions with the use of systems better suitable for NMR (e.g. deuterated NMR solvents) and non-LC matrices, like micelles.

To date, the method is still in a phase of exploratory research, focusing on the understanding of its technical requirements and limitations, in

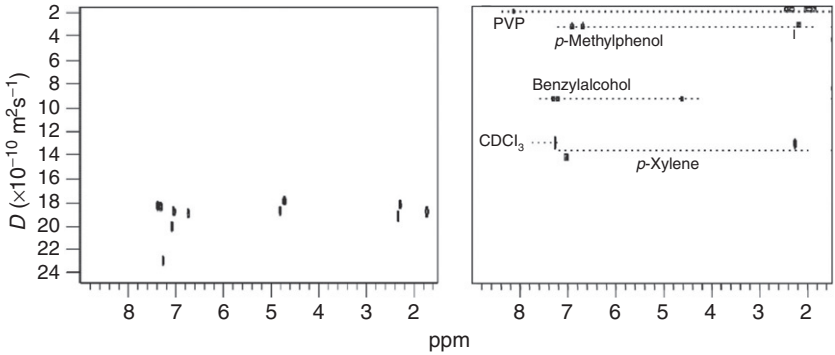

Figure 6 Polymer-induced pseudo-chromatographic effect in NMR diffusometry using polyvinylpyrrolidone (PVP) of an MW of 10,000 in deuterated chloroform. Regular DOSY (left) and chrom-NMR (right) on a mixture of benzylalcohol, *p*-methylphenol and *p*-xylene mixture. Adapted with permission from Ref. 24. Copyright 2009 American Chemical Society.

much a similar way as LC devoted a large effort to categorize the best conditions for specific separations.

ACKNOWLEDGEMENTS

This work was financially supported by ANR (Grant ANR-08-BLAN-273-01) and by the Région Provence-Alpes-Côte d'Azur (APO-G 2009).

REFERENCES

1. J. C. Lindon, J. K. Nicholson, E. Holmes (eds.) The Handbook of Metabonomics and Metabolomics. Elsevier Science, B.V., Amsterdam, 2007.
2. J. L. Ward and M. H. Beale, *in*: Plant Metabolomics, K. Saito, R. A. Dixon, and L. Willmitzer (eds.) Springer, Berlin Heidelberg, 2009.
3. L. Shintu, F. Ziarelli and S. Caldarelli, *Magn. Reson. Chem.*, 2004, **42,** 396–401.
4. L. Shintu and S. Caldarelli, *J. Agric. Food Chem.*, 2005, **53,** 4026–4031.
5. S. W. Provencher, *Comput. Phys. Commun.*, 1982, **27,** 229–242.
6. W. Windig and B. Antalek, *Chemom. Intell. Lab. Syst.*, 1997, **37,** 241–254.
7. M. Delsuc and T. Malliavin, *Anal. Chem.*, 1998, **70,** 2146–2148.
8. G. S. Armstrong, N. M. Loening, J. E. Curtis, A. J. Shaka and V. A. Mandelshtama, *J. Magn. Reson.*, 2003, **163,** 133–148.
9. M. Nilsson and G. Morris, *Magn. Reson. Chem.*, 2006, **44,** 655–660.
10. R. C. Sebastião, C. N. Pacheco, J. Braga and D. Piló-Veloso, *J. Magn. Reson.*, 2006, **182,** 22–28.
11. R. Huo, R. Wehrens and L. M. C. Buydens, *Chemom. Intell. Lab. Syst.*, 2007, **85,** 9–19.
12. M. Nilsson, *J. Magn. Reson.*, 2009, **200,** 296–302.
13. J. A. Jones, P. Hodgkinson, A. L. Barker and P. J. J. Hore, *Magn. Reson. B*, 1996, **113,** 25–34.
14. S. Viel, F. Ziarelli and S. Caldarelli, *Proc. Natl. Acad. Sci. USA*, 2003, **100,** 9696–9698.
15. M. Lin, M. J. Shapiro and J. R. Wareing, *J. Am. Chem. Soc.*, 1997, **119,** 5249–5250.

16. K. F. Morris, P. Stilbs and C. S. Johnson, *Anal. Chem.*, 1994, **66,** 211–215.
17. H. Handel, E. Gesele, K. Gottschall and K. Albert, *Angew. Chem. Int. Ed.*, 2003, **42,** 438.
18. U. Skogsberg, H. Handel, D. Sanchez and K. Albert, *J. Chromatogr. A*, 2004, **1023,** 215–223.
19. S. Schauff, V. Friebolin, M. D. Grynbaum, C. Meyer and K. Albert, *Anal. Chem.*, 2007, **79,** 8323–8326.
20. U. Skogsberg, C. Meyer, J. Rehbein, G. Fischer, S. Schauff, N. Welsch, K. Albert, A. J. Hall and B. Sellergren, *Polymer*, 2007, **48,** 229–238.
21. V. Friebolin, M. P. Bayer, M. T. Matyska, J. J. Pesek and K. Albert, *J. Sep. Sci.*, 2009, **32,** 1722–1728.
22. V. Friebolin, S. Marten and K. Albert, *Magn. Reson. Chem.*, 2010, **48,** 111–116.
23. R. E. Hoffman, H. Arzuan, C. Pemberton, A. Aserin and N. Garti, *J. Magn. Reson.*, 2008, **194,** 295–299.
24. J. S. Kavakka, I. Kilpelainen and S. Heikkinen, *Org. Lett.*, 2009, **11,** 1349–1352.
25. J. S. Kavakka, V. Parviainen, K. Wahala, I. Kilpelainen and S. Heikkinen, *Magn. Reson. Chem.*, 2010, **48,** 777–781.
26. C. F. Tormena, R. Evans, S. Haiber, M. Nilsson and G. A. Morris, *Magn. Reson. Chem.*, 2010, **48,** 550–553.
27. R. Evans, S. Haiber, M. Nilsson and G. A. Morris, *Anal. Chem.*, 2009, **81,** 4548–4550.
28. A. N. Garroway, *J. Magn. Reson.*, 1982, **49,** 168–171.
29. T. M. J. Barbara, *Magn. Reson. A*, 1994, **109,** 265–269.
30. W. E. Maas, F. H. Laukien and D. G. Cory, *J. Am. Chem. Soc.*, 1996, **118,** 13085–13086.
31. F. D. Doty, G. Entzminger and Y. A. Yang, *Concepts Magn. Reson.*, 1998, **10,** 239–260.
32. J. M. Wieruszeski, G. Montagne, G. Chessari, P. Rousselot-Pailley and G. Lippens, *J. Magn. Reson.*, 2001, **152,** 95–102.
33. W. J. Goux, L. A. Verkruyse and S. J. Salter, *J. Magn. Reson.*, 1990, **88,** 609–614.
34. N. Esturau, F. Sanchez-Ferrando, J. A. Gavin, C. Roumestand, M. A. Delsuc and T. Parella, *J. Magn. Reson.*, 2001, **153,** 48–55.
35. S. Viel, F. Ziarelli, G. Pages, C. Carrara and S. Caldarelli, *J. Magn. Reson.*, 2008, **190,** 113–123.
36. H. C. Gaede and K. Gawrisch, *Magn. Reson. Chem.*, 2004, **42,** 115–122.
37. O. M. Cholewa, *J. Chromatogr. A*, 2004, **1046,** 277–287.
38. C. S. Johnson, *Prog. Nucl. Magn. Reson. Spectrosc.*, 1999, **34,** 203–256.
39. C. S. Johnson, Jr., *in*: Encyclopedia of Nuclear Magnetic Resonance, D. M. Grant and R. K. Harris (eds.), Wiley, Chichester, 1996, pp. 1626–1644.
40. E. L. Hahn, *Phys. Rev.*, 1950, **80,** 580–594.
41. P. Thureau, A. Thevand, B. Ancian, P. Escavabaja, G. S. Armstrong and V. A. Mandelshtam, *ChemPhysChem*, 2005, **6,** 1510–1513.
42. J. Karger, *Adv. Colloid Interface Sci.*, 1985, **23,** 129–148.
43. I. Ardelean and R. Kimmich, *Annu. Rep. NMR Spectrosc.*, 2003, **49,** 44–115.
44. F. Stallmach and P. Galvosas, *in*: Annual Reports on NMR Spectroscopy, (G. Webb ed.), Elsevier, 2007, pp. 51–131, Vol. 61.
45. I. Ardelean, G. Farrher, C. Mattea and R. Kimmich, *J. Chem. Phys.*, 2004, **120,** 9809–9816.
46. R. M. Cotts, M. J. R. Hoch, T. Sun and J. T. Markert, *J. Magn. Reson.*, 1989, **83,** 252–266.
47. D. H. Wu, A. D. Chen and C. S. Johnson, *J. Magn. Reson. A*, 1995, **115,** 260–264.
48. F. D'Orazio, S. Bhattacharja, W. P. Halperin and R. Gerhardt, *Phys. Rev. Lett.*, 1989, **63,** 43–46.
49. G. Pages, C. Delaurent and S. Caldarelli, *Angew. Chem. Int. Ed.*, 2006, **45,** 5950–5953.
50. J. Karger, H. Pfeifer, E. Riedel and H. Winkler, *J. Colloid Interface Sci.*, 1973, **44,** 187–188.
51. C. Carrara, G. Pages, C. Delaurent, S. Viel, S. Caldarelli, submitted.
52. G. Pages, C. Delaurent and S. Caldarelli, *Anal. Chem.*, 2006, **78,** 561–566.
53. C. Carrara, S. Viel, C. Delaurent, F. Ziarelli, G. Excoffier and S. Caldarelli, *J. Magn. Reson.*, 2008, **194,** 303–306.

CHAPTER 6

Kinetic Monte Carlo Simulation of DNMR Spectra

Zsófia Szalay and **János Rohonczy**[1]

Contents

Abstract

Conventional dynamic NMR spectrum simulation methods are based on the solution of the phenomenologically extended Liouville–von Neumann equation of spin systems in Liouville space. In this work, we show an alternative method in which the

Department of Inorganic Chemistry, Institute of Chemistry, Eötvös Loránd University, Budapest, Hungary
[1] Corresponding author.

Annual Reports on NMR Spectroscopy, Volume 73
ISSN 0066-4103, DOI: 10.1016/B978-0-08-097074-5.00006-2

effects of the exchange processes and the scalar couplings can be separated. The spin interactions are described by quantum mechanics while the dynamic effects are characterised by statistical methods. The easiest way to handle the latter one is by means of the Kinetic Monte Carlo (KMC) simulation. The KMC calculation method presented here provides a possible extension of the single spin vector model to weakly and strongly coupled spin systems as well. The crucial point is the linear transformation between the basis functions and the eigenfunctions (or coherences) during the detection and exchange processes. The mathematical description based on individual density matrices is complete in the Hilbert space.

Key Words: Dynamic NMR, Kinetic Monte Carlo, Chemical exchange, Spin system, Spin set, Individual density matrix, Trajectory, Eigencoherence, Vector model, Mutual exchange, Nonmutual exchange.

1. INTRODUCTION

Since the dawn of NMR spectroscopy, it is known that the NMR spectrum of certain substances exhibits a strong temperature dependence. When heated the spectral lines of such samples first broaden, then coalesce, and finally they slowly sharpen again, the chemical shifts of the new signal is the weighted average of the individual ones.[1–7] The reason of such behaviour of spectral lines is that the chemical environment is eventually changing around the NMR active nuclei due to a dynamic equilibrium process. There could be several chemical causes for the exchange processes, such as intramolecular conformational motion (rotation, pseudo-rotation, ring inversion, etc.) or intermolecular migration.[8–14] Strong temperature dependence occurs when the mean lifetime of the individual conformers are comparable with the length of acquisition time of the NMR signal (free induction decay (FID)). If the exchange process is slow, that is, the conformer has a long mean lifetime, the NMR signals of the individual conformers are sharp, and the spectrum is composed of the superposition of the spectra of the conformers. With the reduction of lifetime, the spectral lines first broaden, and then they give sharp peaks in the case of extreme fast exchange limit once again (Figure 1).[15] With the simulation of dynamic NMR (DNMR) spectra and their fitting to the experimental ones, the time constants of the exchange processes can be determined on a rather wide, approximately 10^{-1}–10^{6} s^{-1} interval.

The quantum mechanical description of DNMR spectra runs back over several decades.[16] In the widespread theory based on the average density matrix, the quantum mechanical state functions are time dependent;

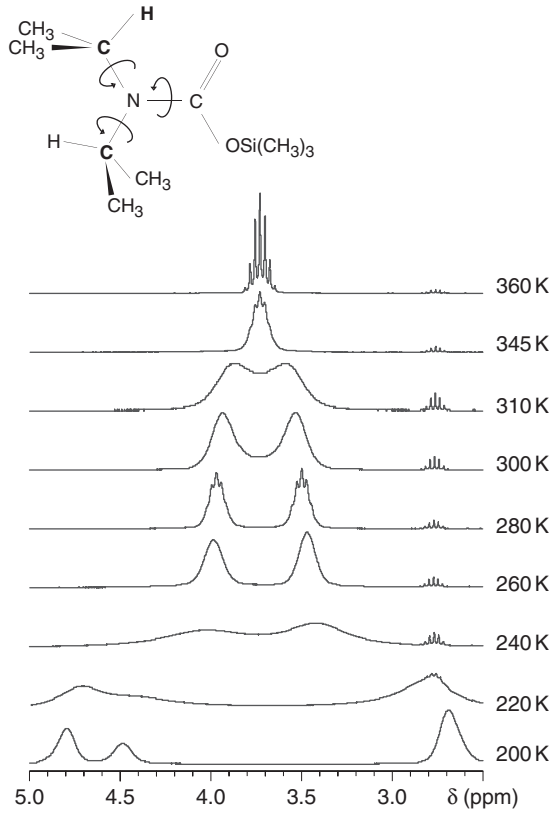

Figure 1 Temperature dependence of the methyne ^{1}H NMR signal of *N*,*N*-diisopropyl carbamic acid trimethyl silyl esther (DMSO-d_6, 250 MHz).[15]

hence the solution of the time-dependent Schrödinger equation describes the system.[12] Accuracy is the advantage of this calculation method; however, the inherent disadvantage is the large memory requirement, which scales exponentially with the number of nuclei. This memory demand restricts the size of the accessible spin systems to 10–15 nuclei.

An alternative method for the simulation of DNMR spectrum in the case of isolated nuclear spins is known for a long time as well.[9] The essence of this method is that magnetisation vectors are assigned to the single quantum coherences which process at a constant speed giving detectable signals in the time intervals between the nuclear exchanges. After the instantaneous exchange, the vectors continue their precession without phase jump with their new frequencies corresponding to their new environment. The macroscopic signal is obtained by the superposition of the signals of several submicroscopic (quantum) systems. They differ from one another in the length and order of the intervals spent at

the certain environments: they start from either of the conformers, change their states randomly but have a well-defined mean lifetime.

This stochastic behaviour of the submicroscopic (quantum) systems can be well described by mathematical models where both the discrete starting state and the time of the conformational change are determined by a roll of dice, that is, with a random number generator. This simple model belongs to kinetic Monte Carlo (KMC) methods,[17] where the behaviour of the macroscopic system arises from the average of some selected microstates. The advantage of this method is its expressiveness on the one hand, and on the other hand, it decouples the time-dependent interactions (the frequency change at the moment of the exchange) to a series of time-independent interactions.

The detectable signal in the time intervals between the moments of exchanges can be determined by solving the time-dependent Schrödinger equation for the specific conformer; however, in this case, the Hamiltonian is independent of time.[18] The advantage of this method is its smaller memory requirement; its disadvantage is the longer computational time because of the Monte Carlo simulation and that it was not possible to apply it to coupled spin systems so far.

The purpose of this publication is to present the DNMR spectra calculation based on a Monte Carlo simulation of coupled spin systems as an alternative to the density matrix-based calculation.

2. STATIC NMR SPECTRA AND THE DESCRIPTION OF DYNAMIC EXCHANGE PROCESSES

2.1. Simulation of static NMR spectra

2.1.1. Constructing the matrix of the Hamiltonian

Calculation of DNMR spectra is based on the construction of operators of interactions of the system and solving their eigenvalue problem. The most complicated interactions are the perturbation effects of the chemical shielding and the scalar coupling on the resonance frequency. The descriptions for these interactions are the same in both dynamic and 'static' (free from chemical exchange processes) systems. Let n be the number of nuclei in a spin system, μ and μ' the indices of the nuclei in it, ν_μ the frequency (in Hz) corresponding to the chemical shift of μ nuclei and $J_{\mu\mu'}$ the coupling constant between nuclei μ and μ'. Then the Hamiltonian for static interactions in the liquid state can be written in frequency units as[19]:

$$\hat{H} = 2\pi \sum_{\mu=1}^{n} \nu_\mu \hat{I}_{z\mu} + \pi \sum_{\mu=1}^{n} \sum_{\mu'=\mu+1}^{n} J_{\mu\mu'} \left(\hat{I}_\mu^+ \hat{I}_{\mu'}^- + \hat{I}_\mu^- \hat{I}_{\mu'}^+ + 2\hat{I}_{z\mu} \hat{I}_{z\mu'} \right), \qquad (1)$$

where $\hat{I}_{z\mu}$ is the z component of the spin operator, while $\hat{I}_{\mu}^{+}$ and $\hat{I}_{\mu}^{-}$ are the raising and lowering operators of nucleus μ.

The orthonormal basis generally prevalent in numerical simulations is composed of the product functions (henceforth, ϕ_a), which are the products of the spin functions of the nuclei in all the possible variations. In this case, the μ index of the nucleus can be abandoned, because the order of the atomic functions already defines it. There are 2^n product functions in the case of n spin-half nuclei. On this basis, the matrix of the Hamiltonian is composed of the following elements:

$$H_{ab} = \delta_{ab}\left(2\pi\sum_{\mu=1}^{n} m_{\mu}^{(a)}\nu_{\mu} + \frac{\pi}{2}\sum_{\mu=1}^{n}\sum_{\mu'=\mu+1}^{n} J_{\mu\mu'}D_{\mu\mu'}^{(a)}\right) + (1-\delta_{ab})\pi\sum_{\mu=1}^{n}\sum_{\mu'=\mu+1}^{n} J_{\mu\mu'}F_{\mu\mu'}^{(ab)}, \tag{2}$$

where δ_{ab} is the Kronecker-delta ($\delta_{ab} = 1$, if $a = b$, otherwise 0), $D_{\mu\mu'}^{(e)} = -1$ or 1, if the μth and μ'th spin functions are antiparallel or parallel in the ath basis function, $m_{\mu}^{(a)}$ is the eigenvalue of operator $\hat{I}_{z\mu}$ corresponding to the ϕ_a basis function and $F_{\mu\mu'}^{(ab)}$ equals 1, if ath and bth basis functions have the same total spin quantum number and they differ from each other exactly by the spin functions of nuclei μ and μ', otherwise they are zero.[19]

The first operand between the parentheses in Equation (2) contains the diagonal, the second one the off-diagonal components of the matrix. The diagonal components are also composed of two members, from which the second one gives the first-order approximation of the coupling.

By diagonalising the matrix, we get the eigenstates (ψ_k) of the system and their corresponding frequencies in angular units (λ_k). The eigenstates can be expressed as a linear combination of the product functions.

$$\psi_k = \sum_a u_{ak}\phi_a, \tag{3}$$

where the u_{ak} coefficients are real and the U matrix constructed of them is unitary.

The differences between the energy levels give the transition frequencies of the spin system. To calculate the intensity of the signals corresponding to the frequencies, the excitation operator of the entire spin system is introduced ($\hat{I}^{+}$):

$$\hat{I}_{+} = \sum_{\mu=1}^{n}\hat{I}_{+\mu}. \tag{4}$$

The intensity of the spectral lines is the product of the excitation operator and those two eigenstates, whose coherence gives the signal of intensity Y:

$$Y_{kl} = \left|\left\langle \psi_k | \hat{I}^{+} | \psi_l \right\rangle\right|^2 = \left(\sum_{a,b} u_{ak} u_{bl} I_{ab}\right)^2, \tag{5}$$

where $I_{ab} = 1$, if the $\phi_a \rightarrow \phi_b$ transition is allowed, otherwise 0.[19]

According to Equation (2), only those H_{ab} off-diagonal elements of the Hamiltonian can differ from 0, in the case of which the total spin quantum number of ϕ_a and ϕ_b basis functions are identical (since $F_{\mu\mu'}^{(ab)} = 1$ can occur this way only). Thus the H matrix can be arranged into blocks according to their total spin quantum number. The total spin quantum number can have $n + 1$ different values in the case of n spin-half nuclei, so the Hilbert-space decomposes into $n + 1$ invariant subspaces according to I_{tot}. Due to the block-diagonal form of the Hamiltonian, each ψ_k eigenfunction is in one of these subspaces.

2.2. Simulation of DNMR spectra with average density matrix method

The average density operator for the macroscopic system is defined as follows:

$$\bar{\rho}(t) = \sum_k p^k \left|\psi^k(t)\right\rangle\left\langle\psi^k(t)\right| = \sum_k p^k \sum_i \sum_j u_i^k(t) u_j^{k*}(t) \left|\phi_i\right\rangle\left\langle\phi_j\right|, \tag{6}$$

where p^k is the probability of kth state.[12] The individual probabilities express the macroscopic distribution of the individual states, so the Boltzmann distribution is describing the thermodynamic equilibrium and the concentration of the conformers in the case of dynamic exchanges.

In the average density matrix method, the equation of motion is based on the Liouville–von Neumann equation, whose commutator form is:

$$\frac{\mathrm{d}\bar{\rho}}{\mathrm{d}t} = -i\left[\bar{H}, \bar{\rho}\right], \tag{7}$$

where $\bar{\rho}$ is the average density matrix of the spin system, t denotes time, while $\bar{H}$ is the Hamiltonian of the system. The later one can be constructed according to Equation (2) taking into account all the nuclei in the spin system, including the spins in the exchange partners as well.[20]

Equation (7) is understood in the space spanned by the ϕ_a basis states (Hilbert space) alike to the simulation of static NMR spectra. This equation describes the interactions between the spins.

Further—phenomenological—components should be added to the equation to include the dynamic effects (relaxation, exchange processes). For describing the exchange processes, the $\Gamma^{(h)}$ transformation matrix (where h denotes the index of the exchange process) should be defined for all the exchange processes, which permute the basis functions of the spin system in the Hilbert space according to the exchange process of the nuclei. Due to this basis transformation, the $\bar{\rho}$ matrix alters, and thus the equation of motion that describes this change of the average density matrix is as follows:

$$\frac{\mathrm{d}\bar{\rho}}{\mathrm{d}t} = \sum_{h=1}^{m'} k_h \left(\Gamma^{(h)} \bar{\rho} \left(\Gamma^{(h)} \right)^{\mathrm{T}} - \bar{\rho} \right), \tag{8}$$

where k_h is the rate coefficient of the hth exchange process, m' is the number of exchange processes defined within the spin system, $(\Gamma^{(h)})^{\mathrm{T}}$ is the transpose (and also the inverse) of $\Gamma^{(h)}$.[21,22]

The relaxation is described exactly by Redfield's operator,[23] which allows the relaxation between any two functions within the spin system. The following simplified equation based on the Bloch equations can be used instead of it as well[8]:

$$\frac{\mathrm{d}\bar{\rho}}{\mathrm{d}t} = \frac{\bar{\rho}_{\mathrm{eq}} - \bar{\rho}}{T_1} - \frac{\bar{\rho}}{T_2}, \tag{9}$$

which is the diagonal approximation of the Redfield's operator (T_1 and T_2 are the time constants of the spin–lattice and the spin–spin relaxations, respectively). Generally, this component can be further simplified while the relaxation operator becomes a scalar, the spectral broadening effect of which can be calculated independently even after the simulation.

The differential equation to be solved for the simulation is the sum of Equations (7)–(9) in the Hilbert space:

$$\frac{\mathrm{d}\bar{\rho}}{\mathrm{d}t} = -\mathrm{i}[H, \bar{\rho}] + \sum_{h=1}^{m'} k_h \left(\Gamma^{(h)} \bar{\rho} \left(\Gamma^{(h)} \right)^{\mathrm{T}} - \bar{\rho} \right) + \frac{\bar{\rho}_{\mathrm{eq}} - \bar{\rho}}{T_1} - \frac{\bar{\rho}}{T_2}. \tag{10}$$

Equation (10) cannot be solved in the Hilbert space, mainly due to the component describing the exchange processes (Equation (8)). To calculate the NMR spectrum, Equation (10) is first transformed into the vector space spanned by the single quantum transitions (the Liouville space the dimension of which is $M = \binom{2n}{n-1}$), and the first-order differential equation obtained is solved in this vector space. During the transformation, the average density matrix ($\bar{\rho}$) becomes a vector, and the dimension of the simulation space becomes larger than that of the Hilbert space. This increase in size is the bottleneck of the method, since it severely restricts the size of the systems to be simulated.

2.2.1. Conventional, deterministic programs for DNMR spectrum simulation

The first programs for calculating dynamic spectra were developed in the 1960s.[24–26] These programs simulate DNMR spectra based on the principles described in the previous chapter. The last known version of the original series was the DNMR5 program,[27] which is the basis for the recently developed DNMR spectra simulating programs. This program suite enables the calculation of spectra of a few (five to six) coupled nuclei, with arbitrary number of (first-order) exchange processes among them.

In the recent years, a program with a new approach named[28–31] MEXICO has been developed. This program also calculates spectra based on the principles described in the previous chapter, but it contains several innovations in programming technique (the efficient storage of sparse matrices,[32] Lanczos-iteration,[33] dynamic memory allocation) which make it significantly faster and more stable than the previous DNMR5. Apparently, MEXICO can only handle two-site exchange processes, and the currently published version gives erroneous results for non-mutual exchanges between coupled spins.

WinDNMR 7.1 program is suitable for the simulation and parameter fitting of DNMR spectra of spin systems containing approximately five nuclei.[34–37] This program works along similar principles as the ones previously mentioned, its easy to use graphical interface helped to become well known in the NMR community.

The TEDDY module of the Bruker BioSpin® GmbH TopSpin™ program[38] for calculating DNMR spectra is based on the Liouville–von Neumann equation extended with the exchange processes as well. The program can handle arbitrary spin systems (up to ~10 nuclei), spin groups described with a pseudo-spin[39] and arbitrary number of exchange processes involving several nuclei.

Apart from the programs mentioned, most spectrum-processing suites contain modules for simulating DNMR spectra and for fitting spectral parameters (MNova™-NMR,[40] iNMR,[41] SpinWorks,[42] NUTS,[43] NMRLoop[44]).

3. CALCULATION OF DNMR SPECTRA WITH THE KINETIC MONTE CARLO METHOD

In general, Monte Carlo simulations are such calculations in which the values of some parameters are determined by the average of some randomly generated individuals.[45–54] In chemistry applications, the most prevalent methods are the so called Metropolis Monte Carlo (MMC)[55] and Reverse Monte Carlo (RMC) ones. The most important quantities in these methods are some kinds of U energy-type potentials (e.g. internal energy, enthalpy,

Helmholtz free energy, Gibbs free energy depending on the physical model or the difference of the calculated and some experimental data in case of RMC). A component of the ensemble gets into the sample with a probability of min[1, exp(− $\Delta U/RT$)], where ΔU is the difference in potential energy between the observed configuration and the last component of the sample. Then the physical quantity in question (e.g. density, surface tension, geometric parameters) is calculated and averaged on the sample. This method was used in several fields of chemistry including material studies,[56–58] biochemistry[59–62] and structural chemistry.[63–88]

In MMC simulations, always a representative parameter of the system being in equilibrium is calculated. These simulations are unsuitable for modelling changes in time.

In a wider sense, Monte Carlo simulation refers to all simulations, in which random numbers receive a role. A group of them—the one of the KMC methods—is suitable for the modelling of dynamic processes. KMC is a method for statistic evaluation, modelling and approximating of concentration relationships in complex systems.[17]

The deterministic methods in Section 2.2.1 numerically solve the differential equations, thus determining the macroscopic composition of the system at a given time. On the contrary, the KMC method determines the time of change (reaction) of a species with the use of a random number generated with an appropriate distribution.[89] The result is the system's composition, as well.

The intrinsic difference between the KMC and the MMC and RMC simulations is that KMC has no explicit selection rule in it. The appropriate weighing of the individual reaction sequences, that is, their appropriate occurrence is ensured by the way of their construction: the more possible trajectories are getting more often in the sample than the less possible ones.

The theory and the mathematical foundations of KMC date back approximately for 40 years and saw widespread application since then.[90–94] Apart from the elucidation of complex reaction mechanisms diffusion and relaxation processes have been modelled with it. In the field of NMR spectroscopy, it has been used, for example, for the evaluation of DOSY spectra[95–98] and relaxation models.[99,100]

In these cases, the result of the KMC simulation is the system's time-dependent concentration profile. In DNMR, the system simulated with the KMC method is in macroscopic equilibrium, and the microscopic changes of a single species are simulated.

3.1. Kinetic description of the exchange processes

Let us consider our system as a mixture of m conformers being in equilibrium. Henceforth, these conformers will be denoted as $A^{(1)}, A^{(2)}, \ldots, A^{(m)}$. Here, nomenclature 'intramolecular exchange processes' incorporate

conformers, rotamers, valence isomers, etc. in the classical sense. In the case of intermolecular exchange processes, the species on either side of the reaction equation will be considered also as conformers and denoted as $A^{(h)}$ (see Figure 2).

The general equation of a reaction is:

$$A^{(h)} \overset{k_{hg}}{\rightarrow} A^{(g)}, \tag{11}$$

where $A^{(h)}$ and $A^{(g)}$ are two out of the possible m conformers and the apparent rate constant of the exchange process is k_{hg}. All reactions are assumed to be pseudo-first order. The condition of a macroscopic equilibrium enables us to handle exchange processes the rates of which depend on the concentration of several components, since the constant concentrations ensure that the apparent rate constants retain their uniformity.

The behaviour of a single molecule is followed with the kinetic model. At the start of our observation, the molecule is in the $A^{(h_1)}$ conformer state. At a certain time point, the molecule changes its conformation instantaneously; from that point, we observe the new $A^{(h_2)}$ conformer. The time of the conformation change is called the exchange point. For the kinetic modelling of this dynamic phenomenon, we have to determine the exchange points, the time elapsed between two of them (these intervals are called time slices henceforth) and the actual conformation of the molecule during these time slices.

The process of the conformational exchange can be divided into two steps from a kinetic point of view[101]: the disappearance of the 'old' conformer (decay) and the 'selection' of the newborn conformer (Figure 3).

During the latter step, the formation of any other conformer is possible after the decay of the $A^{(h)}$ conformer. It is unambiguous in the case of having two conformers in a system only. However, in the case of more than two conformers ($m \geq 3$), the new one is chosen randomly. According

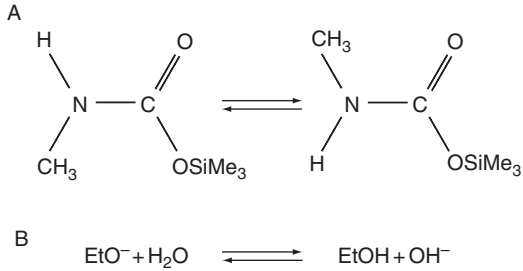

Figure 2 Different interpretations of conformers. (A) Exchange of conformers (rotamers) by the strict chemical convention (size of spin set is $n = 4$ nuclei). (B) Conformers, as sides of a chemical reaction (size of spin set is $n = 2$ nuclei).

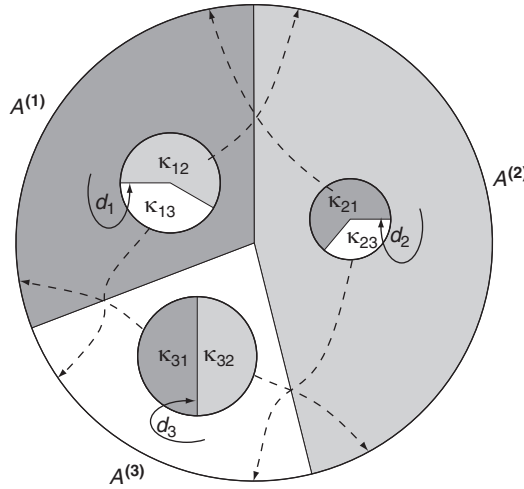

Figure 3 Model of the Monte Carlo simulation of DNMR spectra for three conformers. Length of arcs of the outer circle represents the relative distribution of conformers. Area of the circles inside the sections demonstrates the decay coefficients (d_h), length of the arcs shows the relation of the (κ_{hg}) probabilities. Arrows show the possible movements from one area to another.

to the theory of parallel reactions in reaction kinetics, the new conformers are formed in the ratio of their rate constants k_{hg}, and the probability of forming $A^{(g)}$ from $A^{(h)}$ is κ_{hg}:

$$\kappa_{hg} = \frac{k_{hg}}{\sum_{l=1}^{m} k_{hl}}. \tag{12}$$

Thus the selection of the new conformer can be done according to the roulette principle. A circle is divided into $m-1$ unequal sections, where the slice belonging to $A^{(g)}$ has a central angle of $2\pi\kappa_{hg}$ and we choose a point randomly in the circle (see inner circles in Figure 3).At the start of the detection, the only difference in choosing the initial conformer is that the ratio of the relative equilibrium concentrations $K^{(h)}$ is used to divide the circle (see the slices of the outer circle in Figure 3) instead of using the κ_{hg} probabilities:

$$K^{(h)} = \frac{[A^{(h)}]}{\sum_{g=1}^{m} [A^{(g)}]}, \tag{13}$$

where $[A^{(h)}]$ is the equilibrium concentration of conformer $A^{(h)}$. The calculation of relative concentrations is based on rate constants as follows. The general form of the hth equation of the equation system describing the

kinetic behaviour of the system after having introduced the relative concentrations is:

$$\frac{\mathrm{d}K^{(h)}}{\mathrm{d}t} = \sum_{g=1}^{m} \left(-k_{hg} K^{(h)} + k_{gh} K^{(g)} \right), \tag{14}$$

where $k_{hg} = 0$, for non-existing reactions, h and g span all indices $(1, \ldots, m)$. It is assumed that for all exchange processes, the system is in equilibrium, that is, for all h indices it is true that:

$$\frac{\mathrm{d}[A^{(h)}]}{\mathrm{d}t} = \frac{\mathrm{d}K^{(h)}}{\mathrm{d}t} = 0. \tag{15}$$

By substituting the right side of Equation (15) into Equation (14) for each h, a linear equation system is obtained, the hth equation of which is:

$$0 = \sum_{g \neq h} \left(-k_{hg} K^{(h)} + k_{gh} K^{(g)} \right). \tag{16}$$

By amending this system with the equation

$$\sum_{h} K^{(h)} = 1, \tag{17}$$

and solving the equation system of Equations (16) and (17), the frequency of occurrence of the conformers in the system is determined.At the start of the detection ($t = 0$), the conformation of the simulated spin set is chosen randomly (by choosing a point randomly inside the outer circle in Figure 3) so that the distribution of the probability variable would be the same as the relative concentration $K^{(h)}$.

3.1.1. Discrete description of the decay of the conformers

The molecule under investigation has to 'make decision' again and again, whether it has enough energy to change its conformer or not. We cannot make continuous investigation during the simulation; therefore we check whether there was any change in every dt time interval. The rate constant (d_h) of this simple 'decay' process is defined as:

$$d_h = \sum_{g=1}^{m} k_{hg}, \tag{18}$$

where m is the number of conformers and $k_{hh} = 0$. Based on the rate of the exchange processes, the ($V'_{\mathrm{d}t}{}^{(h)}$) probability of not having any exchange during a dt arbitrary long time slice is:

$$V'^{(h)}_{\mathrm{d}t} = 1 - d_h \mathrm{d}t. \tag{19}$$

To decide whether the decay has happened or not, we 'toss a coin' (not landing on its sides with the same probability) at every dt time interval and if it shows 'unchange', we take one step forward to the next time slice, if not, then the conformational change has happened according to the above described way. Alternatively, a point is chosen randomly from the slice of the conformer $A^{(h)}$ in Figure 3 and if it is inside the inner circle, the decay occurs. In this interpretation, the ratio of area of slice of $A^{(h)}$ and the circle inside should be $1 : V'_{\mathrm{d}t}{}^{(h)}$.Mathematically exchange happens, if:

$$\varepsilon < \sum_g k_{hg} \mathrm{d}t, \tag{20}$$

where ε is a random number with a normal distribution between 0 and 1. The drawback of the method is that it works adequately only if

$$\sum_g k_{hg} \mathrm{d}t \ll 1, \tag{21}$$

however, in this case, a great deal of random numbers have to be generated.

3.1.2. Continuous description of the decay of the conformers

To provide the appropriate distribution of the exchange times, the expected lifetimes of the individual conformers have to be determined. Since all of the reactions are considered to be of first order, the kinetics of the decay for any $A^{(h)}$ species is also of first order, the rate constant of which is d_h as defined in Equation (18).

The $V_{\Delta t}{}^{(h)}$ probability of the spin set remaining in $A^{(h)}$ conformation for a Δt time interval is:

$$V^{(h)}_{\Delta t} = d_h \exp(-d_h \Delta t), \tag{22}$$

thus the distribution of the length of time slices without an exchange is exponential. By knowing the $t^{(r-1)}$ time of the $r-1$th exchange point, the following recursive formula gives the time of the rth one ($t^{(r)}$):[102]

$$t^{(r)} = t^{(r-1)} - \ln(\varepsilon)/d_h, \tag{23}$$

where ε is a random number with a normal distribution between 0 and 1. The time interval between $t^{(r-1)}$and $t^{(r)}$ will henceforth be denoted as the rth time slice, whose length is $\Delta t^{(r)} = t^{(r)} - t^{(r-1)}$.

3.1.3. The Kinetic Monte Carlo method

Time points $t^{(1)}$, $t^{(2)}$, etc. determined according to Equation (23) and the conformations inside the time slices unambiguously describe the trajectory of the examined molecule, that is, its 'behaviour' during the experiment. This method forms the basis of the Monte Carlo simulation presented here. According to the probability Equations (12) and (22), $R-1$ pieces of exchange times are generated via random numbers within the observed time interval of length T, thus getting $t^{(1)}$, $t^{(2)}$, etc. points. The molecule is present as $A^{(1)}$, $A^{(2)}$, etc. conformers between those times. The probability of such a trajectory is the product of the probabilities of the individual conformers and the length of their time slices, since all events are independent of each other:

$$P = K_{h_1}\left(\prod_{r=1}^{R-1} d_{h_r}\exp\left(-d_{h_r}\Delta t^{(r)}\right)\kappa_{h_r h_{r+1}}\right)\exp\left(-d_{h_R}\left(T-t^{(R)}\right)\right). \qquad (24)$$

The random numbers generated with the appropriate distribution ensure that the frequency of occurrence of a trajectory is the same as its probability given in Equation (24). The nature of the simulation also ensures that it is unnecessary to follow up several thousands of trajectories to get a spectrum of acceptable quality; in most cases, a few hundreds are sufficient.

3.2. Kinetic Monte Carlo simulation of DNMR spectra for uncoupled spin systems

3.2.1. The single spin vector model

Spin-half nuclei have two spin states in strong magnetic field (α and β). The energy difference between the two states is typically in the order of magnitude of 100 MHz. The spin states of the isolated nuclei are represented by vectors in the vector model, whose length is $\hbar\sqrt{I(I+1)}$, and they are oriented in such a way that their projection in direction z has a length of $I_z = m\hbar$, where ($m = \pm 1/2$). The I_x, I_y and I_z components of the I operator do not commute with each other, therefore the other two components of these vectors are undefined, they can point in any direction in the xy plane, thus the vectors belonging to a given spin quantum number are on the surface of a cone. The vectors being in α and β states are precessing around the axis of the cone with the frequency corresponding to their energy difference. The resultant vector, that is, the macroscopic magnetisation vector (M), stands in z direction due to the difference in populations of the two cones.

After the initial 90° pulse, the M vector is in the xy plane giving the detectable signal. Due to the precession and the relaxation processes, the signal (FID) is a sine curve with exponentially decreasing amplitude.[11]

The vector model cannot be interpreted in such a simple way in the case of a spin system with more than one nucleus. For weakly coupled spin systems, the single spin vector model may be applied for each nucleus, one after the other. Thus the coupling with the other nuclei can be incorporated into its precession frequency, since the definition of the weak coupling ($J_{\mu\mu'} \ll |\nu_\mu - \nu_{\mu'}|$) means that the transitions of a nucleus only depend on the spin states of the other nuclei in the first order. The detected signal is the sum of the sine curves provided by the individual environment of the nuclei.

The vector model cannot be applied to strongly coupled spin systems, since the precession of the individual nuclei cannot be separated from each other.

3.2.2. Interpretation of the DNMR phenomenon of uncoupled spins

There is a simple and well-known model for the description of DNMR phenomenon, provided no scalar coupling is involved.[11] In Section 3.2.1, the macroscopic magnetisation vector of the vector model gives the detected signal (the FID). This vector rotates in the xy plane perpendicular to the direction of the external magnetic field during the detection; its frequency is determined by the shielding effect of the chemical environment of the nuclei.

Now let us consider a single nucleus, which can be in two distinctive environments denoted as $A^{(1)}$ and $A^{(2)}$. Let $\omega^{(1)}$ and $\omega^{(2)}$ be the frequencies of the nucleus in the two different environments. A pair of exchange processes ensure the transitions between the two states; the rate constants are k_{12} and k_{21} (Equation (11)). In such a simple system, the equation system defined by Equations (16) and (17) becomes much more simple, and an explicit solution can be given. The relative equilibrium concentrations of the two states are:

$$K_1 = \frac{k_{21}}{k_{21} + k_{12}} \quad \text{and} \quad K_2 = \frac{k_{12}}{k_{21} + k_{12}}. \tag{25}$$

During the detection, the examined nucleus is in the two conformers with K_1 and K_2 probabilities. At the start of the detection, the conformation of a given spin set ($A^{(1)}$ in this example) can be determined by knowing these probabilities and by using a pseudo-random number (see Section 3.1). The magnetisation vector starts to rotate with $\omega^{(1)}$ frequency:

$$\mathrm{fid}(t) = \exp\left(\mathrm{i}\omega^{(1)}t\right). \tag{26}$$

The exchange process occurs after some time and alters the chemical environment around the nucleus instantaneously at time point $t^{(1)}$.

From that moment, the precession frequency becomes $\omega^{(2)}$. The detected signal for $t \geq t^{(1)}$ is:

$$\mathrm{fid}(t) = \exp\left(\mathrm{i}\omega^{(2)}\left(t - t^{(1)}\right)\right)\rho^{(1)}, \tag{27}$$

where $\rho^{(1)}$ is the phase of the vector at time point $t^{(1)}$:

$$\rho^{(1)} = \exp\left(\mathrm{i}\omega^{(1)}t^{(1)}\right). \tag{28}$$

Equation (27) remains valid until the point of the next exchange ($t^{(2)}$), where the frequency is altered again alike at the first one, and after the point $t^{(2)}$, the detected signal can be expressed as:

$$\mathrm{fid}(t) = \exp\left(\mathrm{i}\omega^{(1)}\left(t - t^{(2)}\right)\right)\rho^{(2)}, \tag{29}$$

where

$$\rho^{(2)} = \exp\left(\mathrm{i}\omega^{(2)}\left(t^{(2)} - t^{(1)}\right)\right)\rho^{(1)}. \tag{30}$$

In general, the detected signal after the rth exchange is:

$$\mathrm{fid}(t) = \exp\left(\mathrm{i}\omega^{(1,2)}\left(t - t^{(r)}\right)\right)\rho^{(r)}, \tag{31}$$

where the value of $\omega^{(1,\,2)}$ depends on the parity of r, and the phase of the vector at the time of the exchange is:

$$\rho^{(r)} = \exp\left(\mathrm{i}\omega^{(1,2)}\left(t^{(r)} - t^{(r-1)}\right)\right)\rho^{(r-1)}. \tag{32}$$

A FID simulated according to Equations (26)–(32) is shown in Figure 4A. Its discrete Fourier-transform provides the spectrum of the nucleus. The noise level of this spectrum is rather high; nevertheless the shape of the signals can be recognised.[102]

Different nuclei give different FIDs and spectra because of the randomly selected initial conformer and exchange times (Figure 4B–C). In this model, the sum of spectra of a few hundreds of nuclei averages out the numeric noise of the individual nucleus (Figure 4D). The several hundreds of spectra are calculated independently of one another; hence the simulation can be shared among several processor cores (either in kernel[101] or on a GPGPU capable graphics card[103–105]) thus the calculation can be significantly accelerated.

The lengths of the intervals the nuclei are precessing with certain frequencies vary for each nucleus, but the distribution of the lengths of these intervals depend on the rate constants as described by the 'decision criteria' in Equation (23). This distribution function determines how long

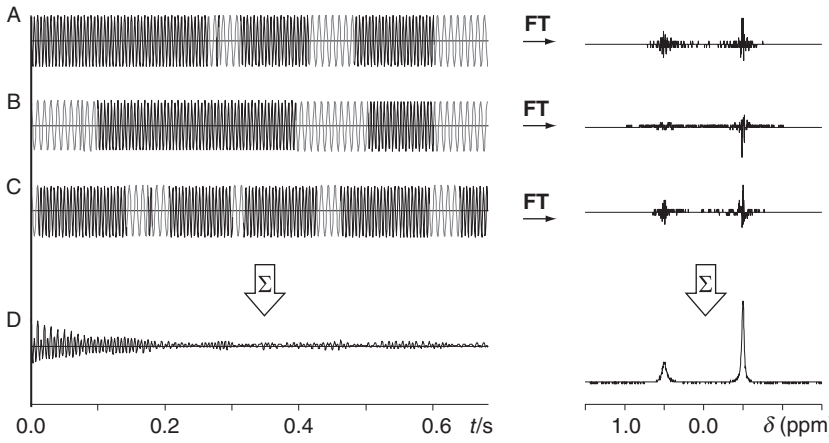

Figure 4 (A–C) Single fids and spectra of three spin sets. (D) Sum of 100 scans.

the nucleus remains in the same conformer at the given point of detection and this is the parameter responsible for the shape of the signals. In the case of slow exchange processes ($k < \Delta\nu$), the separate individual frequencies dominate, so both signals are detected. The increase in the rate constants leads to the mixing of the different frequencies. Further increase of the frequency of the exchanges results in one signal being detected only,[11] which is the average of the two previous signals (Figure 5A). The sum of several FIDs with the same rate constant shows that the FID is the superposition of two sine curves in the case of slow exchanges, while fast exchange gives a single sine curve (Figure 5B). At intermediate rates the FIDs quickly become incoherent and their sum disappears in a short time, hence their spectral curves are extreme wide. This model can be considered as basis of a Monte Carlo simulation because of the use of random numbers and the summating of randomly chosen FIDs.

This interpretation of the dynamic phenomenon is based on the changes of the frequency of the macroscopic magnetisation vector; hence in this form it can be applied to uncoupled spins only.

3.2.3. Interpretation of the DNMR phenomenon of weakly coupled spins

In a coupled spin system, the condition that vectors having distinctive frequencies and those can be assigned to each nucleus fails. Further, the coupling inherently means that the frequency of the observed nucleus depends not only on its own environment but also on the state of the neighbouring nuclei as well. Thus the product functions are introduced to take into consideration the perturbation effect of the neighbouring nuclei

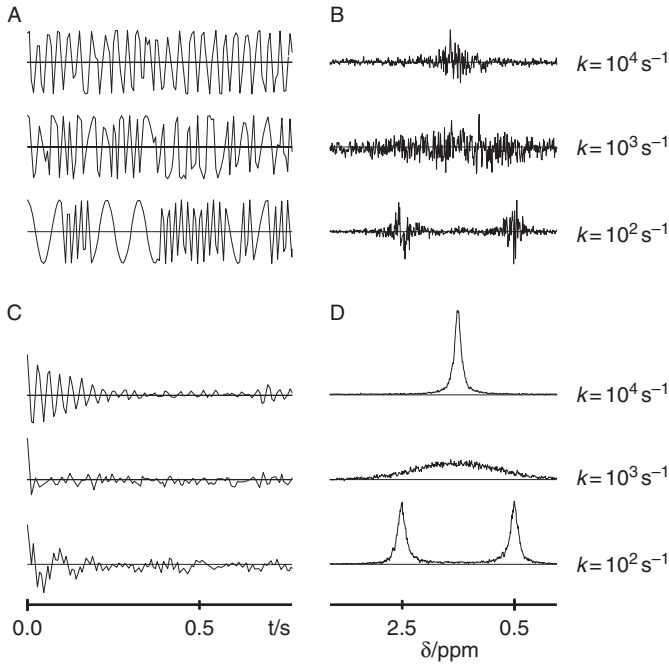

Figure 5 The effect of the number of scans and exchange rates on fid and spectra using Monte Carlo simulation of DNMR spectra for a single spin: (A, B) 1 scan, (C, D) 100 scans.

(i.e. the spins coupled with the nucleus). In the case of weak coupling, the higher order terms of this perturbation are negligible. If solely the first order terms are taken into account, the Hamiltonian is diagonal on the basis of the product functions (see Equation (2)):

$$H_{aa} = 2\pi \sum_{\mu=1}^{n} m_{\mu}^{(a)} \nu_{\mu} + \frac{\pi}{2} \sum_{\mu=1}^{n} \sum_{\mu'=\mu+1}^{n} J_{\mu\mu'} D_{\mu\mu'}^{(a)} \quad \text{and} \quad H_{ab} = 0. \tag{33}$$

Equation (33) means also that spectroscopic terms (energy levels) can be assigned to the product functions and the transitions defined between them have well determined energies (Figure 6). These transitions define the precession frequency of the corresponding single quantum coherences.

The frequencies assigned to the individual coherences are different for any two conformers present in dynamic spin systems. The product functions, that is, the states the terms were assigned to, are identical. The single spin vector model of the previous section can be extended to weakly coupled systems by changing the precession frequencies of the single quantum coherences during the exchanges of the nuclei instead of

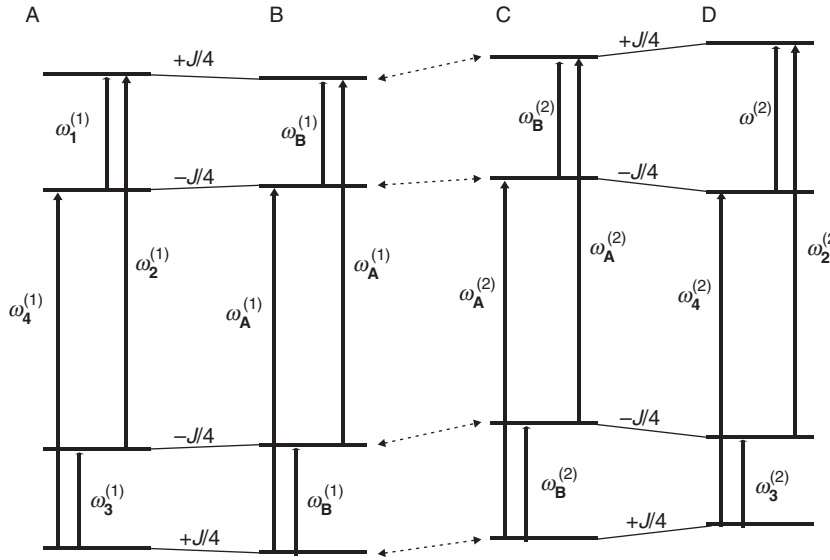

Figure 6 Energy diagram for non-mutual two-site exchange processes of two spins with weak coupling. Dashed arrows indicate exchanges.

the energies of the individual nuclei. As a result, the equations for a single nucleus are modified to include the sum of all possible coherences, that is, the new form of Equation (31) is:

$$\mathrm{fid}(t) = \frac{1}{2^{n-1}} \sum_{j=1}^{n2^{n-1}} \exp\left(\mathrm{i}\omega_j^{(1,2)}\left(t - t^{(r)}\right)\right)\rho_j^{(r)}. \tag{34}$$

Equation (32) gives the phase of the vector in question for a single nucleus at the time of exchange. In the case of weakly coupled spin systems, this relationship remains valid and just has to be amended with index j (the value of ${\omega_j}^{(r)}$ is either ${\omega_j}^{(1)}$ or ${\omega_j}^{(2)}$ depending on the parity of r).

$$\rho_j^{(r)} = \exp\left(\mathrm{i}\omega_j^{(r)}\left(t^{(r)} - t^{(r-1)}\right)\right)\rho_j^{(r-1)}. \tag{35}$$

This model works if, for example, there are two nuclei weakly coupled to each other in the system, having two different environments, so that an AX spin system exchanges with a BY one (AX ↔ BY). On the contrary, this model fails spectacularly if the two nuclei exchange with each other (AX ↔ XA) (Figure 7). In this case, ${\omega_1}^{(1)} = {\omega_2}^{(2)}$ and ${\omega_1}^{(2)} = {\omega_2}^{(1)}$; similarly, ${\omega_3}^{(1)} = {\omega_4}^{(2)}$ and ${\omega_4}^{(2)} = {\omega_3}^{(1)}$. At fast exchange limit, the average values of the frequencies of exchanging coherences appear (Figure 7). The common frequency of the first couple of coherences is:

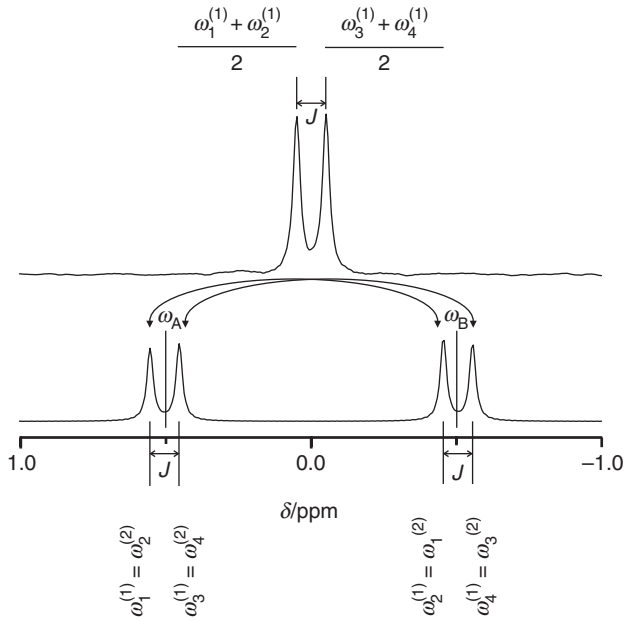

Figure 7 Exchange of spectrum lines in a mutually exchanging AX spin system with coupling between the nuclei.

$$\frac{\omega_1^{(1)}+\omega_2^{(1)}}{2}=2\pi\frac{\nu_1^{(1)}+\nu_2^{(1)}+J}{2}, \tag{36}$$

and that of the second one is:

$$\frac{\omega_3^{(1)}+\omega_4^{(1)}}{2}=2\pi\frac{\nu_1^{(1)}+\nu_2^{(1)}-J}{2}. \tag{37}$$

These two results are clearly different, while they should be equal. The root cause of the problem is that the exchange process is defined between the same nuclei those are coupled to each other and the higher order components of the coupling cannot be neglected any more despite the weak coupling.[18]

The explanation of this phenomenon is clearly visible from the calculation based on the simulation of average density matrix. In this case, Equation (10) can be solved analytically. The detected frequencies and the linewidth of the signals are given by the real and the imaginary part of the following expression:[106]

$$\frac{\bar{\omega}_{1,2}}{2\pi}=\mathrm{i}\frac{\nu_1+\nu_2+lJ}{2}-\frac{k}{2\pi}\pm\frac{\mathrm{i}}{2}\sqrt{(\nu_1-\nu_2)^2+\left(lJ+\frac{\mathrm{i}k}{\pi}\right)^2}, \tag{38}$$

where $l = \pm 1$ depending on the blocks according to the total spin quantum number.

In Equation (38), if k is large, the first part of the expression under the square root, $(\nu_1 - \nu_2)^2$, is negligible as compared to the second one, $(lJ + ik/\pi)^2$. Thus the frequencies can be approximated as:

$$\frac{\bar{\omega}_{1,2}}{2\pi} = i\frac{\nu_1 + \nu_2}{2} + i\frac{lJ + ik/\pi}{2} \pm i\frac{lJ + ik/\pi}{2}, \tag{39}$$

which shows that two of the lines broaden extremely (the plus case of $\pm$) and the two remaining frequencies are at the average of the two Larmor-frequencies (Figure 8). It follows from the above mentioned that, at fast exchange limit, the exchange process amplifies the coupling as compared to the frequency difference and the amplification of the coupling causes the effect of the same coupling to disappear from the spectrum.

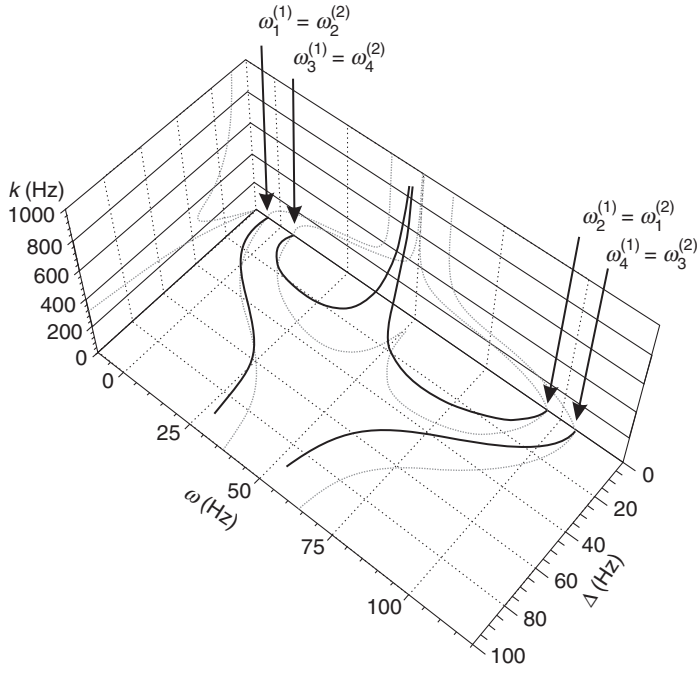

Figure 8 Dependence of the average frequency (ω) and linewidth (Δ) on the exchange rate (k) in a mutually exchanging AX spin system.

3.3. Kinetic Monte Carlo simulation of coupled spin systems

3.3.1. Spin sets and the spin system

In cases of single spins (Section 3.2.2) or systems with weak coupling (Section 3.2.3), it was easy to find the entity (the individual nucleus and the coherences) that enables us to simultaneously handle exchange and precession. In case of strongly coupled spin systems, this entity is the 'spin set', which is an ordered set of S_1, S_2, ..., S_n nuclei which are uncoupled to any other nuclei apart from the elements of the spin set. In dynamic processes, the spin set can occur in several chemical environments. During the reactions between conformers, only the spectral parameters (e.g. chemical shifts, coupling constants) describing the environment of the spin set are changing, the spins and their magnetisations remain unchanged.[107]

On the contrary to spin sets, the spin system contains all the nuclei of all conformers. Therefore, the spin system is a closed set with respect to exchange processes as well, not only to J coupling, and thus it is usually larger than a spin set.

The two definitions and their relationship to the exchange processes are compared in Figure 9. In the spin system, the spins are defined by

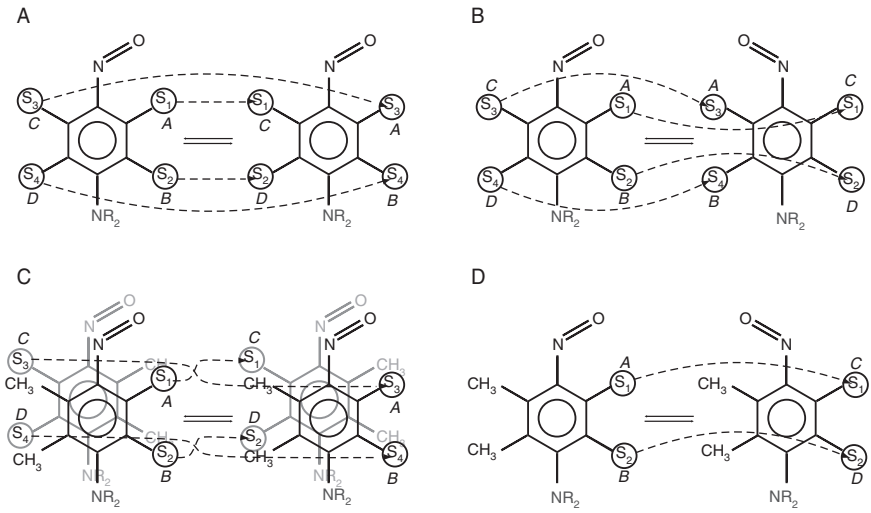

Figure 9 Relation of spins and their environment with exchanges. *S* is for the nuclei of the spin set, (*A*–*D*) the different chemical environments. (A) Modelling of *mutual exchange* in a spin system. (*A*–*D*) denote the environments of the four ^{1}H of the aromatic ring. (B) Same sample as in (A) but modelling with the spin sets. (C) Modelling of *non-mutual exchange* of the aromatic protons in a spin system. (D) Same sample as in (C) but with spin sets.

their magnetic and chemical environments and only the sequence of nuclei alters in the exchange processes. This is shown in Figure 9A through a case of a mutual exchange, where the S_1 ^{1}H nucleus goes from environment A to C, thus converting into the third one, while the original S_3 changes from C to A becoming the first. Similarly, the position of S_2 and S_4 are constantly altering between environments B and D.

In the spin set, however, the spins are defined by their place in the ordered set. This atomic sequence remains unaltered during exchange processes; the description of chemical environment appears only in the conformers. As it can be seen in Figure 9B, the nuclei S_1, S_2, S_3 and S_4 always remain at their respective position while their environments may change from ABCD to CDAB or vice versa. From the point of the spin set, the states on the two sides of the equation mean two distinct conformers disregarding their equivalency.

The difference between spin sets and spin systems is even greater in the case of non-mutual exchanges. In Figure 9C, in the AB ↔ CD non-mutual exchange, the spin system contains four ^{1}H nuclei. To include them in the spin system, the number of molecules has to be duplicated on both sides of the equation. While S_1 and S_2 nuclei are in environments A and B, S_3 and S_4 ones are in C and D. In the exchange process, S_1 and S_3 are swapping their places in the first and the third positions while S_2 with S_4 in the second and fourth positions. The environments of the four nuclei are always the same; even their sequence remains unchanged as being ABCD.

On the contrary, the interpretation based on spin sets (see Figure 9D), the $S_1 - S_2$ nuclei, may be either in environment AB or in CD, and the order of the pairs are *a priori* constants. The atomic sequence of the two nuclei always remains the same during the exchange process. The most important difference from the spin system is that there is no need of duplicating the number of molecules to describe the entire system.

It can be seen that, in the average density matrix formalism which is based on spin system model, the scalar couplings and the exchange processes are handled simultaneously. Thus they cannot be separated and a larger atomic basis (spin system) is required for their description. Meanwhile, the Monte Carlo method based on spin sets separates the two interactions, and thus spin systems can be reduced to smaller spin sets.

The single spin vector model demonstrates well the relationship between spin set and spin system. In the spin system, all possible environments of the nucleus (i.e. all frequencies) are incorporated. Meanwhile, the spin set contains only one nucleus the different frequencies of which are corresponding to the different conformers. So the spin set is rather taken as the extension of the definition of a nucleus than the simplification of a spin system.[102]

3.4. The individual density matrix

The single spin model corresponds well with the spin set one when dealing with exchange processes. However, there is a significant difference in the calculation of spectra, namely a vector can be assigned to a nucleus to simulate its precession that cannot be done to a spin set. In special cases, in weakly coupled spin systems, the introduction of vectors assigned to coherences solved this problem which vectors could be handled independently. In the general case (having strong coupling), these vectors describe the states correctly but the advantages in calculation and interpretation originating in the independent simulations are lost. For easier handling, the vectors assigned to coherences are ordered into a matrix (on the basis of the product functions they are composed from) and to be called as the individual density matrix of the spin set (ρ).

The term density matrix has already occurred in Section 2.2. There the density matrix ($\bar{\rho}$) generally used in simulations was consequently called *average* density matrix. This matrix gives the average state of the spin system, and the spectrum of the whole macroscopic system is determined from this quantity.

However, the individual density matrix models the individual behaviour of the spin sets. An individual density matrix—like the average one—changes due to pulses, precession and exchange processes, and it can be exactly calculated taking these effects into account at any time point. While the average density matrix contains the average state of the spin system at a certain time point, the individual density matrix describes a possible state of the spin set.

The average and the individual density matrices are different from each other very much in the case of non-mutual exchanges as the former one is built on the product functions of the spin system while the latter one is defined on the basis functions of the spin set yielding in a significant difference in dimensions of the matrices. In this case, the two matrices can be compared in the space spanned by the intramolecular transitions of the spin system. This space is the direct sum of the space spanned by the single quantum coherences of the spin set with itself (m times in case of m conformers). This space is spanned by the single quantum coherences of the conformers.

Each element of the average of the individual density matrices is the sum of the corresponding elements of the average density matrix. For example, the sum of the density matrix elements corresponding to the two Φ_1 transitions on the right side of Figure 10B equals to that element of the average of the individual matrices, which one belongs to the Φ_1 transition on the left part of Figure 10B .

In the case of mutual exchanges, the dimensions of two vector spaces (spanned by the basis functions of spin systems and spin set) are equal.

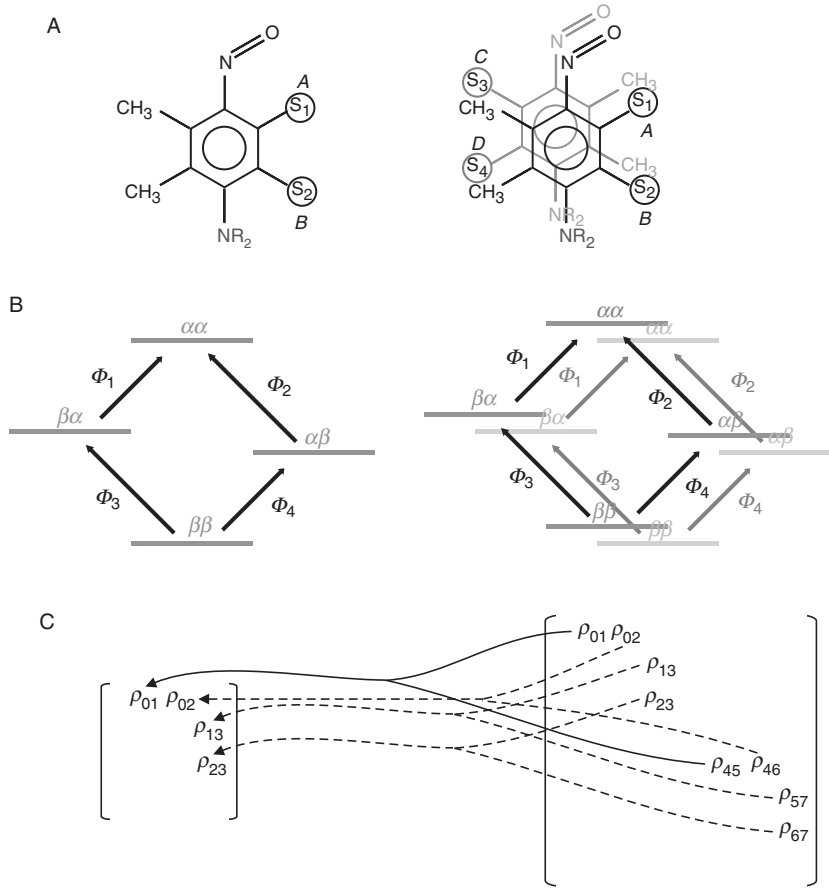

Figure 10 Comparison of individual (left) and average (right) density matrices in the case of a non-mutual exchange. (A) Definition of spin set or spin system (see Figure 9). (B) Basis functions (lines) and intramolecular single quantum coherences (arrows) defined by the spin set or spin system. (C) Elements corresponding to the intramolecular single quantum coherences in the density matrix.

In this case, the average density matrix is the weighted average of all possible individual density matrices where the weighting factors are the same as given in Equation (24) (T acquisition time should be replaced by the t actual time).

Individual density matrices are different due to the different exchange points of the corresponding spin sets. (Similarly, in the single spin vector model, the momentary phase of the different nuclei is different if their exchange points are different.) Thus the spin sets and their individual density matrices are distinguished by their trajectories, involving their individual exchange points and momentary conformers. Thus, in

semi-classical approximation, the individual density matrix describes the average of coherences those trajectories are the same. According to the principles of quantum mechanics, these coherences cannot be distinguished; therefore, their average can be taken as individual. However, the average density matrix averages states those are distinguishable from each other, like coherences of spin sets with different trajectories.

By knowing the trajectory of a spin set, its individual density matrix can be calculated at any time points. The key to the simulation is the determination of the propagating matrix (see Section 3.5). The FID and spectrum of a spin set upon the individual trajectory (one scan) can be determined from the actual values of the time-dependent density matrix.

In the Monte Carlo simulation, a few hundreds (100–2000) of scans are calculated, and the Fourier transform of their sum gives the simulated spectrum. The trajectories of spin sets are individual which makes their scans different providing the variety of the samples necessary for the simulation, similar to the case of the single spin interpretation. The calculation of the scans remains independent of each other; thus the calculation can be parallelised in the case of coupled spin systems as well.[101] The density matrix introduced because of the coupling and the increased amount of calculations on the matrix elements emphasise the use of modern architectures in parallel computation.[104]

3.5. Calculating the FID of a coupled spin system

The parameter sets describing the chemical environment of a spin set are different for each conformer. This results in different Hamiltonians for each one (see Equation (2)):

$$H_{ab}^{(h)} = \delta_{ab}\pi\left(2\sum_{\mu=1}^{n} m_{\mu}^{(a)} v_{\mu}^{(h)} + \frac{1}{2}\sum_{\mu=1}^{n}\sum_{\mu'=\mu+1}^{n} J_{\mu\mu'}^{(h)} D_{\mu\mu'}^{(a)}\right) + (1-\delta_{ab})\pi\sum_{\mu=1}^{n}\sum_{\mu'=\mu+1}^{n} J_{\mu\mu'}^{(h)} F_{\mu\mu'}^{(ab)}, \tag{40}$$

where the notations are similar to the ones used in Equations (1) and (2) and the h superscript denotes the conformer.

In the following calculations, the conformer dependence of the Hamiltonian occurs through its dependence on time slices. Thus, in Equation (40), the index h should be replaced by $h^{(r)}$, which is simplified to a simple index r so the Hamiltonian appears as $H^{(r)}$. The Hamiltonians of the conformers have different eigenvectors and eigenvalues, and this is represented in their notation as well: $\Lambda^{(r)}$ is the diagonal matrix of the eigenvalues and $U^{(r)}$ is the unitary matrix made of the eigenvectors, resulting in the following equation:

$$H^{(r)} = U^{(r)}\Lambda^{(r)}\left(U^{(r)}\right)^{\mathrm{T}}. \tag{41}$$

The equations necessary to calculate the FID can be obtained in the Hilbert space, so there is not need to convert the equations into the Liouville space (unlike in the case shown in Section 2.2), and the increase in the dimension of the vector space used for the simulation is avoided.

The simulation contains two types of events that should be translated into equations: the free precession and the exchange event. A third operation, the calculation of the FID points, does not influence the density matrix, but its importance explains why it should be dealt with in detail in the following sections.

3.5.1. Precession (propagation)

Precession (or propagation) describes the spontaneous evolution of the individual density matrix of a spin set in a time interval with no exchange point. These conditions make the operation called propagation conformer and time slice dependent, but it is independent of the rate coefficients of the exchange processes (unlike to the case in Equation (10)).

The propagation by Δt in time slice r is based on the solution of the Liouville–von Neumann equation:[12]

$$\rho(t+\tau) = \exp\left(-\mathrm{i}H^{(r)}\tau\right)\rho(t)\exp\left(\mathrm{i}H^{(r)}\tau\right) = \left(P^{(r)}\right)^{-1}\rho(t)P^{(r)}, \tag{42}$$

where $H^{(r)}$ is the conformer-dependent Hamiltonian defined in Equation (40). Henceforth, propagation is performed from the beginning of the actual (rth) time slice $t^{(r-1)}$, that is $\Delta t = t - t^{(r-1)}$. To calculate the matrix of the propagator $P^{(r)}$ defined in Equation (42), the real and hermitian $H^{(r)}$ matrix is diagonalised according to Equation (41). Inside time slice r at time point t (t denotes the time elapsed since the start of detection), the $\rho(t)$ time-dependent density matrix is obtained by propagating ($\rho^{(r-1)}$)—the density matrix at the beginning of the time slice—according to Equation (42) using the diagonalised form of $P^{(r)}$ operator derived from Equation (41):

$$\begin{aligned}\rho(t) &= \exp\left(-\mathrm{i}H^{(r)}\Delta t\right)\rho^{(r-1)}\exp\left(\mathrm{i}H^{(r)}\Delta t\right)\\ &= U^{(r)}\exp\left(-\mathrm{i}\Lambda^{(r)}\Delta t\right)\left(U^{(r)}\right)^{\mathrm{T}}\rho^{(r-1)}U^{(r)}\exp\left(\mathrm{i}\Lambda^{(r)}\Delta t\right)\left(U^{(r)}\right)^{\mathrm{T}}.\end{aligned} \tag{43}$$

The first part of Equation (43) can be calculated in several ways. It will be shown later that both the interpretation of the equations and the fastest calculation need a solution based on the diagonalisation of the Hamiltonian, thus further equations will be obtained in the diagonalised form.

3.5.2. Exchange processes

In our model, the instant jump approximation is used thus the relative magnetisation of the ϕ_a basis functions as well as the elements of the density matrix remain unaltered during exchanges. A reaction replaces the actual conformer with a new one; thus the $H^{(r)}$ operator and its eigenfunctions ($\psi_l{}^{(r)}$) and eigenvalues ($\lambda_l{}^{(r)}$) are different before and after the exchange. This replacement alters the operator of propagation as well, and the new one is only valid from the beginning of the new time slice. It means that the density matrix should be calculated at time point $t^{(r)}$ (using the precession operator of time slice r).

To obtain the formula for propagating the ρ matrix from $t^{(r-1)}$ to $t^{(r)}$, the implicit variable t should be replaced by $t^{(r)}$ in Equation (43) (thus substituting Δt by $\Delta t^{(r)}$):[102]

$$\rho^{(r)} = U^{(r)} \exp\left(-\mathrm{i}\Lambda^{(r)}\Delta t^{(r)}\right)\left(U^{(r)}\right)^{\mathrm{T}} \rho^{(r-1)} U^{(r)} \exp\left(\mathrm{i}\Lambda^{(r)}\Delta t^{(r)}\right)\left(U^{(r)}\right)^{\mathrm{T}}, \quad (44)$$

where $\rho^{(r)}$ is the shorter notation for $\rho(t^{(r)})$. Equation (44) is a recursive one, and the density matrix is obtained by the successive implementation of this equation at each exchange point (at the beginning of each time slice), provided the density matrix ($\rho^{(0)}$) is known at the start of detection. In a one-pulse experiment, only transversal magnetisation is present after the 90° pulse ($t = 0$). In this state, the density matrix is proportional to the transpose of the matrix of the excitation operator (I^+) on the basis of the ϕ_a product functions, that is $\rho_{ab}{}^{(0)} = 1$, if the $\phi_a \rightarrow \phi_b$ single quantum transition is allowed and zero otherwise.

3.5.3. Detection

At time point t, the signal, fid(t), generated by a spin set can be determined by the *trace* of the product of the density matrix and the matrix of the I^+ excitation operator:

$$\mathrm{fid}(t) = \mathrm{Tr}(\rho(t) I^+). \quad (45)$$

At time point t (in the rth time slice, meaning $t^{(r-1)} \leq t < t^{(r)}$), the density matrix can be calculated from $\rho^{(r-1)}$ according to Equation (43), and so the detected signal at time point t is given as:

$$\mathrm{fid}^{(r)}(t) = \mathrm{Tr}\left(\left[\left(U^{(r)}\right)^{\mathrm{T}} I^+ U^{(r)}\right] \exp\left(-\mathrm{i}\Lambda^{(r)}\Delta t\right)\left(U^{(r)}\right)^{\mathrm{T}} \rho^{(r)} U^{(r)} \exp\left(\mathrm{i}\Lambda^{(r)}\Delta t\right)\right), \quad (46)$$

where $\rho^{(r-1)}$ should be replaced by the density matrix valid at the beginning of that time slice the detection point is in. The term inside parentheses in Equation (46) is the transformed matrix of the I^+ operator $A^{(r)}$:

$$A^{(r)} = U^{(r)} I^{+} \left(U^{(r)}\right)^{\mathrm{T}}. \tag{47}$$

The physical meaning of the (j, k) element ($A_{jk}^{(r)}$) of the $A^{(r)}$ matrix is the amplitude of the $\psi_k^{(r)} \rightarrow \psi_j^{(r)}$ single quantum transition. Substituting Equation (47) into Equation (46) results in:

$$\mathrm{fid}^{(r)}(t) = \mathrm{Tr}\left(A^{(r)} \exp\left(-\mathrm{i}\Lambda^{(r)}\Delta t\right)\left(U^{(r)}\right)^{\mathrm{T}} \rho^{(r-1)} U^{(r)} \exp\left(\mathrm{i}\Lambda^{(r)}\Delta t\right)\right). \tag{48}$$

Equation (48) gives the value of FID for values of t those are inside timeslice r. Either $t < t^{(r-1)}$ or $t \geq t^{(r)}$ is out of the domain of $\mathrm{fid}^{(r)}(t)$ function.[18]The FID of a single *scan* is the union of the $\mathrm{fid}^{(r)}(t)$ functions of the time slices ($\cup$):

$$\begin{aligned}\mathrm{FID}(t) &= \bigcup_r \mathrm{fid}^{(r)}(t) \\ &= \bigcup_r \mathrm{Tr}\left(A^{(r)} \exp\left(-\mathrm{i}\Lambda^{(r)}\Delta t\right)\left(U^{(r)}\right)^{\mathrm{T}} \rho^{(r-1)} U^{(r)} \exp\left(\mathrm{i}\Lambda^{(r)}\Delta t\right)\right),\end{aligned} \tag{49}$$

where the union of the FIDs of time slices is introduced as follows: its domain is the union of the domains of all $\mathrm{fid}^{(r)}$ functions and at all points t, its value equals to the value of the only $\mathrm{fid}^{(r)}$ function that contains t in its domain. This definition describes the value of FID(t) unambiguously as the domains of the $\mathrm{fid}^{(r)}$ functions those are disjunct and together they fill the whole detection time.The total FID (F) is calculated as the sum of the individual *scan*s:

$$\begin{aligned}F(t) &= \sum_{\varepsilon} \mathrm{FID}(t) \\ &= \sum_{\varepsilon} \bigcup_r \mathrm{Tr}\left(A^{(r)} \exp\left(-\mathrm{i}\Lambda^{(r)}\Delta t\right)\left(U^{(r)}\right)^{\mathrm{T}} \rho^{(r-1)} U^{(r)} \exp\left(\mathrm{i}\Lambda^{(r)}\Delta t\right)\right).\end{aligned} \tag{50}$$

In the simulation, the value of the $F(t)$ function is calculated at discrete points in a finite time interval; then discrete complex Fourier transform is performed on this array to obtain the simulated spectrum.[101]

3.5.4. Transformed density matrix

The $\xi^{(r)}(t)$ notation is introduced for the transformed density matrix as follows:[104]

$$\xi^{(r)}(t) = \left(U^{(r)}\right)^{\mathrm{T}} \rho(t) U^{(r)}. \tag{51}$$

This definition shows that $\xi^{(r)}(t)$ is the density matrix on the basis of the eigenfunctions of the Hamiltonian. Substituting Equation (51) into Equation (44) and rearranging the terms gives:

$$\xi^{(r)}(t) = \exp\left(-\mathrm{i}\Lambda^{(r)}\Delta t\right)\xi^{(r)}\left(t^{(r-1)}\right)\exp\left(\mathrm{i}\Lambda^{(r)}\Delta t\right). \tag{52}$$

Propagating through a full time slice is done in the following way:

$$\xi^{(r)}\left(t^{(r)}\right) = \exp\left(-\mathrm{i}\Lambda^{(r)}\Delta t^{(r)}\right)\xi^{(r)}\left(t^{(r-1)}\right)\exp\left(\mathrm{i}\Lambda^{(r)}\Delta t^{(r)}\right), \tag{53}$$

then transforming it into the eigenfunctions of the new $(r + 1\text{th})$ time slice:

$$\xi^{(r+1)}\left(t^{(r)}\right) = \left(U^{(r+1)}\right)^{\mathrm{T}}\left[U^{(r)}\xi^{(r)}\left(t^{(r)}\right)\left(U^{(r)}\right)^{\mathrm{T}}\right]U^{(r+1)}. \tag{54}$$

Further propagation should be calculated from this matrix. The detected signal can be calculated from the transformed density matrix as:

$$\mathrm{fid}^{(r)}(t) = \mathrm{Tr}\left(A^{(r)}\exp\left(\mathrm{i}\Lambda^{(r)}\Delta t\right)\xi^{(r)}\left(t^{(r+1)}\right)\exp\left(-\mathrm{i}\Lambda^{(r)}\Delta t\right)\right) \tag{55}$$

when t is between $t^{(r\,-\,1)}$ and $t^{(r)}$ (Figure 11).

The most common and usually the fastest way to calculate the exponential function of matrices is done by renormalisation followed by Pade-approximation to fifth order and then successive multiplication.[108,109]

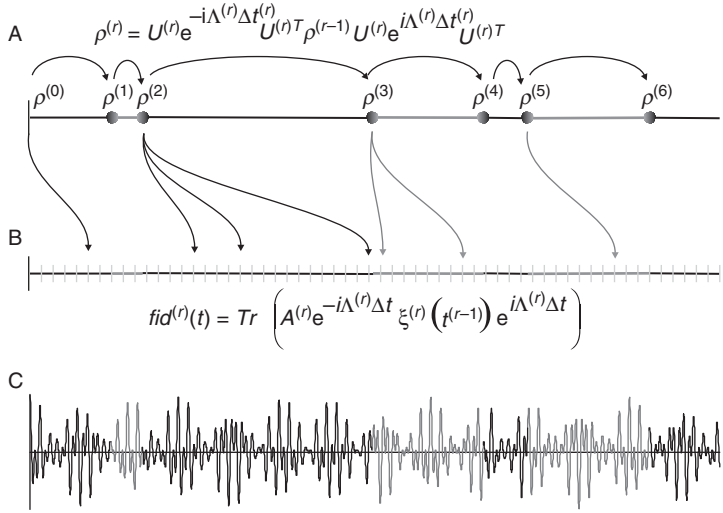

Figure 11 Simulation of the fid of a spin set. (A) Individual density matrix is calculated at each exchange point. (B) Eigencoherence representation of the density matrix is propagated from the beginning of the time slice for each detection point. (C) Simulated fid.

In the case of a single matrix, this solution is much faster than diagonalising the matrix, then calculating the exponential of the diagonal form, that is the method used here. Our case is special because only a few matrices have to be diagonalised, but the exponential of their many different (non integer) multiples has to be calculated many times. Bearing these conditions in mind, the problem needs much less operations using Equations (52)–(55) then by using the Pade-approximation of the exponentials.

3.6. Vector model and density matrix in case of dynamic processes

The elements of the $\rho(t)$ density matrix on the basis of the ϕ_a product functions are denoted as $\rho_{ab}(t)$. The single quantum coherences corresponding to the product function pairs are defined as:

$$\Phi_e = |\phi_a\rangle\langle\phi_b|. \tag{56}$$

In spin systems with weak coupling among the nuclei, the product basis functions are eigenfunctions of the Hamiltonian with well-defined energy levels; thus the single quantum coherences defined by the pairs of them are having characteristic precession frequencies. It follows that these Φ_e coherences are eigenstates of the spin system thus their population is unchanged during precession. Exchange processes leave basis coherences unaltered; thus, in weakly coupled spin systems, the Φ_e coherences remain the same during the whole detection time and their signal can be simulated using their characteristic frequencies. Moreover, the calculation of the coherences can be done independently from each other (see Section 3.2.3). However, in the case of the spin systems with strong coupling, the model is much more difficult as it will be shown in the following sections.

3.6.1. Spin systems with strong coupling

The $(\psi_k^{(r)})$ eigenfunctions of the Hamiltonians of the conformers can be expressed as the linear combination of the product functions, similarly to Equation (3):

$$\psi_k^{(r)} = \sum_a u_{ak}^{(r)} \phi_a, \tag{57}$$

thus the definition of the $u_{ak}{}^{(r)}$ coefficients is:

$$u_{ak}^{(r)} = \left\langle \phi_a | \psi_k^{(r)} \right\rangle = \left\langle \psi_k^{(r)} | \phi_a \right\rangle. \tag{58}$$

The $\psi_k^{(r)}$ eigenfunctions form orthonormalised basis of the Hilbert space as well, thus the product functions can be expressed as their linear combinations:

$$\phi_a = \sum_k u_{ak}^{(r)} \psi_k^{(r)}, \tag{59}$$

where the $u_{ak}^{(r)}$ coefficients are the same as the ones in Equation (57) as the matrix $(U^{(r)})$ built of them is unitary.The eigenfunction pairs of the conformers define the eigencoherences as:

$$\Psi_p^{(r)} = |\psi_j^{(r)}\rangle\langle\psi_k^{(r)}|. \tag{60}$$

The conversion between the coherences defined in Equations (56) and (60) can be deduced form Equation (58) as:

$$\Psi_p^{(r)} = \sum_e u_{ak}^{(r)} u_{bj}^{(r)} \Phi_e, \quad \text{and} \quad \Phi_e = \sum_p u_{ak}^{(r)} u_{bj}^{(r)} \Psi_p^{(r)}. \tag{61}$$

The kth eigenvalue of the Hamiltonian of the rth time slice is denoted by $\lambda_k^{(r)}$, thus the following equation holds:

$$H^{(r)} \psi_k^{(r)} = \lambda_k^{(r)} \psi_k^{(r)}. \tag{62}$$

The frequency of the coherence of the $\psi_k{}^{(r)}$; $\psi_j{}^{(r)}$ function pair is $\omega_p{}^{(r)} = \lambda_j^{(r)} - \lambda_k^{(r)}$, and the amplitude of the corresponding transition is:

$$a_{kj}^{(r)} = \sum_{a,b} u_{ak} u_{bj} I_{ab}. \tag{63}$$

The intensity of the detected signal $(Y_{kj}^{(r)})$ is the square of the $a_{kj}^{(r)}$ amplitude (see Equation (5)).In spin systems with strong scalar coupling, the Φ_e coherences do not have characteristic frequencies; therefore, the spin set can get into any of the M possible basis coherences during precession and it can change its state at any moment as well. Instead of the Φ_e basis coherences, the $\Psi_p^{(r)}$ eigencoherences of the conformers are the ones remaining unaltered during precession as they precess with their characteristic frequencies. These $\Psi_p^{(r)}$ coherences are conformer dependent (represented by the superscript r in the notation) thus their role cannot be understood at exchange points. This duality leads to the fact that both coherence sets are necessary to simulate the trajectory of a spin set: eigencoherences are used for the description of free precession while basis coherences describe the exchange process correctly in the abstract spin space.

The pure basis states of the spin sets lead to mixed eigenstates in coupled spin systems, the extent of mixing is defined by the conformer-dependent probabilities:

$$P_{ak}^{(r)} = \left(u_{ak}^{(r)}\right)^2, \tag{64}$$

The conversion between the basis and eigenstates can be done at any time, but it has significance at the points of exchanges only. A similar connection exists between the coherences, knowing that the occurrence of the two states is independent from each other, thus the probability of the pth eigencoherence in case of the eth basis coherence is:

$$P_{ep}^{(r)} = P_{ak}^{(r)} P_{bj}^{(r)} = \left(u_{ak}^{(r)}\right)^2 \left(u_{bj}^{(r)}\right)^2. \tag{65}$$

If the coherences would be followed one by one, the number of possible pathways would increase enormously. Since the initial basis coherence can be any of the eigencoherences, and after the exchange it can continue with any frequency again, the number of possibilities increases exponentially with each exchange point. However, the system does not have 'spin memory'; at exchange points, it 'forgets' the frequency it precessed with until that time; and only the average of the results is that matters but the individuals do not. Thus the branching pathways of spin sets are meeting again and again at the exchange points, and the information explosion can be avoided.

In Figure 12, the population transfer of a spin set with two nuclei around the rth exchange point is shown. From time point $t^{(r-1)}$ (inside time slice r), the Φ_1 and Φ_2 coherences are distributed between the $\Psi_1^{(1)}$ and $\Psi_2^{(1)}$ eigenfunctions according to the coefficients defined in Equation (57). In the time slice (section D_{r-1}), precession goes on unaltered without any changes in the populations of eigentransitions. At exchange point (X_r), the populations of the $\Psi_1^{(1)}$ and $\Psi_2^{(1)}$ coherences are transferred

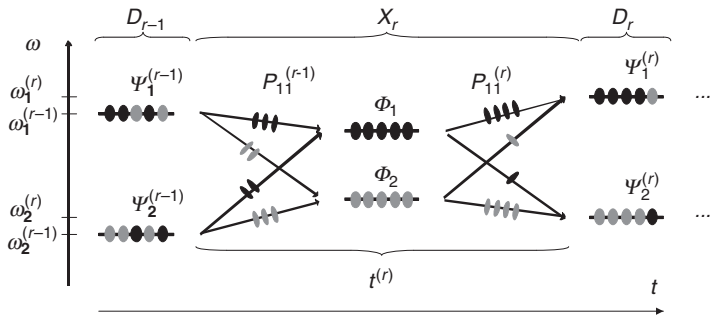

Figure 12 Population transfer during precession (D) and exchanges (X) at the rth exchange. The population of basis coherences (see spots on lines) is transferred to eigencoherences (and vice versa) based on the linear combination of coefficients (spots on arrows). Colours black and grey have no meaning apart from making the alterations in the population of coherences visible.

to the basis coherences. The basis coherences remain unaltered during the exchange, and only their populations are distributed among the new eigenfunctions (of section D_r); the cycle starts again with the only difference that the parameters of the conformer in the rth time slice have to be used.

3.6.2. Strong coupling in the vector model

The vector model of a single spin is the vector representation of the complex number in the individual density matrix of a single nucleus. This density matrix consists of only one complex number thus there is only one vector in the model. In the case of more than one nuclei, the density matrix is larger, there are more single quantum coherences and more vectors belong to one spin set in the model. Moreover, in case of a strongly coupled spin system, the density matrix has different numerical form for different basis sets of the vector space of the simulation (the basis can be one of the $\Psi^{(r)}$ and Φ function sets) thus several vector sets can appear in the vector model.

The aim of this extension of the vector model is to show the connection between the two types of coherences present during precession and exchange processes based on the mathematical formulae in Section 3.5.

The extension is demonstrated on the example of a non-mutual two-site exchange of a spin set of two nuclei. This process can be represented as an AB ↔ CD exchange when there is no coupling between the nuclei on separate sides of the equation. The simulated spectra of such a system are shown in Figure 13. At the slowest exchange rates (k), two overlapping

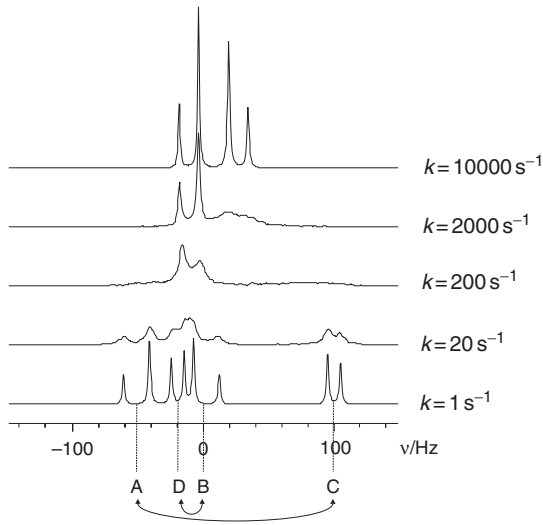

Figure 13 Simulated spectra of a non-mutually exchanging AB–CD spin system at different reaction rates (1000 scans, 512 points).

dublet–dublet pairs (corresponding to the AB and CD conformers) are present which upon increasing k coalesce and then sharpen resulting in a single dublet–dublet pair.

According to our interpretation (see Section 3.3.1), there are two conformers in this system: $A^{(1)}$ was denoted as AB and $A^{(2)}$ was CD. The statistical (KMC) description of the exchange process does not influence the vector model. The only important thing is that there are some exchange points during detection.

The spin set of two spins has four basis coherences ($\Phi_1 = |\alpha\beta\rangle\langle\alpha\alpha|$, $\Phi_2 = |\beta\alpha\rangle\langle\alpha\alpha|$, $\Phi_3 = |\beta\beta\rangle\langle\alpha\beta|$ and $\Phi_4 = |\beta\beta\rangle\langle\beta\alpha|$). Besides that each conformer has four eigencoherences ($\Psi_1^{(h)}$, $\Psi_2^{(h)}$, $\Psi_3^{(h)}$ and $\Psi_4^{(h)}$, where h is the index of the conformer), the characteristic frequencies of which were denoted by $\omega_p{}^{(h)}$ ($p = 1, \ldots, 4$ is the index of eigencoherences). These coherences can be separated into two independent blocks (as the Hamiltonian is blockdiagonal). The example shows only the first block (thus the values of p and e indices can only be 1 or 2).

The complex numbers, $\rho_{ab}(t)$ and $\xi_{kj}{}^{(r)}(t)$, denote the vectors belonging to $\Phi_e = |\phi_a\rangle\langle\phi_b|$ basis coherence and $\Psi_p{}^{(r)} = |\psi_k^{(r)}\rangle\langle\psi_l^{(r)}|$ eigencoherence at time point t (Figure 14). The transformation between these

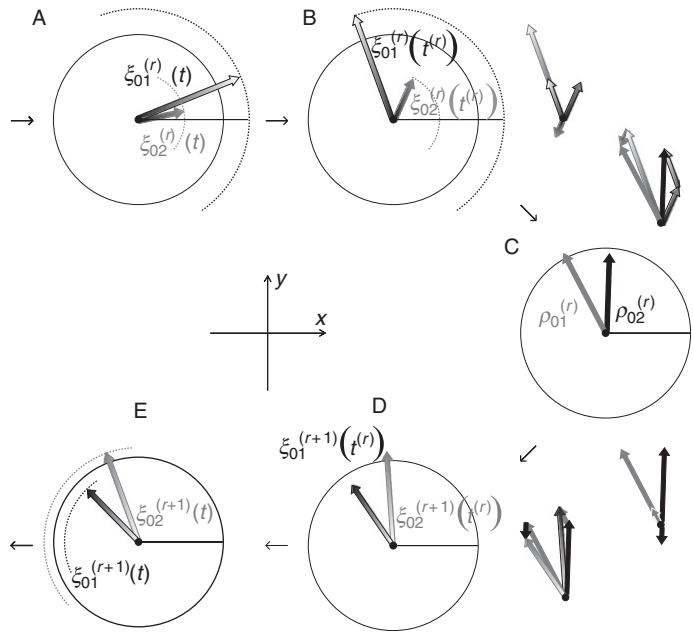

Figure 14 Calculation by vectors. (A) Precession of magnetisation vectors inside one time slice. (B) Position of vectors at the end of time slice ($t^{(r)}$). (C) Basis vectors present at $t^{(r)}$. An exchange is performed in this state. (D) Position of vectors at the beginning of the new time slice (still in $t^{(r)}$). (E) The two new eigenvectors start precessing in time slice $r + 1$.

two types of numbers (vectors) is formally similar to the one of the coherences (see Equation (61)):

$$\xi_{kj}^{(r)}(t) = \sum_{e} u_{ak}^{(r)} u_{bj}^{(r)} \rho_{ab}(t). \tag{66}$$

At a certain time slice (the rth), the $\xi_{kj}^{(r)}$ vectors representing the two eigenfunctions are precessing with $\omega_p^{(r)}$ frequencies (Figure 14A):

$$\xi_{kj}^{(r)}(t) = \exp\left(\mathrm{i}\omega_p^{(r)}\left(t - t^{(r-1)}\right)\right)\xi_{kj}^{(r)}\left(t^{(r-1)}\right). \tag{67}$$

Precession continues until the next exchange point ($t^{(r)}$) as shown in Figure 14B. At this point, the special role of the eigentransitions is lost therefore the vectors should be converted to the basis function representation. This is done according to Equation (66) ($\rho_{ab}^{(r)}$ is the short form for $\rho_{ab}(t^{(r)})$):

$$\rho_{ab}^{(r)} = \sum_{p} u_{ak}^{(r)} u_{bj}^{(r)} \xi_{kj}^{(r)}\left(t^{(r)}\right). \tag{68}$$

The results of this transformation are the $\rho_{ab}^{(r)}$ vectors (C). These vectors represent the basis coherences therefore they remain untouched during the exchange. The reaction itself is interpreted in basis coherence representation at this state. The simulation of the next ($r + 1$th) time slice is started from this point. At the beginning of time slice $r + 1$, the ρ vector is converted to the eigenfunction representation again (D) with the only difference that the parameters of the conformer in time slice $r + 1$ should be used in Equation (66):

$$\xi_{kj}^{(r+1)}\left(t^{(r)}\right) = \sum_{p} u_{ak}^{(r+1)} u_{bj}^{(r+1)} \rho_{ab}^{(r)}. \tag{69}$$

After that conversion precessions restart with the frequencies of the new conformer (E).This interpretation of the vector model shown in Figure 14 describes the evaluation of the elements of the density matrix only but not the detected signal. The FID is calculated from the actual elements of the eigenfunction representation of the density matrix (that is the $\xi_{kj}^{(r)}(t)$ vector) as:

$$\mathrm{fid}(t) = \sum_{p=1}^{2} a_{kj}^{(r)} \xi_{kj}^{(r)}(t), \tag{70}$$

where $a_{kj}^{(r)}$ is the complex amplitude of the corresponding signal as defined in Equation (63). The detected signal at the rth exchange point is shown in Figure 15. It may be noted, as a comparison, that in the case of

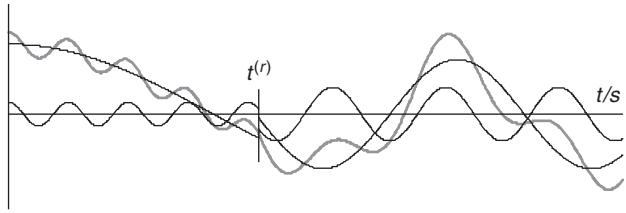

Figure 15 Calculation of the fid at an exchange point. The real part of the fids of two eigenvectors is shown before and after the exchange point. The total FID (grey curve) is the sum of the individual curves.

the single spin vector model or weak coupling $a_{kj}^{(r)} = 1$ for each value of r, k and j therefore the precessing vector represents the detected signal as well.[18]

4. SUMMARY

There is a common agreement among those who deal with the theory of DNMR spectrum simulations that the sum of the Hamiltonian of the whole spin system—incorporating all scalar couplings and exchange processes—and the matrix of the superoperator describing the exchange processes have to be calculated and diagonalised in the space of the single quantum coherences to get the spectrum. However, we have shown that it need not have to be done this way. Taking into account all of the single quantum coherences of the whole spin system is only a necessary enlargement of the simulation space due to the fact that the exchange processes cannot be described in the space spanned by the single quantum coherences of a spin set.

In this work, we have shown that the effects of the exchange processes and the scalar couplings can be separated in the simulation. The spin interactions are described by quantum mechanics while the dynamic effects are characterised by statistical methods. The easiest way to handle the latter one is by means of the KMC simulation.

The calculation method presented here also provides a possible extension of the single spin vector model. This extension is performed in two steps: first to weakly coupled spin systems, then to strongly coupled ones. In the first case, the introduction of the well-known product basis functions and their coherences is sufficient while in the latter one the solution is not so trivial. The crucial point is the interpretation of the linear transformation between the basis functions and the eigenfunctions (or coherences) during the detection and exchange processes. These two processes can be described by the population changes of single quantum

coherences and it cannot be handled by using the connection between basis and eigenfunctions. However, the mathematical description using the individual density matrix is complete in the Hilbert space, and there is no need of calculating in the larger space spanned by the coherences.

ACKNOWLEDGEMENTS

We would like to thank Dr. E. Rohonczy-Boksay for her useful comments. The Hungarian Research Foundation—OTKA (grant no. T-67835), the European Union and the European Social Fund have provided financial support to the project under the grant agreement no. TÁMOP 4.2.1/B-09/1/KMR-2010-0003.

REFERENCES

1. A. Gelling, K. G. Orrell, A. G. Osborne and V. Sik, *J. Chem. Soc., Dalton Trans.*, 1998, 937–945.
2. A. D. Bain, R. A. Bell, D. A. Fletcher, P. Hazendonk, R. A. Maharajh, S. Rigby and J. F. Valliant, *J. Chem. Soc., Perkin Trans.*, 1999, **2,** 1447–1453.
3. M. S. Ward, F. T. Lin and R. E. Shepherd, *Inorg. Chim. Acta*, 2003, **343,** 231–243.
4. F. Gasparrini, L. Lunazzi, A. Mazzanti, M. Pierini, K. M. Pietrusiewicz and C. Villani, *J. Am. Chem. Soc.*, 2000, **122,** 4776–4780.
5. M. Pons and O. Millet, *Prog. Nucl. Magn. Reson. Spectrosc.*, 2001, **38,** 267–324.
6. R. M. Claramunt, C. Lopez, M. D. Santa María, D. Sanz and J. Elguero, *Prog. Nucl. Magn. Reson. Spectrosc.*, 2006, **49,** 169–206.
7. B. M. Rode, C. F. Schwenk, T. S. Hofer and B. R. Randolf, *Coord. Chem. Rev.*, 2005, **249,** 2993–3006.
8. J. I. Kaplan and G. Fraenkel, NMR of Chemically Exchanging Systems. Academic Press, New York, 1980.
9. J. K. M. Sanders and B. K. Hunter, Modern NMR Spectroscopy. Oxford University Press, Oxford, 1993.
10. A. E. Derome, Modern NMR Techniques for Chemistry Research. Pergamon Press, Oxford, 1993.
11. J. Sandstrom, Dynamic NMR Spectroscopy. Academic Press, London, 1982.
12. R. R. Ernst, G. Bodenhausen and A. Wokaun, Principles of Nuclear Magnetic Resonance in One and Two Dimensions. Clarendon Press, Oxford, 1987.
13. L. M. Jackman and F. A. Cotton, Dynamic Nuclear Magnetic Resonance Spectroscopy. Academic Press, New York, 1975.
14. J. W. Emsley, J. Feeney and L. H. Sutcliffe, High Resolution NMR Spectroscopy. Pergamon Press, New York, 1965.
15. J. Rohonczy, D. Knausz, B. Csákvári, P. Sohár, I. Pelczer and L. Párkányi, *J. Organomet. Chem.*, 1988, **340,** 293–302.
16. H. S. Gutowsky and C. H. Holm, *J. Chem. Phys.*, 1956, **25,** 1228.
17. I. G. Darvey and P. J. Staff, *J. Chem. Phys.*, 1966, **44,** 990–997.
18. Z. S. Szalay and J. Rohonczy, *J. Magn. Reson.*, 2009, **197,** 48–55.
19. P. Sohár, Nuclear Magnetic Resonance Spectroscopy. CRC Press Inc., Boca Raton, Florida, 1983.
20. G. Binsch, *J. Am. Chem. Soc.*, 1969, **91,** 1304–1309.
21. R. Kubo, *J. Phys. Soc. Jpn.*, 1954, **9,** 935.
22. R. A. Sack, *Mol. Phys.*, 1958, **1,** 163.

23. A. G. Redfield, *Adv. Magn. Reson.*, 1965, **1,** 1.
24. S. Szymanski and G. Binsch, *J. Magn. Reson.*, 1989, **81,** 104–120.
25. D. S. Stephenson and G. Binsch, *J. Magn. Reson.*, 1978, **32,** 145–152.
26. D. A. Kleier and G. Binsch, *J. Magn. Reson.*, 1970, **3,** 146–160.
27. D. S. Stephenson and G. Binsch, *QCPE*, 1978, **11,** 365.
28. A. D. Bain, *Prog. Nucl. Magn. Reson. Spectrosc.*, 2003, **43,** 63–103.
29. A. D. Bain, D. M. Rex and R. N. Smith, *Magn. Reson. Chem.*, 2001, **39,** 122–126.
30. A. D. Bain and G. J. Duns, *J. Magn. Reson. A*, 1995, **112,** 258–260.
31. A. D. Bain, MEXICO3. http://www.chemistry.mcmaster.ca/bain/exchange.html. Accessed 03. 12. 2010.
32. R. S. Dumont, S. Jain and A. D. Bain, *J. Chem. Phys.*, 1997, **106,** 5928–5936.
33. R. S. Dumont, P. Hazendouk and A. D. Bain, *J. Chem. Phys.*, 2000, **113,** 3270–3281.
34. H. J. Reich, W. S. Goldenberg, B.Ö. Gudmundsson, A. W. Sanders, K. J. Kulicke, S. Simon and I. A. Guzei, *J. Am. Chem. Soc.*, 2001, **123,** 8067–8079.
35. H. J. Reich, *J. Chem. Educ. Software*, 1996, **3D, 2**. [EPub].
36. H. J. Reich, *J. Chem. Educ.*, 1995, **72,** 1086.
37. H. Reich, WINDMR 7.1. http://www.chem.wisc.edu/areas/reich/plt/windnmr.htm.
38. J. Rohonczy, DNMR Lineshape Analysis Software Manual, Version 1.1, Rev. 071103, Bruker BioSpin GmbH, TopSpin 2.1 package, 2007.
39. J. Rohonczy, *Kem. Kozl.*, 1992, **74,** 161–200.
40. MNova-NMR, 2010. http://mestrelab.com/Products/Mnova-NMR/Details.html.
41. iNMR, 2006. www.inmr.net.
42. K. Marat, SpinWorks. http://www.umanitoba.ca/chemistry/nmr/spinworks.
43. NUTS, 2010. http://www.acornnmr.com/nuts.htm.
44. V. F. Galat, A. N. Vdovichenko, A. Y. Chervinskii and L. M. Kapkan, *Theor. Exp. Chem.*, 1995, **31,** 105.
45. S. Chib and E. Greenberg, *Am. Stat.*, 1995, **49,** 327–335.
46. S. Rangełowa, L. Kułak, I. Gryczynski, P. Sakar and P. Bojarski, *Chem. Phys. Lett.*, 2008, **452,** 105–109.
47. M. S. Kelkar, J. L. Rafferty, E. J. Maginna and J. I. Siepmann, *Fluid Phase Equil.*, 2007, **260,** 218–231.
48. T. M. Alam, *J. Non-Cryst. Solids*, 2000, **274,** 39–49.
49. F. Liang and W. H. Wong, *J. Chem. Phys.*, 2001, **115,** 344–351.
50. U. H. E. Hansmann and Y. Okamoto, *Curr. Opin. Struct. Biol.*, 1999, **9,** 177–183.
51. A. F. Bilajev, Fundamentals of the Monte Carlo Method for Neutral and Charged Particle Transport. University of Michigan, Ann Arbor, Michigan, 2001.
52. I. T. Dimov, Monte Carlo Methods for Applied Scientists. World Scientific Publishing, Singapore, 2008.
53. M. Creutz, *Phys. Rev. Lett.*, 1983, **50,** 1411–1415.
54. J. Lee, *Phys. Rev. Lett.*, 1993, **71,** 211–215.
55. N. Metropolis, The beginning of the Monte Carlo method. *Los Alamos Sci.*, 125–130, Special Issue.
56. J. Sanz, C. P. Herrero and J.-L. Robert, *J. Phys. Chem. B*, 2003, **107,** 8337–8342.
57. G. Maurin, P. Senet, S. Devautour, P. Gaveau, F. Henn, V. E. Van Doren and J. C. Giuntini, *J. Phys. Chem. B*, 2001, **105,** 9157–9161.
58. M. O. Coppens, A. T. Bell and A. K. Chakraborty, *Chem. Eng. Sci.*, 1999, **54,** 3455–3463.
59. A. Lemak, C. A. Steren, C. H. Arrowsmith and M. Llinás, *J. Biomol. NMR*, 2008, **41,** 29–41.
60. D. Nathan and D. M. Crothers, *J. Mol. Biol.*, 2002, **316,** 7–17.
61. G. La Penna, A. Mitsutake, M. Masuya and Y. Okamoto, *Chem. Phys. Lett.*, 2003, **380,** 609–619.
62. E. Fieremans, Y. Deene, S. Delputte, M. S. Özdemir, Y. D'Asseler, J. Vlassenbroeck, K. Deblaere, E. Achten and I. Lemahieu, *J. Magn. Reson.*, 2008, **190,** 189–199.

63. L. F. Gladdena, M. Hargreavesa and P. Alexander, *Chem. Eng. J.*, 1999, **74,** 57–66.
64. P. Porion, L. J. Michot, A. M. Faugére and A. Delville, *J. Phys. Chem. C*, 2007, **111,** 5441–5453.
65. S. K. K. Lam, H. Peemoeller and Z. Y. Chen, *J. Colloid Interface Sci.*, 2002, **248,** 255–259.
66. D. N. Sears, R. E. Wasylishen and T. Ueda, *J. Phys. Chem. B*, 2006, **110,** 11120–11127.
67. E. Anoardo, F. Grinberg, M. Vilfan and R. Kimmich, *Chem. Phys.*, 2004, **297,** 99–110.
68. M. C. Böhm, R. Ramírez and J. Schulte, *Chem. Phys.*, 2007, **342,** 1–15.
69. J. S. J. Lee, R. O. Sokolovskii, R. Berardi, C. Zannoni and E. E. Burnell, *Chem. Phys. Lett.*, 2008, **454,** 56–60.
70. C. Chiccoli, P. Pasini, G. Skacej, C. Zannoni and S. Zumer, *Phys. Rev. E*, 1999, **60,** 4219–4225.
71. A. Galindo, G. Jackson and D. J. Photinos, *Chem. Phys. Lett.*, 2000, **325,** 631–638.
72. L. Rui-Yan, Q. Jing-Yu, G. Ting-Kun and B. Xiu-Fang, *J. Non-Cryst. Solids*, 2008, **354,** 1736–1739.
73. K. Itoh, M. Sonobe, M. Sugiyama, K. Mori and T. Fukunaga, *J. Non-Cryst. Solids*, 2008, **354,** 150–154.
74. M. Fábián, E. Sváb, Th. Proffen and E. Veress, *J. Non-Cryst. Solids*, 2008, **354,** 3299–3307.
75. K. D. Machadoa, D. F. Sanchez, J. C. de Limab and T. A. Grandi, *Solid State Commun.*, 2008, **148,** 46–49.
76. S. Mudry, I. Shtablavyi, V. Sklyarchuk and Y. Plevachuk, *J. Nucl. Mater.*, 2008, **376,** 371–374.
77. F. Utsuno, H. Inoue, Y. Shimane, T. Shibuya, K. Yano, K. Inoue, I. Hirosawa, M. Sato and T. Honma, *Thin Solid Films*, 2008, **516,** 5818–5821.
78. W. K. Luo and E. Ma, *J. Non-Cryst. Solids*, 2008, **354,** 945–955.
79. J. C. McLaughlin, S. L. Tagg, J. W. Zwanziger, D. R. Haeffner and S. D. Shastri, *J. Non-Cryst. Solids*, 2000, **274,** 1–8.
80. L. Pusztai, I. Harsányi, H. Dominguez and O. Pizio, *Chem. Phys. Lett.*, 2008, **457,** 96–102.
81. M. H. Sørby, A. Mellergard, B. C. Hauback, H. Fjellvag and R. G. Delaplane, *J. Alloys Compd.*, 2008, **457,** 225–232.
82. S. Takeda, H. Fujii, Y. Kawakita, S. Tahara, S. Nakashima, S. Kohara and M. Itou, *J. Alloys Compd.*, 2008, **452,** 149–153.
83. M. Wilding, Y. Badyal and A. Navrotsky, *J. Non-Cryst. Solids*, 2007, **353,** 4792–4800.
84. J. C. McLaughlin and J. W. Zwanziger, *J. Mol. Graph. Model.*, 1999, **17,** 275–284.
85. F. L. Tobiason, G. Vergotenb and J. Mazurierc, *J. Mol. Struct. THEOCHEM*, 1997, **395–396,** 173–185.
86. P. H. He, Y. Wu and R. F. Wu, *Curr. Appl. Phys.*, 2007, **7S1,** e63–e67.
87. J. D. Beek, B. H. Meier and H. Schäfer, *J. Magn. Reson.*, 2003, **162,** 141–157.
88. T. K. Hitchens, J. A. Lukin, Y. Zhan, S. A. McCallum and G. S. Rule, *J. Biomol. NMR*, 2003, **25,** 1–9.
89. D. T. Gillespie, *J. Comp. Phys.*, 1976, **22,** 403–434.
90. D. T. Gillespie, *J. Chem. Phys.*, 2000, **113,** 297–306.
91. M. Rathinam, R. L. Petzold, Y. Cao and D. T. Gillespie, *J. Chem. Phys.*, 2003, **119,** 12784–12794.
92. A. Slepoy, A. P. Thompson and S. J. Plimpton, *J. Chem. Phys.*, 2008, **128,** 205101.
93. D. T. Gillespie, *J. Chem. Phys. A*, 2002, **106,** 5063–5071.
94. B. H. Robinson, A. W. Reese, E. Gibbons and C. Mailer, *J. Phys. Chem. B*, 1999, **103,** 5881–5894.
95. M. Carl, G. W. Miller, J. P. Mugler, III, S. Rohrbaugh, W. A. Tobias and G. D. Cates, Jr., *J. Magn. Reson.*, 2007, **189,** 228–240.
96. C. Caia, Z. Chena, S. Caia and J. Zhong, *J. Magn. Reson.*, 2005, **172,** 242–253.
97. S. Vasenkov, J. Kärger, D. Freude, R. A. Rakoczy and J. Weitkamp, *J. Mol. Catal. A*, 2000, **158,** 373–376.

98. D. S. Grebenkov, G. Guillot and B. Sapoval, *J. Magn. Reson.*, 2007, **184,** 143–156.
99. D. Idiyatullin, S. Michaeli and M. Garwood, *J. Magn. Reson.*, 2004, **171,** 330–337.
100. E. L. Kovrigin, J. G. Kempf, M. J. Grey and J. P. Loria, *J. Magn. Reson.*, 2006, **180,** 93–104.
101. Z. S. Szalay and J. Rohonczy, *J. Magn. Reson.*, 2008, **191,** 56–65.
102. Z. S. Szalay and J. Rohonczy, *Prog. Nucl. Magn. Reson. Spectrosc.*, 2010, **56,** 198–216.
103. CUDA, http://www.nvidia.com/object/cuda_home.html.
104. Z. S. Szalay and J. Rohonczy, Fast calculation of DNMR spectra on CUDA enabled video card. *J. Comp. Chem.*, in press. DOI: 10.1002/jcc.2170.
105. CUDA 2.3 Programming Manual, http://developer.download.nvidia.com/compute/cuda/2_3/toolkit/docs/NVIDIA_CUDA_Programming_Guide_2.3.pdf. CUDA 2.0 Programming Manual, http://developer.download.nvidia.com/compute/cuda/2_0/docs/NVIDIA_CUDA_Programming_Guide_2.0.pdf.
106. A. D. Bain, *Conc. Magn. Reson. A*, 1998, **10,** 85–98.
107. M. Cuperlovic, G. H. Meresi, W. E. Palke and J. T. Gerig, *J. Magn. Reson.*, 2000, **142,** 11–23.
108. R. C. Ward, *SIAM J. Numer. Anal.*, 1977, **14,** 600–610.
109. N. J. Higham, Functions of Matrices: Theory and Computation. SIAM, Philaderphia, 2008.

SUBJECT INDEX